Space Geodetic Constraints on Plate Motion, Fault Creep, and Megathrust Coupling

Thesis by

Yuan-Kai Liu

In Partial Fulfillment of the Requirements for the
Degree of
Geophysics

CALIFORNIA INSTITUTE OF TECHNOLOGY
Pasadena, California

2026
Defended October 22, 2025

Yuan-Kai Liu
ORCID: [0000-0003-4032-9444]

To my family

For Elasticity is the temper of matter
to recover its place with vehemence.

—Christopher Smart (1722–1771)
Jubilate Agno

Curiouser and curiouser!

—Lewis Carroll (1832–1898)
Alice's Adventures in Wonderland

ACKNOWLEDGEMENTS

I am deeply indebted to my research advisor, Mark Simons, without whom I would not have begun and completed my PhD at Caltech Seismolab. His vision to see the broader picture and his "geophysical sense of smell" for linking observations to solid-Earth processes, geodynamics, and methods across different fields have been inspiring. Despite the weight of his responsibilities at JPL, he always made himself available when I needed guidance, yet gave me the trust and space to steer my own research and family life. I have always valued his humor, his candid and confident brilliance (sometimes mistaken for arrogance), and his persuasive, almost aggressive storytelling. I believe all these reflect his genuine and sincere commitment to both science and mentorship. I am grateful for his patience and support, and I hope this thesis marks not an end, but the beginning of my continued geophysical education and my connection to him as a mentor.

I thank Zachary Ross, my co-advisor, who welcomed me into his group during my first two years and guided my initial project. His keen sense for earthquake science, data-driven inference, and mathematics introduced me to a field as rich in research questions as it is in seismic events. He consistently encouraged me to self-learn and concentrate on what truly interested me. His ongoing patient and candid advice, even after I transitioned out of his group, has proved invaluable.

I thank my thesis committee members, Zhongwen Zhan and my academic advisor, Jennifer Jackson. The discussions whether in committee meetings or passing in the hallway, were often helpful to clarify the link between my work and the others'. Their deep engagement with diverse seismological and deeper Earth topics has been a constant source of fuel of my eagerness and ignorance to learn more.

My gratitude also extends to the many faculty members who generously shared their knowledge and perspectives. I thank Mike Gurnis, Rob Clayton, Joann Stock, Jean-Philippe Avouac, Nadia Lapusta, Allen Husker, Tom Heaton, Egill Hauksson, Hiroo Kanamori, and Sylvain Barbot for opening doors to fascinating fields I knew little about. The conversations during Coffee Hours, with papers and figures spread across the table, showed me how people in this building think about problems. If I leave the Seismolab feeling I have only scratched the surface of geophysics, it is in large part because of the high standard they have set.

I thank Howard Zebker, our common sabbatical visitor and my future postdoc

advisor, for patiently walking me through the mathematics of space geodesy during his sabbatical and for entrusting me with the opportunity to continue this work alongside him.

I have enjoyed discussions over the years with fellow graduate students, postdocs, cohorts, and colleagues. I especially thank my senior mentors inside Simon's group, Yunjun Zhang, Cunren Liang, Oliver Stephenson, Tobias Köhne, Yujie Zheng, and Rishav Mallick, for guiding me to navigate through the data, methods, and explore modelings. Without them, my PhD journey would have been much longer.

I am also grateful to my South Mudd 362 office mates from before and during COVID: Voon-Hui Lai, Zhichao Shen, Jorge Castellanos, Jack Muir, and Mara Ruso. Their consistent early-bird presence, daily greetings, and occasional lunch together provided steady support. Later, I was fortunate to share the office for quite some time with Leonid Pereiaslov, Yuri Tamama, Young Ho Aladro, Eitan Rapaport, and Jackson Fellows. All of these individuals have shaped my daily life in the Seismolab over the years. Though we mostly worked on our own tasks, the occasional chitchat and the simple act of seeing others steadily at work were always amusing and encouraging. A special mention goes to Yuri, your baking is truly the best in the building ever since Erin Hightower!

The collaborative atmosphere in Seismolab has been one of the most rewarding parts of my time there. I am grateful to my 2019 cohort—Yan Yang, Jimmy Atterholt, Benjamin Strozewski, and Ojashvi Rautela—for making the first two years of coursework a supportive journey, and for the continued camaraderie that followed. It has been an honor to grow alongside them, and I wish them the very best in their paths beyond the doctorate. Later, I came to appreciate even more how ideas in our lab often originate from sparks of brief, spontaneous discussions to quickly expand into real projects. The lab's smallness and the focus on solid-Earth processes is precisely what makes this kind of intellectual exchange enjoyable. In that spirit, I thank Ollie Stephenson and Yunjun Zhang for bringing me into their plate-motion and geolocation efforts. I thank Zhichao for our joint exploration of glacier repeating earthquakes in West Antarctica. I am grateful to Leonid for involving me in his coseismic inference studies from Türkiye to the Kuril Islands, and to Jack Wilding and Tayi Wang for inviting me to work on the compelling Santorini seismic swarm beneath the Aegean Sea.

I am also deeply grateful to the staff members at the Seismolab (South Mudd 252), whose support has been invaluable throughout my time here. In particular,

I thank Kim, Rosemary, Donna, Priscilla, Sarah, Alex, Monica, Ruth, Chelsea, America, and Joana. I am likewise grateful to Julie Lee and Jen Shechet in the Arms building for consistently looking after me. Their cheerfulness, humor, and unfailing reliability have made a genuine difference, and I especially appreciate the care they have extended not only to me but also to my family. They are, and will continue to be, the heart of the Seismolab in South Mudd.

I thank the people at JPL who have guided me since my first day in learning interferometry and synthetic aperture radar, both in and outside their duties: David Bekaert, Heresh Fattahi, Piyush Agram, Marin Govorcin, Grace Bato, Paul Rosen, and Eric Fielding. I wish them all the best as they navigate the challenges and/or new opportunities of their careers, both within and beyond JPL.

I thank my previous advisor during my master study, Sigurjón Jónsson, and the groups in CDI and Martin Mai's group at KAUST. They opened the door that made my path possible.

I owe more than words can express to my parents, grandparents, extended family, and especially my brother, who stayed with my parents when I could not. They have supported, loved, and forgiven me unconditionally through these years of absence. To my late father, whom I could not be with when he passed, I owe my deepest and most enduring gratitude. Their steady presence made all of this possible.

Switching between family and work is difficult for everyone, and I have often felt on the edge of failing at both. Thankfully, my two little girls keep me grounded and save me from becoming too obsessive or pedantic. They remind me of what matters beyond graduate school and show me how to explore the world again like a child. Most of all, the largest credit goes to my lifelong partner, Chia-Ying. Her role is multifaceted—it sometimes tests my sanity and, more often, sustains it. She is my companion while we bike, hike, drive, cook, care for and teach our children. She is both a good teacher and an earnest student. She listens to me talking about my work and asks questions I cannot always answer. When I am lost in idealistic visions or indecision, she is the rationale in the house. And while I have been doing this work, she has been doing everything else.

ABSTRACT

Earthquakes release centuries of accumulated elastic strain in seconds, yet where and how this strain builds up across fault systems remain only partly understood. The contrast between seismogenic asperities—regions that lock and rupture in earthquakes—and aseismic barriers that creep or remain stable defines the scale, frequency, and segmentation of major ruptures. Constraining the spatial extent and temporal persistence of these regions requires geodetic observations that resolve deformation from local fault zones to plate-wide strain fields.

In this thesis, I use spaceborne geodesy, specifically Interferometric Synthetic Aperture Radar (InSAR), to complement sparse Global Navigation Satellite System (GNSS) networks in quantifying crustal deformation and inferring tectonic processes across a continuum of spatial and temporal scales. We strive to understand how strain accumulates, transfers, and is released along major plate boundary systems within a probabilistic framework that explicitly incorporates uncertainty and prior assumptions.

I begin with the central San Andreas Fault (Chapter 1), where locked, transitional, and creeping segments coexist within a narrow zone of complex mechanical interaction. By jointly analyzing geodetic coupling and seismicity, I find that the fraction of background earthquakes scales with the aseismic slip rate normalized by the plate rate, suggesting a phenomenological link between fault coupling and micro-earthquake clustering.

I then address a broader methodological challenge in InSAR geodesy—the treatment of reference-frame motion and its influence on long-wavelength deformation gradients (Chapter 2). After applying refined tropospheric and ionospheric corrections and inversion of large-scale InSAR velocity fields, I show that the absolute Euler rotation of a tectonic plate can be directly estimated from InSAR data, offering an independent constraint on plate kinematics. This capability extends InSAR beyond local fault studies, enabling continental and even global mapping of tectonic deformation, which is a prospect that becomes increasingly viable with the advent of modern L-band radar missions capable of penetrating vegetation and maintaining coherence over wide spatial and temporal baselines.

Next, I examine the southern Dead Sea Transform and Gulf of Aqaba, where the Arabian and Nubian plates undergo transtensional motion as the transform transi-

tions into the Red Sea rift (Chapter 3). By compiling a decade of Sentinel-1 data, I map along-strike variations in fault coupling and localized extension toward the rift triple junction, delineating the gradual shift from strike-slip shear to crustal rifting.

Finally, I combine InSAR and GNSS time series to construct a spatially continuous model of interseismic coupling along the Nazca-South America margin (Chapter 4). The results reveal strong spatial correlations between heterogeneity in fault coupling and subducted bathymetric highs, underscoring the mechanical role of subducted topography in segmenting megathrust behavior and strain accumulation.

Through these studies, I demonstrate how integrating long-wavelength geodetic imaging allows one to map crustal deformation continuously from fault to plate scales with quantified confidence, while explicitly identifying regions where the data remain uninformative or ambiguous. In doing so, we aim to bridge observation and theory to connect the patterns we see from orbit to the physics that govern the accumulation of strain and seismic release of elastic strain within the Earth's dynamic lithosphere.

PUBLISHED MATERIALS

Liu, Y.-K., Ross, Z. E., Cochran, E. S., & Lapusta, N. (2022). A unified perspective of seismicity and fault coupling along the San Andreas Fault. *Science Advances*, 8(8), eabk1167. https://doi.org/10.1126/sciadv.abk1167

Y.K.L. participated in the conception of the project, performed the analysis, wrote the code, and drafted the original manuscript. This is Chapter 1.

Stephenson, O. L., Liu, Y., Yunjun, Z., Simons, M., Rosen, P., & Xu, X. (2022). The Impact of Plate Motions on Long-Wavelength InSAR-Derived Velocity Fields. *Geophysical Research Letters*, *49*(21), e2022GL099835. https://doi.org/10.1029/2022GL099835

Y.K.L. participated in the conception of the project, performed part of the analysis, and wrote the published code.

Liu, Y.-K., Yunjun, Z., & Simons, M. (2025). Inferring Tectonic Plate Rotations From InSAR Time Series. *Geophysical Research Letters*, *52*(12), e2025GL115137. https://doi.org/10.1029/2025GL115137

Y.K.L. participated in the conception of the project, performed the analysis, wrote the published code, and drafted the original manuscript. This is Chapter 2.

TABLE OF CONTENTS

LIST OF ILLUSTRATIONS

Number *Page*

LIST OF TABLES

INTRODUCTION

The topics covered in this thesis share a unifying goal: To measure and understand active tectonic processes operating along and across plate boundary zones. Ultimately, we aspire to reveal the mechanics and physics that govern these systems. In practice, however, I choose to begin not with theoretical equations, but with observations. We first have to measure, to filter, and to infer what the Earth is telling us. Only then can we test hypotheses about the underlying processes.

Tectonic processes on Earth span an immense range of spatial and temporal scales, from crystal-scale plastic deformation observed in laboratory experiments to continent-scale plate motions across thousands of kilometers. This thesis focuses on the latter: Quantifying crustal motion from observations to link measurable surface kinematics with relatively simple theoretical models of tectonics and fault mechanics assuming an elastic lithosphere. While some natural processes unfold within seconds, such as earthquake rupture, the emphasis here is on slow and quasi-steady deformation measured over multi-year timescales, with which we capture secular motion, yet still short compared to the full earthquake cycle or geological evolution.

This work comprises three overlapping foci, a structure borrowed from my advisor on the day I first stepped into his office. The first focus concerns the data itself—the effort to measure crustal deformation. From Harry Fielding Reid's triangulation survey after the 1906 San Francisco earthquake (Reid, 1910) to Japan's early coastal leveling following the 1923 Kantō event (Rikuti, 1930; Muto, 1932; Tsuboi, 1932), geophysicists sought to distinguish local elastic strain from broader crustal motion. In the language of continuum mechanics, the separation process corresponds to decomposing the total deformation (rate) tensor into a rigid–body component and a strain (or strain rate) component. Once a reference frame is defined, the remaining signal represents the crustal strain responsible for accumulating elastic stress and eventual failure in the form of earthquakes. For those primarily interested in the strain (rate) field, the rigid-body motion becomes a nuisance term that must be inferred and removed. In addition, each geodetic technique can introduce its own sources of complexities: from instrumental drift in leveling or gravimetry, common-mode errors in GNSS, to the atmospheric and range-dependent propagation delay in Interferometric Synthetic Aperture Radar (InSAR) measurements. These instrumental characteristics can convolve with the reference motion and worse, can contaminate estimates of strain. A large portion of this thesis focuses on obtain-

ing large-scale deformation measurements that are precise and relevant to tectonic processes of interest. This focus is the geodetic science.

The second focus concerns the inverse mapping from data to model. Here, the emphasis is not directly on reproducing Earth's physics, but on the mathematics of how we assign meaning to observations. Inverse problems that relate surface deformation to subsurface slip or strain are intrinsically ill-posed, requiring assumptions about smoothness, regularization, and prior information on the model. Different choices of priors or assumptions can yield equally good fits to the data yet imply different physical interpretations. Many models that begin with similar datasets diverge because of differences in model configuration and underlying assumptions. A goal of this thesis is to make these assumptions explicit and to quantify their influence within a probabilistic framework where appropriate. Thus, the second focus of this thesis is the inference science. In the context of linear inverse formulations, the emphasis is placed on examining the structure of the error model, the propagation of uncertainty, and the characterization of the resulting posterior distribution (e.g., Tarantola, 2005).

The third focus is to understand why faults and the lithosphere behave heterogeneously. Why some segments creep while others are coupled, and what constitutive laws in the medium govern the long-term deformation. These "holy-grail" questions belong to the realm of geophysical science. In this thesis, such discussions remain largely qualitative. The interpretations derived from the first two foci should be regarded as consequences of the elastic dislocation modeling—a purely kinematic description—rather than as fully mechanical explanations (e.g., the interpretation of the "coupling" we estimate is not a mechanical one (Wang & Dixon, 2004a)). Topics such as postseismic relaxation following great megathrust earthquakes in Chile, the relation between plate interface coupling and the subduction of seamounts and bathymetric highs along the trench, the thermal and extensional conditions driving transtensional rifting in the southern Gulf of Aqaba and Red Sea, or the hypothesis between rigid-plate versus diffuse deformation of continental interiors, all point to broader physical processes that this thesis just begins to touch. While these aspects extend beyond what I address here, the geodetic and inferential groundwork developed here forms a foundation to be built on in the future.

0.1 Modern large-scale tectonic geodesy

Geodetic observations of crustal deformation are fundamental for quantifying strain accumulation between earthquakes and constraining fault and plate kinematics. Global Navigation Satellite Systems (GNSS) have long served as the cornerstone of such measurements (e.g., Blewitt et al., 2018), providing millimeter-level precision but limited spatial density, especially near plate boundaries and in remote regions. Modern geodesy increasingly complements these sparse point observations with spaceborne imaging systems such as Interferometric Synthetic Aperture Radar (InSAR) (Bürgmann et al., 2000; Hanssen, 2001; Simons & Rosen, 2015). With the expanding archives from Sentinel-1 (Geudtner et al., 2014; Xu et al., 2021) and the newly launched NASA–ISRO Synthetic Aperture Radar (NISAR) mission (Rosen et al., 2025), InSAR now achieves millimeter-per-year precision over continental scales, providing unprecedented spatial continuity in velocity fields (e.g., Weiss et al., 2020; Lemrabet et al., 2023; Watson et al., 2024).

Interpreting InSAR velocity fields, however, requires careful treatment of correlated noise and long-wavelength covariance structures (Hanssen, 2001; Fournier et al., 2011; Parizzi et al., 2021). In early deformation studies focused on coseismic or postseismic events (e.g., Massonnet et al., 1993; Simons, 2002; Fialko, 2006), long-wavelength signals in interferograms were commonly removed empirically as orbital or atmospheric artifacts. While such deramping was acceptable for local fault-scale deformation, it inevitably flattened interesting tectonic gradients in regional to continental analyses. To recover meaningful large-scale deformation, we must now explicitly correct as much as possible for sources of propagating delay beyond the tectonic signal of interest. Modern satellites benefit from precise orbital ephemerides (Peter et al., 2020; Peter et al., 2021), while improved tropospheric (Jolivet et al., 2014; Hersbach et al., 2020) and ionospheric (Gomba et al., 2016; Fattahi et al., 2017b; Liang et al., 2019) correction schemes now allow us to preserve more long-wavelength signals with confidence. At even broader scales, corrections for solid Earth tides and ocean tidal loading are essential (DiCaprio & Simons, 2008; Milbert, 2018; Yunjun et al., 2022). Finally, recent advances have clarified how to interpret InSAR velocities within the satellite reference frame (Bähr et al., 2012; Bähr, 2013; Stephenson et al., 2022), enabling us to extract true crustal deformation gradient at the given reference plate. In effect, our understanding in InSAR has matured to the level where it can now complement GNSS in recovering both relative and absolute motions across Earth's surface.

This thesis contributes directly to the development of spaceborne geodesy, including improving ionospheric correction strategies, refining the treatment of reference-frame motion, and applying these methods to large-scale tectonic systems. The work demonstrates how InSAR and GNSS together can constrain plate-scale kinematics and internal strain consistently, thereby enabling us to bridge the scales between individual faults and that of the lithosphere and upper mantle.

0.2 Overview of the Thesis

Observations of active crustal deformation before, during, and after earthquakes provide critical constraints on how strain accumulates and is released along plate boundaries. Such measurements illuminate the regional strain budget, the seismogenic potential of faults, and the mechanical properties of the crust and upper mantle. In this thesis, I examine active deformation across multiple spatial and temporal scales—ranging from discrete fault zones to diffuse plate boundaries—using spaceborne geodetic data. In particular, Interferometric Synthetic Aperture Radar (InSAR) time series now permit large-scale (hundreds to thousands of kilometers) and high-resolution observations of crustal motion. These data, when interpreted within probabilistic frameworks, allow us to infer fault kinematics and the degree of mechanical coupling with quantified uncertainty.

In Chapter 1, we focus on the central San Andreas Fault (CSAF), a microcosm that exhibits nearly the full spectrum of fault slip behavior—from fully locked to steadily creeping segments. By jointly analyzing the spatial–temporal distribution of seismicity from earthquake catalogs and the geodetic coupling derived from space-based geodesy, we find that the aseismic slip rate scales consistently with the rate of background (non-clustered) earthquakes. We propose that when the seismic record spans multiple cycles and is sufficiently instrumented, the fraction of such background events can serve as a practical proxy for the geodetic coupling coefficient. This relationship may represent a fortuitous case along the San Andreas Fault, where the duration and completeness of the instrumental era happen to be just long enough to reveal such a correlation. While the relationship is undoubtedly over-simplified, it supports a generalized view of fault kinematics in which spatial variations in seismic clustering reflect differences in mechanical coupling and stress release. These coupling–seismicity correlations provide a phenomenological bridge between geodetic and seismic observations and offer a conceptual basis for interpreting interseismic processes along other fault systems.

In Chapter 2, we examine crustal motion at the plate scale and address a long-standing challenge in InSAR geodesy—the influence of reference-frame motion. Historically, broad long-wavelength gradients in InSAR velocity fields were often treated as orbital artifacts or atmospheric noise and consequently removed during processing. However, with recent advances in ionospheric correction, tropospheric modeling, and orbital control in modern satellites, these gradients can now be preserved and interpreted as genuine signals of large-scale crustal motion. Building on this capability, and motivated by earlier findings (Stephenson et al., 2022), we show that the bulk plate motion expressed in the International Terrestrial Reference Frame (ITRF) can be directly inferred from the spatial gradients in InSAR velocities. Rather than applying predefined plate-motion corrections, we take an inverse approach to infer the Euler rotation of the plate directly from the InSAR data. Using a geologically rigid plate as a test case, we demonstrate that, although GNSS remains superior for absolute kinematic constraints, under favorable conditions, InSAR can contribute to absolute reference-frame determination consistent with GNSS-based solutions. This work contributes to our understanding of the role of large-area InSAR imaging to determining reference frame motion.

In Chapter 3, we focus on the Dead Sea Transform Fault and the Gulf of Aqaba, an active transtensional boundary between the Arabian and Nubian plates that has produced large earthquakes up to M_w 7.2. Previous GNSS-based studies revealed heterogeneous fault locking but were limited by sparse spatial coverage. By exploiting a decade of Sentinel-1 InSAR data, corrected for ionospheric and tropospheric delays, we resolve interseismic deformation at sub-millimeter-per-year precision over a 250 km-wide zone. The results reveal spatial variations in locking depth and highlight extension toward the southern Gulf of Aqaba, where the transform fault transitions into the opening Red Sea rift system. This study illustrates how dense geodetic imaging measured from multiple line-of-sight viewing geometries can constrain slow deformation that bridges the strike-slip creep and extensional regimes.

In Chapter 4, we turn to a subduction environment to examine the large-scale interplate coupling along the Peruvian–Chilean margin. Here, the Nazca Plate subducts beneath South America at ~67 mm yr^{-1} (Altamimi et al., 2012; Métois et al., 2012; Jarrin et al., 2023), producing repeated great earthquakes and a strongly segmented megathrust (e.g., Ruiz et al., 2014; Lay & Nishenko, 2022). By jointly inverting a decade of InSAR and GNSS observations (2014–2025), we derive one of the first

continuous, InSAR-based interseismic coupling models for a continental subduction zone. The results reveal strong correlation between coupling heterogeneity and subducting bathymetric features—such as the Nazca, Iquique, Copiapó, and Challenger ridges—highlighting the role of subducted topography and fluids in modulating frictional behavior and seismic segmentation along the Andean margin.

Together, these chapters demonstrate significant progress in our ability to integrate InSAR and GNSS data to recover crustal motion and interplate coupling across different tectonic environments, from transform faults to subduction zones. The approaches described herein provide a unified toolbox and perspective for geodetic mapping and interpreting strain accumulation throughout the seismic cycle, bridging plate-scale kinematics and fault-scale deformation through large-area geodetic observations.

Editorial note:

To enhance the clarity and readability of the introductory text, I used ChatGPT and the Overleaf LanguageTool for proofreading and linguistic refinement. All scientific content including chapter abstracts, introductions, methods, data analysis, figures, captions, tables, discussions, and conclusions was written by me. In Chapters 3 and 4 (currently unpublished), ChatGPT was employed as a language assistant to suggest grammatical corrections, alternative wordings, and concise rephrasing of the introductory sections, based entirely on my original text. Whenever these tools were used, the use was indirect and iterative: all outputs were reviewed, revised, and finalized by me. No part of the published articles in Chapters 1 and 2 was edited by these tools.

Chapter 1

A UNIFIED PERSPECTIVE OF SEISMICITY AND FAULT COUPLING ALONG THE SAN ANDREAS FAULT

This chapter has been published in:

Liu, Y.-K., Ross, Z. E., Cochran, E. S., & Lapusta, N. (2022). "A unified perspective of seismicity and fault coupling along the San Andreas Fault." *Science Advances*, 8(8), eabk1167. https://doi.org/10.1126/sciadv.abk1167

ABSTRACT

The San Andreas Fault (SAF) showcases the breadth of possible earthquake sizes and occurrence behavior; in particular, the central SAF is a microcosm of such diversity. This section also exhibits the spectrum of fault coupling from locked to creeping. Here, we show that the observations of aseismic slip, temporal clustering of seismicity, and spatial variations in earthquake size distributions are tightly connected. Specifically, the fraction of non-clustered earthquakes for the period 1984-2020 is shown to be directly proportional to the creep rate (normalized by the plate rate) along the central SAF. This relationship provides a unified perspective of earthquake phenomenology along the SAF, where fault segments with lower coupling manifests in weaker temporal clustering, with repeating earthquakes as an end-member. This new paradigm provides additional justification for characterizing the northwest ~75 km of the creeping segment as a transition zone, with potential implications for seismic hazard.

Authors' note (2025)— While this chapter reproduces the 2022 publication (Liu et al., 2022), it should be emphasized that the observed proportionality relies on an earthquake catalog ideally spanning a full seismic cycle (or even multiple cycles), which may approximately hold for the central SAF since the 1980s. In addition, both the creep rate and seismicity clustering are instantaneous observations made over a limited instrumental window (from a few years to several decades). This behavior is not necessarily stationary in geological time.

1.1 Introduction

Active fault zones exhibit remarkable diversity in their seismic activity over space and time. Some fault zones are silent, not producing even a single detectable earthquake over decades, while others produce incessant, steady activity on a daily basis (Sanders & Kanamori, 1984). In some places, the spatial distribution of seismicity is highly localized to small zones that are hundreds of meters wide (Shearer, 2002), but in other places is distributed across tens of kilometers (Ross et al., 2017). The San Andreas Fault (SAF) in California is perhaps the epitome of such varied behavior, as it demonstrates essentially the entire spectrum of earthquake behavior along its ~1100 km length. Such variability can even occur over relatively short distances, as seen for example on the central section of the fault (Fig. 1.1), which produces large damaging earthquakes, repeating earthquakes (Uchida & Bürgmann, 2019), tectonic tremor (Shelly, 2010), and occasional swarms.

Variability in the spatial and temporal distributions of earthquakes may result from differences in the mechanical properties of the fault. In particular, frictional properties can have a first-order effect on most aspects of earthquake source processes (Kanamori & Brodsky, 2004), and variations in such properties should have a major impact on the space-time patterns of the seismicity (Ben-Zion & Lyakhovsky, 2006; Kaneko et al., 2010; Barbot et al., 2012). Perhaps the strongest observational evidence of the link between frictional properties and earthquake behavior comes from faults exhibiting assorted aseismic slip phenomena, such as slow slip transients, steady creep, and postseismic deformation (Bürgmann, 2018). The presence (or lack thereof) of aseismic processes is often explained with the concept of fault coupling (Pacheco et al., 1993; Wang & Dixon, 2004b; Avouac, 2015), whereby fault behaviors lie on a spectrum from fully-locked to fully-creeping. Here, we use the term coupling to represent a purely kinematic notion defined by the ratio of the slip deficit rate to the total slip rate from plate motion models or geologic records. Faults with low coupling are often seen to have seismicity patterns distinct from those with strong coupling, which include characteristically repeating earthquakes (Waldhauser & Schaff, 2008; Uchida & Bürgmann, 2019), pronounced spatial streaks of seismicity (Rubin et al., 1999), and a lack of moderate-to-large earthquakes. In several subduction zones, aftershock productivity and spatial density have been shown to correlate with coupling estimates from fault slip across seismic cycles (Zakharova et al., 2017; Hainzl et al., 2019). Together, these studies provide clues linking coupling variations to aftershock productivity. Despite these seminal observations, we still lack a comprehensive and unified understanding of

how the dynamics of seismicity is related to the degree of coupling on major faults, like the SAF.

Geodetic investigations of faults have revealed that coupling often varies strongly in space (Avouac, 2015; Bürgmann, 2018), with more strongly-coupled faults defining potential areas of coseismic moment release during great earthquakes (Konca et al., 2008). Faults with low coupling accommodate most of their slip as stable sliding (Scholz, 1998). Factors controlling coupling include a combination of effective stress and frictional properties related to rheological and geometrical changes on the fault interface (Moore & Rymer, 2007; Saffer & Wallace, 2015; Sun et al., 2020). Earthquakes are associated with stick-slip failure of asperities (i.e. regions that experience coseismic slip with negligible interseismic creep), which fail recurrently as strain accumulates (Brace & Byerlee, 1966; McLaskey & Glaser, 2011). This leads to the expectation that seismicity rates should be generally higher along faults with higher slip rates. For example, subduction zones around the Pacific show a positive correlation between the background rate of earthquakes and the plate convergence rate (Ide, 2013).

Among major fault systems worldwide, the SAF stands out as demonstrating the complete range of interseismic coupling along-strike (Titus et al., 2006; Maurer & Johnson, 2014; Jolivet et al., 2015). In fact, this variability can be seen within just the central ~225 km section of the fault (Fig. 1.1), despite a relatively uniform long-term right-lateral slip rate of 34 ± 3 mm per year from both geologic and geodetic observations (Titus et al., 2011). These aspects, together with the wealth of available high-quality seismic and geodetic observations, make the central SAF an ideal setting to study the relationship between fault coupling and the dynamics of seismicity over decadal timescales.

1.2 Methods

To characterize the long-term behavior of seismicity, we use a simple measure of the average temporal clustering, which we refer to as the fraction of non-clustered events. This metric lies between zero and one, and follows long-standing practices in statistical seismology that model seismicity rates as composed of a homogeneous Poisson process background, along with a branching-process-type mechanism for generating earthquake clustering e.g. Ogata, 1988; Zaliapin & Ben-Zion, 2013. To estimate the fraction of non-clustered events in an earthquake catalog, we calculate the mean of the normalized interevent times (waiting times between consecutive

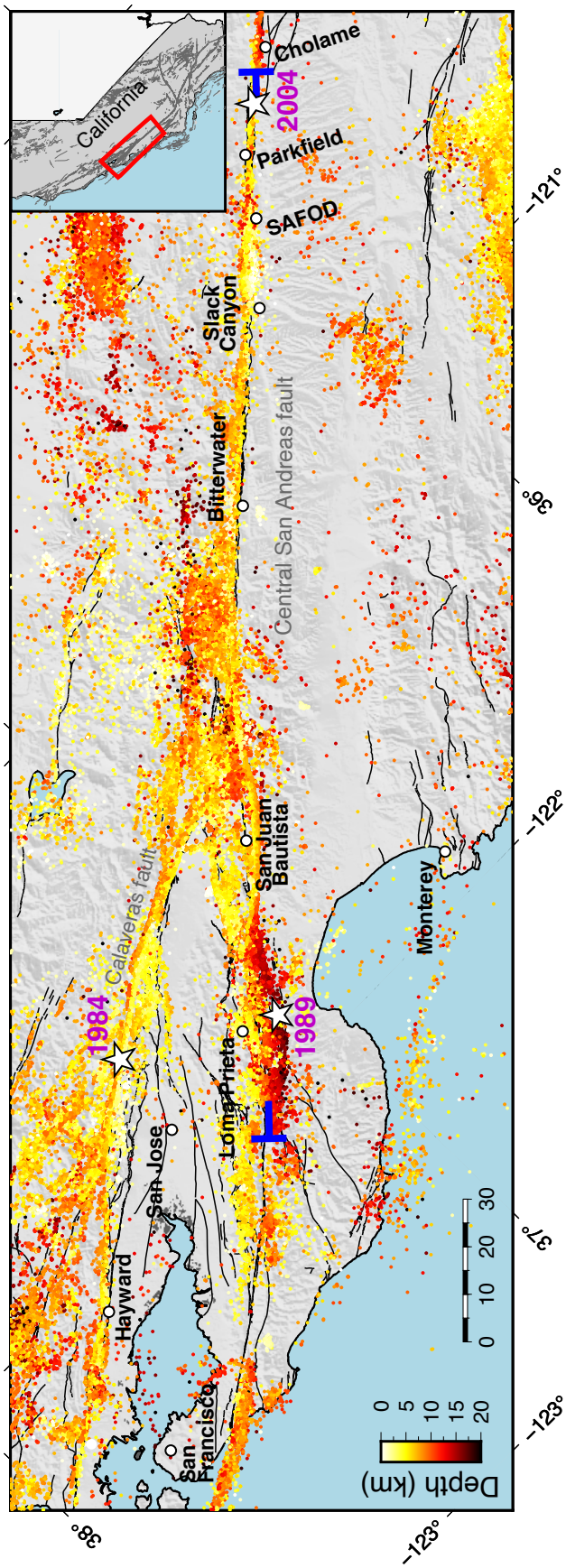

Figure 1.1: Seismicity near the central San Andreas Fault. Our analysis covers seismicity between blue "T" symbols and within 5 km of the fault trace, except for regions north of San Juan Bautista where ±10 km is used to include deep seismicity on a dipping fault. Large historical earthquakes are plotted with white stars, corresponding to the 1984 M6.2 Morgan Hill, 1989 M6.9 Loma Prieta, and 2004 M6.0 Parkfield events. Fault surface traces marked by solid black lines are from the U.S. Geological Survey Quaternary Fault and Fold Database (U.S. Geological Survey and California Geological Survey, 2006).

earthquakes) over the variance of the normalized interevent times. This is equivalent to fitting a Gamma distribution to the interevent times (details are shown in Supplementary Materials) of the seismicity under the assumption that the general seismicity population is comprised of Poissonian-distributed independent non-clustered events superimposed with triggered aftershocks following the Omori law (Molchan, 2005; Hainzl et al., 2006). This method of interevent-time statistics does not rely on any particular triggering mechanism or declustering algorithm. Under this framework, the fraction of non-clustered events in a pure aftershock sequence that follows the modified Omori law (Utsu & Ogata, 1995) is assumed to be zero. We note that some aftershock models treat every earthquake as a background event e.g. Dieterich, 1994, in which they do not decompose the rates into clustered and non-clustered.

Seismicity catalog

The dataset used in this work is the Northern California Seismic Network double-difference (DD) earthquake catalog (Schaff & Waldhauser, 2005; Waldhauser & Schaff, 2008; Waldhauser, 2009). The automatic and routinely relocated earthquake catalog was downloaded from the Northern California Earthquake Data Center. The catalog covers events of the entire central and northern California since January of 1984 to February of 2021. We further select a subset of this catalog along the strike of the 225-km-long central San Andreas Fault (central SAF) extending from around Loma Prieta in the northwest (122.25°W, 37.40°N) to near the Carrizo segment in the southeast (120.14°W, 35.59°N) within ±5 km distance from the fault. The majority of the hypocenters locate at around 2 to 8 km depth (Fig. S1). To include the deeper events from the 1989 Loma Prieta sequence which sit on a dipping fault plane, we increase the width of our data selection to ±10 km for the region north of San Juan Bautista.

The regions further north of the Loma Prieta and further south of Cholame (the Carrizo segment) are dominated by rarely occurring historic large mainshocks and aftershocks. These include the 1857 M7.9 Fort Tejon earthquake (Sieh, 1978) in the south, 1906 M7.9 San Francisco earthquake (Wald et al., 1993) in the north. The above segments at the both ends of our study profile have insufficient events during periods devoid of large shocks for interevent-time analysis and thus can easily lead to overestimation of the fraction of non-clustered seismicity due to the sampling bias (Marsan et al., 2013). We hereby exclude these portions of the central SAF from our discussion.

Magnitude of completeness estimation

The magnitude of the catalog is duration magnitude (M_d). We assess the magnitude of completeness (M_c) using the maximum curvature (MAXC) method (Wiemer & Wyss, 2000). This method defines the point of the maximum curvature as the magnitude of completeness by computing the maximum value of the first derivative of the frequency-magnitude distribution curve. In practice, it is equivalent to the magnitude bin with the highest frequency of events in the non-cumulative frequency-magnitude distribution. Since the MAXC technique tends to slightly underestimate the magnitude of completeness, we add 0.2 for correction (Woessner & Wiemer, 2005). Based on the selected subset of the catalog, we estimate M_c for every year from 1984 to 2021 and find that the values are within the range of 0.8–1.5 (Fig. S2). We thus set a constant minimum magnitude M_{min}=1.5 for the entire analysis, which results in 24,082 events over 37 years (Fig. S3). With this subset catalog, we apply a moving spatial window along the fault (15 km along-strike by 10 km fault-normal, step size 1 km) and compute properties of seismicity within the spatial window. We also make sure that, within each window, there are more than 1,000 events larger than M_c. The computed seismicity properties, including b-values, non-clustered seismicity rate, and fraction of non-clustered seismicity, are described in the following sections.

b-value estimation

We estimate the b-value of the dataset with the maximum likelihood method proposed by Aki (Aki, 1965), where, for each subset of events within the spatial window, the b-value is computed as:

$$b = \frac{log_{10}(e)}{\overline{M} - M_{min}}$$

where e is the Euler's number, $\overline{M}$ is the mean magnitude of the seismicity, and M_{min} = 1.5 is the chosen cutoff magnitude. The estimated b-values in our dataset range from 0.6 to 1.2 along the central SAF.

Non-clustered seismicity rate and fraction of non-clustered seismicity

Under the framework of Epidemic-type Aftershock-sequences Model (Kagan & Knopoff, 1981; Ogata, 1988; Ogata, 1999), we assume that the earthquake catalog is composed of two types of events in terms of temporal clustering behavior: one

is the clustered seismicity which is triggered by other events and their occurrences follow the Omori law (Utsu & Ogata, 1995; Ogata, 1999). The other type is the non-clustered seismicity which are independent from each other and follows the homogeneous Poisson process. The former is equivalent to aftershocks, while the later represents the background seismicity. Our analysis in the main text is based on the fraction of non-clustered seismicity in the earthquake catalog. Based on the mild assumptions that general seismicity has Poissonian non-clustered events superimposed with triggered aftershocks that follow the Omori law, it has been shown that the non-clustered seismicity rate could be estimated with methods based on the distribution of waiting times (interevent times), Δt, between consecutive earthquakes (Corral, 2004) proposed that the probability density function of interevent times of general seismicity can be approximated as a Gamma distribution:

$$P(\Delta t) = C \cdot \Delta t^{\gamma-1} \cdot \exp^{-\Delta t \mu}$$

i.e.,

$$\Delta t \sim \Gamma(\gamma, \mu)$$

where C is a normalization constant, μ is the non-clustered seismicity rate, and γ is a model parameter. The Gamma distribution, $\Gamma(\gamma, \mu)$, is assumed to be flexible enough to capture a range of behavior that the interevent times of seismicity could exhibit. Molchan (Molchan, 2005) and Hainzl et al. (Hainzl et al., 2006), based on the theoretical analysis, further showed that the non-clustered seismicity rate, μ, can be estimated from the first two sample moments of the interevent times:

$$\mu = \frac{E\{\Delta t\}}{var\{\Delta t\}} = \frac{\overline{\Delta t}}{\sigma^2_{\Delta t}}$$

Here, $E\{\Delta t\} = \overline{\Delta t}$ denotes the mean, and $var\{\Delta t\} = \sigma^2_{\Delta t}$ is the variance of the interevent times. Alternatively, we can have a similar form based on the normalized interevent times, τ (where $\tau = \Delta\, t/\overline{\Delta\, t}$), relative to the mean value of a set of events (16):

$$p(\tau) = C' \cdot \tau^{\gamma'-1} \cdot \exp(\tau/\beta)$$

$$\frac{1}{\beta} = \frac{E\{\tau\}}{var\{\tau\}} = \frac{\overline{\tau}}{\sigma_\tau^2} = \frac{1}{\sigma_\tau^2} = \frac{\mu}{\lambda}$$

where λ is the total seismicity rate ($\lambda = 1/\Delta t$). Therefore, the dimensionless factor, $1/\beta$ encapsulates the fraction of non-clustered seismicity in the catalog, ranges from 0 to 1, generally. With $1/\beta = 1$, there are no triggered and temporally clustered earthquakes, and all events are non-clustered events; While $1/\beta = 0$ denotes all events are triggered and clustered seismicity as a pure aftershock sequence that follows Omori law would exhibit. Intermediate values in between represent the relative measure of non-clustered events activity in the catalog. Note that the branching ratio (the fraction of triggered events in a catalog) is just the fraction of non-clustered seismicity subtracted from one.

$$n = 1 - \frac{1}{\beta} \in [0, 1]$$

Therefore, by calculating the mean of interevent times over the variance of interevent times, we have an estimate of the non-clustered seismicity rate in the catalog. Further normalizing the non-clustered seismicity rate with respect to the total seismicity rate gives us the fraction of non-clustered events. Rather than relying on any particular triggering mechanism or declustering algorithm, this technique is robust given the seismicity catalog is complete. It only depends on a simple metric of interevent times from a set of events, and magnitude is not considered into this formulation.

However, event subsets are not ideal under this framework if they deviate significantly from the general mixture of independent non-clustered events (Poisson point process) and triggered events (following the Omori law). For example, fitting a Gamma distribution to a perfect characteristic repeating earthquake sequence with exactly the same interevent times would result in a non-clustered rate of infinity, thus an infinite fraction of non-clustered events. Although observed repeater sequences rarely recur with an exactly constant time interval, the high periodicity of a repeater sequence can still result in a non-clustered event fraction larger than 1.0 based on this model, which is unphysical. A combination of many different repeating earthquake sequences (different interevent times) with many non-repeating events may be fine in adopting this framework. Also, event subsets with only aftershocks are also shown to give an overestimated non-clustered fraction (Marsan et al., 2013).

Uncertainty of the estimates of the seismicity:

We use confidence intervals to present the uncertainty of estimates on seismicity properties. The 95% confidence interval of the non-clustered seismicity rate, the fraction of non-clustered seismicity, and the b-value presented in Fig. S4, are based on the bootstrapping method. We repeatedly and randomly resample the magnitude data for 10,000 times with replacement and calculate the b-value each time. We also repeatedly resample the interevent-time data with replacement and calculate the non-clustered seismicity rate and the fraction of non-clustered seismicity. For these 10,000 sets of sampling distributions, we take the 2.5^{th} and 97.5^{th} percentiles to represent the lower bound and the upper bound of the 95% confidence interval.

1.3 Results

We estimate the fraction of non-clustered events along the 225-km-long section of the central SAF, starting from the rupture of the 1989 M_w 6.9 Loma Prieta earthquake in the northwest to Cholame Valley in the southeast (Fig. 1.1, 1.2a). The fraction of non-clustered events strongly varies along strike from less than 0.1 to ~0.8 (Fig. 1.2a). A high fraction of non-clustered events is observed near Slack Canyon, with a value of ~0.8. The segment with the highest fraction of non-clustered events stretches from ~5 km north of SAFOD (San Andreas Fault Observatory at Depth) to the vicinity of Bitterwater (near the southern termination of another fault with creep, the Calaveras Fault). These large values indicate that, despite considerable seismic activity since 1984, there has been a near-absence of temporal clustering in the seismicity. This 60-km-long segment coincides with the highest creep rates anywhere on the SAF, which are close to the plate rate of ~3 cm/yr (Titus et al., 2011). The interseismic surface creep rate in the satellite line-of-sight direction, measured with Interferometric Synthetic Aperture Radar (InSAR), was found to range from 6 to 7 mm yr^{-1} within this segment; this corresponds to 25-30 mm yr^{-1} of right-lateral plate motion parallel to the fault (Tong et al., 2013a; Jolivet et al., 2015).

Farther northwest along the fault, from the northern edge of the fast creeping segment to San Juan Bautista, we observe an intermediate value for the fraction of non-clustered events between 0.4 to 0.5. Thus, a larger portion of these events are aftershocks, compared with the fast creeping segment. The InSAR line-of-sight creep rate is also lower along this segment, at about 4 mm per year (Jolivet et al., 2015). Northwest of San Juan Bautista, along the Loma Prieta segment, the fraction of non-clustered events drops to less than 0.1 and corresponds to minimal creep

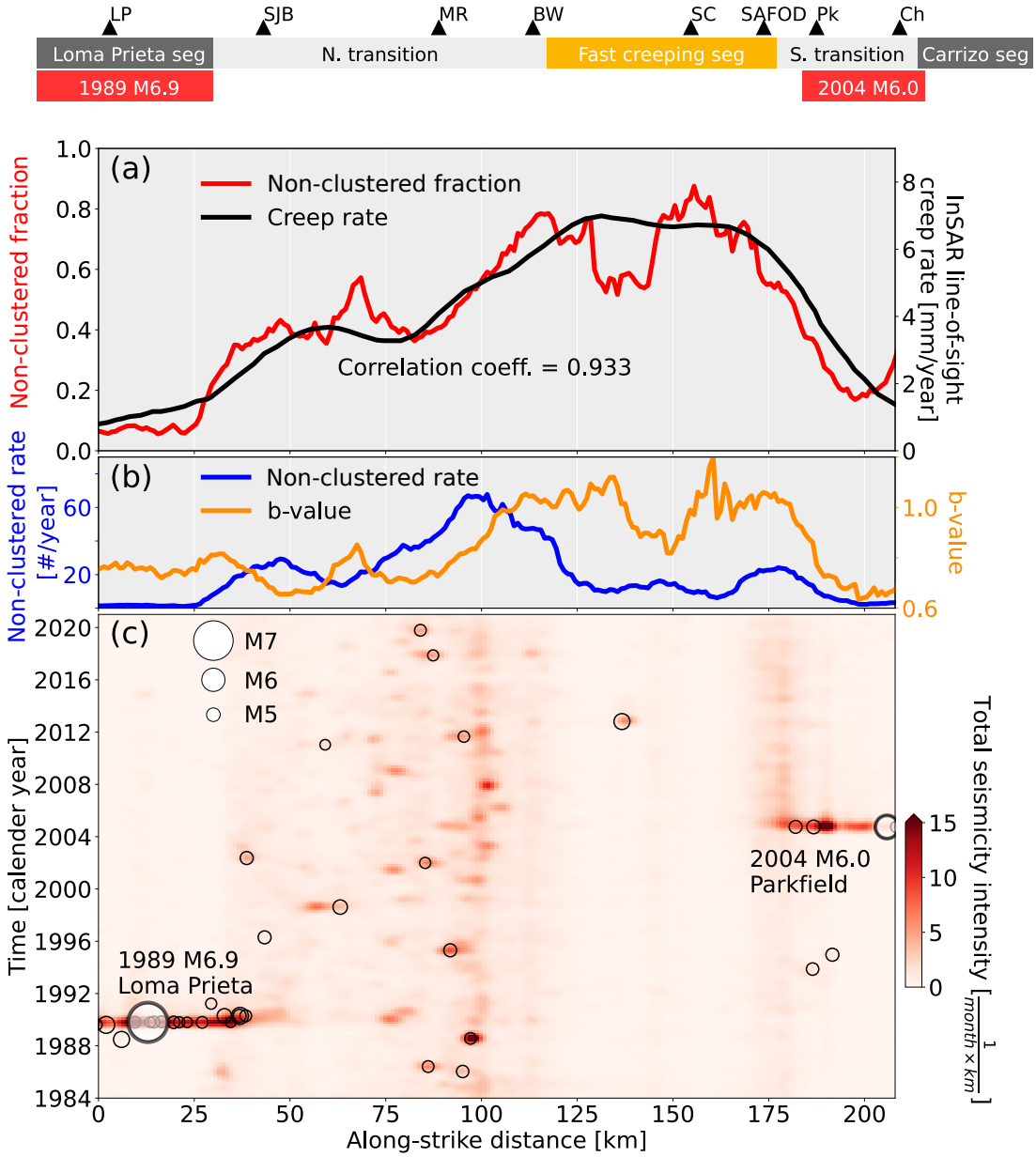

Figure 1.2: Seismicity patterns along the central SAF. (a) Comparison of the fraction of non-clustered events with creep rate. Smoothed InSAR line-of-sight creep rate is from (Jolivet et al., 2015). (b) Non-clustered seismicity rate and b-values along fault estimated using the same 15-km long moving window as in (a). (c) Space-time distribution of seismicity intensity ($M \geq 1.5$) calculated from a two-month by 1-km window and smoothed by a Gaussian filter. Circles indicate earthquakes larger than M4.5. LP: Loma Prieta; SJB: San Juan Bautista; MR: Melendy Ranch; BW: Bitterwater; SC: Slack Canyon; SAFOD: San Andreas Fault Observatory at Depth; Pk: Parkfield; Ch: Cholame.

(~1 mm yr^{-1}) (Jolivet et al., 2015). This segment of the SAF hosted the 1989 M6.9 Loma Prieta earthquake. We also observe that the southeastern-most segment, the Parkfield segment, has a low fraction of non-clustered events decreasing from ~0.5 to ~0.1 from SAFOD to Cholame. Similarly, we observe the InSAR line-of-sight creep rate sharply declining from ~7 mm per year to ~1 mm per year. This segment also corresponds to the coseismic rupture extent of the 2004 M6.0 Parkfield earthquake. Regions at both ends of the profile have been excluded from the analysis due to the lack of sufficient events over four decades.

The definition of fraction of non-clustered events is an intrinsically independent observable from the coupling estimates. Yet, we find the fraction of non-clustered events and the creep rate to be highly correlated, with a correlation coefficient of 0.933. This indicates that the degree of temporal clustering is closely tied to the interseismic coupling over the entire central SAF.

While the fraction of non-clustered events is highly correlated with the creep rate, this is not the case for the rate of non-clustered seismicity, defined as the fraction of non-clustered events times the total seismicity rate. The non-clustered rate varies substantially along-strike (Fig. 1.2b), even in the fault segments with nearly constant long-term geodetic slip rates. In fact, the non-clustered rate throughout the fast creeping segment is almost an order of magnitude lower than the peak non-clustered rate along the central SAF. It is noteworthy that the peak non-clustered rate instead locates in the transition zone, between the creeping and the locked segments, about 20 km to the northwest of Bitterwater. This ~75 km-long transition region has the highest non-clustered rates of the central SAF. The largest creep rates and the largest fraction of non-clustered events coincide with the largest b-values along the central SAF, indicating that the total seismicity rate is increasingly being taken up by smaller non-clustered events in this mostly-creeping segment.

The space-time distribution of earthquakes along the central SAF provides a complementary picture of earthquake clustering behavior (Fig. 1.2c). The Loma Prieta and Parkfield segments at both ends show extremely strong clustering of events related to the 1989 and 2004 mainshocks but generally have low intensity (number of events in a space-time window) for most of the interseismic period. The transition zones, especially in the north, show episodically clustered events with moderate intensity. These spatially localized little clusters are caused by small-sized mainshocks generally less than M4.5. Finally, the creeping segment generally has low event intensity from 1984 to the present. The only visible cluster is caused by a

M5.3 earthquake that occurs in October 2012 at ~137 km and is associated with a decrease in both the non-clustered fraction and the b-value (Fig. 1.2a). This cluster corresponds to a slight reduction of geodetic creep. This observation highlights the potential of sampling local heterogeneity in the fault coupling using characteristics of the clustering behavior of seismicity.

Seismicity catalogs are always incomplete below some minimum magnitude, which often leads to the question of whether the results are affected by the cutoff magnitude chosen. For this case, the magnitude of completeness is about M1.5 (Fig. S2-3). We tested whether the results are sensitive to the cutoff magnitude chosen by repeating the analysis using different completeness magnitudes (M1.5, 2.0, and 2.5). We find that the trend of non-clustered fraction does not change and is insensitive to the cutoff magnitude, when the cutoff value is greater than the magnitude of completeness (Fig. S7-8).

While the fraction of non-clustered events is computed as a single value over nearly 40 years, the fault coupling and the seismicity dynamics may be far from stationary throughout the seismic cycle (Marsan et al., 2017). The variations of non-clustered fraction through time can be approximately quantified by computing the statistics in moving time windows. We briefly discuss the fraction of non-clustered events for different time periods using four subsets of seismicity along the fault (Fig. S6). In time periods consisting of predominantly large mainshocks and associated aftershocks, the non-clustered fraction is usually small; during periods with only small-magnitude non-clustered events, it is generally large. In the fast creeping segment, the fraction of non-clustered events is generally around 0.6 to 0.9. The north transition shows less variablity through time. The values are only perturbed by small-sized (less than M4.5) episodic aftershock sequences and fluctuate around 0.5. In contrast, the fraction of non-clustered events fluctuate strongly over time for the Loma Prieta and the Parkfield subsets, where the regions experienced mostly seismic quiescence with rare and major aftershock sequences. For those regions, one should expect large uncertainties in time windows with little seismicity and care should be used when evaluating short time periods (Marsan et al., 2013). We further discuss the need for sufficient earthquakes for this analysis in the following section.

1.4 Discussion and Conclusion

We find that the temporal distribution of seismicity, as characterized by the fraction of non-clustered events, is closely tied to the interseismic creep rate along the central

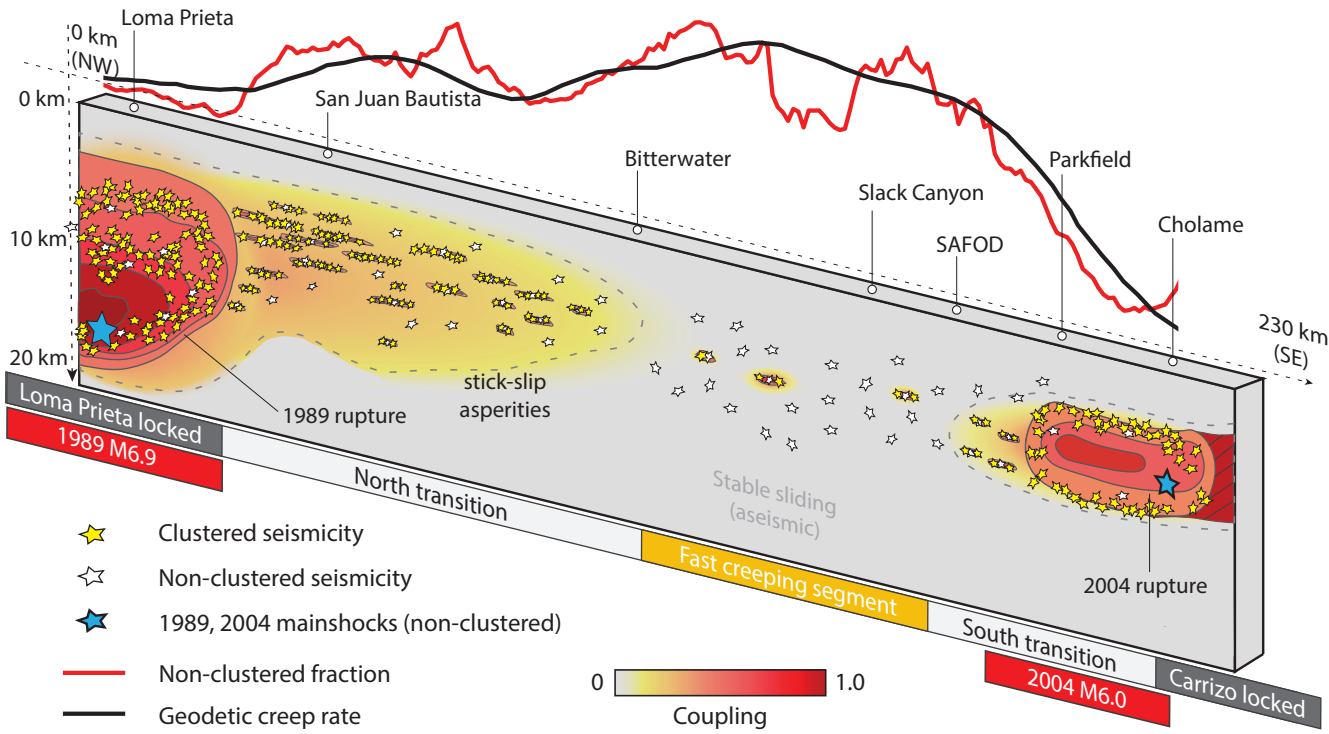

Figure 1.3: Cartoon summarizing the unified observations. The central SAF from northwest to southeast covers several segments with continuous transitioning of fault coupling, creep rates, and seismicity patterns. The seismic transition zone from the creeping to non-creeping segment in the north is longer than the transition in the south.

SAF (Fig. 1.2). Together, these observations suggest that they are two different manifestations of a single unified process. The joint perspective of creep rate and non-clustered event fraction illustrates a fault with spatially varying properties, including aseismic slip, interplate coupling, and the size and spatial distribution of asperities (Fig. 1.3).

For regions that exhibit strong coupling, earthquakes mainly occur as clustered mainshock-aftershock sequences on large and/or densely distributed stick-slip asperities, resulting in a low fraction of non-clustered events. These regions have lower b-values and therefore statistically higher magnitudes. The aseismic slip rate is relatively low since the total long-term slip rate is mostly released on asperities as earthquakes. This is the scenario for the Loma Prieta, Parkfield, and Carrizo segments. Given the nearly-constant long-term slip rate along the central SAF, a lower interseismic coupling in the creeping segment implies larger aseismic slip rate around smaller and fewer asperities. Seismicity is thus prone to occur without

strong clustering in the form of mainshock-aftershock sequences, leading to a high fraction of non-clustered events. In the most extreme case, the fault is fully creeping except for a handful of tiny locked asperities, resulting in characteristic repeating earthquakes along the creeping segment (Nadeau & McEvilly, 2004; Uchida & Bürgmann, 2019).

The transition zones show an intermediate fraction of non-clustered events and thus represent a moderate degree of fault coupling. The gradual change of non-clustered event fractions along the hundreds of kilometers-long fault entails the continuous changeover between fully locked and fully creeping behaviors. While the northern transition zone documents the highest non-clustered seismicity rate, the episodic clusters of triggered aftershocks seem to equalize the non-clustered earthquakes, retaining an intermediate fraction of non-clustered events (Fig. 1.2). This is consistent with the seismicity streaks (Rubin et al., 1999) and the intensive microearthquakes (Jolivet et al., 2015). The pronounced productivity may suggest that the locked-creeping transition can promote microseismicity due to changes of frictional properties (Jiang & Lapusta, 2016).

Some previous observations have linked strain rate and seismic activity. Subduction zones worldwide with relatively high background seismicity rates seem to be anti-correlated with regions that have extremely large earthquakes (Ide, 2013), which is consistent with our observation along the central SAF. A linear relationship was observed between the background seismicity rate and plate velocity for global seismicity, most notably for the Tonga-Kermadec subduction zone and southwestern Pacific (Bird et al., 2009; Ide, 2013). However, the relationship between coupling and the fraction of background events was not examined. At smaller spatial scales, a ~20 year change in background seismicity rate was observed near the Japan Trench that was not attributable to changes in the convergence rate alone (Marsan et al., 2017); transient decoupling on decadal timescales during slow slip events were instead suggested to explain these observations. Rates of repeating earthquakes were also shown to be consistent with the background seismicity and inferred coupling changes (Uchida & Matsuzawa, 2013).

Aftershock rates have been proposed as having a linear dependence on fault coupling based on observations from the Chilean subduction zone (Hainzl et al., 2019). However, there is considerable scatter in the data, most likely due to the uncertainty of the coupling models determined by inverting geodetic observations. A linear spatial relation between coupling and secondary aftershock productivity was also

found following great megathrust earthquakes (Zakharova et al., 2017). A damage rheology model (Ben-Zion & Lyakhovsky, 2006) predicts that aftershock productivity should decrease with the quantity R, which is the ratio of the timescale for brittle deformation to the timescale for viscous relaxation. An observational study (Yang & Ben-Zion, 2009) found that R was inversely proportional to the degree of seismic coupling, and was related to the heat flow and the thickness of sedimentary layers in southern California.

The above studies have addressed quasi-linear relations between the background seismicity and the plate rate, and between aftershock productivity and the degree of coupling. These observations complement each other, and they are compatible with our findings. Our results add an important insight that fault coupling and fraction of non-clustered earthquakes can be tightly linked.

It is important to discuss the role of the length of the available catalog in our analysis. We have studied the seismicity behavior over a nearly 40-year period in an effort to capture as long of a time period as possible without sacrificing catalog quality. Our analysis benefits from the long history of earthquake monitoring in California. At the same time, there has not been a M $\geq$ 6.0 event on the San Andreas (aside from Loma Prieta) since the 1906 San Francisco earthquake. For most of the central San Andreas, this means we are looking at the seismicity during an interseismic period. At this scale, even the 1989 Loma Prieta rupture is only a small portion of the study area. On the one hand, this enables us to interpret the results with some added confidence because the majority of the seismicity are not aftershocks of a large event, and hence our catalog is long enough in that sense. On the other hand, this means that our catalog could be potentially short compared to the recurrence time of the much larger events that could rupture the entire central SAF, and the results in Fig. 1.2 may vary for different 40-year time windows within that much larger recurrence time, for example, right after such a potential large earthquake event. If the relation between the fault coupling and the fraction of non-clustered seismicity indeed varies over that larger timescale, then an interesting question is whether the strong correlation that we find here is indicative of how far along that larger recurrence interval the fault currently is. Numerical studies and further observational studies in other fault zones may shed light on this question; however, whether our approach could be extended to other continental strike-slip faults globally is presently unclear, as it would require careful consideration of the data and associated limitations of the catalog length and quality. Other factors can

make the results in Fig. 1.2, 1.3 vary over different timescales. The lithospheric and mechanical properties and the associated coupling over the next century or a longer geologic timescale could be distinct from the picture of Fig. 1.3, particularly if faults evolve irreversibly with progressive damage generated by large ruptures (Ben-Zion & Sammis, 2003). Shorter-timescale perturbations related to fluid flow (Khoshmanesh & Shirzaei, 2018), solid Earth tides, and ocean tides (Thomas et al., 2009) could add higher frequency variations to our inference averaged over four decades.

Sub-dividing the earthquake catalog to resolve spatial and temporal variations of non-clustered seismicity may introduce various issues (Supplementary Materials). The method based on interevent-time statistics is prone to obtaining a minimum event rate (the background forcing) from an inhomogeneous Poisson process (Hainzl et al., 2006; Marsan et al., 2013). The non-clustered rate tends to approach the total seismicity rate for subsets with scarce events, thus overestimating the non-clustered fraction. In addition, for event subsets that do not satisfy the assumption of the interevent-time probability distribution (Hainzl et al., 2006), the estimated parameters can be biased. An example is an instantaneous time bin that samples short time intervals compared to the long recurrence time of the largest earthquake. Thus, the event subsets are not ideal if they deviate significantly from the general mixture of independent non-clustered events (Poisson point process) and triggered events (following the Omori law). Subsets with only aftershocks are also shown to give an overestimated non-clustered fraction (Marsan et al., 2013). This is risky in small time windows that only cover periods including and directly following large earthquakes, however as described above, is not an issue for our analysis. An appropriate time-series analysis was proposed (Marsan et al., 2013) by adjusting the time windows to avoid probing only aftershocks.

The central SAF is of major interest from a hazard perspective because it accommodates nearly all of the plate motion in this part of California. One of the main questions regarding seismic hazard for this region is whether large ruptures can propagate through the creeping segment (Field et al., 2014; Harris, 2017). Indeed, there has been a general sentiment that such a scenario is unlikely (Ben-Zion et al., 1993; Bakun et al., 2005; Kaneko et al., 2010; Toké & Arrowsmith, 2013; Schwartz, 2018), although some studies consider it possible based on simulations (Noda & Lapusta, 2013) and geodetic inferences on strain accumulation (Titus et al., 2006; Ryder & Bürgmann, 2008; Maurer & Johnson, 2014; Jolivet et al., 2015). A more

subtle but fundamental conclusion of our study is that the portion of the creeping segment with near-zero seismic coupling, as viewed under the paradigm of seismicity and creep presented here, is only about 60 km long. The transition zone on the northwest side, however, is nearly 75 km in length and, given our findings of a high fraction of non-clustered events in this region, could potentially host slip during a through-going large earthquake. Assuming the deep slip rate proposed by the current geodetic model (Jolivet et al., 2015) is constant over four decades, the accumulated moment due to the slip deficit over the entire transition zone is nearly 100 times the seismic moment released in the same period. The stored moment is equivalent to a M_w7.0 earthquake. This estimate agrees with the calculation of a M_w7.2 ~7.4 from Ryder and Bürgmann for a 150 year period (Ryder & Bürgmann, 2008), where the time window and the moment are about four times our estimate. Whether this moment would be released in the form of clustered seismicity, mainshocks on sporadic asperities, or both, our observations strengthen the possibility of seismic ruptures occurring, leaking into, or penetrating across the transition zone.

In summary, our findings reveal a close connection between seismic coupling of the fault and the fraction of non-clustered earthquakes. We find that, rather than accounting for the aftershock rate or non-clustered rate alone, the fraction of clustered to non-clustered events is a more direct proxy to fault coupling. These results provide an important additional observational constraint on numerical modeling of the diversity of fault slip modes on the central SAF that may help narrow down the distribution of frictional and other properties along the fault. Further, the successive transitioning of the fraction of non-clustered events, as well as creep rate, suggests that the varied behavior along the San Andreas can be viewed as effectively continuously varying superposition of stick-slip and creeping behaviors. Finally, the northern transition of the central SAF exhibits an intermediate level of clustering, and thus seismic potential. Consequently, this could increase the likelihood of a rupture propagating through the fully-creeping segment (Noda & Lapusta, 2013).

APPENDIX A: SUPPLEMENTARY MATERIALS FOR CHAPTER 1

A.1 Supplementary Text

The non-clustered fractions in depth

To better compare with fault slip models in two dimensions, we conduct the same analysis in along-strike and depth cells (Fig. S5). We apply the calculation of non-clustered fractions to cells on the fault plane with along-strike width of 2.5 km and a depth bin of 1.0 km. We omit the cells with less than 20 events. The histogram counting the number of events in depth is also binned into every 1 km.

The overall variation of the non-clustered fraction is consistent with the geodetic slip model (Jolivet et al., 2015), where both ends are strongly coupled at nearly all depths, and the middle section is weakly coupled. Limited by the seismicity distribution, we can only image the non-clustered fraction at a narrow width at depth (mostly from 4 km to 12 km depth).

The consistency surprisingly exists in detail. The southern transition has a small patch with a low non-clustered fraction at ~195 km distance and 5–8 km depth (the cyan circle, A). This patch corresponds to an asperity inferred from the geodetic model (Jolivet et al., 2015) 8 km below Parkfield. In their model, a larger locked asperity has been inferred in the northern transition 40 km south of San Juan Bautista. This asperity aligns with an area with low non-clustered fraction at 75–90 km distance and 5–9 km depth (the purple circle, B). There is an asperity within the fast-creeping segment at a distance ~135 km and 7–10 km depth (red circle, C) caused by the 2012 M5.3 event at 8.6 km depth. This patch is consistent with the geodetic model as well (Maurer & Johnson, 2014; Jolivet et al., 2015).

The depth-dependent non-clustered fractions are also consistent with the previously observed microseismicity. The low non-clustered fractions within the north transition zone (the purple circle) could be linked to the localized clusters (Fig. 2b and c in the main text) of intense streaks of microearthquakes (Rubin et al., 1999; Jolivet et al., 2015). Yet, the paucity of events limits us from obtaining estimates on the fault plane with even finer resolution and reasonable uncertainties.

The time-series of non-clustered fractions:

This section corresponds to Fig. S6 of this document. To ensure having enough events for temporal analysis, we must sacrifice the spatial resolution with only four subsets of the entire central SAF. The four subsets are: (1) the Loma Prieta segment; (2) the north transition zone; (3) the fast-creeping segment; (4) the south transition zone near Parkfield. The blue curves in Fig. S6 show the resulting time-series of the non-clustered fraction in four subsets, respectively. The length of the moving time window is fixed at two years, with a step of two months.

As explained in the main text, there are issues when dividing the catalogs into fine time windows due to a lack of events to fit a Gamma distribution of the interevent times properly. Marsan et. al. (Marsan et al., 2013) proposed a better time-series analysis, which we did not pursue in our study. The basic idea is to adjust and extend the time windows adaptively to avoid only covering aftershocks.

The effect of cutoff magnitude:

The estimated magnitude of completeness in our entire catalog is about M1.5 (Fig. S2–S3). The interevent-time statistics below that cutoff magnitude is uncertain. Nevertheless, we can explore the influences of choosing different cutoffs by incrementally increasing the cutoff magnitude, M_c, and calculate the non-clustered fractions. The results are presented in Fig. S7 ($M_c = 2.0$) and Fig. S8 ($M_c = 2.5$). The general trend of non-clustered fractions along the fault does not change. The fractions still correlate well with the surface creep rate regardless of different cutoffs. But, by choosing a larger cutoff magnitude, the small aftershocks that are excluded outnumber the mainshocks (non-clustered events). Using a larger cutoff magnitude results in slightly higher values of non-clustered fractions, especially where small aftershocks are populated. Nevertheless, the main point here is that the non-clustered fraction is indicative to the coupling ratio. This conclusion is always obvious in the different magnitude ranges we tested.

The unreleased moment within the north transition zone:

The transition zone north of the central creeping section may have the potential to produce large earthquakes based on the intermediate level of coupling, which motivates an investigation of the seismic moment release and accumulation. Assuming a conservative long-term plate motion of 34 mm yr^{-1} (Sieh & Jahns, 1984; Titus et al., 2011) and the averaged interseismic creep rate at 8 km depth of ~9.8 mm yr^{-1}

(Jolivet et al., 2015) along the transition zone, there is a slip deficit of 2.4 cm/yr. From 1984 to present (37 years), this deficit corresponds to $3.0 \times 10^{19}\ N \cdot m$ of moment on a rectangular fault plane which is 75 km long and 15 km wide, given a shear modulus of 30 GPa. Based on our dataset, the released seismic moment by the seismicity within the transition zone adds up to only $3.3 \times 10^{17}\ N \cdot m$, which is nearly two orders of magnitude smaller than the moment deficit. The total unreleased moment for the north transition zone over 1984–2020 is equivalent to a M_w 7.0 earthquake.

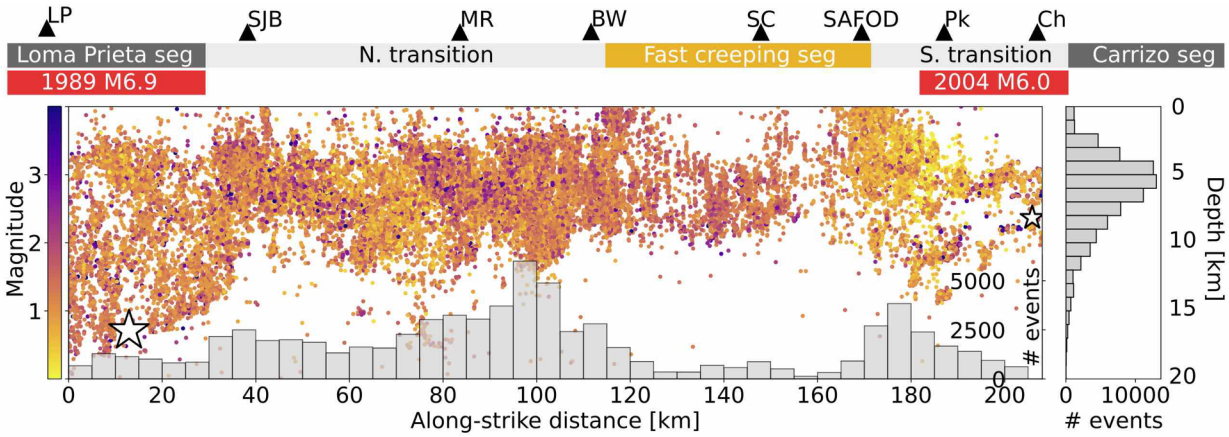

A.2 Supplementary Figures

Fig. S1. Hypocenters of the seismicity along the central SAF. The color is coded by event magnitude. White stars mark the 1989 M6.9 Loma Prieta and the 2004 M6.0 Parkfield mainshock. Red bars marked the 1989 Loma Prieta and the 2004 Parkfield rupture extent, respectively. LP: Loma Prieta; SJB: San Juan Bautista; MR: Melendy Ranch; BW: Bitterwater; SC: Slack Canyon; SAFOD: San Andreas Fault Observatory at Depth; Pk: Parkfield; Ch: Cholame.

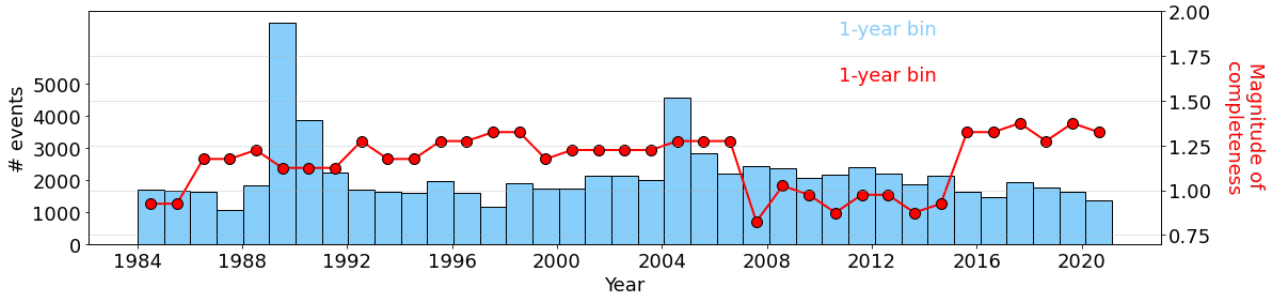

Fig. S2. Number of earthquakes each year from 1984 to 2021 (blue rectangles). The magnitude of completeness estimated from the MAXC method are plotted with red dots. The values of the magnitude of completeness range from 0.8–1.5. We thereby set a conservative minimum magnitude M_{min} = 1.5 for our entire analysis in this study.

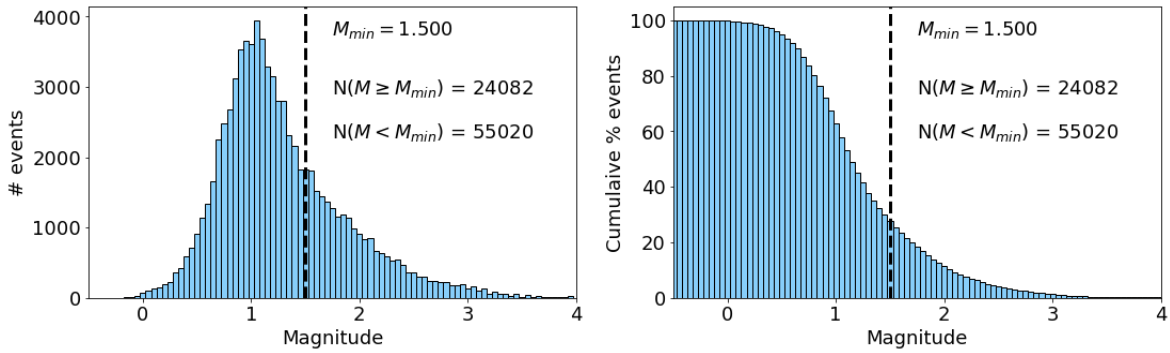

Fig. S3. Magnitude-frequency distribution of the earthquake catalog. Based on the assessment on the magnitude of completeness, we specify a minimum magnitude, M_{min} = 1.5, which gives us 24,082 events for our analysis over three decades from 1984 to 2021.

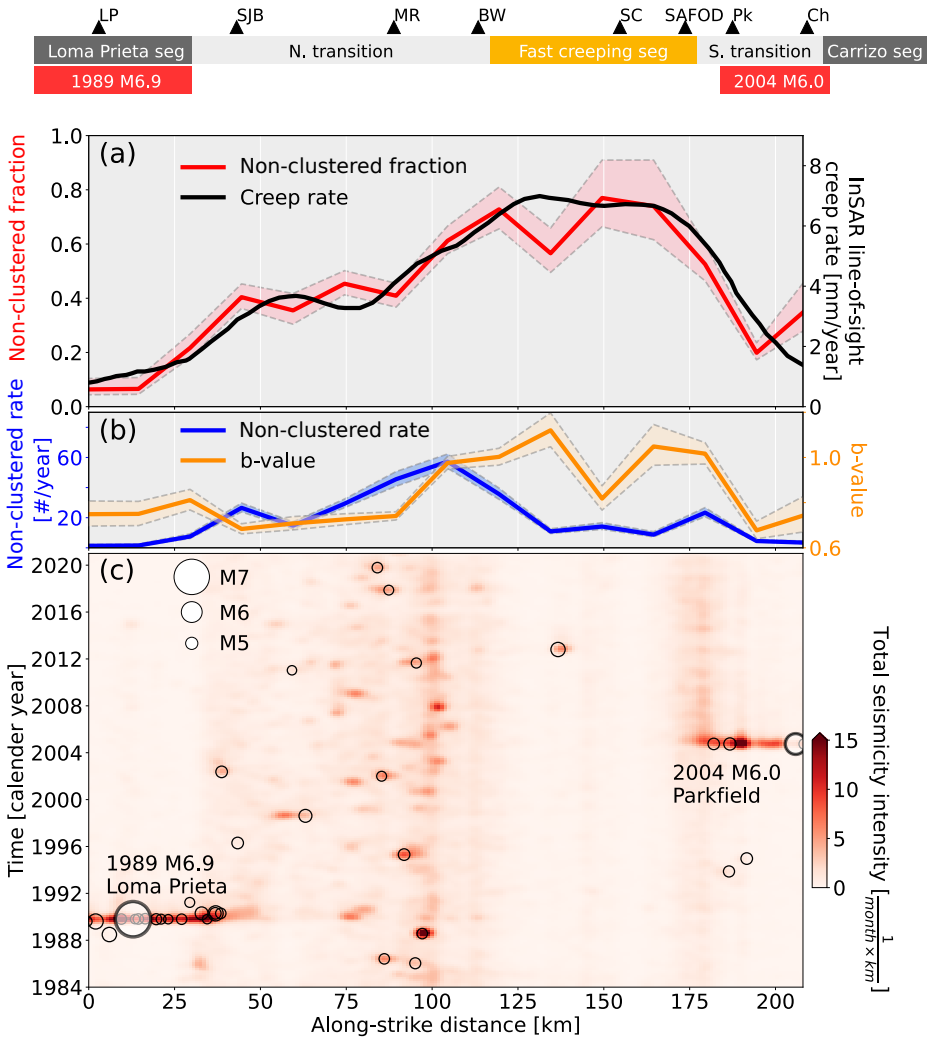

Fig. S4. Non-clustered fraction, non-clustered rate, b-value, and the seismicity intensity along the central SAF. Similar analysis to Fig. 2 of the main text. But the calculation here is only applied to 14 separate along-strike windows, each 15-km wide, rather than a sliding window as in Fig. 2. This is meant to show proper bootstrapping uncertainties with independent samples between spatial windows. The red, blue, and orange shading shows the 95% confidence interval of the estimates. See Supplementary Text in the section "Uncertainty of the estimates of the seismicity".

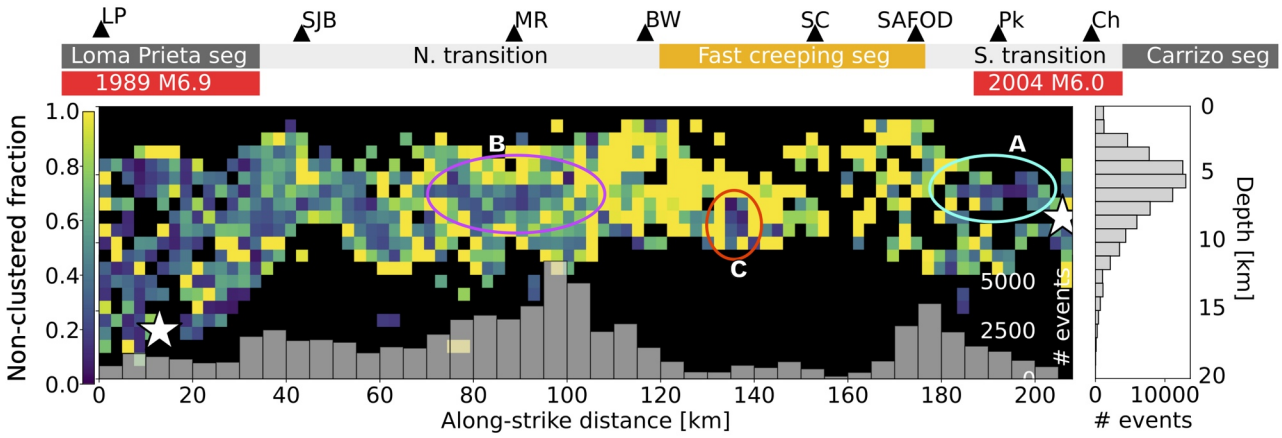

Fig. S5. Non-clustered fraction estimated on a regular along-strike (2.5 km) and depth (1.0 km) cells. The two white stars marked the hypocenters of the 1989 and the 2004 earthquakes. The grey histogram on the right shows the depth distribution of events. Cells containing less than 20 events are colored as black to avoid biased interpretation. The colored circles indicate the fault areas discussed in Supplementary Text in the section "The non-clustered fractions in depth".

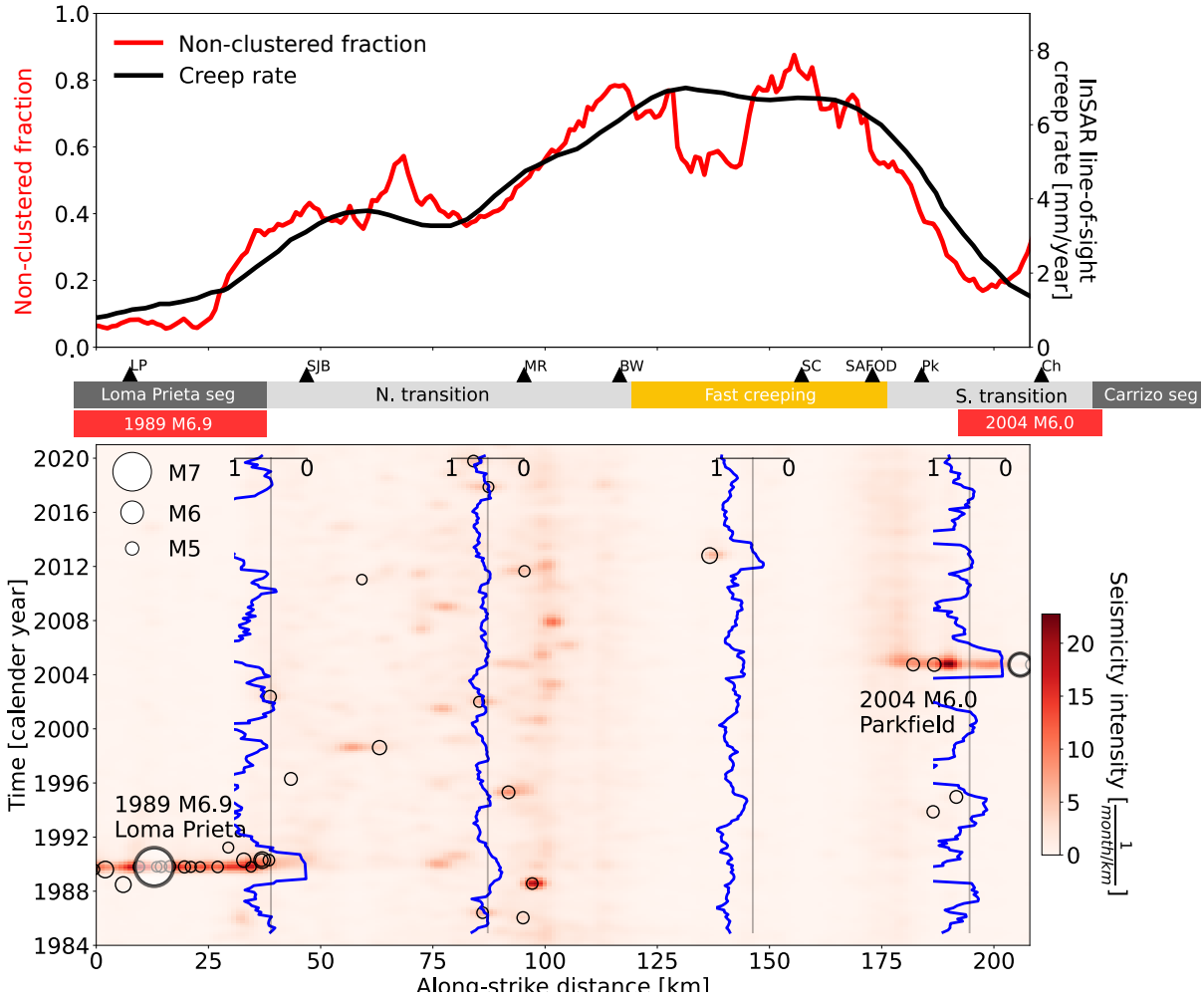

Fig. S6. The blue curves in the lower panel show the time-series of the non-clustered fractions. The length of the moving time window is two years, and the step size is two months. See Supplementary Text in the section "The time-series of non-clustered fractions".

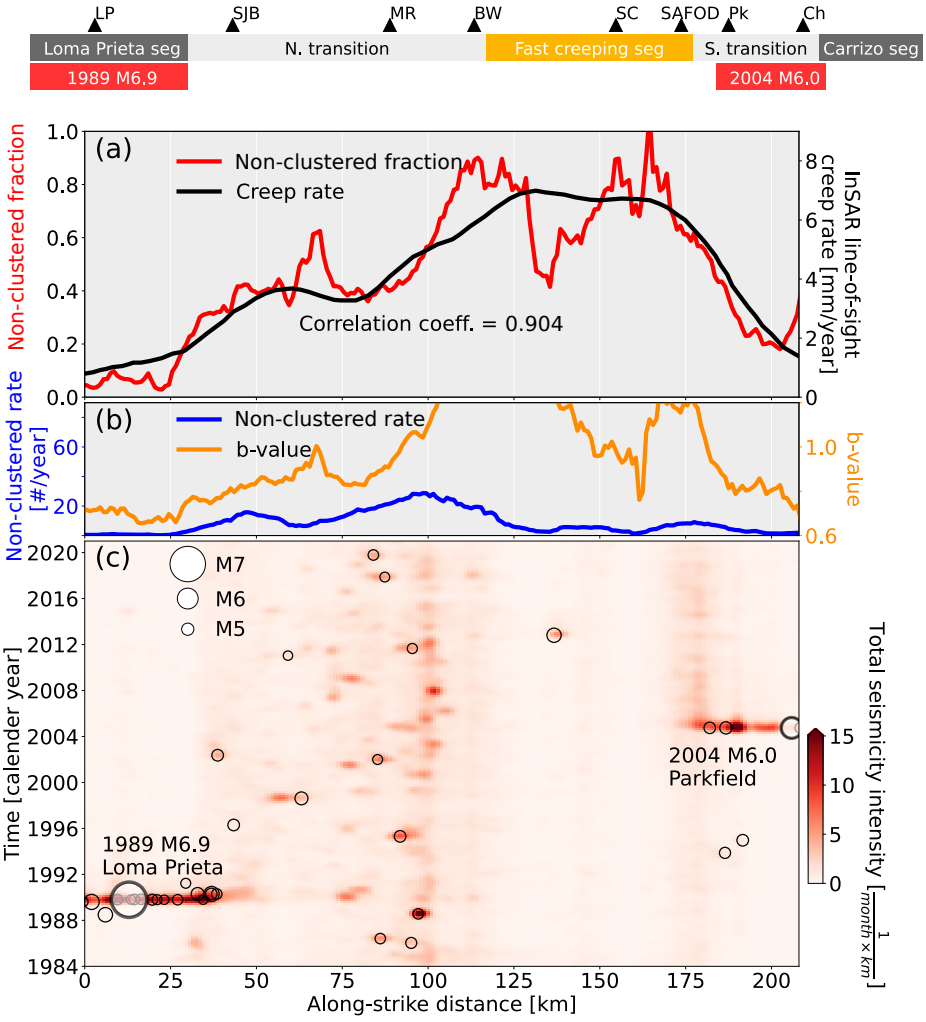

S7. Similar to Fig. S4. Analysis using a cutoff magnitude of M 2.0.

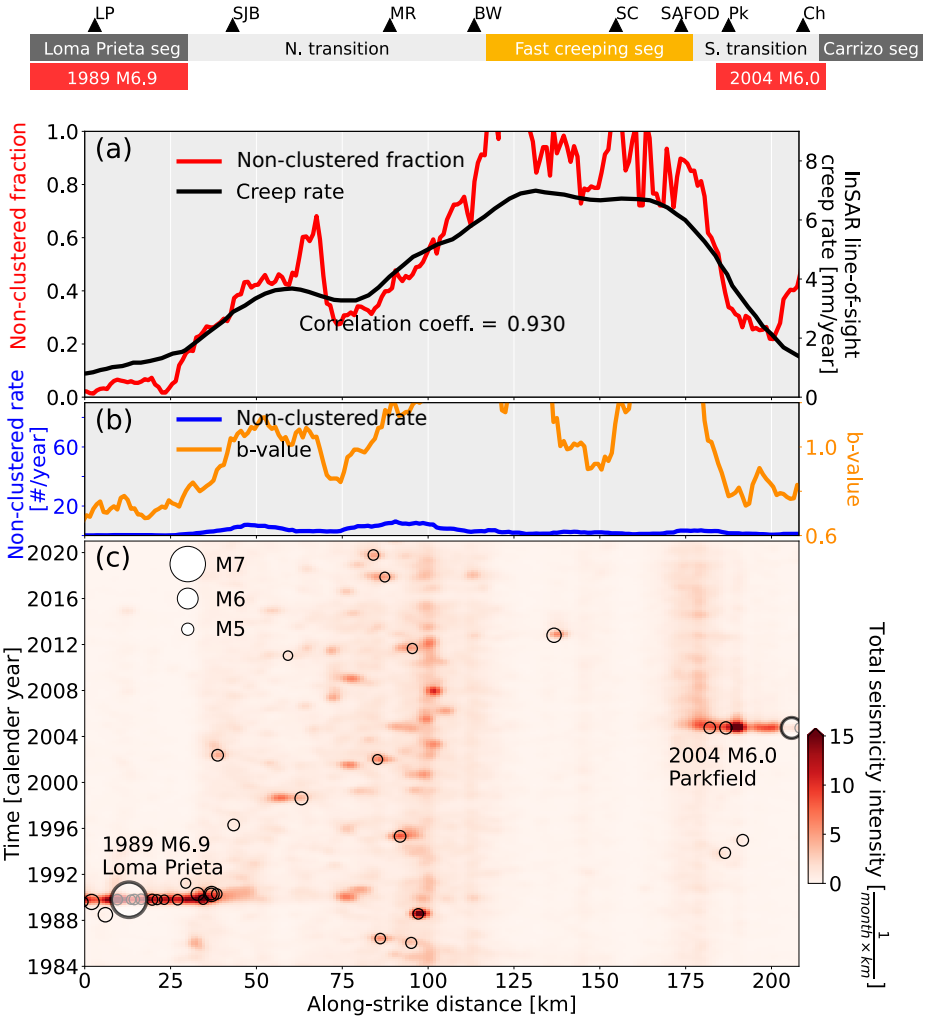

Fig. S8. Similar to Fig. S4. Analysis using a cutoff magnitude of M 2.5.

Chapter 2

INFERRING TECTONIC PLATE ROTATIONS FROM INSAR TIME SERIES

This chapter has been published in:

Liu, Y.-K., Yunjun, Z., & Simons, M. (2025). "Inferring tectonic plate rotations from InSAR time series." *Geophysical Research Letters*, 52(12), e2025GL115137. https://doi.org/10.1029/2025GL115137

ABSTRACT

Interferometric Synthetic Aperture Radar (InSAR) provides constraints on lithospheric kinematics at high spatial resolution. Interpretations of InSAR-derived deformation maps at continental scales are challenged by long-wavelength correlated noise and the inherent limitation of measuring relative displacements within the data footprint. We address these issues by applying corrections to InSAR time series to estimate ground velocity fields with millimeter-per-year precision over hundreds of kilometers. We use these velocity fields to determine the angular velocity of a local tectonic plate, assuming negligible long-wavelength vertical and intra-plate deformation. The uncertainty of the angular velocity is primarily influenced by observational errors and the limited imaging geometries available. Using the Arabian plate as an example, this work demonstrates the potential to improve plate motion models and evaluate intra-plate deformation in regions with sparse ground-based instrumentation.

Keypoints

1. We demonstrate that large-scale InSAR line-of-sight velocity gradient can be used to infer the angular velocity vector of the Arabian plate.

2. Accounting for atmospheric path delays enables matching the GNSS-derived angular velocity vector with mm/year uncertainty.

3. The current lack of sensitivity to north-south motions from InSAR data accounts for most of the uncertainty in the determination of plate rotations.

Plain language summary

Quantifying how tectonic plates move is key to understanding how Earth's surface deforms over time. Plate motions have traditionally been estimated using GNSS (Global Navigation Satellite System) observations. However, GNSS stations are often unevenly distributed, especially away from active plate boundaries, making it harder to precisely determine broad-scale plate motions. InSAR, a satellite-based radar technique, offers widespread spatial coverage but is often contaminated by long-wavelength noise. Here, we explore using InSAR to constrain the rotation field of the rigid Arabian plate. We developed a method to correct for long-wavelength contributions of non-tectonic sources and extract absolute plate rotation from spatial gradients in InSAR-measured relative velocities. By assuming negligible large-scale vertical motion and horizontal intra-plate deformation, InSAR velocity alone can determine a plate's Euler pole in the International Terrestrial Reference Frame (ITRF2014). This approach demonstrates the broader potential for combining satellite and ground data to better understand tectonic plate kinematics and eventually dynamics of lithospheric processes.

2.1 Introduction

Geodetic observations of the partitioning of deformation across plate boundaries are crucial for understanding lithospheric dynamics. Key issues include the consistency of geodetic and geologic deformation rates, the appropriateness of the rigid plate approximation, and the rate of seismogenic strain accumulation (e.g., Argus & Gordon, 1996; McCaffrey, 2005; Loveless & Meade, 2010; Tong et al., 2014). Global models of rigid plate motion provide the context for assessing deformation partitioning (e.g., DeMets et al., 2010; Argus et al., 2011; Kreemer et al., 2014). Traditionally, these plate motion models are predicted from plate angular velocity vectors derived using GNSS observations and are limited by instrumental coverage,

especially in plate interiors. However, large-scale (10^2–10^3 km) surface motion can now be mapped with great precision using InSAR (e.g., Weiss et al., 2020; Xu et al., 2021; Ou et al., 2022; Stephenson et al., 2022; Lemrabet et al., 2023), thereby providing useful constraints in sparsely instrumented regions.

Despite the near-complete spatial continuity of InSAR-derived velocity fields, their long-wavelength information is often underutilized (Chaussard et al., 2016; Parizzi et al., 2021). For example, when studying seismic processes along active fault zones, an empirical low-order polynomial velocity field is typically removed to alleviate long-wavelength orbital or atmospheric effects (e.g., Massonnet et al., 1993; Simons et al., 2002; Pritchard & Simons, 2006; Ryder et al., 2007; Biggs et al., 2007; Cavalié et al., 2008). For long-wavelength (10^2–10^3 km) distributed strain, InSAR velocity fields are often aligned to deformation models derived from dense GNSS networks (e.g., Fialko, 2006; Tong et al., 2013b; Jolivet et al., 2015; Neely et al., 2020; Lemrabet et al., 2023), which simultaneously mosaics individually referenced velocity fields to an internally consistent reference frame. When such a network is unavailable, unassisted use of InSAR-derived velocities over continental scales requires accounting for spatially correlated signals of confounding origins (Fattahi & Amelung, 2014; Chaussard et al., 2015a; Chaussard et al., 2015b), including spatiotemporal variations of troposphere (Tarayre & Massonnet, 1996; Emardson et al., 2003; Onn & Zebker, 2006), ionosphere (Gray et al., 2000; Meyer, 2010; Gomba et al., 2016) and the lithospheric responses to tides and surface mass loading (Biggs et al., 2007; DiCaprio & Simons, 2008; Xu & Sandwell, 2020).

Recent large-area studies demonstrate the potential to constrain lateral plate motions using InSAR observations. Lazecký et al. (2023) apply burst-overlap interferometry (Grandin et al., 2016; Li et al., 2021) over regions including the Alpine-Himalayan Belt yields averaged horizontal velocities that agree with the ITRF2014 plate motion model, with median 2-sigma errors of 4 mm yr^{-1} northwards and 23 mm yr^{-1} eastwards. When inferring interseismic fault coupling of the East Anatolian and North Anatolian Faults, Bletery et al. (2020) combine InSAR and GNSS observations to estimate local Euler vectors of Arabia and Anatolia. Using exclusively InSAR-derived relative LOS velocities, Stephenson et al. (2022) show that plate motions manifests themselves as velocity gradients (see also Bähr et al., 2012; Bähr, 2013), consistent with the ITRF2014 plate motion model (Altamimi et al., 2017) within 0.2 mm yr^{-1}/100 km in Makran, Arabia, and Australia. Later, Lemrabet et al. (2023) show that large-scale velocity ramps can be used to retrieve the plate motion

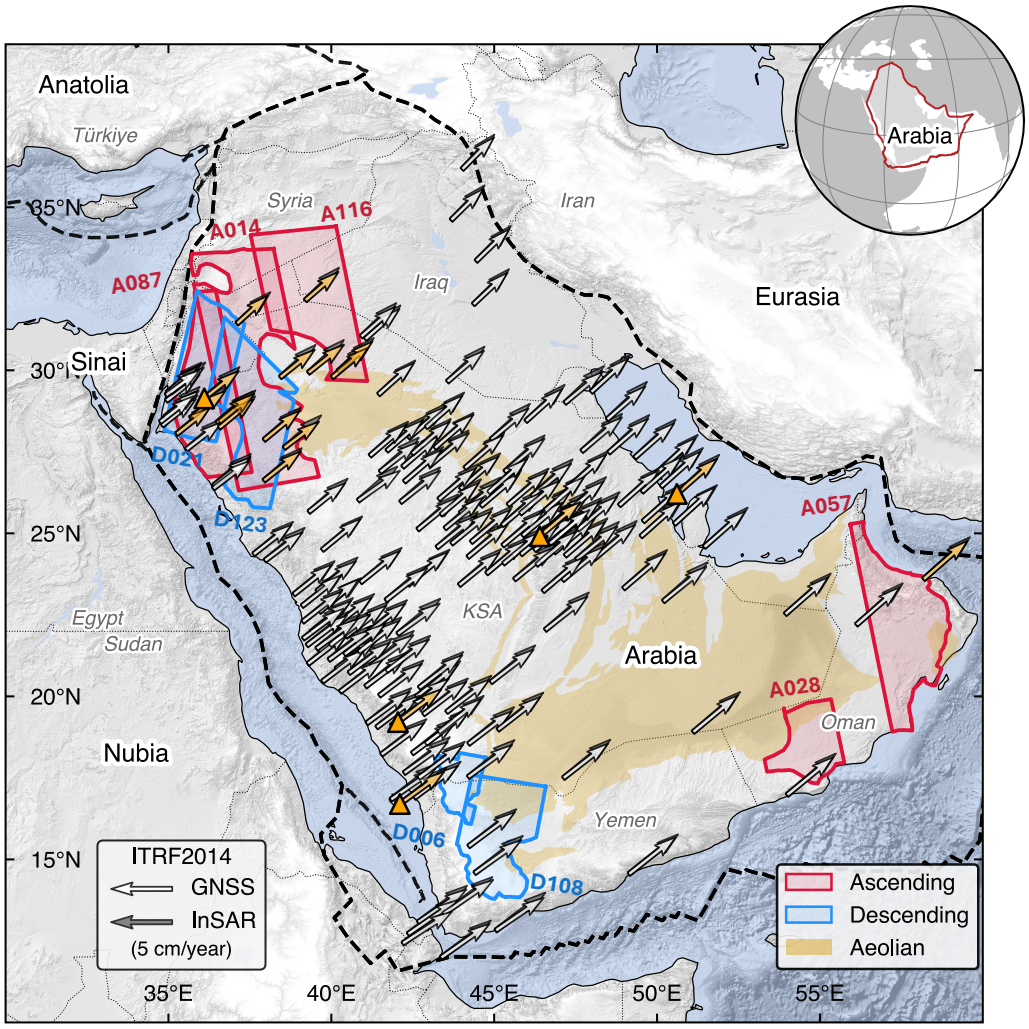

Figure 2.1: Arabian plate velocities predicted by GNSS-derived (Viltres et al., 2022, shown as white arrows. The orange arrows are stations used for our geometry tests in Section 3.3. Supplementary Text S1) and our InSAR-derived (dark arrows) Euler vector in ITRF2014. The orange triangles indicate the GNSS stations used to derive the Arabian Euler vector by Altamimi et al. (2017). Brown shading marks dune regions that decorrelate interferograms. The red (ascending) and blue (descending) rectangles indicate the extent of the InSAR data used in this study. Plate boundaries are compiled from Bird (2003), Argus et al. (2011), and Viltres et al. (2022).

in the ITRF reference frame and quantify their consistency against GNSS derived plate motion. Here, we address the inverse problem and use long-wavelength InSAR velocity fields from multiple orbital tracks to determine the Euler vector for the Arabian plate.

2.2 Methods

Interferograms processing and velocity corrections

We process nine tracks of Sentinel-1A Interferometric Wide Swath mode Level-1 SLCs (single-look complex images, each covering 250 × 250 km; Figure 2.1) spanning 2014–2023 (~250 epochs). SLCs from the same track are coregistered using precise orbits and the 1-arcsecond SRTM v3.0 elevation model (Farr et al., 2007), all relative to the WGS84 ellipsoid. For finer azimuthal coregistration, We apply a network-based enhanced spectral diversity approach (Fattahi et al., 2017a). We construct a fully-connected, small-baseline interferometric network (Berardino et al., 2002) by pairing each acquisition with all the neighbors within 2 months and with the acquisitions that were acquired 4 months apart. Approximately 900 interferograms per track are multilooked to ~500-m ground-pixel resolution, filtered using a power-spectrum adaptive filter with an exponent of 0.5 (Goldstein & Werner, 1998), and unwrapped using a minimum cost-flow algorithm (Chen & Zebker, 2002).

We estimate deformation time series using a least-squares inversion weighted by the inverse of phase variance (Tough et al., 1995; Guarnieri & Tebaldini, 2008) while minimizing the implied velocities in all time intervals (Berardino et al., 2002; Yunjun et al., 2019). In the time-series domain, we apply corrections to account for stratified tropospheric delays (Jolivet et al., 2011; Jolivet et al., 2014) based on the ECMWF ReAnalysis model (ERA5) (Hersbach et al., 2020), ionospheric effects using a range split-spectrum method (Liang et al., 2019), solid earth tides (SET) (Milbert, 2018; Yunjun et al., 2022), the elastic response to ocean tidal loading (OTL) (Martens et al., 2019), phase closure bias (Zheng et al., 2022), and residual baseline-related topographic phases (Fattahi & Amelung, 2013). We fit pixel-wise time series to a temporal function consisting of a secular velocity plus an annual and a semi-annual sinusoids (Supplementary Text S2; Hetland et al., 2012). Low-quality pixels with temporal coherence < 0.9 are masked (Yunjun et al., 2019), as are pixels where the cumulative closure phase exceeds three times the standard deviation (Zheng et al., 2022). We exclude clearly deforming regions near (within 60 km) the Dead Sea Transform Fault to reduce the effects of seismic cycle and rifting processes (Klinger et al., 1999; Reilinger et al., 2006; Li et al., 2021; Castro-Perdomo et al., 2021). For simplicity, we do not model the relative motion of the Sinai subplate to Arabia (Mahmoud et al., 2005). The final velocity field is geocoded and downsampled to a 2.5 km posting.

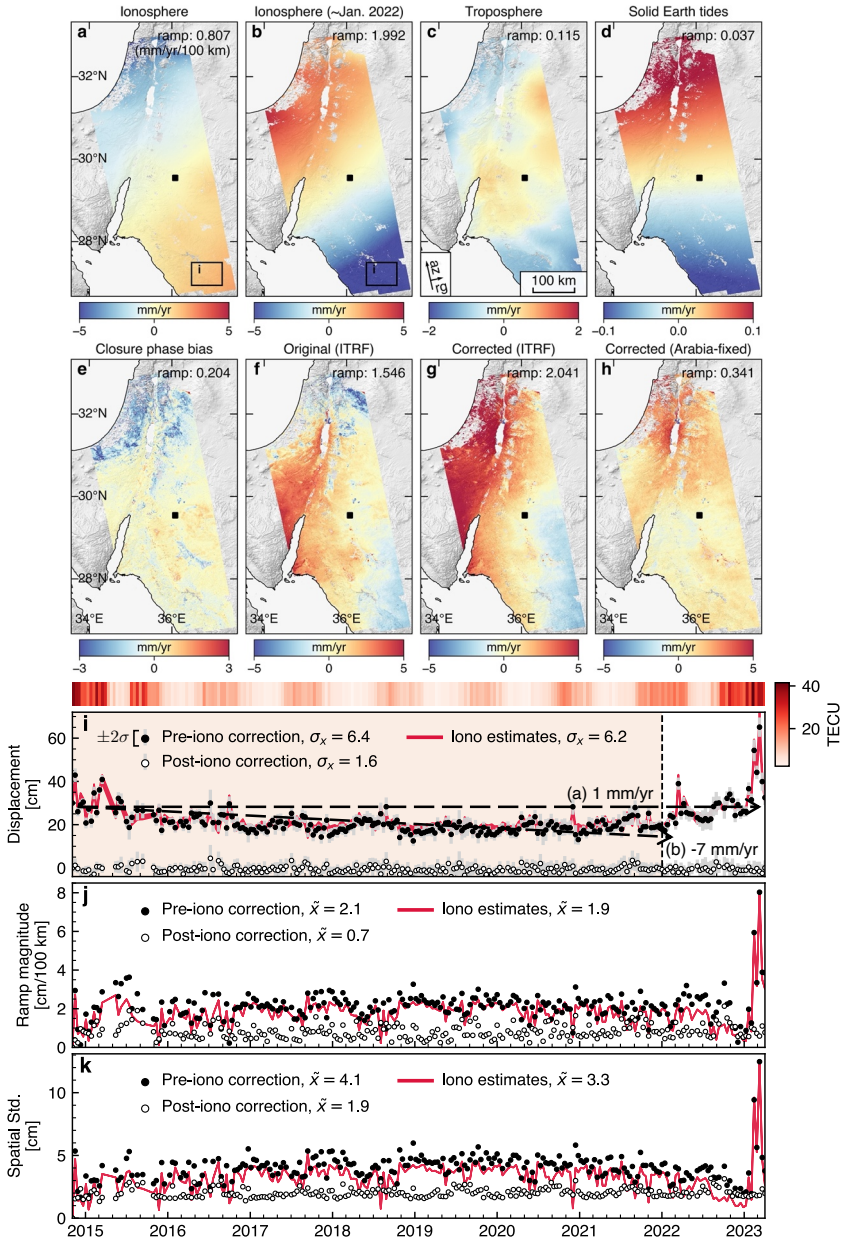

Figure 2.2: Time-series corrections applied to track A087 in northwest Arabia. Velocities are relative to the reference point (black square) near the GNSS site HALY. Positive velocities move toward the satellite. The L2-norm of the best-fit linear ramp coefficients to the velocity field (Supplementary Text 2-2) is shown in the upper right of each panel. **(a–e)** Apparent LOS velocities of each correction term (note varying color scale ranges). **(a)** The ionospheric delay estimated from December 2014 to February 2023. **(b)** Same as (a), but only considering data until January 2022. **(f–h)** The original velocity in ITRF, after corrections in ITRF2014, and after corrections in the Arabia-fixed frame. The TECU (total electron content unit) shows annual and 11-year fluctuations of the ionosphere (Noll, 2010). **(i)** Time series averaged over the black rectangle at the southeast of panels a and b. The dashed lines indicate the best-fit apparent velocity depending on the time period being considered. σ_x denotes the temporal standard deviation. **(j)** L2-norms of the linear ramp coefficients in all epochs. **(k)** Standard deviations of the displacement fields in all epochs. $\tilde{x}$ indicates the temporal average for each quantity.

InSAR-based Euler vector estimation

Leveraging spatially relative InSAR measurements to constrain the absolute rotation of tectonic plates in a global reference frame forms a central tenet of this work. This apparent contradiction is resolved by exploiting the intrinsic geometric properties of radar imaging. The systematic variation in the satellite's look angle across the imaging swath induces a predictable quasi-range-dependent LOS velocity gradient that, under the assumption of rigid plate motion and negligible long-wavelength vertical motion, becomes proportional to the absolute angular velocity vector (Bähr et al., 2012; Stephenson et al., 2022; Lemrabet et al., 2023).

InSAR LOS measurements and the derived velocities are with respect to the orbital positions of Sentinel-1 in no-net-rotation (NNR) ITRF2014 (Peter, 2021). Assuming the large-scale vertical motion can be ignored, we write the ground velocity in ITRF projected along the satellite LOS as a sum of the following components:

$$\mathbf{d} = \mathbf{d}_B + \mathbf{d}_\varepsilon, \tag{2.1}$$

where $\mathbf{d}_B$ is the linear velocity due to plate rotation and $\mathbf{d}_\varepsilon$ is the internal deformation relative to $\mathbf{d}_B$, including elastic strain of plate boundaries and distributed intra-plate strain (e.g., Meade & Loveless, 2009). When $\mathbf{d}_\varepsilon$ negligible, the ground velocity can be modeled as an Euler vector (i.e., angular velocity vector), $\mathbf{m} = [m_x, m_y, m_z]^\intercal$ (rad/yr) (McKenzie & Parker, 1967; Morgan, 1968; Cox & Hart, 1986). The Euler vector maps to the pixel-wise LOS velocity $\mathbf{d}$ for P number of pixels via a linear transformation matrix, $\mathbf{G}$, which is fully determined by the coordinates and LOS angles of each InSAR pixel (Supplementary Text S3) such that

$$\mathbf{d} = \mathbf{G}\,\mathbf{m} \tag{2.2}$$

where $\mathbf{d}$, $\mathbf{G}$, and $\mathbf{m}$ have dimensions $[P \times 1]$, $[P \times 3]$, and $[3 \times 1]$, respectively. The InSAR displacement and velocity is usually described relative to a reference pixel (e.g., Massonnet & Feigl, 1998), $\mathbf{r}^*$, where the derived velocity is zero. To align the linear model with our relative measurements, we reference $\mathbf{G}$ to the common reference pixel in each track by subtracting the row corresponding to the reference pixel, $\mathbf{G}^* = \mathbf{G} - \mathbf{G}_{\mathbf{r}^*}$. We then can formulate a linear problem with the measured relative velocity, $\mathbf{d}^*$

$$\mathbf{d}^* = \mathbf{G}^* \mathbf{m} \tag{2.3}$$

Consequently, the local velocity gradient tensor observed in each relative InSAR track $\mathbf{d}^*$, encode information about the absolute Euler vector $\mathbf{m}$ in ITRF2014, and the mapping relation is defined by the sensing matrix $\mathbf{G}$. The maximum likelihood solution is given by

$$\hat{\mathbf{m}} = \mathbf{C}_{\hat{\mathrm{m}}} \mathbf{G}^{*\intercal} \mathbf{C}_{\mathrm{d}^{-1}} \mathbf{d}^* \tag{2.4}$$

with covariance

$$\mathbf{C}_{\hat{\mathrm{m}}} = (\mathbf{G}^{*\intercal} \mathbf{C}_{\mathrm{d}^{-1}} \mathbf{G}^*)^{-1} \tag{2.5}$$

where the estimate of the Euler vector, $\hat{\mathbf{m}}$, and its model covariance, $\mathbf{C}_{\hat{\mathrm{m}}}$, depends on the observational covariance $\mathbf{C}_{\mathrm{d}}$ which is dictated by measurement uncertainty.

Covariance model at a single reference

Residual noise remains in interferometric phase measurements even after applying deterministic corrections, introducing uncertainties in ground velocity estimates. We assume there is no bias in the long-wavelength velocity gradient, and following previous studies (e.g., Agram & Simons, 2015), we model the short- to intermediate-wavelength (< 100 km) phase noise as stochastic variables in the velocity fields

$$\mathbf{d}^* = \mathbf{G}^* \mathbf{m} + \mathbf{d}_{\mathrm{resid}}, \tag{2.6}$$

where the stochastic component

$$\mathbf{d}_{\mathrm{resid}} = \mathbf{d}_{\mathrm{corr}} + \mathbf{d}_{\mathrm{uncorr}} + \mathbf{d}_{\mathrm{ref}}. \tag{2.7}$$

The first two terms represent the deviations of pixel-wise velocities from pure ground displacements in imperfect measurements. $\mathbf{d}_{\mathrm{corr}}$ represents apparent velocity contribution due to spatially correlated residual noise (uncertainties in the

atmospheric structures), and $\mathbf{d}_{\text{uncorr}}$ represents the velocity noise due to the phase contribution from spatio-temporally uncorrelated noise sources (e.g., decorrelation noise, uncorrelated troposphere in time, phase unwrapping errors). It is reasonable to assume these sources of noise to be zero mean random variables and describe the observational covariance matrix as

$$\mathbf{C}_{\text{d}} = \mathbf{C}_{\text{d}_\text{s}} + \mathbf{C}_{\text{d}_\text{t}}, \tag{2.8}$$

where $\mathbf{C}_{\text{d}_\text{s}}$ accounts for the stationary and isotropic intermediate-wavelength spatial correlation of $\mathbf{d}_{\text{corr}}$ (Hanssen, 2001). We remove a quadratic ramp from velocity before computing $\mathbf{C}_{\text{d}_\text{s}}$ using a distance-dependent exponential function fitted to the sampled variogram for data point pairs within 300 km (Jónsson et al., 2002; Simons et al., 2002; Lohman & Simons, 2005). The characteristic length scales of the modeled covariance are 50–100 km. $\mathbf{C}_{\text{d}_\text{t}}$ accounts for $\mathbf{d}_{\text{uncorr}}$ and is a diagonal matrix populated with the variances of the pixel-wise velocity estimates determined by the functional-fit residuals assuming uniform Gaussian errors at all epochs (Fattahi & Amelung, 2015). The median of diagonals in $\mathbf{C}_{\text{d}_\text{t}}$ and $\mathbf{C}_{\text{d}_\text{s}}$ are of comparable magnitude, ranging from 0.4 to 0.8 mm yr^{-1} (Supplementary Text S4-2).

Posterior from ensemble references

Our velocities, observational errors, and the linear operator $\mathbf{G}^*$ are all described relative to a set of reference pixels (Equation 2.6). While guidelines exist for selecting such candidate pixels (Yunjun et al., 2019; Zhang et al., 2024), any real or apparent displacement (e.g., from atmospheric path delays) of the reference pixel, $\mathbf{d}_{\text{ref}}$, will be redistributed to all the other pixels. To account for this limitation, we consider multiple realizations of the velocity field using different reference points. Specifically, we conduct 1,000 realizations of the Euler vector inversion (Equations 2.4 and 2.5), where each is based on velocity fields using randomly picked reference points for each track (Figure S4). We restrict the choice of reference such that it lies below an elevation of 1500 m and must be at least 25 km from masked areas). The measurement error, $\mathbf{C}_{\text{d}_\text{t}}$, in each realization updates with the chosen reference, while $\mathbf{C}_{\text{d}_\text{s}}$ remains unchanged due to the stationarity assumption of the deramped noise structure. These realizations yield an ensemble of Euler vectors (Section 2.3), from which we introduce and derive a mismodelling covariance matrix, $\mathbf{C}_{\text{p}}$, to quantify the ensemble posterior. We estimate $\mathbf{C}_{\text{p}}$ using the second moment of the ensemble predictions over all realizations (Duputel et al., 2012; Vasyura-Bathke et al., 2021):

$$(\mathbf{C}_\mathrm{p})^{ij} = \frac{1}{\mathrm{L}} \sum_{k=1}^{\mathrm{L}} (\mathbf{d}^i(\hat{\mathbf{m}}_k) - \bar{\mathbf{d}}^i)(\mathbf{d}^j(\hat{\mathbf{m}}_k) - \bar{\mathbf{d}}^j) \tag{2.9}$$

where i, j denote the rows and columns in the data covariance matrix; the total number of realizations, L = 1,000; $\mathbf{d}^i(\hat{\mathbf{m}}_k)$ represents the predicted data at pixel i with the k^{th} realized Euler vector, corresponding to a reference point at $\mathbf{r}_k$. The term $\bar{\mathbf{d}}^i = \frac{1}{\mathrm{L}} \sum_{k=1}^{\mathrm{L}} \mathbf{d}_k^i(\hat{\mathbf{m}}_k)$ is the population mean of predictions at pixel i. We append this epistemic covariance to the total noise covariance matrix as $\mathbf{C}_\chi = \mathbf{C}_\mathrm{d} + \mathbf{C}_\mathrm{p}$ and invert for the posterior and uncertainty of the Euler vector using Equations 2.4 and 2.5, with $\mathbf{C}_\chi$ replacing $\mathbf{C}_\mathrm{d}$.

2.3 Results and Discussions

The long-wavelength velocity field

We demonstrate the process of inferring the long-wavelength velocity field using ascending (dusk) track A087 in northwest Arabia (Figure 2.2). The time series of ionospheric delay in dusk tracks contributes to secular apparent velocity with a gradient of ~0.8 mm yr^{-1}/100 km. Due to solar cycles, the apparent velocity depends on the time span, and the gradient increases to ~2.0 when fitted to data before January 2022. The ionospheric correction reduces ramp magnitudes and spatial standard deviation for all epochs (Figure 2.2i–k).

The tropospheric model reduces temporal fluctuations, lowering median post-fit residuals by 10.1 mm for northwest Arabia, 6.1 mm for Oman, and 5.1 mm for Yemen tracks. The apparent velocity gradient predicted from ERA5 is minimal, at 0.1 mm yr^{-1}/100 km, similar to a kriging-interpolated method (Cao et al., 2021) and the GACOS (Yu et al., 2017) model. The largest tidal constituents, M2 and O1, have aliased periods of 64.1 and 77.7 days, respectively, when sampled every 12 days (Xu & Sandwell, 2020), so SET and OTL have minimal impact on decadal timescales. Phase closure biases and topographic residuals are localized and do not produce a velocity gradient greater than 0.1 mm yr^{-1}/100 km. After all corrections, we account for 70% of the ramps at the epoch level (Supplementary Text S2-2, Figure S1), leaving the final time series with standard deviations of 1.6–3 cm. The standard deviations of velocity estimates relative to the reference points are 0.4–0.8 mm yr^{-1} (Figure 2.2i, Figure 2.3b) in the far field.

Quasi-range-dependent velocity gradients of ~2.1 mm yr^{-1}/100 km are present in multiple velocity tracks (Figures S2 and S10). A joint inversion of nine InSAR

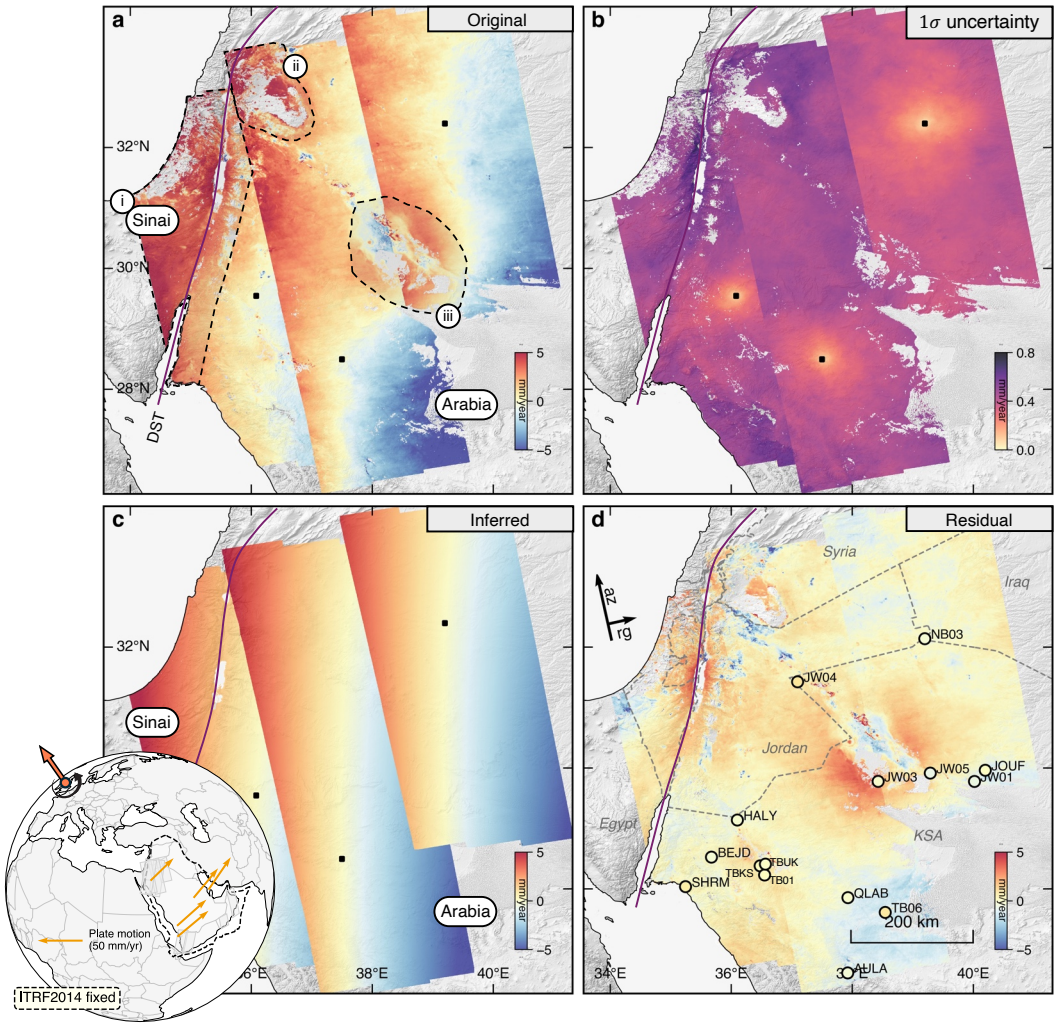

Figure 2.3: Three overlapping ascending tracks of velocity in northwest Arabia showing the consistent impact of Arabian motion in ITRF2014. **(a)** Observed LOS velocities referenced to the black squares in each of the respective tracks. We masked out areas (i) near and west of the Dead Sea Transform Fault, (ii) a large decorrelated area, and (iii) areas with > 100 km wide uplift in Wadi Sirhan Basin. **(b)** The 1-σ uncertainties of velocities, i.e., the diagonals of $\mathbf{C}_{d_t}^{0.5}$. **(c)** Inferred Arabian rotation. **(d)** Arabian-fixed LOS velocities after removing the inferred rotation from (a). Circles: GNSS observations color-coded by radar satellite LOS velocities projected from their horizontal components. Inset globe: the inferred Euler pole from all InSAR tracks and the modeled horizontal motions at the five stations used in defining the Arabian Euler vector in ITRF2014 (Altamimi et al., 2017).

tracks arrives at an ITRF2014 Euler vector $\hat{\mathbf{m}} = [0.358, -0.055, 0.418]$ °/Ma. This predicts the same ~2.1 mm yr^{-1}/100 km velocity gradient and horizontal velocities of 38–54 mm yr^{-1} across the Arabian plate (Figure 2.3c). Subtracting the prediction from the angular velocity of the plate, the residual velocity fields of ±2 mm yr^{-1} represent motion relative to the Arabian reference frame, which agree with horizontal GNSS data (Viltres et al., 2022) (Figure S11-S13). The largest discrepancies occur near the Dead Sea (4–5 mm yr^{-1} of lithospheric rebound), the Wadi Sirhan Basin near GNSS site JW03 (Figure 2.3d), and potential ionospheric correction artifacts near site TB06.

The inferred Euler vector

Several Euler vectors exist for the Arabian plate, including MORVEL56-NNR (Argus et al., 2011), GSRM v2.1 (Kreemer et al., 2014), the ITRF2014 plate model (Altamimi et al., 2017), and a recent GNSS-derived vector (Viltres et al., 2022). The rigid block approximation is appropriate in Arabia, and the Arabian vector of Altamimi et al. (2017) aligns well with Le Pichon & Kreemer (2010) and Viltres et al. (2022). Therefore, we use Altamimi et al. (2017) as the benchmark for comparisons (Figure 2.4).

The vector derived from the single realization of the velocities shown in Figure 2.3a lies between the MORVEL and Altamimi et al. (2017) ("x" marker in Figure 2.4a-c). For 1000 random reference points, the Euler vector realizations are distributed within 13.7° in latitude, 27.9° in longitude, and 0.1°/Ma in rotation rate. Significant trade-offs occur along N60°E in geographic and latitudinal-rate spaces. The posterior Euler vector $\hat{\mathbf{m}} = [0.353, -0.049, 0.421]$ °/Ma is 182.7 km from the pole of Altamimi et al. (2017), with a 0.037°/Ma faster rotation rate. Our 2-sigma error bound overlaps with Altamimi et al. (2017). The mean differences in horizontal velocities are 1.015 mm yr^{-1} (east) and 3.269 mm yr^{-1} (north), indicating less constraint on north-south motion. Euler vector parameters and covariances are tabulated in Table S1. Our inversion does not account for uncertainty in the long-wavelength velocity gradient. Following the approach in Lemrabet et al. (2023) we empirically estimate the uncertainty of the long-wavelength velocity to be approximately $0.001 - 0.004$ mm yr^{-1}/km and can accumulate to $1 - 3$ mm yr^{-1} across the track (Supplementary Text S2-3).

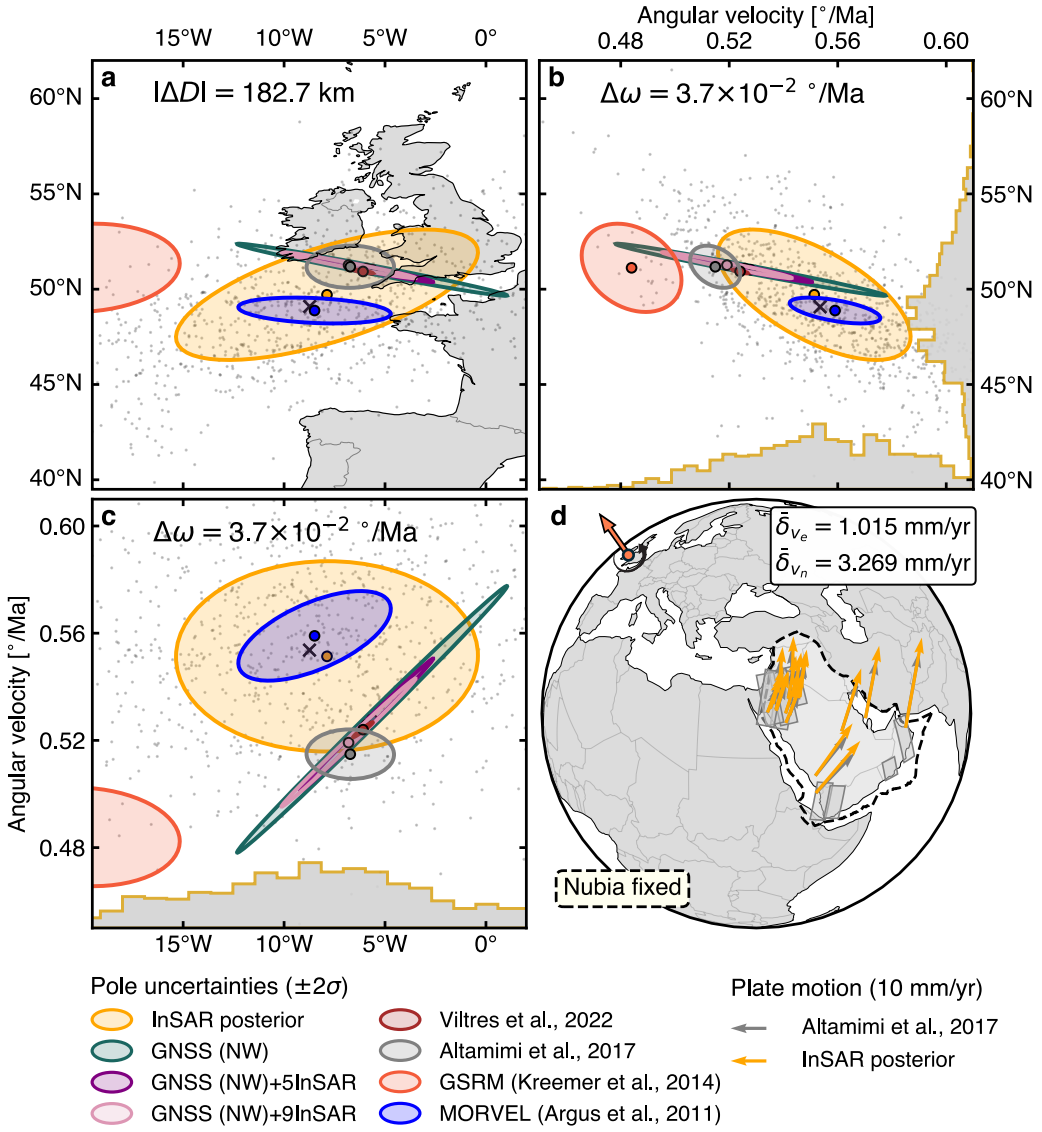

Figure 2.4: **(a-c)** Arabian plate Euler vectors (defined in ITRF2014) and uncertainties. The "x" marker shows the vector derived from velocities in Figure 2.3a. Scattered gray points represent the ensemble of Euler vectors estimated using different reference pixels, with marginal distributions plotted as histograms. The orange ellipse marks the final posterior vector. GNSS(NW) is based on 15 GNSS stations in northwest Arabia (Viltres et al., 2022), GNSS(NW)+5InSAR is the joint inversion with five InSAR tracks in NW Arabia, and GNSS(NW)+9InSAR is a joint inversion including all InSAR datasets. $|\Delta D|$ and $\Delta\omega$ are the distance and rotation rate differences between our InSAR-derived vector and Altamimi et al. (2017). **(d)** Predicted horizontal velocities (in stable Nubia) of the InSAR-only posterior vector evaluated at GNSS sites. The mean differences in east ($\bar{\delta}_{v_e}$) and north ($\bar{\delta}_{v_n}$) components are compared with Altamimi et al. (2017).

Impact of InSAR imaging geometry

The uncertainty in the Euler vector depends on how well the measurement aperture spans the local rotational component of the velocity gradient tensor. The trade-off between the distance between the sites and the pole and the angular velocity creates an elongation of the error ellipse of the Euler pole along this radial direction (e.g., d'Alessio et al., 2005; Elliott et al., 2010). For example, 15 GNSS sites from Viltres et al. (2022) (Supplementary Text S1) in northwest Arabia yield a Euler pole with high uncertainty normal to the plate motion (GNSS (NW) in Figure 2.4). Joint inversion with collocated InSAR velocities over northwest Arabia reduces the trade-off by a factor of two (GNSS (NW)+5InSAR in Figure 2.4). However, further including the InSAR data in Yemen and Oman only impacts the estimate marginally, presumably due to the poor data quality in those regions (Supplementary Text S2).

We further evaluate the effects of imaging geometry through synthetic scenarios with varying data availability: GNSS-only, InSAR LOS, or InSAR LOS combined with along-track velocity constraints (e.g., pixel tracking (Fialko et al., 2001) or burst-overlap interferometry (Grandin et al., 2016)). We use the Euler vector from Altamimi et al. (2017) to predict horizontal and LOS velocities as the synthetic inputs for SAR and GNSS inversions, respectively. For tests including SAR synthetics, we assume measurement errors $\mathbf{C}_{\mathrm{d_t}}$ as referenced in Figure 2.3a and neglect $\mathbf{C}_{\mathrm{p}}$. For the GNSS-only synthetics, we adopt the measurement errors of Viltres et al. (2022). In each case, we compute (1) the Euler vector, $\hat{\mathbf{m}}$ and its covariance matrix, $\mathbf{C}_{\hat{\mathrm{m}}}$, (2) the system's condition number, (3) the angular velocity difference from the input, $||\hat{\mathbf{m}} - \mathbf{m}_{\text{Altamimi et al., 2017}}||$ (°/Ma), and (4) the post-fit residual RMS (Figure 2.5).

The best solution is achieved using the full GNSS network (gnss). Using 20 stations spanning the breadth of the plate (gnssEW) reaches a similar result. However, when using only 15 stations from northwest Arabia (gnssNW), the yielded Euler vector has high trade-off. For InSAR scenarios, using exclusively ascending or descending geometries results in significant bias in the pole location and large $\mathbf{C}_{\hat{\mathrm{m}}}$. For example, the 1A (one Ascending track), 1D (one Descending), and 2A (two Ascending) cases ($|\Delta D| > 708.9$ km) are ill-conditioned and prone to over-fitting (low post-fit RMS), exhibiting spurious north-south motion (Figure 2.5 and the labels defined therein). Two or more LOS geometries are needed to constrain an Euler vector with a reasonable 2-sigma bound that overlaps the benchmark.

Due to the near-polar orbit and consistent right-looking geometry of conventional satellites like Sentinel-1, the sensitivity to the north-south displacement field is

limited (e.g., Brouwer & Hanssen, 2023). The null space associated with the limited diversity of imaging geometry absorbs non-rotational signals in the LOS measurements by inflating the apparent north-south motion. Residual noise of at mm yr^{-1} level both at the reference pixel and in long wavelengths can elongate the error ellipse of the derived Euler vector along N60°E (Figure 2.4a). As a result, while synthetic scenarios 3A (three Ascending), 4AD (two Ascending and two Descending), etc., constrain the Euler vector within the 2-sigma bounds of the solution from Altamimi et al. (2017), our observations do not. Incorporating azimuthal displacements or future left-looking measurements could improve the solution (e.g., Wright et al., 2004; Rosen & Kumar, 2021).

Referencing multi-track InSAR velocities

Multi-track InSAR velocities are typically stitched to form a regional-scale deformation field by empirically aligning each track or frame to collocated GNSS (e.g., Weiss et al., 2020; Xu et al., 2021; Ou et al., 2022; Lemrabet et al., 2023). However, this data-driven approach ties InSAR long-wavelength components to GNSS, and requires a well-distributed GNSS network. By inferring and removing the Arabian block rotation, we isolate intra-plate deformation from the observed velocities, thus providing a potentially more independent approach for referencing multi-track InSAR velocities.

Our Arabia-fixed velocities are consistent across multiple tracks and with GNSS LOS velocities (Viltres et al., 2022) without empirical adjustments (Figures 2.3d and S12). The consistency suggests that (1) the overlapping tracks do not experience significant relative intra-plate deformation nor vertical motion; (2) the relative horizontal and vertical motion between the reference pixels are negligible; (3) the effect of residual tropospheric noise on velocities sampled at different days by radar satellites are negligible. Thus, we infer that the velocity field primarily characterize the underlying rigid Arabian plate (Vigny et al., 2006; ArRajehi et al., 2010; Viltres et al., 2022), and the post-fit residuals are localized deformation confined within areas such as Dead Sea and the Wadi Sirhan Basin. In regions where large-scale vertical or distributed deformation ($\mathbf{v}_\varepsilon$) across multiple tracks cannot be overlooked (e.g., Great Lakes and Western US), a rigid plate assumption is inappropriate and the inversion will be biased. In such cases, one must account for the impact of mean rotation in ITRF on apparent strain or reconcile with existing GNSS networks empirically.

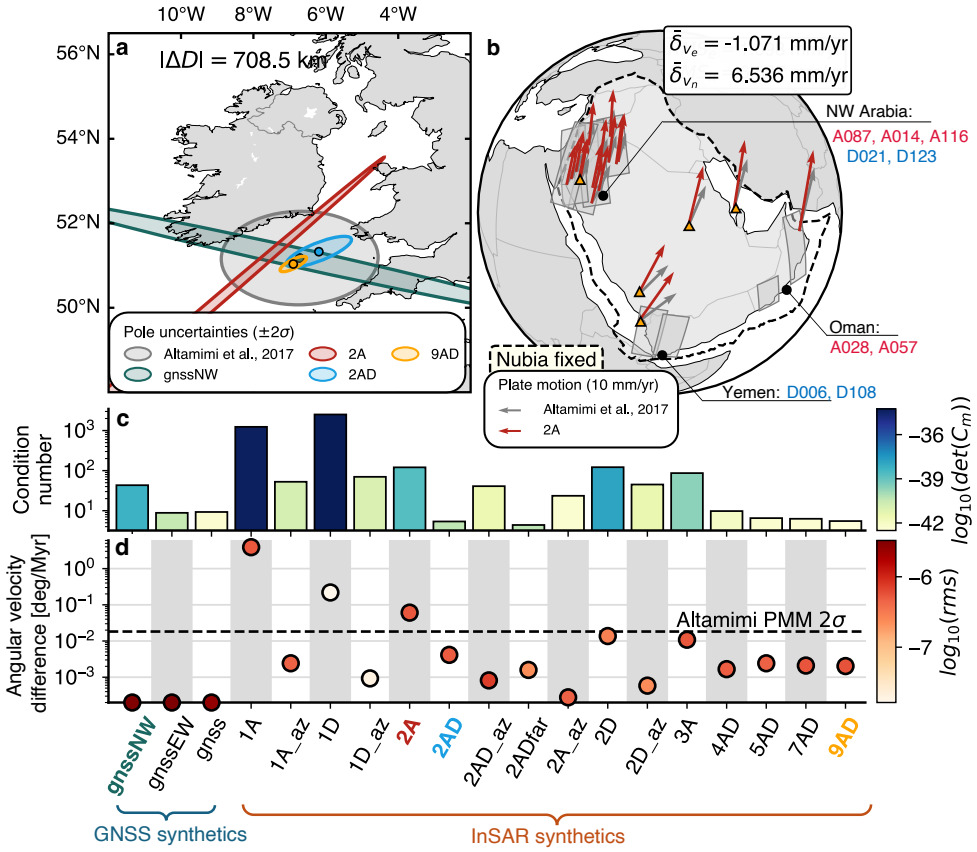

Figure 2.5: Synthetic scenarios with various sensing geometries. **(a)** Same style as Figure 2.4a. $|\Delta D|$ denotes the distance of 2A from Altamimi et al. (2017). **(b)** Same style as Figure 2.4d. **(c)** Model sensitivity: the condition number of $\mathbf{G}$ and the determinant of $\mathbf{C}_{\hat{\mathbf{m}}}$. **(d)** Angular velocity difference from Altamimi et al. (2017) in Cartesian space. Dots are colored by residual RMS. Labeling for GNSS-only synthetics: gnssNW denotes 15 stations in NW Arabia; gnssEW denotes 20 sparse GNSS sites in panel (b). gnss denotes the full GNSS network in Arabia (Figure 2.1). Labeling for InSAR synthetics: the numeric denotes the total number of track(s), "A" denotes ascending data, and "D" for descending data. 1A: one ascending track, A087. 1D: one descending track, D021. 2A: two ascending tracks, A087 and A014. 2ADfar: one ascending in NW Arabia and one descending in Oman, A057 and D021. 2D: D021 and D123. 2AD: A087 and A014. 3A: A087, A014, and A116. 4AD: 3A and D021. 5AD: five tracks in northwest Arabia. 7AD: seven tracks in northwest Arabia and Oman 9AD: all InSAR tracks. The subscript "az" indicates inclusion of the synthetic azimuthal velocity.

2.4 Conclusions

We infer the angular velocity vector of the Arabian plate using large-scale InSAR velocity fields in ITRF14. Plate rotation, manifested as a relative velocity gradient of ~2.1 mm yr^{-1}/100 km due to varying line-of-sight sensitivity, is extracted after mitigating long-wavelength path delays. Ionospheric effects emerge as the dominant nuisance origin, contributing to 0.8–2.0 mm yr^{-1}/100 km of apparent gradient in C-band velocity fields, an order of magnitude larger than tropospheric and tidal signals. The InSAR-derived Euler vector agrees with GNSS-based results exhibiting mean differences of 1.0 (east) and 3.3 (north) mm yr^{-1}. A persistent misfit in the InSAR-based solution arises from poor north-south sensitivity coupled with unaccounted-for long-wavelength noise. This work demonstrates the methodology to assess reference frame effects in InSAR velocity fields and to integrate them with conventional ground networks for high-resolution plate kinematic models. However, caution is warranted when extending this approach to regions with significant large-scale vertical motion and distributed intra-plate deformation.

APPENDIX B: SUPPLEMENTARY MATERIALS FOR CHAPTER 2

B.1 Supplementary Text

GNSS network for the inversion

In the Main Text, we utilize the GNSS dataset from Viltres et al. (2022). This work compiles the most recent and complete GNSS-derived velocities from 168 stations across the Arabian plate for the regional kinematic block model. The GNSS velocities closely fit the Arabian plate motion, with the exception of five stations located near and within the Danakil block (Afar depression in the SW of the map). A single Euler pole at 50.93 ± 0.15N, 353.91 ± 0.25E, with a rotation rate of 0.524 ± 0.001/Ma, effectively explains nearly all the GNSS station velocities relative to the ITRF14 reference frame (Figure 2.18), confirming the large-scale rigidity of the plate (Le Pichon & Kreemer, 2010; Viltres et al., 2022).

In our joint inversion presented in the Main Text (Figure 4), the aim is to demonstrate InSAR's contribution to enhancing GNSS ability to infer the Euler vector when they are limited specifically in the northwest Arabia. Therefore, we only include the 15 GNSS sites located within the InSAR footprint in the NW Arabia (including station HALY, which was used to determine the ITRF2014 Arabian Plate Motion Model).

For the GNSS synthetic tests in Main Text Section 3.3, we further include stations from the eastern side of the Arabian Peninsula to cover a broader range of the rotational field, thereby reducing the uncertainty in the inferred Euler vector. These stations include SQUO in Muscat (Oman), and the four stations used to determine the ITRF2014 Arabian Plate Motion Model (Altamimi et al., 2017): NAMA, JIZN, SOLA, and BAHR. For a rigid plate like Arabia, a sparse but widely distributed GNSS network can adequately constrain the angular velocity vector by properly sampling the rotation field. Consequently, InSAR may not be essential with high-fidelity GNSS stations spanning the plate's width.

InSAR velocity estimates

Secular velocity and uncertainty

After applying corrections for solid-earth tides (SET), ERA5 weather model, ocean-tidal loading effects (OTL), ionospheric phases, and DEM error estimates, we model the time series at each pixel using the following equation:

$$d(t_k) = a_0 + \dot{a}t_k + a_{c_1}\cos(2\pi t_k) + a_{s_1}\sin(2\pi t_k) + a_{c_2}\cos(4\pi t_k) + a_{s_2}\sin(4\pi t_k) + \epsilon(t_k) \tag{2.10}$$

We solve for the parameters (intercept a_0, linear rate $\dot{a}$, and annual/semi-annual periodic terms $a_{c_1}, a_{c_2}, a_{s_1}, a_{s_2}$) using a least-squares approach. The linear rate $\dot{a}$ is extracted as the velocity estimate (Figure 2.7). We compute the standard deviation of the residuals, $\sigma_{\epsilon(t_k)}$, and propagate it to estimate the velocity uncertainty (Figure 2.7 and 2.15), assuming uncorrelated Gaussian errors at all epochs (Fattahi & Amelung, 2015), with:

$$\dot{\sigma}_{\mathrm{v}} = \frac{\sigma_{\epsilon(t_k)}}{\sqrt{\mathrm{N}-6}\sigma_t} \tag{2.11}$$

where N is the number of epochs (K), N − 6 represents the degrees of freedom in Equation (2.14), and σ_t is the standard deviation of all time epochs in years.

Velocity maps derived from Sentinel-1 TOPS (Terrain Observation with Progressive Scans) interferograms (Figure 2.15) exhibit noise, particularly at burst boundaries, manifesting as intra-burst phase ramps and inter-burst discontinuities. These are primarily attributed to ionospheric effects causing azimuthal misregistration, which our split-band ionospheric correction did not fully account for (Gomba et al., 2017; Liang et al., 2019). Our processing only corrects for the range phase group delay caused by spatially smooth Total Electron Content (TEC). While intra-burst phase ramps could be removed by estimating azimuthal misregistration and related ramps due to TEC spatial gradients (Liang et al., 2019), this method relies on detailed quality checks of the estimated TEC gradient, which we consider more susceptible to unwrapping errors in sub-band ionospheric phases. Given our focus on the long-wavelength gradient of the velocity field, we did not address these higher-frequency effects.

The uncertainty of the velocity field (quantified by the standard deviation of the velocity fit) varies spatially, with higher uncertainty in the tracks over Oman and Yemen (the row of Std. in Figure 2.15). These four tracks also show lower average coherence across all interferograms. Several factors likely contribute to this reduced coherence in Yemen and Oman (typically $\gamma \sim 0.7 - 0.8$) compared to NW Arabia ($\gamma > 0.9$): (1) Steeper terrains, such as the southern Sarawat Mountains (e.g.,

near Jabal An-Nabī Shu'ayb), with significant elevation changes (< 1 km to 4 km within 100 km), cause geometric decorrelation and phase noise. (2) Tropospheric conditions: Yemen and Oman, located in more tropical latitudes, experience greater water vapor variability (e.g., wet delays of 5–20 cm), contrasting with the more stable, arid climate of NW Arabia. (3) Surface decorrelation: Extensive sand dune fields in Yemen and Oman (e.g., Rub' al Khali) lead to temporal decorrelation due to surface changes, unlike the stable rocky surfaces in NW Arabia.

Performance of time-series corrections in reducing ramps

To quantify the effectiveness of time-series corrections (solid-earth tides (SET), ERA5 weather model, ocean-tidal loading effects (OTL), ionospheric phases, and DEM error estimates), we assess the agreement between the model-predicted ramp and the ramp observed in the data. We fit linear spatial ramps to the displacement data at each time-series epoch:

$$d(t_k) = r_x x + r_y y + d_r(t_k) = r(t_k) + d_r(t_k) \tag{2.12}$$

where $d(t_k)$ represents the displacement map at time t_k (the k-th epoch in the time series of K total dates, $t = t_1, t_2, ..., t_k, ..., t_K$). At each t_k, the spatial linear ramp $r(t_k) = r_x x + r_y y$ is defined relative to a reference point and characterized by slopes r_x and r_y (in mm/km) along the longitude (x) and latitude (y) grids, respectively. The term $d_r(t_k)$ represents the residual higher-frequency component of the time-series map. This same linear ramp fitting procedure is applied to the correction models (ERA5, SET, Ionosphere, and OTL). For each epoch, we compute the ramp magnitude $|r_k| = \sqrt{r_x^2 + r_y^2}$. The comparison between the data-derived ramps and the model-predicted ramps is illustrated in Figure B.2, highlighting that the ionosphere and troposphere are the primary contributors to these ramps.

We also estimate the ramps of the velocity field using the form:

$$v = r_x x + r_y y + v_r = r + v_r \tag{2.13}$$

where v is the velocity track. x and y are the east-west and north-south location grid coordinates in kilometers. The parameters r_x and r_y are different than the ones in the time-series ramps in Equations 2.12. The ramp magnitude is defined as the L-2 norm

of the ramp parameters, $|r| = \sqrt{r_x^2 + r_y^2}$, and has a unit of mm yr^{-1}/km. We compute the apparent velocity from the each correction term and report their corresponding velocity ramp magnitude (scale to mm yr^{-1} per 100 km for readability) in the upper-left corner of Figure 2 (a-h) in the Main Text.

Uncertainty in the long-wavelength velocity

When characterizing the observational errors in the InSAR velocity fields, we removed quadratic ramps from the velocity fields before semi-variogram fitting (Main Text Section 2.3 and Supplement Text 4-2), yielding noise correlation lengths of approximately 30–100 km. The deramping ensures the inversion will not penalize the spatial coherence at the longest-wavelength signal across the InSAR scene, and the angular velocity vector can fit the long-wavelength gradient from plate motions. Therefore, by design, our Euler pole inversion assumes unbiased long-wavelength ramps in the observations. However, noise at longer wavelengths (e.g., across the whole 250 km track) was not accounted for. Such long-wavelength ramp noise may originate from different sources than smaller-scale noise, including baseline errors or inaccuracies in estimated ionospheric phases.

The low coherence observed in Yemen and Oman suggests the potential for unidentified sub-band ionospheric unwrapping errors in the corresponding InSAR velocity fields. These errors can propagate into the estimated ionospheric phase, introducing uncertainties in the long-wavelength velocity fields, which could bias the inferred Euler pole. To empirically quantify this gradient uncertainty, we adopt the method from Lemrabet et al. (2023) and compute the ramp rate error from the time series.

For each InSAR time-series track, following corrections for solid-earth tides, the ERA5 weather model, and ionospheric effects, we fit linear spatial ramps to each epoch as described in Equation 2.12. We then parameterized the ramp time series $r(t_k)$ with a temporal function (intercept b_0, linear rate $\dot{b}$, annual and semi-annual periodic terms b_{c_1}, b_{s_1}, b_{c_2}, and b_{s_2}) as shown in Equation (2.14):

$$r(t_k) = b_0 + \dot{b}t_k + b_{c_1}\cos(2\pi t_k) + b_{s_1}\sin(2\pi t_k) + b_{c_2}\cos(4\pi t_k) + b_{s_2}\sin(4\pi t_k) + \epsilon_r(t_k) \tag{2.14}$$

Note that the linear rate $\dot{b}$ is primarily governed by the plate motion in ITRF2014. As the Euler pole inversion mainly utilizes long-wavelength velocity gradients, our

aim here is to estimate the uncertainty of its empirical proxy: the ramp rate $\dot{b}$. To do this, we compute the ramp in the residuals $\epsilon_r(t_k)$ and determine the standard deviations across all t_k. The standard deviations of the residual ramp parameters in the east-west and north-south directions, $\sigma_{\epsilon_{r_x}}$ and $\sigma_{\epsilon_{r_y}}$, are linearly propagated to approximate the standard deviation of the velocity ramp rate $\dot{\sigma}_{\text{ramp}}$ (Fattahi & Amelung, 2015; Lemrabet et al., 2023):

$$\dot{\sigma}_{\text{ramp}} = \frac{\sigma_{\text{ramp}}}{\sqrt{\text{N} - 6}\sigma_t} \tag{2.15}$$

where σ_{ramp} represents either $\sigma_{\epsilon_{r_x}}$ or $\sigma_{\epsilon_{r_y}}$, and $\dot{\sigma}_{\text{ramp}}$ is the corresponding ramp rate uncertainty. N is the number of epochs (K), and N − 6 represents the degrees of freedom in Equation (2.14). σ_t is the standard deviation of all time epochs in years.

For velocity tracks in NW Arabia (Figure B.2), the standard deviations of the east-west ramp rate are approximately 0.0005 mm/year/km, corresponding to about 0.125 mm/year across a 250 km longitude span. The north-south ramp rate error is around 0.0012 mm/year/km, equating to 1.2 mm/year along a 1000 km latitudinal track. Ramp rate errors in Oman and Yemen are significantly higher due to lower coherence and rougher terrain hindering reliable ionospheric phase estimation. The east-west errors range from 0.0016 to 0.004 mm/year/km (0.4 to 1.0 mm/year across 250 km), and the north-south errors range from 0.0023 to 0.0034 mm/year/km (2.3 to 3.4 mm/year along 1000 km). Generally, likely due to stronger north-south ionospheric phase gradients in the region, the north-south ramp rates exhibit larger errors than the east-west ones when residual ionospheric effects are present. Although we estimate this ramp rate error for all the tracks, we did not include this error into the inversion of the Euler pole. While this could be done to re-weight different track's data, the results might not be altered significantly due to the magnitude of the error ($< 10\%$ of the actual plate motion gradient).

Euler rotation pole

In this section, we describe the equations of Euler pole inversion using InSAR line-of-sight (LOS) velocity fields.

The mathematical notation

The Sentinel-1 orbit is defined relative to the International Terrestrial Reference Frame 2014 (ITRF2014). ITRF2014 is an Earth-centered, Earth-fixed (ECEF) reference frame with no net rotation (NNR) of the Earth's surface. Observations of absolute ground motion relative to the satellite are therefore also described in ITRF2014 (Peter, 2021; Stephenson et al., 2022; Lazecký et al., 2023).

If the ground motions can be simplified as rigid rotation of a plate, the line-of-sight (LOS) velocities measured in Sentinel-1, $\mathbf{d}$, can be described as rotation around an Euler vector (McKenzie & Parker, 1967; Morgan, 1968; Cox & Hart, 1986) as

$$\begin{aligned} \mathbf{d} &= \mathbf{G}\,\mathbf{m} \\ [P \times 1] &= [P \times 3]\dot{[}3 \times 1]. \end{aligned} \tag{2.16}$$

The Euler vector, $\mathbf{m}$, denotes the angular velocities in three orthogonal components in the Cartesian coordinates, $\mathbf{m} = [\mathrm{m_x}, \mathrm{m_y}, \mathrm{m_z}]^\intercal$ $(rad/year)$. The Euler pole rotation vector is linearly mapped to the LOS velocities at each pixel by the linear operator $\mathbf{G}$, which is fully determined by the coordinates and the radar line-of-sight vector of each ground pixel i out of a total number of P pixels for which we estimate a deformation velocity

$$\begin{aligned} \mathbf{G} &= \begin{bmatrix} \mathbf{G}^1 \\ \vdots \\ \mathbf{G}^i \\ \vdots \\ \mathbf{G}^P \end{bmatrix} \\ i &\in [1, \ldots, P], \end{aligned} \tag{2.17}$$

and each row encapsulates three transformation matrices for each pixel independently:

$$\begin{aligned} \mathbf{G}^i &= \mathbf{T}^i_\Lambda\, \mathbf{T}^i_\Theta\, \mathbf{T}^i_\mathrm{X} \\ [1 \times 3] &= [1 \times 3] \cdot [3 \times 3] \cdot [3 \times 3], \end{aligned} \tag{2.18}$$

where $\mathbf{T}^i_{\mathrm{X}}$ is a cross-product matrix to map the rotation Euler pole to the Cartesian velocities at a Cartesian location $\mathbf{r}^i = [x, y, z]$, i.e., $\mathbf{v}(\mathbf{r}^i) = \mathbf{r}^i \times \mathbf{m} = \mathbf{T}^i_{\mathrm{X}} \cdot \mathbf{m}$, and

$$\mathbf{T}^i_{\mathrm{X}} = \begin{bmatrix} 0 & z & -y \\ -z & 0 & x \\ y & -x & 0 \end{bmatrix}_i . \tag{2.19}$$

The 3-dimensional location in the Cartesian coordinate $\mathbf{r}^i = [\mathrm{x}, \mathrm{y}, \mathrm{z}]$ is determined by the latitude λ, longitude ϕ, and height h, at pixel i on an assumed ellipsoid with an equatorial radius R_{e} and an eccentricity e (Bowring, 1976; Sanz Subirana et al., 2011a):

$$\mathbf{r}^i = \begin{bmatrix} x \\ y \\ z \end{bmatrix} = R_{\mathrm{e}}(1 - e^2 \sin^2 \lambda)^{-1/2} \begin{bmatrix} 1 + h \\ 1 + h \\ (1 - e^2) + h \end{bmatrix} \cdot \begin{bmatrix} \cos\lambda \cos\phi \\ \cos\lambda \sin\phi \\ \sin\lambda \end{bmatrix} . \tag{2.20}$$

The matrix $\mathbf{T}^i_{\Theta}$ transforms from the Cartesian velocity at a given longitude ϕ and latitude λ into the local planar motion in east, north, and up components (Sanz Subirana et al., 2011b):

$$\mathbf{T}^i_{\Theta} = \begin{bmatrix} -\sin\lambda & \cos\lambda & 0 \\ -\sin\phi\cos\lambda & -\sin\phi\sin\lambda & \cos\phi \\ \cos\phi\cos\lambda & \cos\phi\sin\lambda & \sin\phi \end{bmatrix}_i . \tag{2.21}$$

The velocities in east, north, and up are then projected into the LOS direction of the satellite by the array $\mathbf{T}^i_{\Lambda} = [\mathrm{l}_1, \mathrm{l}_2, \mathrm{l}_3]$, yielding the LOS velocity $\mathbf{d}$. $\mathbf{T}^i_{\Lambda}$ is a unit vector pointing along the observed motion. It is often called the line-of-sight (LOS) vector in the context of InSAR, along which the range change, or the LOS motion is derived from the phase interferometry. Note that any motion in the Euclidean space can be represented as a LOS motion with a magnitude along its unit vector of motion. Thus, this projection unit vector can be generalized to map between the east, north, up components and any 3 dimensional motion, including observations from InSAR range change, radar or optical image offset tracking, and two- or three-component GNSS displacements. In such case, $\mathbf{d}$ can be populated by east, north, and up velocities of multiple stations along the single-column vector. Accordingly, $\mathbf{T}^i_{\Lambda} = [1, 0, 0]$ corresponds to the east row of $\mathbf{d}$, $\mathbf{T}^i_{\Lambda} = [0, 1, 0]$ corresponds to the north row, and $\mathbf{T}^i_{\Lambda} = [0, 0, 1]$ corresponds to the up row, respectively. But, one

would remove the vertical component from GNSS in a rotation problem on Earth's surface because it will never be fitted. In our special case of single-component InSAR velocity where the LOS projection at each pixel is dictated by the satellite incidence angle θ and azimuth angle ψ, we can write the projection vector as

$$\mathbf{T}_{\Lambda}^{i} = \begin{bmatrix} -\sin\theta\sin\psi \\ \sin\theta\cos\psi \\ \cos\theta \end{bmatrix}_{i}^{\mathsf{T}} . \tag{2.22}$$

Note that the plate motion can be measured because incidence and azimuth angles vary across the SAR scene, so θ and ψ here should differ from pixel to pixel. Plug in Equation 2.17 to 2.22, each row of $\mathbf{G}^{i}$ can be constructed as

$$\mathbf{G}^{i} = \begin{bmatrix} -\sin\theta\sin\psi \\ \sin\theta\cos\psi \\ \cos\theta \end{bmatrix}_{i}^{\mathsf{T}} \begin{bmatrix} -\sin\lambda & \cos\lambda & 0 \\ -\sin\phi\cos\lambda & -\sin\phi\sin\lambda & \cos\phi \\ \cos\phi\cos\lambda & \cos\phi\sin\lambda & \sin\phi \end{bmatrix}_{i} \begin{bmatrix} 0 & z & -y \\ -z & 0 & x \\ y & -x & 0 \end{bmatrix}_{i} , \tag{2.23}$$

and Equation 2.16 can be solved simultaneously for all P InSAR pixels, from one or more orbital tracks. The above expression generates an absolute velocity in the reference frame. However, InSAR measurements are always described with respect to a reference point at $\mathbf{r}^{*}$. There is an unknown constant shift, b, between the measured relative velocity and the absolute velocity in ITRF, $\mathbf{d}^{*}$ by $\mathbf{d} = \mathbf{d}^{*} + b$. This shift is track-specific and represents the absolute plate motion at the reference pixel when the atmospheric noise and the unrecognized internal deformation at that pixel can be ignored. Unless pre-determined by independent GNSS, we need to estimate these shifts and the Euler pole simultaneously by

$$\mathbf{d}^{*} = \mathbf{G}^{+}\,\mathbf{m}^{+} \quad , \tag{2.24}$$

where the model parameter vector having the shift term in this InSAR track becomes

$$\mathbf{m}^{+} = \begin{bmatrix} \mathrm{m_x} \\ \mathrm{m_y} \\ \mathrm{m_z} \\ b \end{bmatrix} \quad . \tag{2.25}$$

And, we append a column of ones, **1**, to the linear operator

$$\mathbf{G}^{+} = \begin{bmatrix} \mathbf{G} & \mathbf{1} \end{bmatrix} \quad . \tag{2.26}$$

However, since the similarity of the azimuth angles across the scene (varies < 1.6°), InSAR LOS velocity with residual noise permits high trade-offs between the pole parameters. The extra unknown shifts in the problem only exacerbate these trade-offs. Consequently, a biased Euler pole can be deceptively compensated by a floating shift for the whole track, fitting the observation equally well. Alternatively, we can adjust the linear model to a common reference pixel in data by subtracting the row corresponding to the reference pixel, $\mathbf{G}^{*} = \mathbf{G} - \mathbf{G}_{\mathbf{r}^{*}}$. This approach offers two advantages: it avoids additional trade-offs in model parameters and references the linear model to the same reference point as in the InSAR measurements and their observational errors. The formulation we use becomes

$$\mathbf{d}^{*} = \mathbf{G}^{*}\,\mathbf{m} \quad . \tag{2.27}$$

Transformation between the Cartesian and Spherical expressions

The Euler pole $(\hat{m}_x, \hat{m}_y, \hat{m}_z)$ in ECEF Cartesian coordinates can be transformed to the spherical expression (pole latitude λ_p, pole longitude ϕ_p, and pole angular velocity ω_p)

$$\begin{cases} \lambda_p = \arctan\left(\dfrac{m_z}{\sqrt{m_x^2 + m_y^2}}\right) \\ \phi_p = \arctan\left(\dfrac{m_y}{m_x}\right) \\ \omega_p = |\mathbf{m}| = \sqrt{m_x^2 + m_y^2 + m_z^2} \end{cases} \tag{2.28}$$

and vice versa

$$\mathbf{m} = w_p \begin{bmatrix} \cos\lambda_p \cos\phi_p \\ \cos\lambda_p \sin\phi_p \\ \sin\lambda_p \end{bmatrix} \quad . \tag{2.29}$$

The transformation of the model covariance matrix from the Cartesian to Spherical expression is through a Jacobian matrix, $\mathbf{J}_{\mathrm{C2S}}$ (Goudarzi et al., 2014):

$$\hat{\mathbf{C}}_{\mathrm{m}}^{\mathrm{sph}} = \mathbf{J}_{\mathrm{C2S}} \hat{\mathbf{C}}_{\mathrm{m}} \mathbf{J}_{\mathrm{C2S}}^{\intercal} \quad , \tag{2.30}$$

where

$$\mathbf{J}_{\mathrm{C2S}} = \begin{bmatrix} \frac{\partial \lambda_{\mathrm{p}}}{\partial \mathrm{m_x}} & \frac{\partial \lambda_{\mathrm{p}}}{\partial \mathrm{m_y}} & \frac{\partial \lambda_{\mathrm{p}}}{\partial \mathrm{m_z}} \\ \frac{\partial \phi_{\mathrm{p}}}{\partial \mathrm{m_x}} & \frac{\partial \phi_{\mathrm{p}}}{\partial \mathrm{m_y}} & \frac{\partial \phi_{\mathrm{p}}}{\partial \mathrm{m_z}} \\ \frac{\partial \omega_{\mathrm{p}}}{\partial \mathrm{m_x}} & \frac{\partial \omega_{\mathrm{p}}}{\partial \mathrm{m_y}} & \frac{\partial \omega_{\mathrm{p}}}{\partial \mathrm{m_z}} \end{bmatrix} = \begin{bmatrix} \frac{-\mathrm{m_x m_z}}{w_{\mathrm{p}}^2 \sqrt{\mathrm{m_x^2 + m_y^2}}} & \frac{-\mathrm{m_y m_z}}{w_{\mathrm{p}}^2 \sqrt{\mathrm{m_x^2 + m_y^2}}} & \frac{\sqrt{\mathrm{m_x^2 + m_y^2}}}{w_{\mathrm{p}}^2} \\ \frac{-\mathrm{m_y}}{\mathrm{m_x^2 + m_y^2}} & \frac{\mathrm{m_x}}{\mathrm{m_x^2 + m_y^2}} & 0 \\ \frac{\mathrm{m_x}}{w_{\mathrm{p}}} & \frac{\mathrm{m_y}}{w_{\mathrm{p}}} & \frac{\mathrm{m_z}}{w_{\mathrm{p}}} \end{bmatrix} . \tag{2.31}$$

The inverse transformation from the Spherical to Cartesian expression is through:

$$\hat{\mathbf{C}}_{\mathrm{m}} = \mathbf{J}_{\mathrm{S2C}} \hat{\mathbf{C}}_{\mathrm{m}}^{\mathrm{sph}} \mathbf{J}_{\mathrm{S2C}}^{\intercal} \quad , \tag{2.32}$$

where

$$\mathbf{J}_{\mathrm{S2C}} = \begin{bmatrix} \frac{\partial \mathrm{m_x}}{\partial \lambda_{\mathrm{p}}} & \frac{\partial \mathrm{m_x}}{\partial \phi_{\mathrm{p}}} & \frac{\partial \mathrm{m_x}}{\partial w_{\mathrm{p}}} \\ \frac{\partial \mathrm{m_y}}{\partial \lambda_{\mathrm{p}}} & \frac{\partial \mathrm{m_y}}{\partial \phi_{\mathrm{p}}} & \frac{\partial \mathrm{m_y}}{\partial w_{\mathrm{p}}} \\ \frac{\partial \mathrm{m_z}}{\partial \lambda_{\mathrm{p}}} & \frac{\partial \mathrm{m_z}}{\partial \phi_{\mathrm{p}}} & \frac{\partial \mathrm{m_z}}{\partial w_{\mathrm{p}}} \end{bmatrix} = \begin{bmatrix} -w_{\mathrm{p}} \sin\lambda_{\mathrm{p}} \cos\phi_{\mathrm{p}} & -w_{\mathrm{p}} \cos\lambda_{\mathrm{p}} \sin\phi_{\mathrm{p}} & \cos\lambda_{\mathrm{p}} \cos\phi_{\mathrm{p}} \\ -w_{\mathrm{p}} \sin\lambda_{\mathrm{p}} \sin\phi_{\mathrm{p}} & w_{\mathrm{p}} \cos\lambda_{\mathrm{p}} \cos\phi_{\mathrm{p}} & \cos\lambda_{\mathrm{p}} \sin\phi_{\mathrm{p}} \\ w_{\mathrm{p}} \cos\lambda_{\mathrm{p}} & 0 & \sin\lambda_{\mathrm{p}} \end{bmatrix} . \tag{2.33}$$

An example of linear operator, G

Each pixel in InSAR data contributes the pixel-wise LOS velocity, d_i, to one row of the $\mathbf{d}^*$ vector in Equation (12). Each pixel in InSAR data has the unique coordinates and radar imaging geometry that dictate each row, $\mathbf{G}_i = [g_{i1}, g_{i2}, g_{i3}]$ in the linear operator $\mathbf{G}$ (using Equation (8)), such that $d_i = \mathbf{G}_i\mathbf{m}$. We keep the 1-by-3 vector $[g_{i1}, g_{i2}, g_{i3}]$ in a variable form for the convenience of notation, where the first subscript index i is the pixel index and the second subscript index is the column index in $\mathbf{G}$. With total P pixels of velocity observations, we have $\mathbf{d}$ (size of P-by-1) and a design matrix $\mathbf{G}$ (size of P-by-3):

$$\mathbf{G} = \begin{bmatrix} g_{11} & g_{12} & g_{13} \\ & \vdots & \\ g_{i1} & g_{i2} & g_{i3} \\ & \vdots & \\ g_{P1} & g_{P2} & g_{P3} \end{bmatrix} \quad . \tag{2.34}$$

After constructing the operator $\mathbf{G}$, we subtract the row corresponds to the reference pixel, $\mathbf{G}^* = \mathbf{G} - \mathbf{G}_{\mathbf{r}^*}$, and follow the formulation in Equation 2.27 to solve the problem with any least-squares method. The example of the linear operator $\mathbf{G}$ is shown in Figure 2.12.

The P pixels of velocity observations ($\mathbf{d}$) can be acquired from one or several satellite tracks as long as the pixel-wise LOS velocity d_i corresponds to the unique radar imaging geometry used in the linear operator $\mathbf{G}_i$. For example, having totally Q tracks of InSAR velocity fields (e.g., multiple ascending and descending), we concatenate the linear operator in the vertical direction as

$$\mathbf{G} = \begin{bmatrix} \mathbf{g}_1^1 & \mathbf{g}_2^1 & \mathbf{g}_3^1 \\ \mathbf{g}_1^2 & \mathbf{g}_2^2 & \mathbf{g}_3^2 \\ \vdots & \vdots & \vdots \\ \mathbf{g}_1^q & \mathbf{g}_2^q & \mathbf{g}_3^q \\ \vdots & \vdots & \vdots \\ \mathbf{g}_1^Q & \mathbf{g}_2^Q & \mathbf{g}_3^Q \end{bmatrix} \quad , \tag{2.35}$$

where in each row, $\mathbf{g}_1^q$, $\mathbf{g}_2^q$, $\mathbf{g}_3^q$ denotes the column vectors in Equation 2.34 for the q-th InSAR track:

$$\mathbf{g_1^q} = \begin{bmatrix} g_{11} \\ \vdots \\ g_{i1} \\ \vdots \\ g_{P_q 1} \end{bmatrix}, \mathbf{g_2^q} = \begin{bmatrix} g_{12} \\ \vdots \\ g_{i2} \\ \vdots \\ g_{P_q 2} \end{bmatrix}, \mathbf{g_3^q} = \begin{bmatrix} g_{13} \\ \vdots \\ g_{i3} \\ \vdots \\ g_{P_q 3} \end{bmatrix} \quad . \tag{2.36}$$

The pixel index i ranges from 1 to the total number of pixels, P_q, in the q-th InSAR track.

Observational covariance matrix, $\mathbf{C_d}$

We characterize the observational error in InSAR-derived velocities using the data covariance matrix, which captures the variance and covariance features Hanssen (2001). The data covariance matrix has a dimension of P-by-P (P being the number of pixels in an InSAR track) and consists of two components,

$$\mathbf{C}_\mathrm{d} = \mathbf{C}_{\mathrm{d_t}} + \mathbf{C}_{\mathrm{d_s}} \quad . \tag{2.37}$$

The temporal term, $\mathbf{C}_{\mathrm{d_t}}$, is a diagonal matrix populated with the variances of the velocity estimates at pixel i, σ_i, determined by the functional-fit residuals assuming uniform Gaussian errors at all epochs as

$$\mathbf{C}_{\mathrm{d_t}} = \begin{bmatrix} \sigma_1 & 0 & 0 \\ 0 & \ddots & 0 \\ 0 & 0 & \sigma_P \end{bmatrix} \quad . \tag{2.38}$$

The spatial term, $\mathbf{C}_{\mathrm{d_s}}$, accounts for the stationary and isotropic noise correlation between nearby pixels, which we attribute to the remaining atmospheric effects after corrections. We use sample semi-variograms $\gamma(h)$ to estimate the InSAR variances as a function of distance between any pixel pair. Due to potential bias from the imperfect assumption of the stationary process of noise, we do not use a sample covariogram method. However, it should be equivalent to the sample semi-variogram method in an ideal case.

The discrete sample semi-variogram value for binned distance class h_c is

$$\gamma(h_c) = \frac{1}{2\mathrm{N}} \sum_{\substack{i=1 \\ \|\mathbf{r}_i - \mathbf{r}_j\| \simeq h_c}}^{N} [v(\mathbf{r}_i) - v(\mathbf{r}_j)]^2 \quad , \tag{2.39}$$

where N being the number of data-point pairs at locations $\mathbf{r}_i$ and $\mathbf{r}_j$ such that $\|\mathbf{r}_i - \mathbf{r}_j\|$ falls inside a distance bin h_c. Thus, when assuming isotropic noise, the semi-variogram depends only on distance h between data points.

We first uniformly downsample the velocity fields to approximately 2.5 km posting. The goal here is to quantify the intermediate range noise structure without sacrificing the ability to fit the longest-wavelength plate motion, thus we first remove a quadratic ramp from the velocity fields before sampling the semi-variograms (Figure 2.10). The quadratic ramp is parameterized in the form of $v = \mathrm{u}x^2 + \mathrm{v}y^2 + \mathrm{w}xy + \mathrm{a}x + \mathrm{b}y + \mathrm{c}$, where v is the velocity track. x and y are the east-west and north-south location grid coordinates in kilometers. The parameters a, b, c, u, v, and w are estimated in a least-squares sense. Then, we randomly pick velocity pairs $v(\mathbf{r}_i)$ and $v(\mathbf{r}_j)$ with distances h up to 300 km for each track. We then form the sample semi-variogram $\gamma(h)$ by taking the average in 1-km intervals. The data variance is estimated from the level at which the sample semi-variogram $\gamma(h)$ forms a plateau (called "sill") at distances larger than the characteristic length scale of correlation (Figure 2.11).

For a continuous description of the variogram we fit functions to the sample-variogram. The variance is a positive-definite function. Therefore, we use a function type ensuring positive definiteness, an inverse exponential decay function as

$$\gamma(h) = -(A^2) \exp(\frac{-h}{\lambda}) + \sigma \quad , \tag{2.40}$$

where A is the scaling factor, λ is the characteristic length of the correlation, and σ is the sill. The covariance function is then the mirror of the semi-variogram, expressing the degeneration of the covariance. In the presence of white noise, the covariance function has a step at a zero lag. We thus parameterize the spatial covariance matrix, $\mathbf{C}_{d_s}$ using the covariance function

$$\mathbf{C}_{d_s} = \mathbf{C}(h) = (A^2) \exp(\frac{-h}{\lambda}) + \sigma \quad . \tag{2.41}$$

Based on this function, we create the spatial covariance matrix, $\mathbf{C}_{\mathrm{d_s}}$. The diagonals are populated with a constant value of σ, the off-diagonals are computed based on

the distance separations of pixel pairs, h. Our covariance matrices are shown in Figure 2.13 and 2.14.

Unwrapping error correction

Unwrapping errors refer to the wrong integer numbers of cycles (2π radians) being added to the interferometric phase during the two-dimensional phase unwrapping. Unwrapping errors will propagate to the Small-BAseline-Subset (SBAS) time-series phases and bias the phase history. Our datasets contain unwrapping errors near Wadi Arabah valley in Egypt in tracks A058, D094 (the data from these two tracks in the Sinai subplate are not being used in the analysis described in the Main Text), and north-west Arabia track D021.

Since the errors are potentially due to intense tropospheric delay variation occurring in areas with sharp elevation change, we first remove the ERA5 model predicted phase from the wrapped interferograms and unwrap the phase (Jolivet et al., 2011). In addition to the stratified tropospheric phases, we also remove the ionospheric phases estimated from the split-spectrum method from the interferograms to further reduce the spatial phase gradients. These approaches do not clear all the unwrapping errors, leaving considerable remaining discontinuities in the velocity fields. Thus, other more delicate methods to correct for the unwrapping errors are needed (Figure 2.19).

Several methods to correct for the unwrapping errors, such as bridging (Biggs et al., 2007; Yunjun et al., 2019) and phase closure (Yunjun et al., 2019) rely on the properly labeled phase connected areas, called connected components. Each component is isolated by the unwrapping error to its neighboring one. However, the connected components in `SNAPHU` algorithm are not always identified and labeled correctly (also seen in Oliver-Cabrera et al. (2022)). Thus, many of the unwrapping errors present in our datasets are not properly labeled (Figure 2.19). Therefore, we attempt to come up with a way to re-generate the informative labels quantitatively, so that we can apply the unwrapping error correction based on these new labels.

We first make sure to minimize the phase gradients in the interferograms as much as possible before unwrapping. We remove the stratified tropospheric phases using either ERA5 or GACOS. We also remove the estimated ionospheric phases. To re-generate a better set of connected components for all pixels, we compute the number of triplets having non-zero integer ambiguity of closure phase (T_{int} in Yunjun et al. (2019)). Pixels in the same connected region would have the same number of non-zero closure triplets. Thus, we run a clustering algorithm to group the areas based on their T_{int} and generate a new set of connected components. To estimate the number of integer ambiguities in the network, we assume triplet phases should

be within $\pm\pi$ and implement a region-based inversion to minimize the regularized L1-norm. To reduce computation, instead of inverting every pixel for the integer ambiguity, we randomly select 100 pixels for each common connected component and conduct the inversion. The median of inverted numbers is used for all pixels within this common component and removed from the phase time series (Yunjun et al., 2019). This approach successfully mitigate the unwrapping errors in tracks D094 over the Sinai Peninsula (Figure 2.19), D021 in the northwest Arabia, and A058 along the Nile river.

B.2 Supplementary Figures

Table S1: InSAR-derived Euler vector parameters of the Arabian plate.

Spherical expression[a]	Unit[c]	Value	1σ
Pole latitude	deg	49.7081	1.7108
Pole longitude	deg	−7.8751	3.7392
Rotation rate	deg/Ma	0.5514	0.0178
	mas/yr	1.9849	0.0639
Cartesian expression[b]	Unit	Value	1σ
m_x	deg/Ma	0.3532	0.0206
	mas/yr	1.2715	0.0742
m_y	deg/Ma	−0.0489	0.0243
	mas/yr	−0.1759	0.0875
m_z	deg/Ma	0.4206	0.0105
	mas/yr	1.5140	0.0380

The full covariance, $\mathbf{C}_m$ (mas^2/yr^2):

xx	xy	xz
2.67×10^{-11}	-1.08×10^{-11}	4.68×10^{-12}
yy	yz	zz
3.72×10^{-11}	9.74×10^{-12}	6.99×10^{-12}

[a] The spherical expression is often referred to as the Euler pole location and the rotation rate.

[b] The Cartesian expression denotes the angular velocity vector. The three orthogonal axes x, y, and z align with the (0°N, 0°E), (0°N, 90°E), and 90°N directions, respectively.

[c] deg: degrees; Ma: million years; yr: years; mas: milliarcsecond; rad: radian.

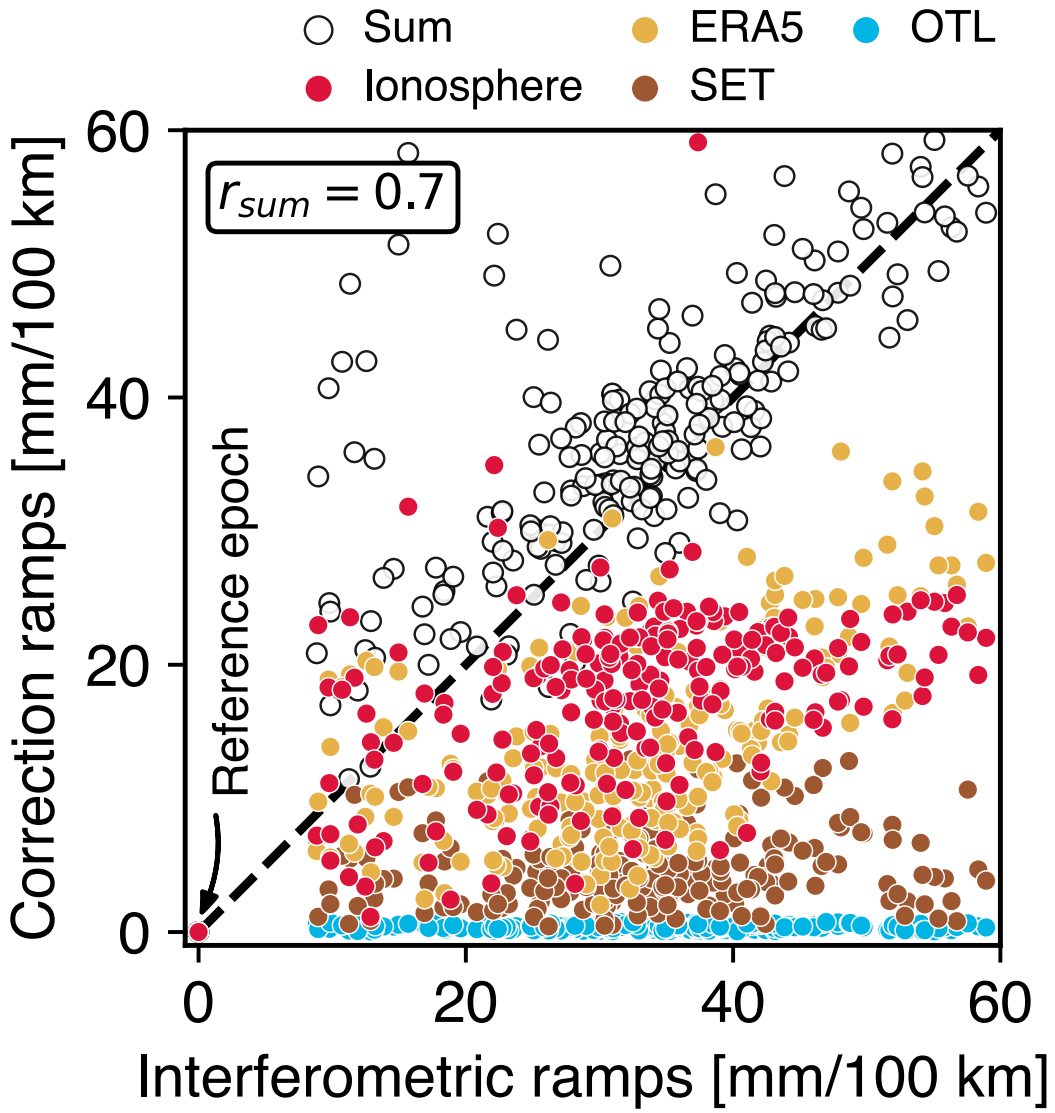

Figure 2.6: Fitted ramp magnitude at each time-series epoch (observations on x-axis and correction predictions on y-axis). r_{sum} is the correlation coefficient between ramps predicted by the sum of all correction terms and the observed ramps.

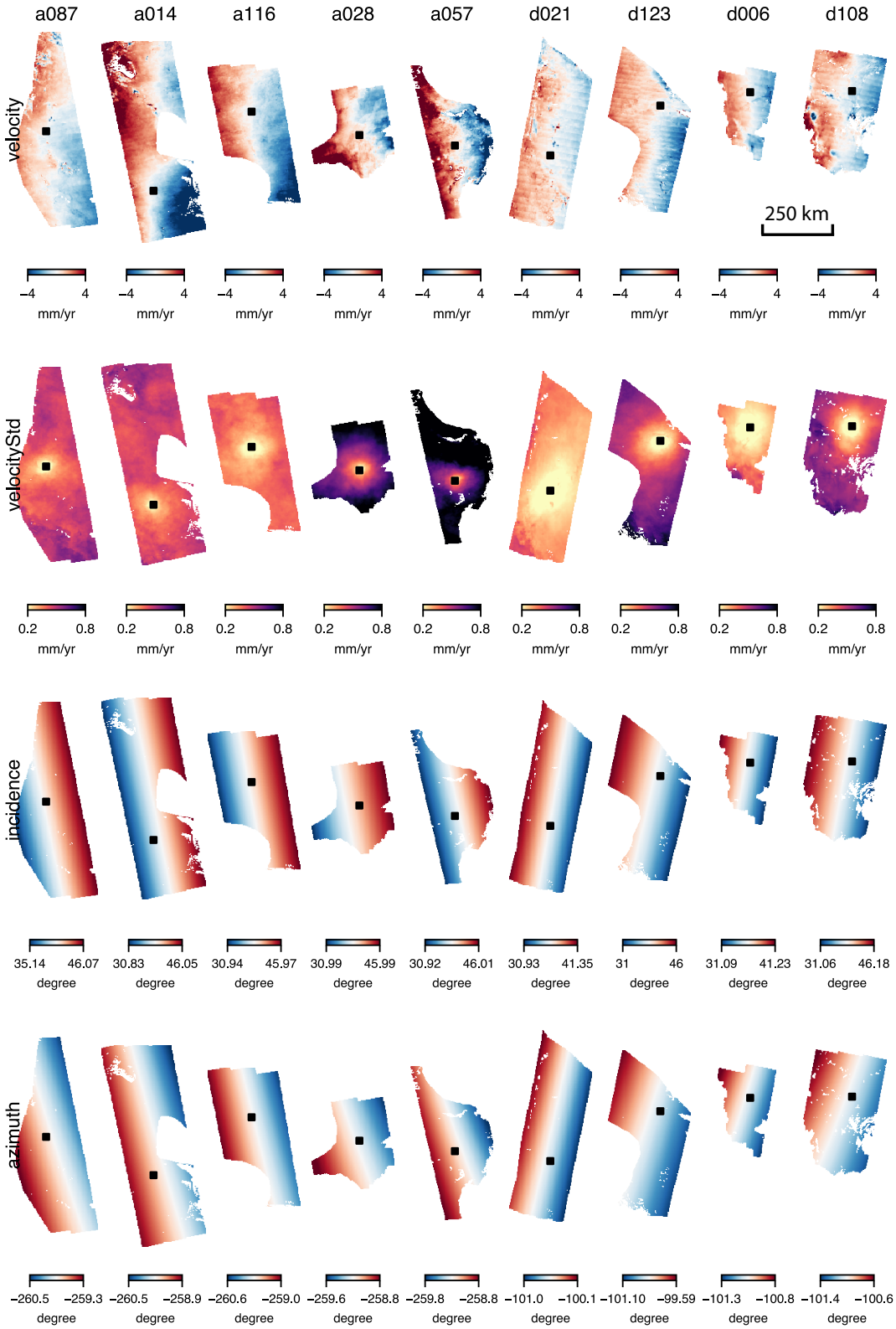

Figure 2.7: Caption next page.

Figure 2.7: The LOS velocity fields, standard deviations, incidence, and azimuth angles from all nine Sentinel-1 tracks. Velocities and errors are referenced to our prior-selected reference points, the black squared markers.

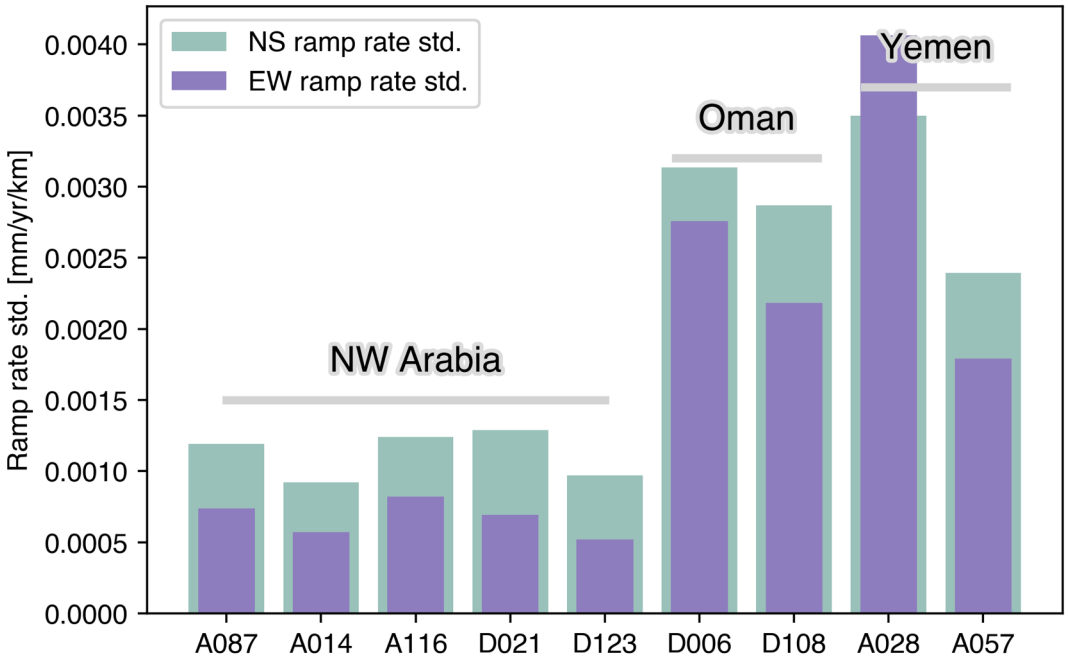

Figure 2.8: Standard deviations of the ramp rate, corresponding to $\dot{\sigma}_{\text{ramp}}$ in Equation 2.15.

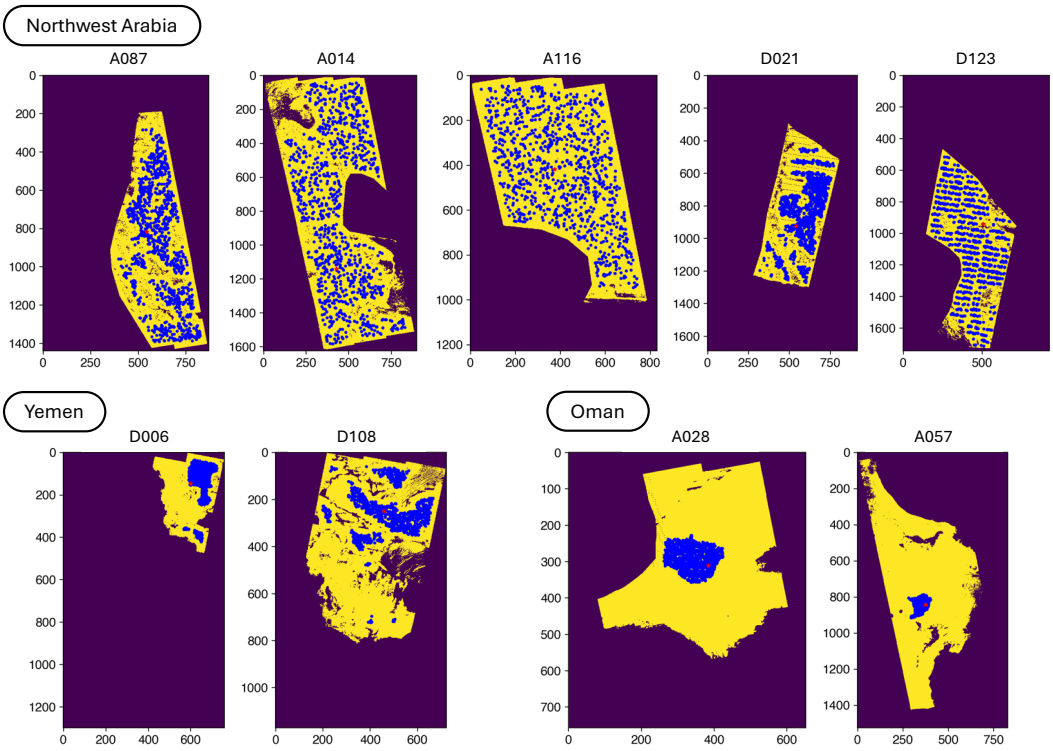

Figure 2.9: The 1,000 sets of randomly selected reference points. The criteria for random selection is: temporal coherence > 0.9 (Yunjun et al., 2019), cumulative closure phase exceeds three times the standard deviation (Zheng et al., 2022), an elevation below 1500 m, and be at least 25 km from masked areas. See the Main Text Section 2.3.

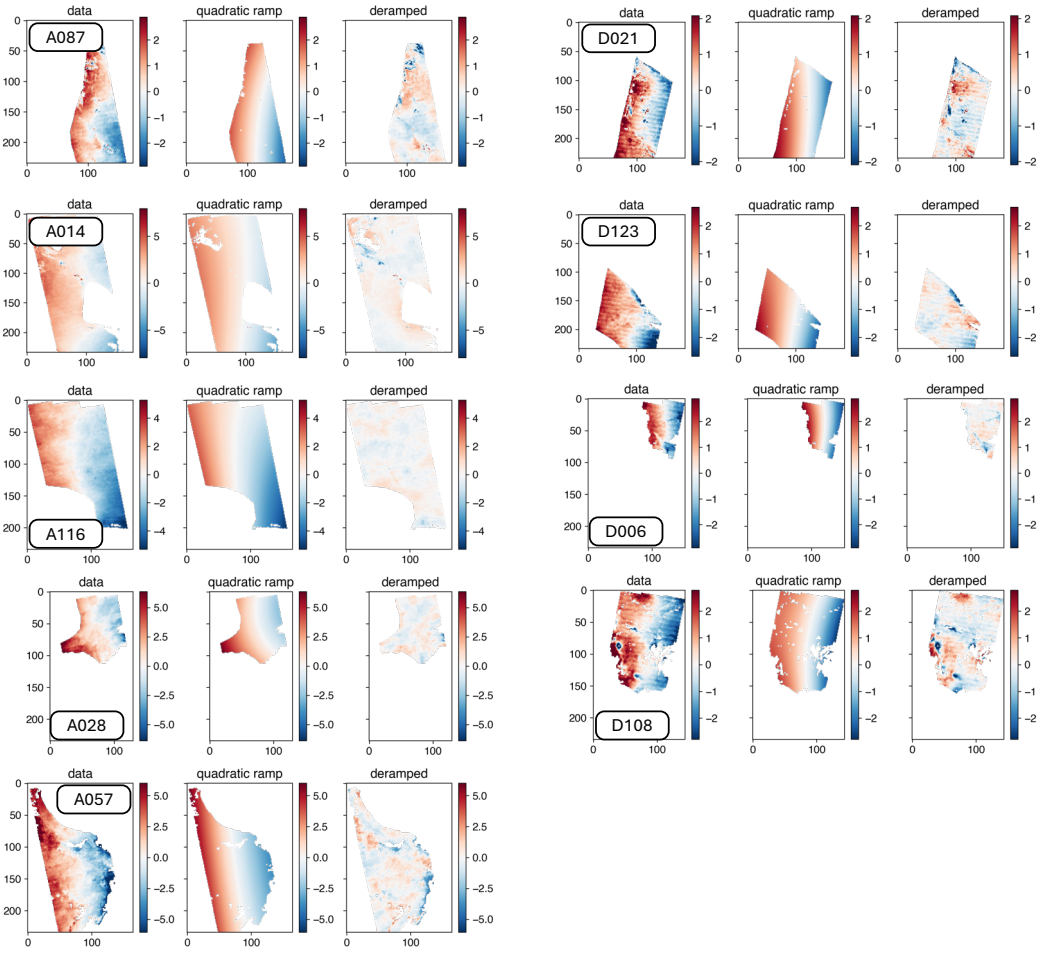

Figure 2.10: Quadratic deramping before sampling the semi-variograms. See Suppl. Text S4-2.

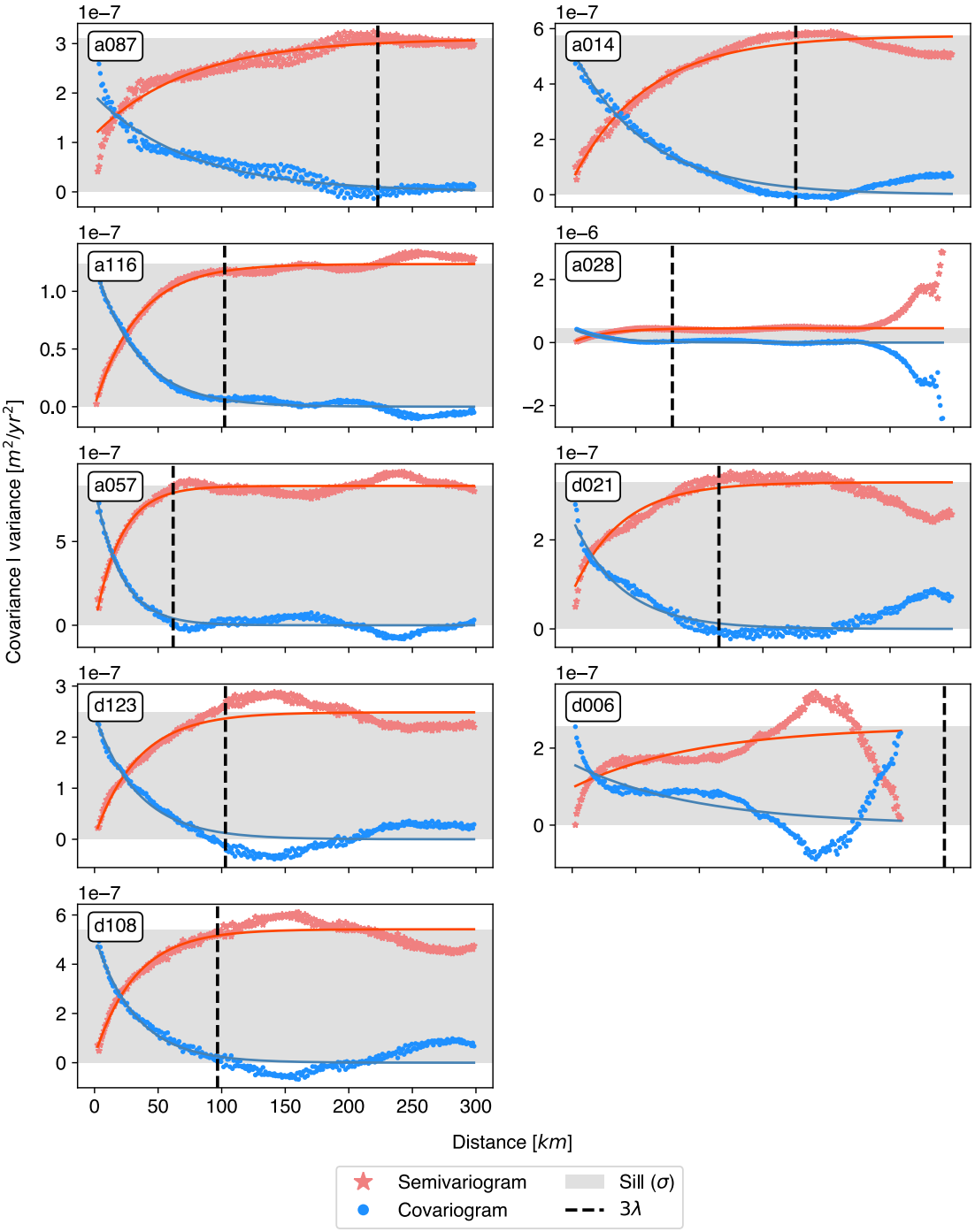

Figure 2.11: Sample semi-variograms and covariograms. The exponential functions fitted the sample covariograms. The sill σ is marked by the grey band. The value of σ is used to fill in the diagonals of the covariance matrix, $\mathbf{C}_{d_s}$. Three times of the characteristic length scales λ is marked by the dashed line. See Suppl. Text S4-2.

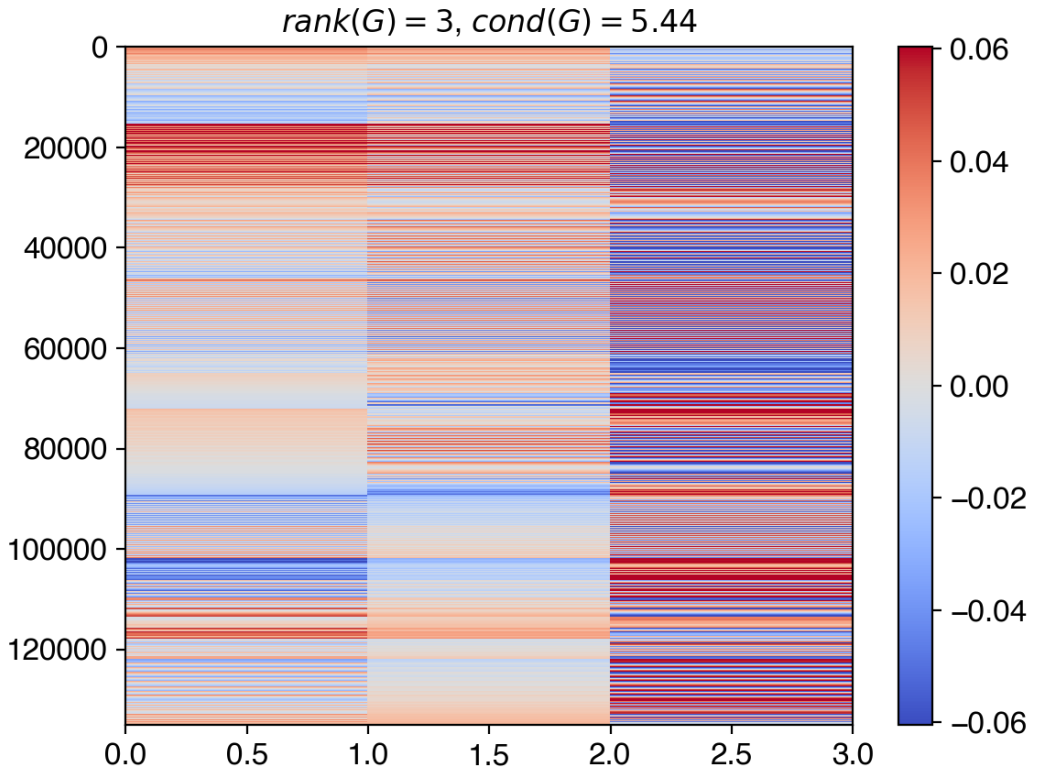

Figure 2.12: The linear operator **G**, which transforms the Cartesian rotation parameters to the nine InSAR LOS velocities, normalized by the Earth's radius 6378.137 km. See Suppl. Text S3-1.

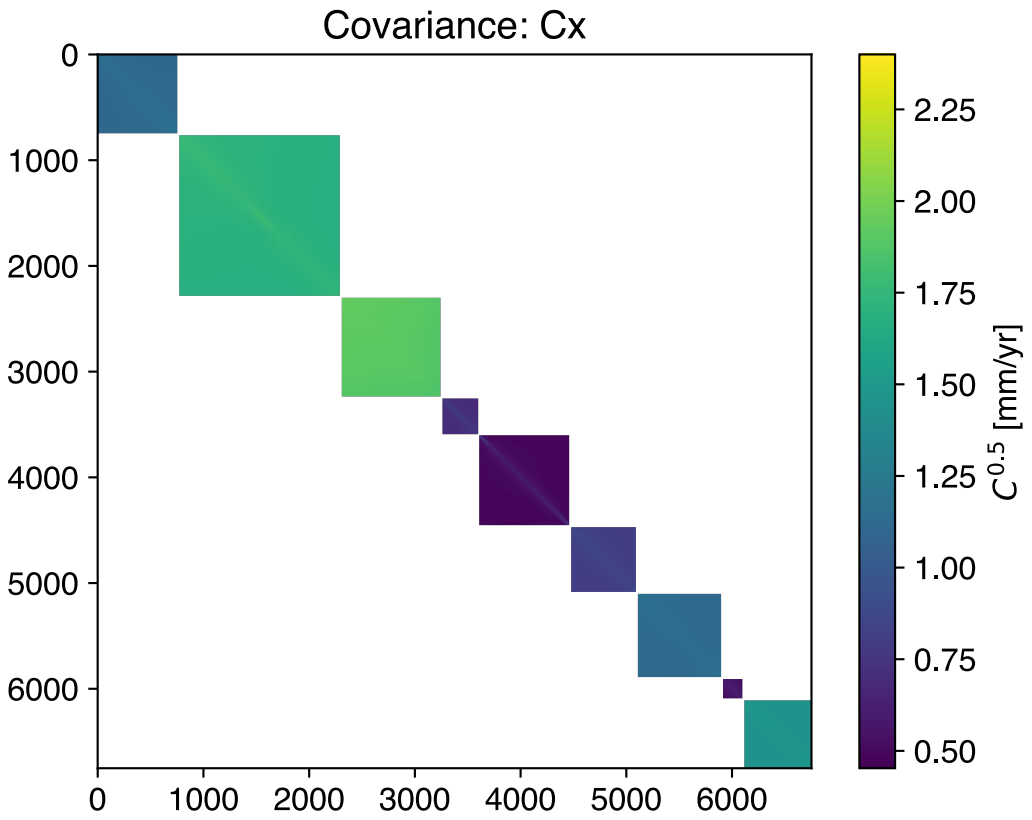

Figure 2.13: The data covariance matrices $\mathbf{C}_\chi = \mathbf{C}_\mathrm{d} + \mathbf{C}_\mathrm{p}$. To display the variability of dynamic range, the color bar shows the squared root of $\mathbf{C}_\chi$. The observational covariance is composed of the temporal term, $\mathbf{C}_{\mathrm{d_t}}$ based on the prior-selected reference points (Figure 2.7), and the spatial term, $\mathbf{C}_{\mathrm{d_s}}$ from the semi-variograms (Figure 2.11). $\mathbf{C}_\mathrm{p}$ quantifies the uncertainty due to the reference point, see Main Text Section 2.3 and Suppl. Text S3-2.

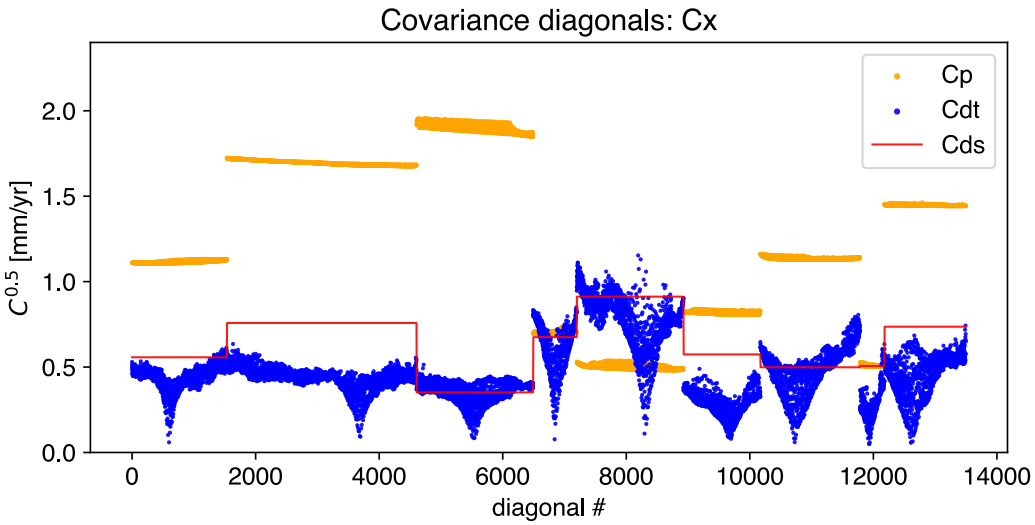

Figure 2.14: The diagonals of the covariance matrices in Figure 2.13. The values displayed here are the squared roots of the covariance for plotting purposes. The blue dots indicate the diagonals of $\mathbf{C}_{d_t}$, in which the lowest point marks the chosen reference pixel in each track in this realization. The red line indicates the diagonals of $\mathbf{C}_{d_s}$, which is constant within each velocity track. The orange dots indicate the epistemic uncertainty, $\mathbf{C}_p$, of the reference point estimated from the entire 1,000 realizations.

Figure 2.15: Caption next page.

Figure 2.15: Euler fitting results. Rows from top to bottom: Observed velocity, velocity standard deviation, the velocity field from the estimated Euler pole, post-fit residual velocity, the velocity predicted from the ITRF2014 plate motion model, the difference between our pole and the ITRF2014 pole. See the Main Text Figure 3 and the pole marked by "x" in Figure 4.

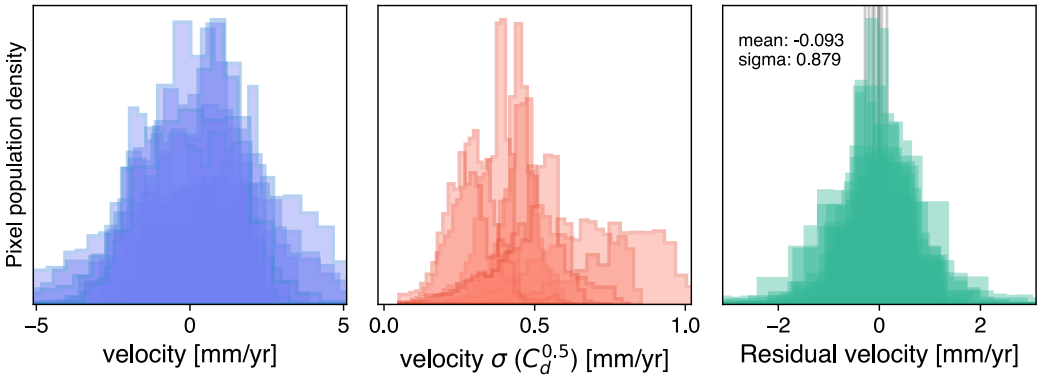

Figure 2.16: The histograms of velocities, standard deviations, and post-fit residuals, for all the tracks. These corresponds to the data and post-fit residuals in Figure 2.15.

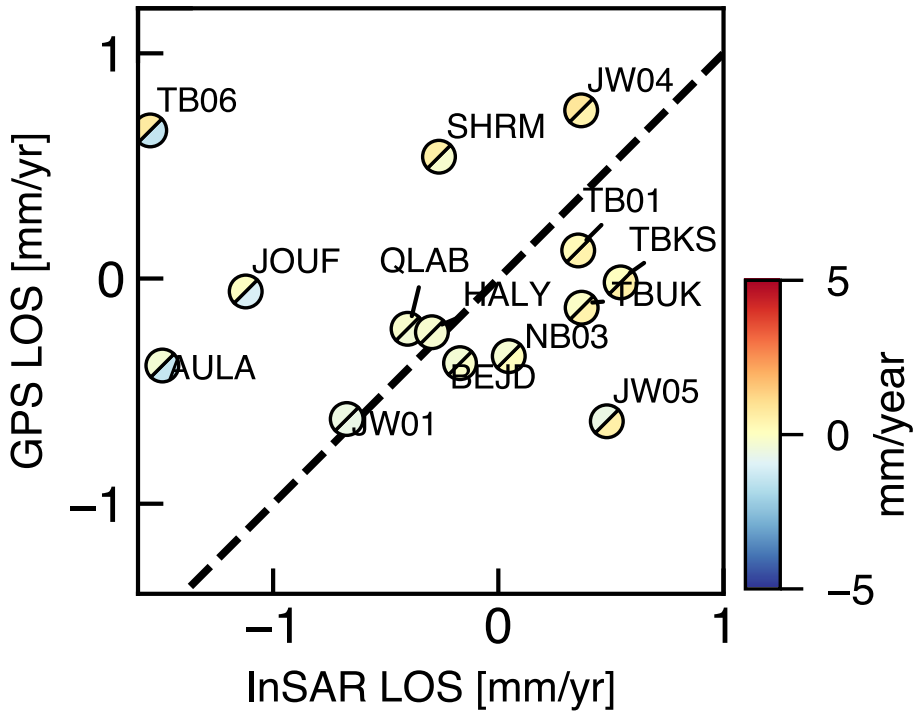

Figure 2.17: The comparison with GNSS horizontal velocities projected to LOS in the Arabian-fixed reference frame. Values are taken from the Main Text Figure 3d.

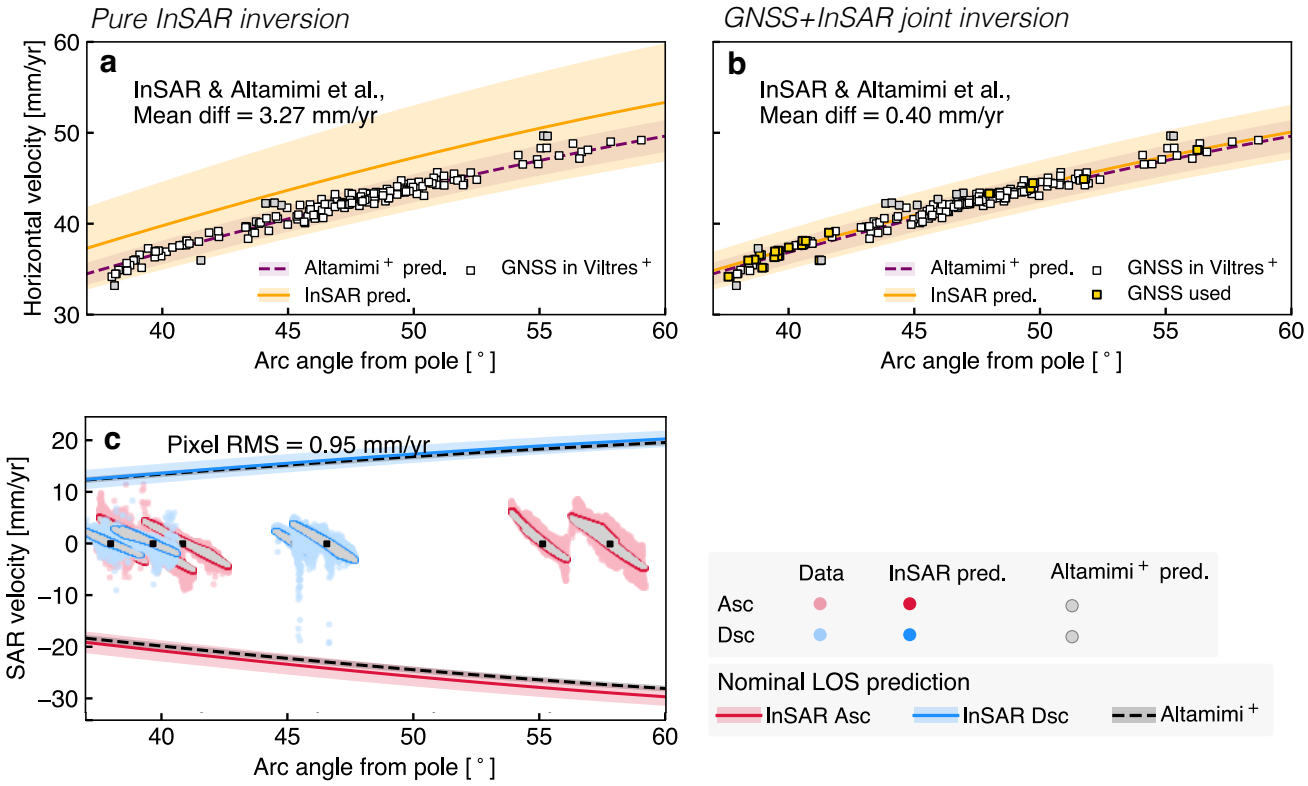

Figure 2.18: Profiles horizontal velocities tangential to the plate motion direction of the ITRF2014 Arabia model (Altamimi et al., 2017). The x-axis is the great-arc angle from the ITRF2014 pole. **(a)** The pure InSAR-derived pole is the posterior after considering the ensemble of the random reference points in the Main Text. **(b)** The joint inversion with InSAR-collocated GNSS stations taken from the network (white squares) in Viltres et al. (2022). The outlier sites (outside the 2-sigma bound of Altamimi et al., prediction; the grey squares) are stations close to the Afar rifting zone and the Dead Sea Transform. **(c)** The line-of-sight (LOS) velocities from nine InSAR tracks. The red and blue scatter dots are ascending and descending pixel-wise LOS velocities in each track, with lighter color indicating the observations and darker color the posterior pole predictions. The grey dots is the prediction from Altamimi's pole using the same pixel-wise LOS geometries. The lines indicate the predicted LOS velocity profiles using a nominal LOS geometry across the plate. Red and blue lines are InSAR's posterior predictions, while the grey line is predicted using Altamimi's pole.

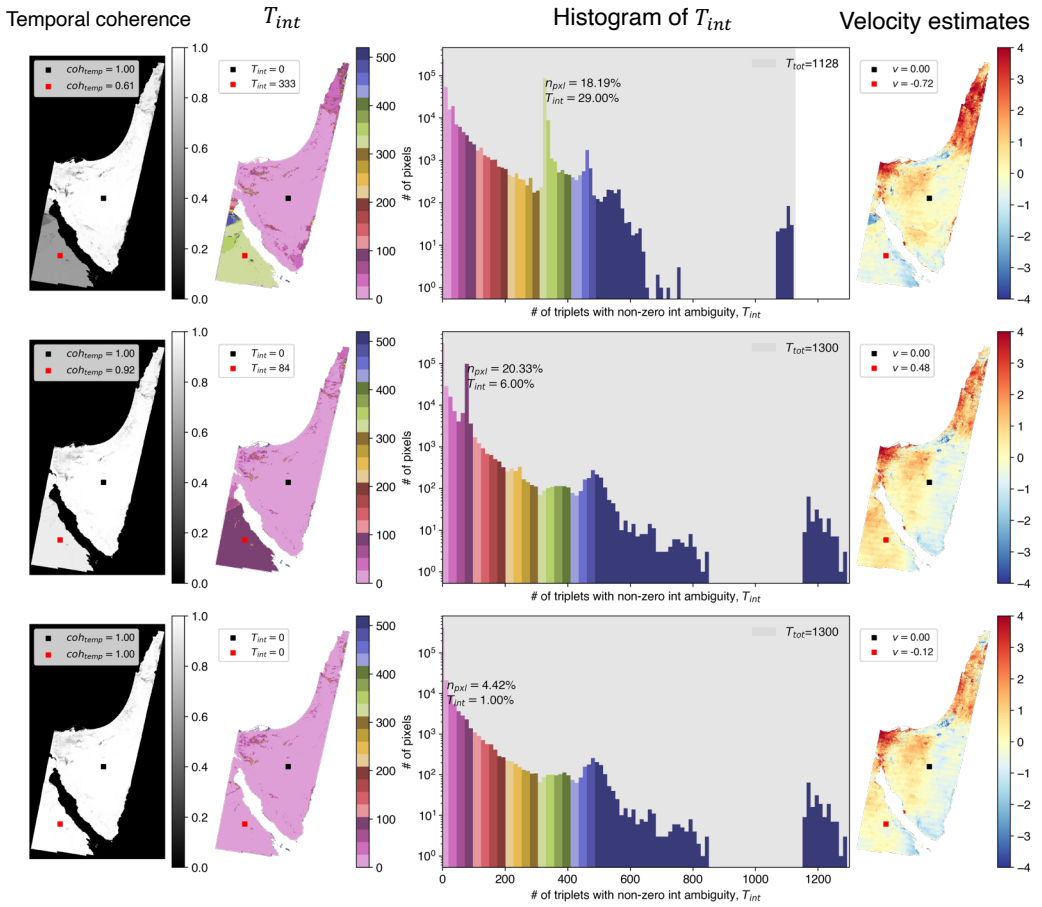

Figure 2.19: The correction of unwrapping errors using phase misclosure, demonstrated using descending track D094 in the Sinai Peninsula. Top: the original interferometric stack following the processing workflow described in Main Text Section 2.1. Middle: The results from a stack of interferograms with tropospheric model subtracted before unwrapping. Bottom: The results from a stack of interferograms with both model and ionospheric delays subtracted before unwrapping, then apply the phase-closure unwrapping error correction based on T_{int}, as described in Supplementary Text S3. We can visually see unwrapping errors in the temporal coherence and the velocity fields. The data from this orbital track is not used in the Main Text.

Chapter 3

INTERSEISMIC TRANSTENSION ALONG THE SOUTHERN DEAD SEA TRANSFORM SUGGESTED BY INSAR

ABSTRACT

We present new geodetic constraints on interseismic deformation along the southern Dead Sea Transform (DST) and the Gulf of Aqaba. By combining a decade of Sentinel-1 InSAR time series (2014–2025) with regional GNSS velocities, we resolve along-strike variations in fault coupling and identify an extensional component near the southern termination of the transform. Two-dimensional elastic dislocation models show that a purely strike-slip configuration cannot reproduce the observed line-of-sight (LOS) velocity gradient across the gulf, whereas the inclusion of a shallow tensile fault provides a consistent first-order fit. The preferred solutions indicate a southward decrease in locking depth from ~10–15 km beneath Wadi Arabah to ~4 km below the southern gulf, and an extension rate of ~2 mm yr^{-1}, in agreement with the GNSS velocities on the western side of the gulf. Predicted vertical deformation remains below the current InSAR detection threshold (<1 mm yr^{-1}), consistent with the minimal observed secular uplift.

These results suggest that the Gulf of Aqaba accommodates left-lateral shear together with distributed crustal extension within the upper lithosphere, which is consistent with the regional tectonic block motion inferred from geological and geodetic studies. The interseismic extension inferred here likely represents the elastic phase of the same process that produces oblique-normal slip during major earthquakes, as observed in the 1995 M_w 7.2 Nuweiba event. The deformation reflects intra-crustal transtension within a strike-slip system that gradually accumulates horizontal and vertical offsets over earthquake cycles. Ongoing three-dimensional and distributed-slip modeling will further quantify this partitioning and its implications for crustal weakening and fault-zone evolution at the southern end of the DST.

3.1 Introduction

The Dead Sea Transform (DST) is a major left-lateral strike-slip boundary separating the Arabian and Sinai subplates and forming the northern continuation of the Red Sea rift system. It has accommodated the northward motion of Arabia relative to Sinai at an average rate of $\sim 5 \pm 1$ mm yr^{-1} (Klinger et al., 2000; Le Beon et al., 2008; Lefevre et al., 2018). The ~1000 km-long DST is commonly divided into three principal domains: (1) a transpressional section in Lebanon and Syria, (2) a dominantly strike-slip section through the Jordan Valley and Wadi Arabah, and (3) a southern offshore continuation into the Gulf of Aqaba, where left-stepping en échelon faults form deep pull-apart basins and introduce a transtensional component of motion (Ben-Avraham, 1985; ArRajehi et al., 2010; Ribot et al., 2021; Li et al., 2021; Castro-Perdomo et al., 2021; Viltres et al., 2022).

The Gulf of Aqaba is the most seismically active segment of the DST, experiencing dense microseismicity, earthquake swarms, and several major historical ruptures, including the 1995 M_w 7.2 Nuweiba earthquake (Klinger et al., 1999; Baer et al., 1999; Bektaş et al., 2024). Despite this activity, the region remains poorly constrained geodetically because of sparse near-field instrumentation and the offshore location of the main faults. A recent revisit analysis of the 1995 rupture using interferometric synthetic aperture radar (InSAR) and teleseismic backprojection revealed a discontinuous rupture geometry with substantial shallow normal faulting and extensional opening during the coseismic phase, highlighting the faulting complexity and oblique-slip character of the southern DST (Vasyura-Bathke et al., 2024).

Recent advances in InSAR time-series techniques have provided new opportunities to resolve the interseismic deformation field across this region. Using Sentinel-1 burst-overlap interferometry (BOI), Li et al. (2021) recovered the left-lateral velocity across a wide zone of the DST and inferred a systematic southward decrease in locking depth—from ~16 km in Wadi Arabah to ~4 km in the southern Gulf of Aqaba. Castro-Perdomo et al. (2021) combined 27 new survey-mode GNSS sites with permanent stations to evaluate the fault locking, finding similar slip rates ($4.9^{+0.9}_{-0.6}$ mm yr^{-1}) and shallow locking depths ($6.8^{+3.5}_{-3.1}$ km at Elat and $0.8^{+3.4}_{-0.8}$ km at Arnona). These results point to a southward shallowing of fault locking plus minor amount of extension. In addition, distributed deformation is observed in a systematic residual at sub-millimeters-per-year, especially on the west side of the gulf.

These prior studies delineate a first-order along-strike variations in the locking depth

of DST, while also allude to more complex deformation as the DST approaches the Red Sea but they are not able to resolve more details due to either the sparsity of data and the lack of three-dimensional observation. Several key aspects remain unresolved: (1) Whether the apparent shallow interseismic creep in the southern end of Gulf of Aqaba is a true mechanical transition or simply an artifact of fault geometry and data resolvability and (2) the relative contributions of strike-slip versus extensional strain accumulation near the southern gulf in the upper lithosphere.

In this study, we integrate Sentinel-1 InSAR time-series (2014–2025) with GNSS velocities (1997–2023) to construct a spatially continuous velocity field across the Wadi Arabah–Gulf of Aqaba region. We employ elastic dislocation models incorporating both strike-slip and tensile-opening components to reproduce the observed line-of-sight (LOS) velocity asymmetries and refine the effective locking depth model of the southern DST. Our kinematic results reveal an extensional component consistent with the coseismic normal-faulting mechanisms observed during the 1995 Nuweiba earthquake (Vasyura-Bathke et al., 2024), reinforcing the view that the southern DST represents a transtensional boundary in transition toward the nascent rifting regime of the northern Red Sea.

3.2 Methods

InSAR data processing

We use Sentinel-1A C-band TOPS-mode SAR imagery (2014–2023) to form small-baseline (SBAS) interferograms for estimating surface displacement time series. Sentinel-1A, operated by the European Space Agency (Peter, 2021; Peter, 2023), provides eight tracks of Level-1 range–Doppler single-look complex (SLC) data from both ascending and descending geometries, covering western Arabia near the Dead Sea Transform (Figure 3.1). From 2014 to 2024, a total of $\sim$ 250 acquisitions and $\sim$ 1000 pairs of interferograms were processed for each track, each spanning approximately 250×250 km^2. The data processing follows the procedure described in Chapter 2.

Interferogram formation and coregistration were performed using the `stackSentinel` module (Fattahi et al., 2017a) within the `ISCE2` framework (Rosen et al., 2012). The common-reference coregistration scheme requires only $O(N)$ resampling operations, offering substantial computational efficiency compared to the pairwise approach with $O(N^2)$. We apply split-band processing to estimate and correct ionospheric phase contributions, which we then invert and subtract from the raw InSAR

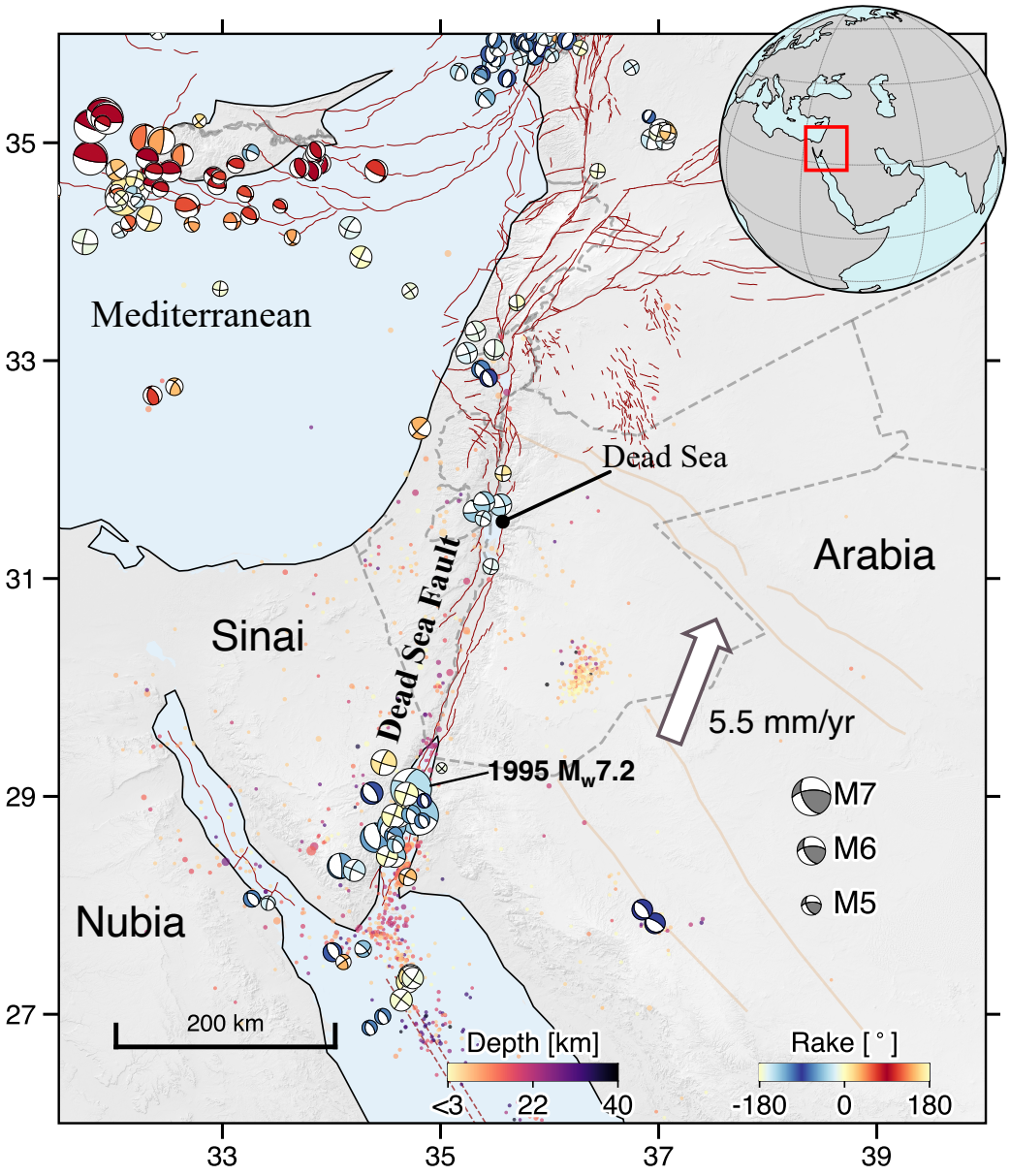

Figure 3.1: Regional tectonics of the southern Dead Sea Transform and the Gulf of Aqaba. Major fault strands (dark grey lines) delineate the plate boundary between the Sinai microplate and the Arabian Plate. The Gulf of Aqaba (Elat) is a series of deep pull-apart basins that accommodate both strike-slip motion and localized extension near the transition to the Red Sea rift. Triangles mark the Global Navigation Satellite System (GNSS) stations used in this study; The arrows denote horizontal GNSS velocities relative to stable Arabia. Sentinel-1 data coverage spans the entire map. The dashed box outlines the focus region of the Gulf of Aqaba. Seismicity and the events larger than Mw 5.0 are colored with depth (Saudi Geological Survey, pers. comm. through T. Aldaajani).

time series.

For each acquisition, interferograms were formed between the nearest 3–5 consecutive images, including skip-10 pairs (~120 days temporal baseline), to ensure sufficient temporal sampling and reduce non-closure phase biases. Each track comprises roughly 800–1000 interferograms (mean ~947) spanning 200–250 acquisition epochs (mean ~224), depending on data availability and orbital configuration. The interferograms were multilooked 5×20 in azimuth and range, yielding a ground pixel spacing of approximately 70.5×82 m.

Time-series inversion was carried out using a distributed scatterer SBAS approach (Berardino et al., 2002) implemented in `MintPy` (Yunjun et al., 2019). Manual adjustments were made to the interferogram network to maintain full temporal connectivity and remove low-coherence or anomalous pairs. The network of M interferograms was inverted for N epoch-wise phase estimates using a weighted least-squares formulation:

$$\widehat{\boldsymbol{\phi}} = \arg\min_{\boldsymbol{\phi}} \|\mathbf{W}(\mathbf{d} - \mathbf{A}\boldsymbol{\phi})\|_2^2, \tag{3.1}$$

where $\mathbf{d}$ is the vector of unwrapped interferometric phases, $\mathbf{A}$ is the design matrix relating each interferogram to its two epochs, and $\mathbf{W}$ is a diagonal weighting matrix.

Unweighted inversions were first performed for quality control to inspect residuals and verify network closure. Final time series were obtained using variance-based weighting, where each interferogram ℓ is assigned a weight proportional to the inverse of its estimated phase variance (Tough et al., 1995; Guarnieri & Tebaldini, 2008; Yunjun et al., 2019):

$$\mathbf{W} = \mathrm{diag}(w_1, w_2, \ldots, w_M), \qquad w_\ell = \frac{1}{\sigma_{\phi,\ell}}, \tag{3.2}$$

where the phase variance is approximated by (Tough et al., 1995)

$$\sigma_{\phi,\ell}^2 \approx \frac{1 - \gamma_\ell^2}{2\,\gamma_\ell^2\,L}, \tag{3.3}$$

with γ_ℓ denoting interferometric coherence and L the multilooking factor. Thus, in the weighted inversion implementation in `MintPy`, the weight for each interferogram is (Yunjun et al., 2019)

$$w_\ell \propto \sqrt{\frac{2\,\gamma_\ell^2\,L}{1 - \gamma_\ell^2}}, \tag{3.4}$$

so that interferograms with higher coherence or more independent looks contribute more strongly to the inversion, while low-coherence pairs are naturally down-weighted.

The resulting epoch-wise phase time series $\widehat{\phi}(t_n)$ were converted to line-of-sight (LOS) displacement via

$$\widehat{u}_{\mathrm{LOS}}(t_n) = \frac{\lambda}{4\pi}\,\widehat{\phi}(t_n). \tag{3.5}$$

Pixels with low temporal coherence were masked out, where temporal coherence for each pixel $\mathbf{x}$ is defined as (Yunjun et al., 2019)

$$\gamma_t(\mathbf{x}) = \frac{1}{N}\left|\sum_{\ell=1}^{N} \exp\left(i\,\phi_\ell^{\mathrm{res}}(\mathbf{x})\right)\right|, \tag{3.6}$$

and ϕ_ℓ^{res} denotes the residual that does not close the inteferometric phase across all triplets in the network. Pixels with low γ_t indicates there are significant closure phase issues (decorrelation, unwrapping errors, changes of scattering properties, etc.) and were excluded from the final velocity field to minimize contamination from general decorrelation and/or unwrapping artifacts.

Corrections for Non-Tectonic Signals in InSAR Observations

For an interferogram formed between acquisition epochs t_i and t_j, the observed interferometric phase can be expressed as the linear superposition of independent physical contributions:

$$\begin{aligned}\phi_{ij}(\mathbf{x}) = \frac{4\pi}{\lambda}\,\vec{l}(\theta,\alpha)\cdot\Delta\mathbf{u}_{ij}(\mathbf{x}) \\ + \phi_{ij}^{\mathrm{orb}}(\mathbf{x}) + \phi_{ij}^{\mathrm{topo}}(\mathbf{x}) + \phi_{ij}^{\mathrm{tropo}}(\mathbf{x}) + \phi_{ij}^{\mathrm{iono}}(\mathbf{x}) \\ + \phi_{ij}^{\mathrm{tide}}(\mathbf{x}) + \phi_{ij}^{\mathrm{clo}}(\mathbf{x}) + \varepsilon_{ij}(\mathbf{x}),\end{aligned} \tag{3.7}$$

where λ is the radar wavelength, $\vec{l}(\theta,\alpha)$ is the line-of-sight (LOS) unit vector for incidence angle θ and azimuth α, and $\Delta\mathbf{u}_{ij} = \mathbf{u}(t_j) - \mathbf{u}(t_i)$ is the 3-D surface displacement between epochs. Each term represents a distinct contribution: orbital baseline errors (ϕ^{orb}), topographic residuals (ϕ^{topo}), tropospheric and ionospheric delays (ϕ^{tropo}, ϕ^{iono}), solid-Earth tides (ϕ^{tide}), closure or soil-moisture biases (ϕ^{clo}), and random noise ε_{ij}. Because these effects are additive, each component can be modeled and corrected independently within the InSAR framework.

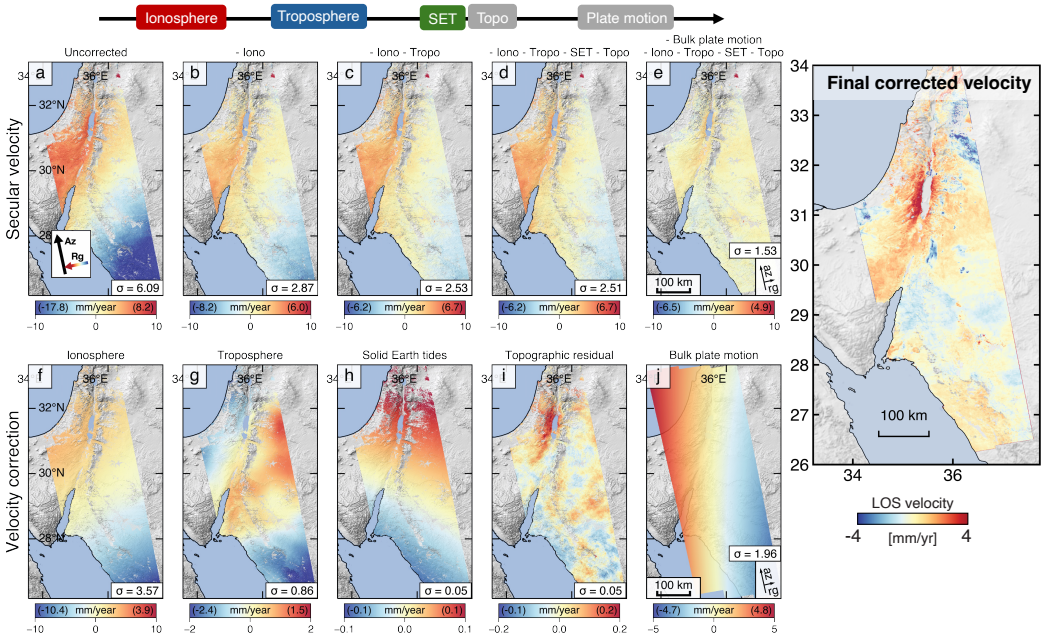

Figure 3.2: Sequential corrections applied to the Sentinel-1 ascending track A087 in northwestern Arabia. Positive LOS velocities indicate motion toward the satellite. The upper-right annotation in each panel gives the L_2-norm of the best-fit planar ramp coefficients (see Text S2.2 in Supporting Information S1). **(a–e)** LOS velocity fields after each correction step. **(f–j)** Individual correction components: ionospheric delay, tropospheric delay, solid Earth tides, topographic residuals, and rigid plate motion. Note the different color scales. The rightmost panel repeats (e) but with a ±4 mm yr^{-1} color range. The σ value in each panel denotes the spatial standard deviation of that field.

Most standard InSAR processors (e.g., `SNAP/Sentinel-1 Toolbox`, `GAMMA`, `GMTSAR` Sandwell et al. 2011, `StaMPS` Hooper 2008, `LiCSBAS` Lazecký et al. 2020, and `NSBAS`) perform atmospheric and orbital corrections on individual interferograms prior to time-series inversion. While effective for short or sparsely sampled datasets, such pairwise correction schemes can propagate residual biases when correction quality varies among interferograms, potentially degrading the temporal coherence of the inferred displacement field.

Here, all modeled and data-driven corrections are applied *after* the network inversion in the temporal domain. By jointly analyzing all interferograms contributing to a given epoch, we achieve greater robustness through ensemble averaging, mitigating stochastic tropospheric turbulence, unwrapping errors, and decorrelation noise (Yunjun et al., 2019). The uncertainty of the corrected time series scales

approximately as

$$\sigma_{\text{time}} \approx \frac{\sigma_{\text{ifg}}}{\sqrt{N}}, \tag{3.8}$$

where σ_{ifg} is the characteristic standard deviation of a single interferogram and N is the number of independent interferograms contributing to each epoch. This $1/\sqrt{N}$ relation reflects the noise suppression gained from network redundancy and yields smoother temporal and spatial estimates of non-tectonic signals.

Phase corrections are applied sequentially (Figure 2.2).. We first remove externally modeled effects—(1) atmospheric delays from ERA5 and (2) solid-Earth tides from astronomical ephemerides—followed by data-driven corrections for ionospheric delay, topographic residuals, and closure or soil-moisture biases. Finally, a reference-frame adjustment for steady plate motion (ITRF2014) is applied to the velocity field to ensure global consistency.

The following subsections describe each correction in detail.

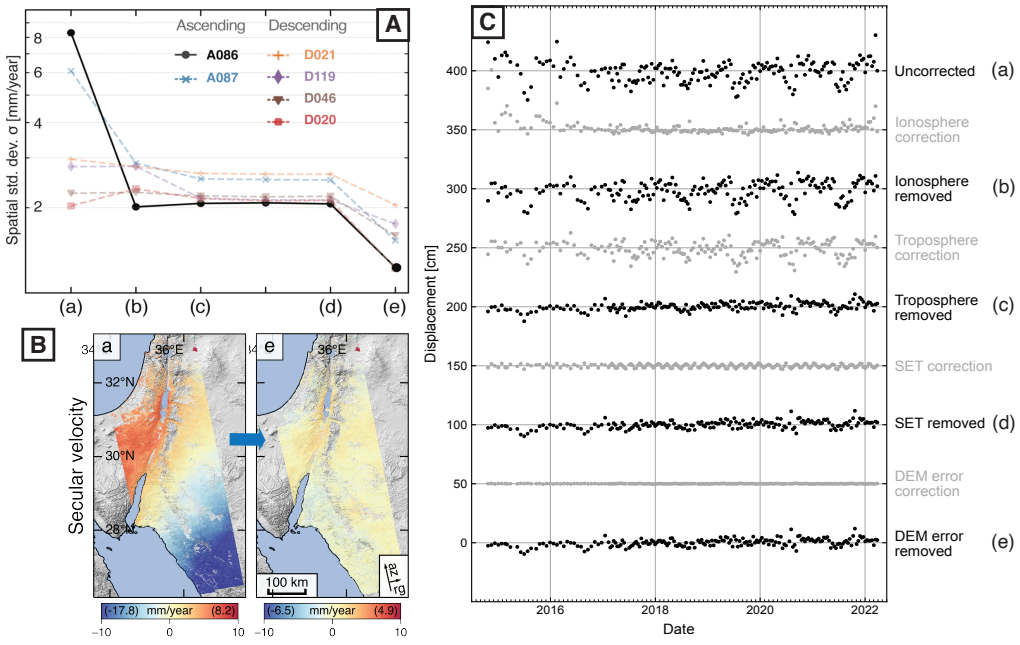

Figure 3.3: The effect of applied corrections on reducing the apparent velocity gradient and scatters in the time series. **(A)** The spatial standard deviation, σ, decrease as corrections applied (stages a to e) on the velocity fields. The black line is the ascending track 86. Other tracks are shown with different colors in dashed lines. **(B)** The corresponding LOS velocity in stage (a) and (e). The dynamic range of the velocity field largely reduced. **(C)** An example time series of a pixel at 31.25 N, 35.38 E.

Solid-Earth Tides (SET).

We correct for solid-Earth tidal displacements using `solid` (Milbert, 2018) and its Python interface `PySolid` (Yunjun et al., 2022). The model computes the elastic response of the Earth up to degree 2 based on ephemerides of the Sun and Moon and precise satellite orbits. The LOS tidal phase is

$$\phi^{\text{tide}}(\mathbf{x}, t) = \frac{4\pi}{\lambda} \vec{l}(\theta, \alpha) \cdot \mathbf{u}^{\text{tide}}(\mathbf{x}, t), \tag{3.9}$$

where $\mathbf{u}^{\text{tide}}$ is the modeled 3-D tidal displacement. We have model and evaluated the effect of ocean tidal loading for the InSAR track abutting the Gulf of Aqaba. The changes in the secular rate due to ocean tide is negligible (as described in Chapter 2), thus is systematically estimated for all tracks.

Tropospheric Corrections.

Tropospheric delays are corrected using the ECMWF ERA5 global reanalysis model (Hersbach et al., 2020), accessed via the Copernicus Climate Data Store and interpolated with `PyAPS` (Jolivet et al., 2011; Jolivet et al., 2014). The LOS delay is expressed as

$$\phi^{\text{tropo}}(\mathbf{x}, t) = \frac{4\pi}{\lambda} \Delta r^{\text{tropo}}(\mathbf{x}, t), \tag{3.10}$$

where Δr^{tropo} is the slant-range delay due to temperature, pressure, and water-vapor stratification. To assess model sensitivity, we compare the spline interpolation in `PyAPS` with kriging-based resampling implemented in `ICAMS` (Cao et al., 2021), which incorporates the covariance structure of model grids and better captures sharp coastal moisture gradients—particularly along the eastern Gulf—yielding smaller velocity variance in humid regions. However, we did not adopt `GACOS` products because their batch access is incompatible with automated `MintPy` workflows.

Ionospheric Phase Correction.

Ionospheric delays, dispersive and proportional to $1/f^2$, are corrected using the split-spectrum method (Liang et al., 2019). Two subbands with center frequencies f_1 and f_2 yield the non-dispersive (ND) and dispersive (D) components:

$$\phi^{\text{ND}} = \frac{f_1^2 \phi_1 - f_2^2 \phi_2}{f_1^2 - f_2^2}, \qquad \phi^{\text{D}} = \frac{\phi_1 - \phi_2}{1 - \left(\frac{f_2}{f_1}\right)^2}. \tag{3.11}$$

Split-band interferograms are generated in `ISCE2` and inverted via uniform-weight SBAS to obtain ionospheric time series, which are then subtracted from the deformation series. Because the total electron content (TEC) varies over scales of $O(10^2)$ km (e.g., Meyer, 2010; Gomba et al., 2017; Fattahi et al., 2017b; Liang et al., 2019) and is modulated by diurnal and solar-cycle effects, corrections are essential to recover long-wavelength secular deformation. We mask and filter the estimated ionosphere interferograms to reduce the impact from decoreelation and unwrapping errors. The detailed method is described later in Chapter 4. We also identify anomalously noisy interferograms during high solar activity (e.g., 2014 and 2023) and exclude them from the dataset.

Topographic (DEM) Residuals.

Residual topographic phase due to DEM error $h_{\text{err}}(\mathbf{x})$ is approximated (Fattahi & Amelung, 2013; Yunjun et al., 2019) as

$$\phi_{ij}^{\text{topo}}(\mathbf{x}) \approx \frac{4\pi}{\lambda} \frac{B_{\perp,ij}}{r \sin\theta} h_{\text{err}}(\mathbf{x}), \tag{3.12}$$

where $B_{\perp,ij}$ is the perpendicular baseline and r is the slant range. This linear dependence motivates a regression of phase against baseline to estimate h_{err} and mitigate DEM-induced artifacts, which are localized in steep terrain and do not affect long-wavelength tectonic signals.

Phase Closure Bias and Soil Moisture.

Non-zero closure phases arise from nonlinear scattering or soil-moisture variations (De Zan et al., 2014; Zheng et al., 2022). For each interferogram triplet (i, j, k),

$$C_{ijk}(\mathbf{x}) = \text{wrap}\big(\phi_{ij} + \phi_{jk} + \phi_{ki}\big)(\mathbf{x}) \equiv 0 \quad \text{(for consistent phases)}. \tag{3.13}$$

Persistent non-zero C_{ijk} indicates local bias evaluated across a triplet of date i, j, and k. Since we believe the effects of phase closure bias is not going to dominate the long-wavelength geophysical signals, for simplicity, we do not estimate the full closure-phase time series and correct for it. Rather, we estimate the mis-closure values for each pixel following Zheng et al. (2022) and mask out affected pixels at 3σ of the estimated mis-closure in the final velocity products. These masked out pixels correspond to regions such as dry riverbeds, wetlands, and agricultural zones.

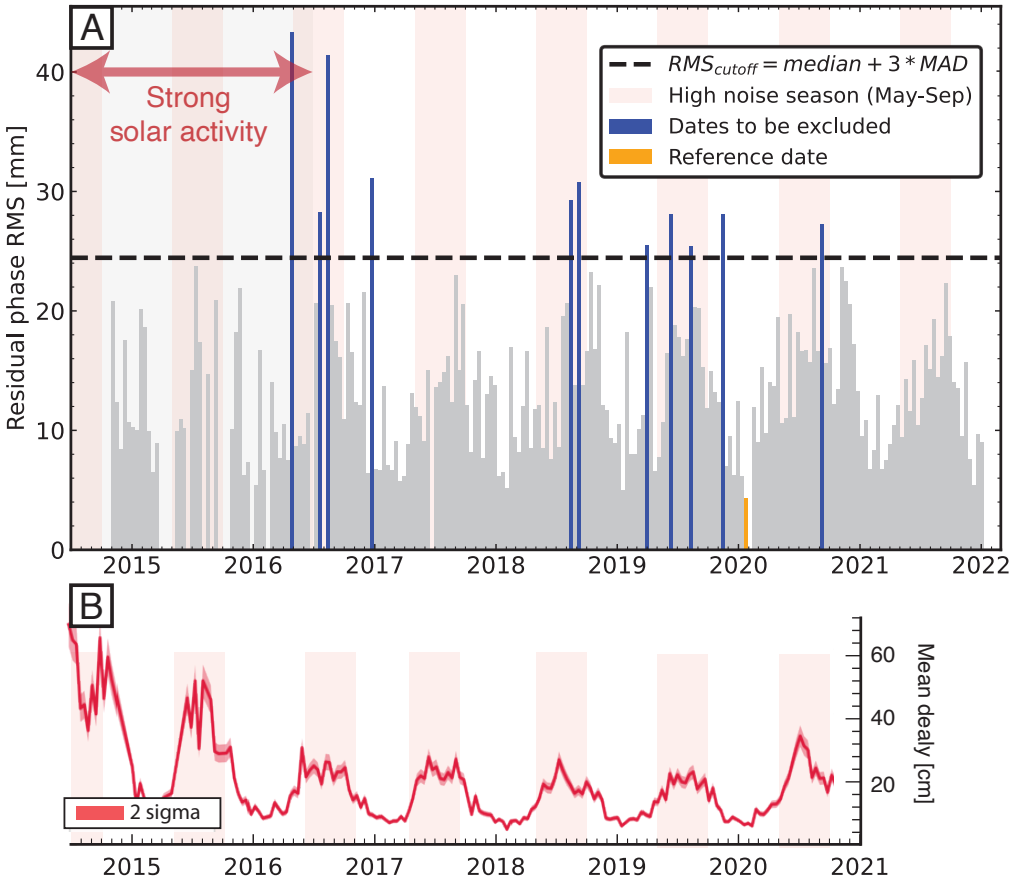

Figure 3.4: Correlation between ionospheric corrections and residual time-series noise after fitting linear trends plus seasonal terms. Data shown for a pixel at 31.25°N, 35.38°E. **(A)** Root-mean-square residuals of the time-series fits, representing the unmodeled noise level. Pink shading highlights periods of elevated residual variance. **(B)** Predicted ionospheric delay from the global Total Electron Content (TEC) model (Noll, 2010), showing pronounced annual variability and modulation by the 11-year solar cycle.

Phase Unwrapping Errors.

Phase unwrapping (PU) errors are detected through closure-phase consistency and temporal coherence (Yunjun et al., 2019). Although the arid Arabian Peninsula generally exhibits high coherence, localized PU errors occur in rugged terrain (e.g., Wadi Araba), seasonally moist surfaces, or zones of radio frequency interference. These manifest as non-zero integer closure ambiguities or discontinuities along burst edges. We inspect pixel-wise closure-phase integers and temporal coherence, masking or correcting anomalous regions. To minimize aliasing from tropospheric

gradients, interferograms are unwrapped after removing ERA5-derived atmospheric screens, then the screens are re-added. Unwrapping is performed using `SNAPHU` (Chen & Zebker, 2002) with uniform weights, initialized via a minimum-cost-flow solution and smooth-solution cost parameters.

Common-Scene Stacking (CSS)

The common-scene stacking (CSS) method was developed to mitigate atmospheric noise in a stack of interferometric data and serve as efficient technique to mitigate the noise to further bias the time series and the final linear velocity estimates (Tymofyeyeva & Fialko, 2015; Zebker et al., 2023). Unlike conventional stacking, which averages all differential displacements and mixes correlated atmospheric signals, CSS isolates uncorrelated noise by averaging interferograms sharing a fixed common center scene. Earlier applications to pre-Sentinel datasets showed noise variance reductions of about a factor of two (Tymofyeyeva & Fialko, 2015).

With the dense and regularly sampled Sentinel-1 archive, CSS provides only negligible benefit beyond standard SBAS processing. This is due to the fact that our correction on the atmospheric modeling of troposphere and the split-band estimates of ionosphere has already reduced a lot of the noise. In addition, the redundancy in our network inversion further suppresses the random noise in the time series. We find that CSS adds little value to dense, well-modeled Sentinel-1 networks. Improvements in residual precision are more effectively achieved through refined noise modeling, phase-closure inspection, and adaptive weighting of anomalous interferograms.

Velocity Estimates

To estimate the secular velocity field, we fit a parametric temporal function to each corrected LOS displacement time series. The model combines a linear interseismic trend with periodic and, when necessary, transient terms that capture seasonal and postseismic variations. This method is also described in Chapter 2 and Chapter 3, and originally in Hetland et al. (2012).

For a time series $u_{\mathrm{LOS}}(t)$ at a given pixel, the general functional form is

$$u_{\mathrm{LOS}}(t) = v\,t + u_0 + A_1 \sin(2\pi t/T_1 + \phi_1) + A_2 \sin(2\pi t/T_2 + \phi_2) + \sum_{k=1}^{N_s} S_k\, H(t - t_k) + \sum_{m=1}^{N_\ell} L_m \ln\left(1 + \frac{t - t_m}{\tau_m}\right) + \sum_{n=1}^{N_e} E_n \left[1 - \exp\left(-\frac{t - t_n}{\tau_n}\right)\right] + \varepsilon(t), \tag{3.14}$$

where v is the linear velocity (the primary parameter of interest for interseismic deformation), u_0 is the reference displacement offset. A_1 and A_2 are the amplitudes of annual ($T_1 = 1.0$ yr) and semi-annual ($T_2 = 0.5$ yr) sinusoidal terms with phases ϕ_1, ϕ_2. S_k are the amplitudes of step functions $H(t - t_k)$ representing coseismic offsets or other abrupt changes at epochs t_k. L_m and E_n are the amplitudes of logarithmic and exponential postseismic decay terms with respective relaxation times τ_m, τ_n, and $\varepsilon(t)$ denotes residual noise, assumed zero-mean and temporally uncorrelated after atmospheric correction.

The linear term vt captures the long-term interseismic deformation rate; the sinusoidal terms describe seasonal variations in the atmospheric or hydrological loading. We include both annual and semi-annual terms into the periodic functions not because we expect natural processes to occur exactly at semi-annual periods (every six months) but because adding this semi-annual term allows for asymmetric periodic processes when combined with the annual term. The optional transient terms model coseismic steps and postseismic relaxations when present.

For the interseismic analysis presented here, we retain only the first three terms of Eq. (3.14):

$$u_{\mathrm{LOS}}(t) = v\,t + u_0 + A_1 \sin(2\pi t/T_1 + \phi_1) + A_2 \sin(2\pi t/T_2 + \phi_2) + \varepsilon(t), \tag{3.15}$$

which provides the best-fitting linear rate v while accounting for residual annual and semi-annual components in the data. The velocity v is solved for each pixel by linear least squares, and the corresponding uncertainties are estimated from the covariance of the fitted parameters.

3.3 Results

Performance of time-series corrections

We demonstrate the full correction sequence using the Sentinel-1 ascending (dusk) track A087 in northwestern Arabia. The initial uncorrected velocity field exhibits

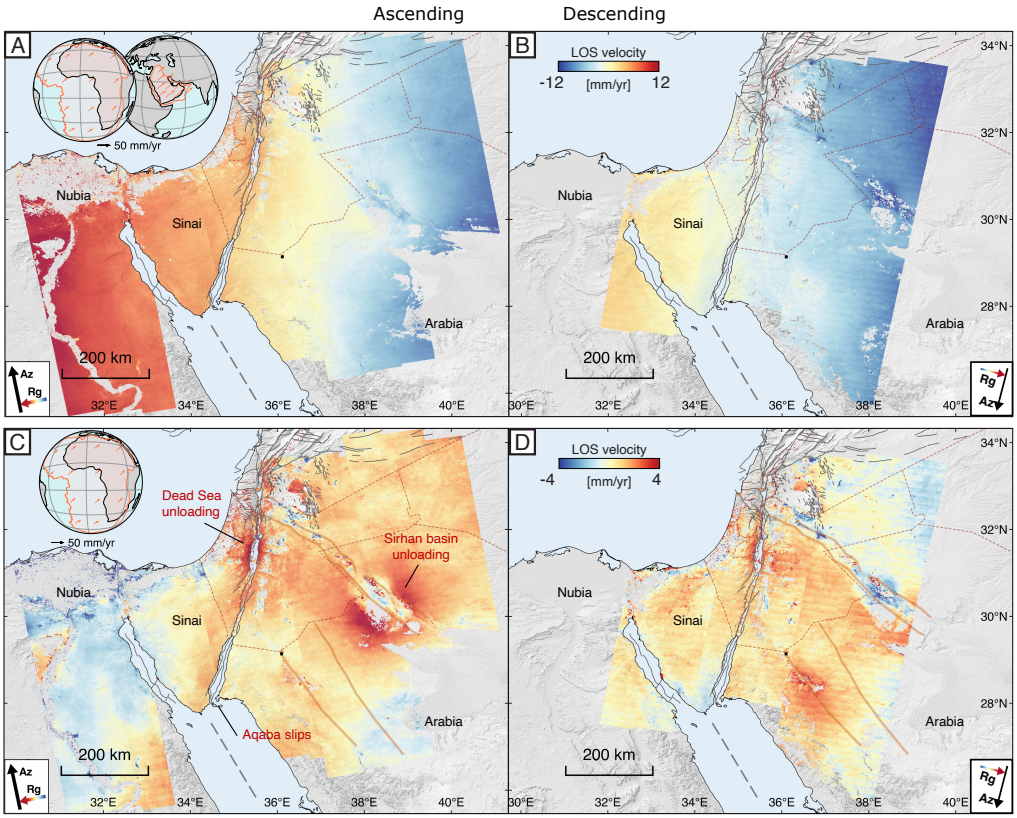

Figure 3.5: Line-of-sight (LOS) velocity fields derived from both ascending and descending Sentinel-1 viewing geometries. Individual track mosaics are merged by adjusting constant offsets between neighboring swaths to ensure cross-track continuity. **(A)** Ascending velocity (positive LOS indicates motion toward the satellite, as shown by the LOS symbol), in ITRF2014. **(B)** Descending velocity, in ITRF2014. **(C)** Ascending velocity in the stable Arabian reference frame. **(D)** Descending velocity in the stable Arabian reference frame.

a pronounced along-track gradient exceeding ~4 mm yr^{-1}/100 km, dominated by ionospheric and plate-motion effects. Sequential application of the modeled and data-driven corrections systematically reduces this apparent gradient and spatial variance (Figure 3.2, Figure 3.3A–B).

The ionospheric delay, most significant for dusk acquisitions, contributes a secular LOS velocity gradient of ~0.8 mm yr^{-1}/100 km on average, increasing to ~2.0 mm yr^{-1}/100 km when the fit is restricted to early acquisitions before 2022 due to enhanced solar activity. This behavior is consistent with the split-spectrum phase delay time series and the predicted total electron content (TEC) from the global model (Noll, 2010), both exhibiting strong annual and solar-cycle modula-

tion (Figure 3.4B). After ionospheric correction, the ramp magnitude and swath-wide standard deviation decrease markedly in all epochs (Figure 3.4). Compared to L-band SAR systems, the C-band Sentinel-1 signal remains affected by dusk-time ionospheric variations but at reduced amplitude (Liang et al., 2019; Stephenson et al., 2022).

The ERA5-based tropospheric model significantly improves temporal stability of the time series, reducing median post-fit residuals by 10 mm for northwest Arabia. Apparent velocity gradients from the modeled troposphere are negligible (<0.1 mm yr^{-1}/100 km), comparable to those estimated using kriging-based interpolation (Cao et al., 2021) and the GACOS empirical model (Yu et al., 2017). Residual DEM-correlated atmospheric delays, evaluated by regressing phase against perpendicular baseline, contribute less than ~0.1 mm yr^{-1}/100 km.

Solid Earth tides' influence is minimal at decadal scales: the dominant constituents M2 and O1 have aliased periods of 64.1 days and 77.7 days, respectively, under the 12-day Sentinel-1 sampling interval (Xu & Sandwell, 2020). Consequently, both solid-Earth and ocean tidal loading terms are small (<0.1 mm yr^{-1}) and largely averaged out in the long-term velocity inversion (described in Chapter 2). However, at shorter time scales like a few months when aliased periodic signal does not averaged out to zero trend, accounting for both the crustal response from the solid earth tides and ocean tides could still be important (DiCaprio & Simons, 2008; Yu et al., 2020).

Phase closure biases and topographic residuals are confined to localized areas (e.g., steep slopes, alluvial fans) and do not contribute to long-wavelength deformation (e.g., Zheng et al., 2022). After all corrections, approximately 70% of the epoch-level phase ramps are accounted for (Figure 3.3a), leaving time-series standard deviations of 1.6–3.0 cm per epoch and velocity uncertainties of 0.4–0.8 mm yr^{-1} (Figure 3.3b–c). These results collectively demonstrate that the corrections effectively suppress both the temporal scatter and the spatial long-wavelength bias in the InSAR time series, enabling sub-millimeter-per-year accuracy in the final velocity fields (Figures 3.2–3.4).

Line-of-Sight Velocity Fields and Arabian Plate Motion

After corrections, we adjust the constant offset between neighboring tracks to visualize the velocity field over a wider region. We observe consistent velocity fields across multiple ascending and descending tracks (Figure 3.5). Despite these correc-

tions, significant residual long-wavelength gradients persist across multiple tracks. The apparent east–west ramp in the LOS velocity field, with magnitudes of order 2 mm yr^{-1} per 100 km, cannot be attributed to atmospheric or orbital errors. Instead, this gradient arises from the projection of rigid plate motion onto the radar line of sight, due to the Earth's curvature and the varying incidence and azimuth geometry of Sentinel-1 acquisitions Stephenson et al. (2022) and Liu et al. (2025). Thus, the LOS-dependent gradient is a reference frame's motion (the angular rotation of Arabian plate) observed in the global no-net-rotation of the Sentinel-1 Satellite, International Terrestrial Reference Frame (ITRF2014) (Bähr et al., 2012; Bähr, 2013).

We compute the rigid angular rotation of the Arabian plate using the Euler pole in ITRF2014 (Altamimi et al., 2017) in radar LOS and subtract it from the observed velocity fields. The resulting Arabia-fixed velocity fields reveal coherent patterns of residual deformation that were otherwise dwarf by the dynamic range of the rigid plate motion. Both long-wavelength and small-scale features that were previously obscured by the global gradient, now emerge clearly. For example, the localized subsidence and uplift near the Wadi Arabah and the flanks of the Dead Sea basin.

When viewed together, the overlapping ascending and descending tracks display internally consistent velocity field across the entire southern DST system. The cross-track coherence confirms that the long-wavelength signals have been effectively isolated, and that the remaining patterns represent the ground motion. This consistency implies that (1) the relative horizontal and vertical motions between reference pixels across tracks are negligible; (2) the western Arabian region bounded by 35°E–39°E and 26°N–32°N behaves kinematically as a rigid block within current geodetic precision; and (3) the impact of residual tropospheric noise after correction is minimal.

The Arabian-fixed velocity field highlight regions of localized and distributed deformation. The velocity is generally consistent with previous GNSS and leveling observations (e.g., Vigny et al., 2006; ArRajehi et al., 2010; Viltres et al., 2022), delineate the principal fault-zone deformation along the southern DST. As shown in Chapter 2, the InSAR-derived velocity fields agree with GNSS velocities from Castro-Perdomo et al. (2021) and Reilinger et al. (2006) at the millimeter-per-year level without any empirical alignment (Figure 3.6). We can identify several regions of localized deformation—for example, near Al Jawf (site JOUF), where InSAR reveals broad subsidence (Figure 3.7), and near Tabuk (TB06), where localized

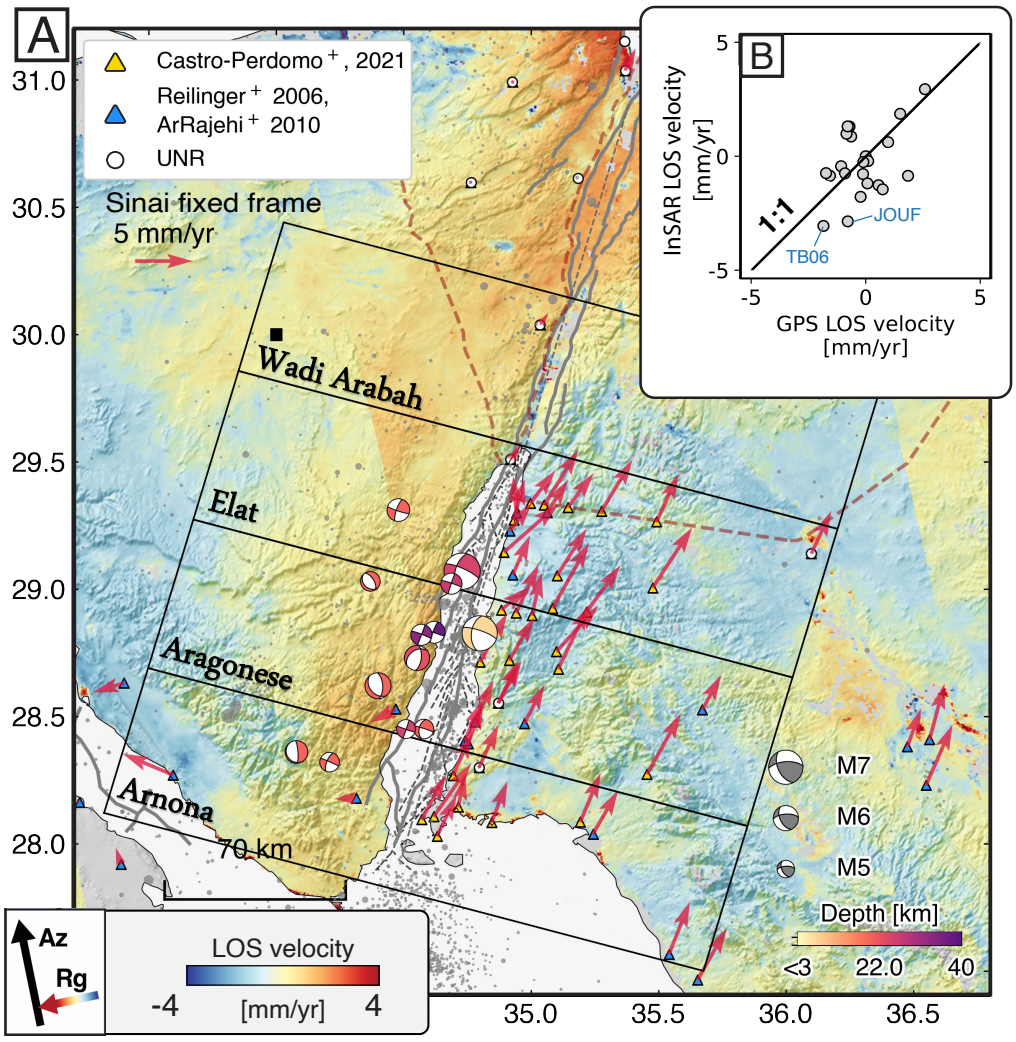

Figure 3.6: Near-field line-of-sight (LOS) velocity along the Gulf of Aqaba. **(A)** Ascending-track LOS velocity mosaic showing ~1.5 mm yr^{-1} of differential motion across the gulf. GNSS velocities relative to the stable Sinai plate indicate right-lateral motion along the Dead Sea Transform (DST). Several campaign GNSS sites (Castro-Perdomo et al., 2021) near the southern tip of Sinai suggest minor extensional motion at the <1 mm yr^{-1} level. Uncertainties of the campaign GNSS vectors are omitted for clarity. Earthquake focal mechanisms with $M_w > 5$ from the ISC catalog (International Seismological Centre, 2025) are shown and color-coded by depth. **(B)** Comparison between GNSS LOS-projected velocities and InSAR-derived LOS velocities.

ground subsidence is evident. Because GNSS measurements record primarily horizontal motion, they underestimate total ground displacement in these regions. We also observe elastic rebound and groundwater-related subsidence near the Dead Sea basin Nof et al., 2012; Feinstein et al., 2013; Li, 2023.

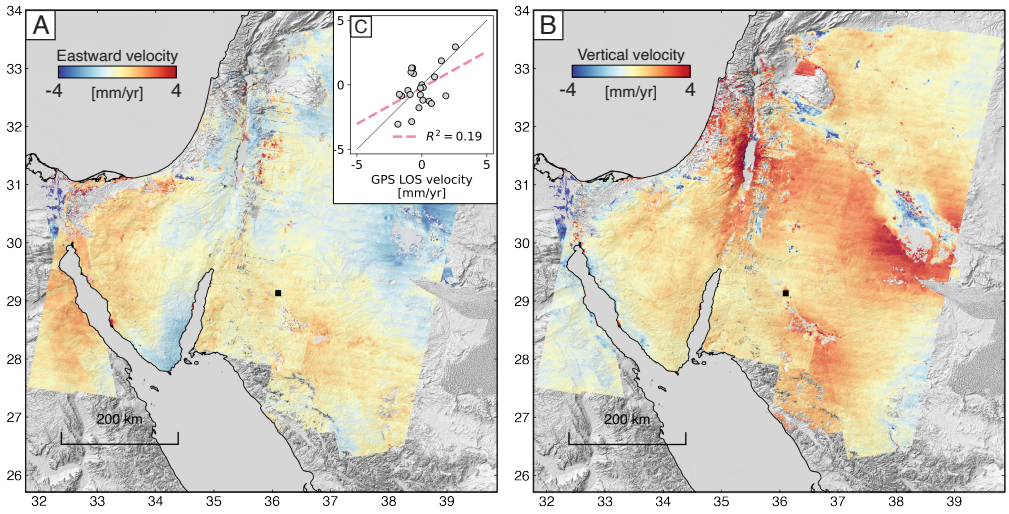

Figure 3.7: Quasi-decomposition of horizontal and vertical velocity fields derived from the combined ascending and descending Sentinel-1 geometries shown in Figure 3.5. Because the descending tracks are nearly parallel to the fault strike (N16°E), the decomposition is poorly conditioned and should be interpreted with caution. **(A)** Quasi-east velocity component in the stable Arabian reference frame. **(B)** Quasi-up (vertical) velocity component in the stable Arabian reference frame.

We combine ascending and descending mosaics to infer the quasi-vertical and quasi-horizontal components by assuming negligible northward motion (Figure 3.7). The decomposition primarily serves as a visualization tool for vertical motion, since the quasi-horizontal estimates contain significant bias. The bias is due to the interseismic horizontal motion occurs along the N16°E fault strike. Because the descending track geometry is nearly parallel to the strike direction of DST, its LOS sensitivity to strike-slip motion is minimal. Consequently, the quasi-horizontal and quasi-vertical fields are effectively constrained only by the ascending datasets, and the formal error amplification (dilution of precision (Wright et al., 2004)) propagates and scale up any original data error to the along-fault component. Therefore, the two viewing angles does not provide complementary sensitivity to decompose both fault-perpendicular and fault-parallel displacements. Nevertheless, the east–west and up–down components remain sufficiently stable for visualizing vertical deformation patterns and any significant east-west motion.

Near-field velocity fields across the southern portion of the DST show strain accumulation along the Wadi Arabah segment. In addition, the central and southern Gulf of Aqaba exhibit opposing LOS motions on both flanks of the gulf, which suggests ongoing extension (also see Figure 3.7A). We evaluate in detail in the following

section.

3.4 Interseismic deformation across DST

We extract line-of-sight (LOS) velocities from InSAR tracks abutting the Gulf of Aqaba region: ascending Sentinel-1 tracks 087 and 160, and descending tracks 021 and 094. Profiles are taken along three fault segments (Figure 3.6): the Upper Aqaba (Elat fault), Central Aqaba (Aragonese fault), and Lower Aqaba (Arnona fault) sections. These correspond to the three en echelon, left-stepping subfaults that compose the southern Dead Sea Transform (DST) (Ben-Avraham & Tibor, 1993). Similar profiles and fault segmentation were used in recent geodetic studies to infer locking of the fault (Li et al., 2021; Castro-Perdomo et al., 2021; Li et al., 2024).

2-dimensional analytical model

To quantify interseismic strain accumulation, we model the fault-parallel GNSS velocity using a anti-plane screw-dislocation formulation for each segment independently. Each segment is approximated as an infinitely long, vertical dislocation buried in a homogeneous elastic half-space with a locking depth D_L and a far-field slip rate v_0 (Chinnery & Petrak, 1968; Savage & Burford, 1973),

$$v(x) = \frac{v_0}{\pi} \arctan\left(\frac{x - X_0}{D_L}\right) + c, \tag{3.16}$$

where D_L is the effective locking depth from the surface to a depth of D_L km, c is a small reference offset, and X_0 is a distance is to account for unsure fault location. This model captures the first-order transition from locked to fully slipping behavior while minimizing parameter degeneracy.

Albeit simple in form, the forward model in Equation 3.16 is nonlinear in D_L, and its posterior distribution is strongly correlated with v_0. To estimate the joint probability of these parameters, we perform a Markov Chain Monte Carlo (MCMC) inversion using the `PyMC` framework (Abril-Pla et al., 2023), which implements Hamiltonian Monte Carlo sampling (Neal, 2011). We adopt uniform priors of

$$v_0 \in [-10,\ 10]\ \text{mm yr}^{-1}, \quad D_L \in [0,\ 60]\ \text{km}.$$

Posterior estimates of D_L and v_0 thus reflect both data uncertainty and parameter trade-offs inherent to the elastic dislocation model.

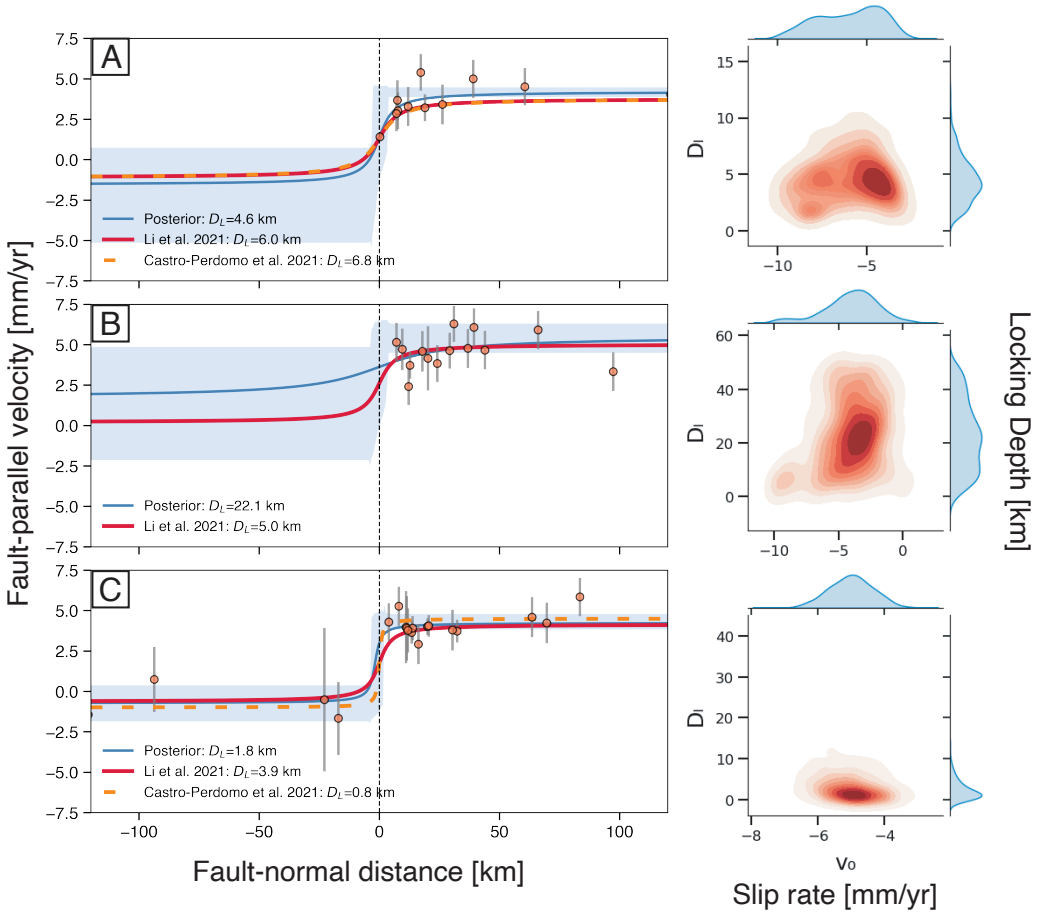

Figure 3.8: The posterior of screw-dislocation models explaining the GNSS fault-parallel velocity along DST. **(A)** Upper Aqaba (Elat fault), **(B)** Central Aqaba (Aragonese fault), and **(C)** Lower Aqaba (Arnona fault). Right panels show the posterior distributions of locking depth (D_L) and slip rate (v_0) from the MCMC inversion. Blue curves indicate this study's results; orange curves correspond to the burst-overlap interferometry models from Li et al. (2021). GNSS data are from Castro-Perdomo et al. (2021).

Our results show that the DST from Upper to Lower Aqaba exhibits a nearly uniform interseismic slip rate, consistent with previous large-scale GNSS inferences (e.g., Reilinger et al., 2006; ArRajehi et al., 2010). In addition, the inferred locking depth systematically shallows southward, decreasing from ~4.5 km beneath the Elat fault to ~1.8 km beneath the Arnona fault. This trend agrees with earlier InSAR–GNSS joint studies (Li et al., 2021; Castro-Perdomo et al., 2021). In the central Gulf, the lack of GNSS stations on the west (Sinai Peninsula) limits the resolution of both slip rate and locking depth; the constraint there mainly comes from the velocity curvature on the east side (the Arabian side) near the coastline. By contrast, the

Lower Aqaba segment, where GNSS stations exist on both sides of the gulf, yields the tightest posterior distributions for v_0 and D_L.

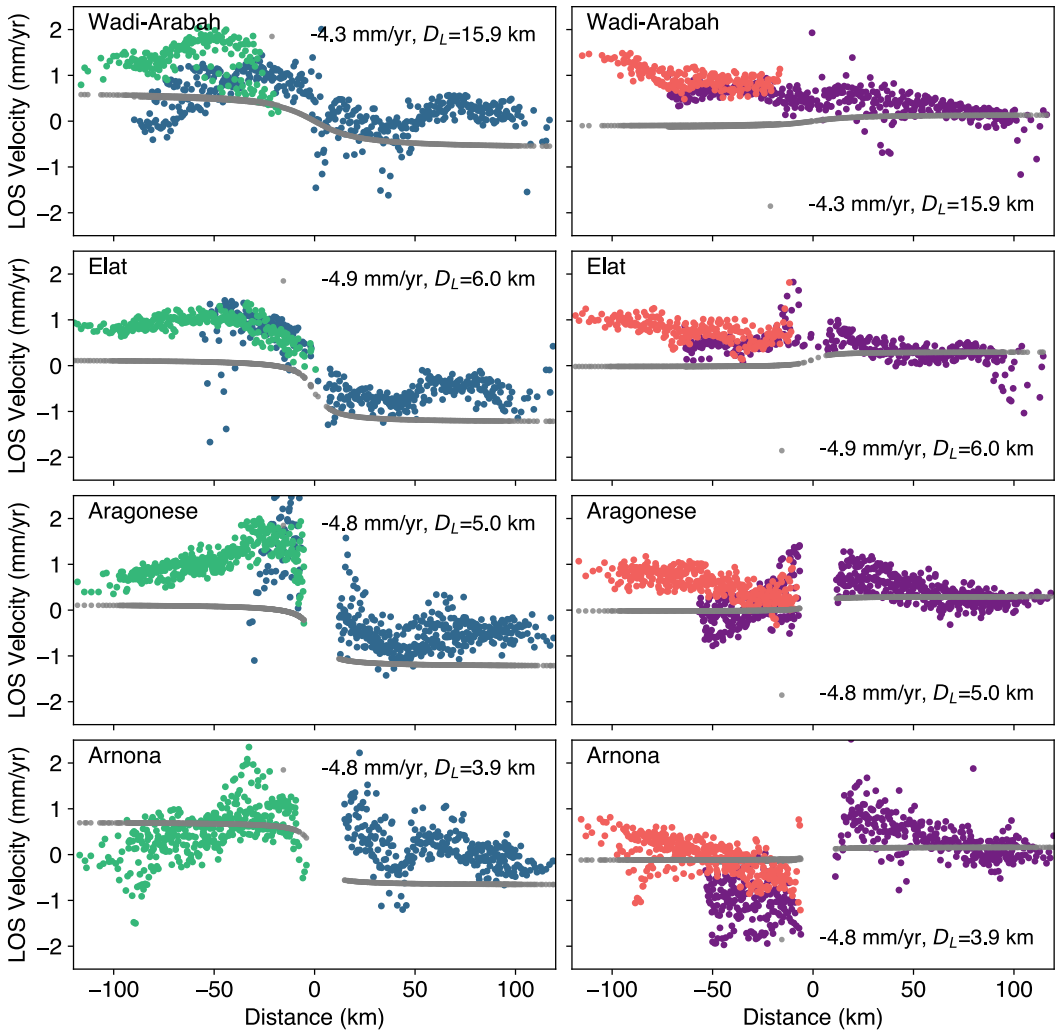

Figure 3.9: Forward model of screw-dislocation. **(A)** Wadi Arabah segment, **(B)** Upper Aqaba (Elat fault), **(C)** Central Aqaba (Aragonese fault), and **(D)** Lower Aqaba (Arnona fault). Model parameters are adopted directly from Figure 3.8, consistent with the burst-overlap interferometry models of Li et al. (2021).

If we incorporate the InSAR results from this study, the LOS velocity profiles appear more complex than the simple two-dimensional, fault-parallel view. The LOS signal represents a slant projection of the full three-dimensional surface displacement onto the radar LOS direction. Because the interseismic strike-slip motion is primarily north-south oriented, both ascending and descending geometries are largely insensitive to this component, with only about ~10% of the north–south motion projected into the LOS, with one of the track (descending) completely blind on the strike-slip

motion. The east–west motion is sensed more effectively, contributing up to ~60% of its true amplitude to the LOS signal. The vertical deformation projects most efficiently into the LOS direction due to the radar incidence geometry of Sentinel-1, with approximately 70% (far range) to 85% (near range) of the true vertical motion mapped into the observed LOS velocities.

GNSS velocity vectors indicate a measurable east–west extensional component across the Gulf of Aqaba between stations on the Sinai and Arabian sides. The Arabia–Sinai Euler-pole rotation (Reilinger et al., 2006; Altamimi et al., 2017; Viltres et al., 2022; Castro-Perdomo et al., 2021) likewise predicts $\gtrsim$ 2 mm yr^{-1} of fault-normal velocity across the gulf. Since extensional regimes frequently co-occur with vertical strain (Heki et al., 1993; Riel et al., 2015; Anderson et al., 2019) (e.g., dike intrusion and the associated surface uplift/subsidence) the superposition of fault-parallel shear, fault-normal extension, and vertical motion produces asymmetric, tilted LOS velocity gradients that cannot be explained by a simple two-dimensional screw–dislocation model alone (Figure 3.9).

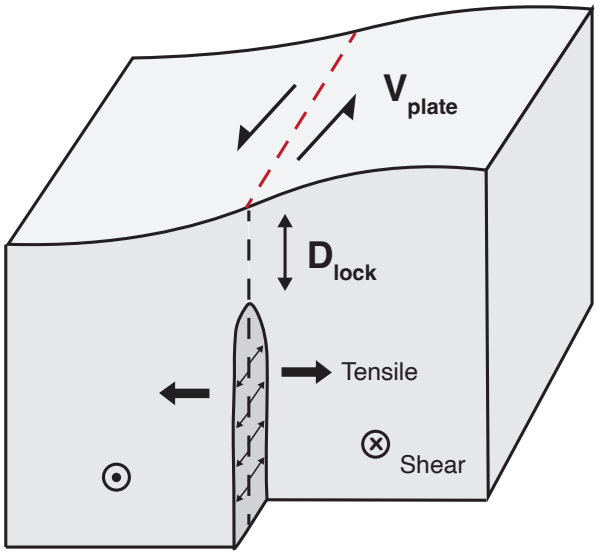

Figure 3.10: Kinematic model incorporating both a screw-dislocation (left-lateral shear component) and a tensile dislocation (opening component) below the locking depth D_{lock}. The plate boundary is driven by a far-field plate velocity V_{plate}.

Additional deformation mechanisms are therefore required to account for the residual tilt and curvature observed in the LOS velocity fields. We include a modest but non-negligible extensional component by constructing a composite model with an anti-plane (strike–slip) dislocation and an in–plane (tensile) opening dislocation

(Figure 3.10). The latter serves as an analogue for buried, dike-like extension and is expressed in a closed form derived from Volterra's representation (see Segall, 2010; T. Wang, pers. comm.), yielding both across–dike (horizontal) and vertical surface displacements. In a local dike–normal coordinate ξ_1 at free surface ($\xi_2 = 0$) and depths d_1 (top) and d_2 (bottom), the surface displacements from a vertically oriented opening segment with tensile opening S_1 are

$$u_1(\xi_1, \xi_2 = 0) = \frac{S_1}{2\pi}\left(2\arctan(\frac{-d_1}{\xi_1}) - 2\arctan(\frac{-d_2}{\xi_1}) + \sin\left(2\arctan(\frac{-d_1}{\xi_1})\right) - \sin\left(2\arctan(\frac{-d_2}{\xi_1})\right)\right) \tag{3.17}$$

$$u_2(\xi_1, \xi_2 = 0) = -\frac{S_1\xi_1^2}{\pi}\left[-\frac{1}{(\xi_1^2 + d_1^2)} + \frac{1}{(\xi_1^2 + d_2^2)}\right]. \tag{3.18}$$

Here, u_1 is the surface displacement perpendicular to the dike plane, and u_2 is vertical. We can further project the dike-centric displacements into east, north, up, and radar LOS.

For simplicity, we prescribe the parameters of both the strike-slip and tensile dislocations by forward modeling, aiming for a qualitative yet physically interpretable fit to the data. We cap the tensile dislocation segment at depth $d_2 \approx 25$ km depth to avoid block-like far-field motion that would otherwise appear if the dike extended indefinitely. We do not observe this far-field offset in the data. The uppermost extent of the tensile crack is set at the strike-slip fault locking depth $d_1 = D_L$ to couple with interseismic shear faulting. The slip rate and locking depth are adopted from previous GNSS- and BOI-based inversions (Li et al., 2021; Castro-Perdomo et al., 2021) as shown in Figure 3.8. A uniform tensile opening of approximately 2 to 3 m provides a satisfactory first-order fit to the observed LOS profiles, capturing the broad tilt and asymmetry of deformation in the central and lower Aqaba. While not a rigorous inversion, this simplified two-source model account for strike-slip shear and extensional opening in shaping the observed complex velocity profiles.

Including this opening term substantially improves the fit, particularly in reproducing the broad, tilted LOS gradients across both flanks of the gulf. However, systematic residual tilts of about 1 mm yr^{-1} across 100 km remain, particularly for descending tracks. The descending-track velocities show clear residual ramp from the Wadi Araba to the Arnona fault. Increasing either the fault slip rate or the opening magnitude cannot explain these long-wavelength residuals. This residual ramp

introduces a trade-off with the fault-locking parameters, making a direct inversion non-trivial. We therefore fix the screw-dislocation source parameters and estimate the tensile opening for each profile individually using a Markov Chain Monte Carlo (MCMC) approach. The resulting posterior opening estimates and predicted profiles are shown in Figure 3.12.

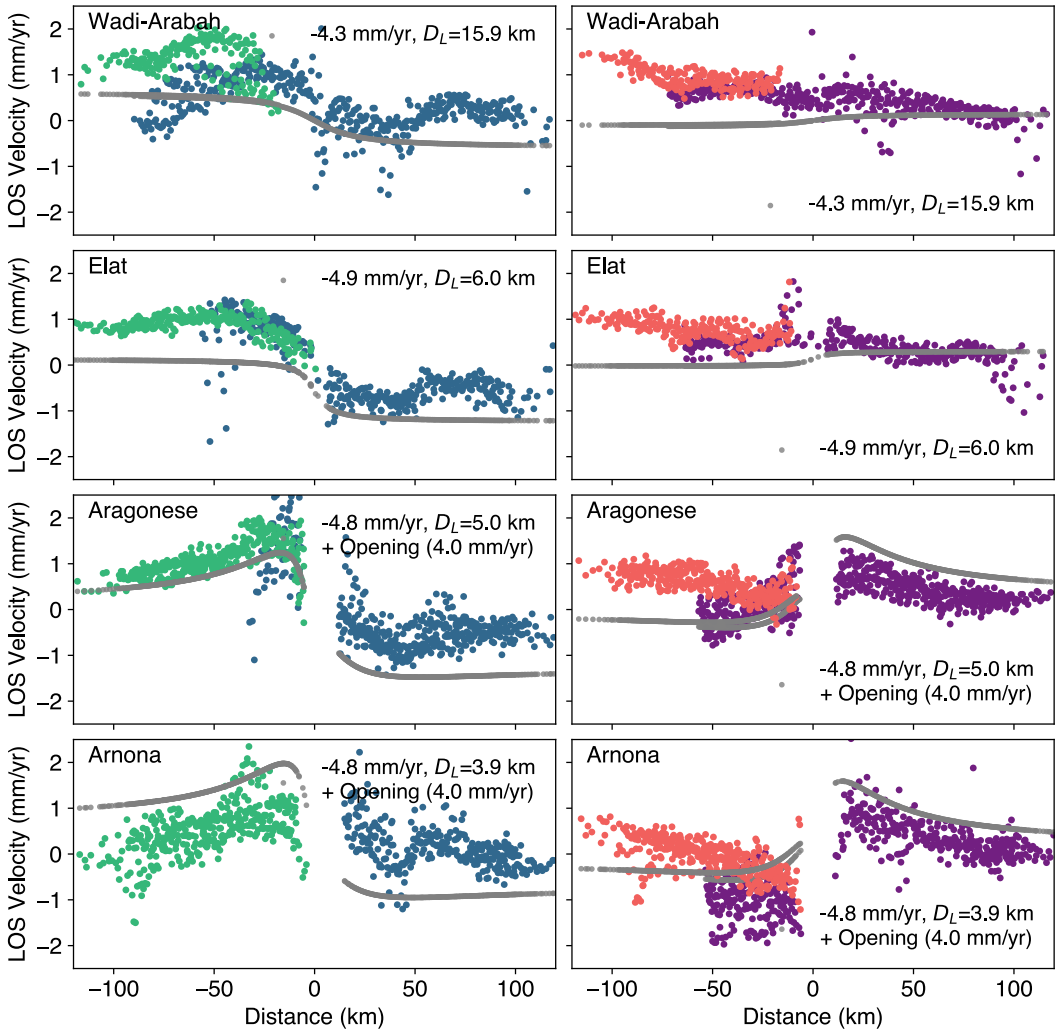

Figure 3.11: Forward model of screw-dislocation combined with a tensile crack. **(A)** Wadi Arabah segment, **(B)** Upper Aqaba (Elat fault), **(C)** Central Aqaba (Aragonese fault), and **(D)** Lower Aqaba (Arnona fault). Model parameters are adopted directly from Figure 3.8. Tensile crack extends from 25 km depth upward to the locking depth in each panel.

For the Wadi Araba, located onshore and distant from the Gulf, we did not estimate opening. The Elat fault, situated in the upper Gulf of Aqaba, shows a posteriori opening consistent with zero. In the lower Gulf of Aqaba, the Aragonese and Arnona

faults yield estimated opening rates of 1.2 and 2.6 mm/yr, respectively.

A crucial next step is to resolve the origin of this persistent long-wavelength ramp and fully invert for the posterior on both the strike-slip and the opening components of the fault using both GNSS and InSAR data. However, we expect qualitatively, at least 2 mm/yr of the extensional dislocation will still be required to explain the observed tilt across the fault zone.

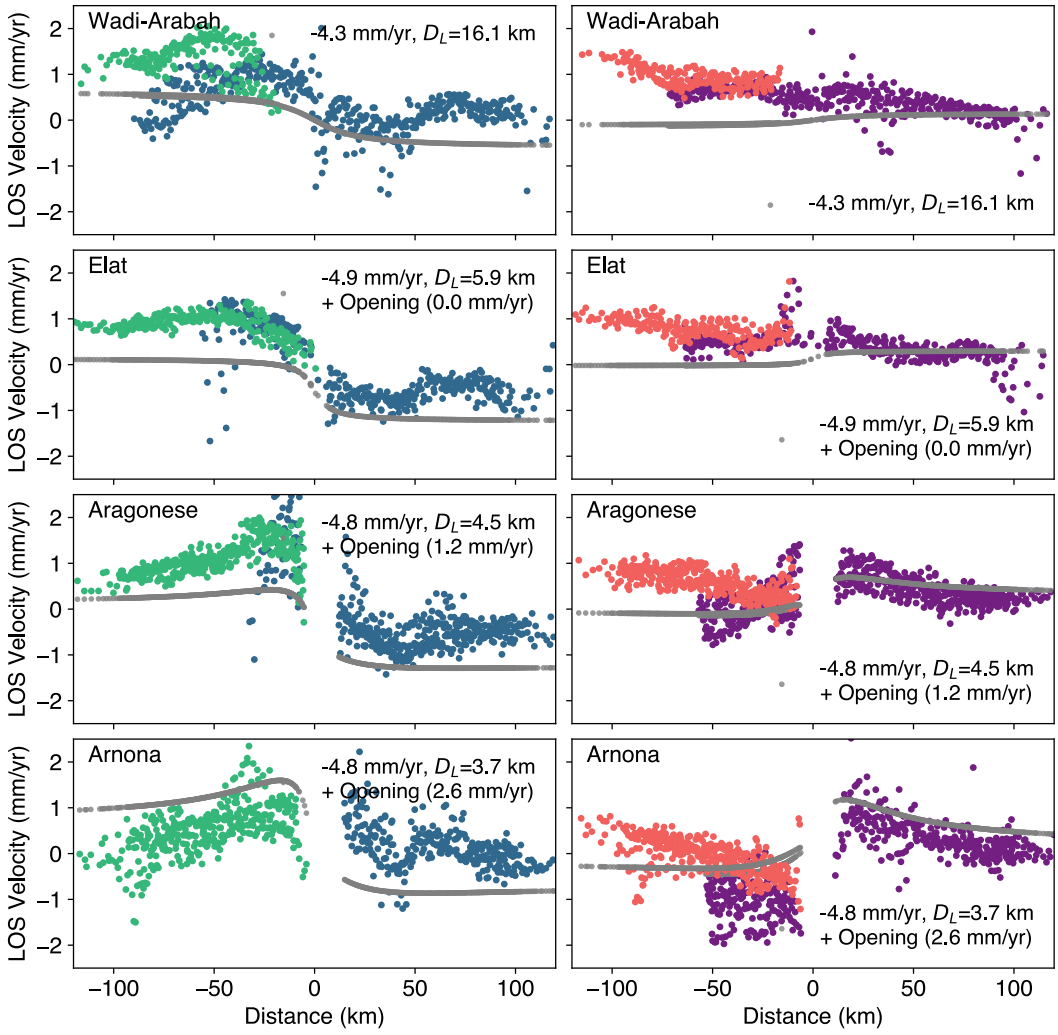

Figure 3.12: Same as Figure 3.11, but using the Markov Chain Monte Carlo sampling to find the maximum a posteriori parameters of the tensile opening, given a tight constraints on the screw-dislocation parameters from previous works. Tensile crack extends from 25 km depth upward to the locking depth in each panel.

3.5 Discussions

Interseismic Locking Variations along the Dead Sea Transform

Our InSAR velocity fields reveal along-strike variations in strain accumulation along the southern Dead Sea Transform (DST). In the northern and central segments, particularly across the Wadi Arabah segment, the interseismic deformation is distributed over a broad zone, consistent with a locking depth of roughly 16 km. Toward the southern end of the system, however, both GNSS and InSAR data indicate a progressive shallowing and localization of the locked zone. Time-series InSAR analyses exploiting Sentinel-1 burst-overlap interferometry show that the effective locking depth decreases systematically southward, from $\gtrsim$ 10 km inland to only $\sim$ 6–7 km beneath the Gulf of Aqaba (Li et al., 2021). Independent GNSS inversions across the same region yield comparable results, with a left-lateral slip rate of $4.9^{+0.9}_{-0.6}$ mm yr^{-1} and a locking depth of $6.8^{+3.5}_{-3.1}$ km (Castro-Perdomo et al., 2021). However, by inverting the GNSS data in a 2-D strike-slip dislocation model, the posterior ensemble allows for a wide range of scenario of locking depths, including models with creep extending to the surface. The large model uncertainty primarily reflects the limited data coverage on both sides of the fault.

When incorporating our InSAR observations from this study and the burst-overlap inversion (BOI) of Li et al. (2021), the optimal locking depth converges near 3.9 km, substantially deeper than the 0.8 km inferred from GNSS alone. The smoother curvature and gradual velocity transition in our InSAR profiles are more consistent with the $\sim$ 4 km locking case than with the shallower solution, which would produce an unrealistically sharp velocity gradient near the fault. Therefore, the true locking depth along the southernmost DST likely lies between 0.8 and 3.9 km. Our joint inversion combining the GNSS and InSAR datasets yields consistent estimates of the locking depth within this range. However, to further narrow down and quantify the degree of shallow creep remains challenging, due both to the lack of near-fault observations and to the trade-off with the extensional motion in the gulf.

Seismicity and interseismic deformation together reveal a north–south difference in strain accumulation along the Gulf of Aqaba. The northern and central segments repeatedly host large strike–slip earthquakes, including the 1995 M_w 7.2 Nuweiba event (e.g., Klinger et al., 1999), whereas the southern segment has remained quiescent since at least the 16th century (Bektaş et al., 2024). Interseismic velocities indicate that the northern and central segments are accumulating shear strain, consistent with episodic rupture of discrete, en echelon fault strands. In contrast, the

southern segment shows little to no elastic strain buildup, suggesting a combination of reduced locking, near-surface creep, and extension in the pull-apart basins. The 1995 rupture and its subevents demonstrate that oblique–normal faulting can cascade across adjacent strands (Klinger et al., 1999; Vasyura-Bathke et al., 2024), accommodating both strike–slip and extensional components during a single earthquake sequence. Our interseismic observations capture the elastic loading associated with this behavior: strain accumulates across the locked northern and central strands and is periodically released through complex, multi-segment ruptures, while the southern segment participates primarily through aseismic or extensional processes.

Extensional and Vertical Deformation

Our InSAR observations provide new quasi-three-dimensional constraints on surface deformation near the southern Dead Sea Transform (DST). The line-of-sight (LOS) velocity patterns exhibit complex tilts and asymmetries that cannot be explained by a purely strike-slip interseismic model. Incorporating a tensile-opening component at seismogenic depths reproduces the observed deformation qualitatively, suggesting a non-negligible extensional contribution to the surface velocity field. A first-order estimate indicates an extension rate of ~2–3 mm yr^{-1} across the southern DST. This rate agree with campaign GNSS sites near the southern Sinai (DAHA and NABQ) which show roughly westward motion of ~1 mm yr^{-1} relative to the north in Israel (Piersanti et al., 2001; Pietrantonio et al., 2016; Castro-Perdomo et al., 2021). The base of the tensile crack must lie shallower than ~30 km, since extending the dislocation to deeper depths would generate a block-like far-field motion that is not observed within the ±250 km velocity profiles. The curvature associated with the extension is restricted to the near-field (within ~50 km of the fault), implying a finite down-dip extent of the tensile crack. This geometry suggests that the opening is not a through-going rift penetrating the upper mantle, but rather a shallow tensile zone within the upper lithosphere, which is likely organized in en echelon, flower-like structures typical of transtensional fault systems (Ribot et al., 2021; Barjous & Mikbel, 1990; Hartman et al., 2014).

Vertical deformation naturally accompanies extension (Heki et al., 1993; Anderson et al., 2019). Joint ascending–descending InSAR decomposition reveals that the quasi-vertical component across the Gulf of Aqaba is minimal, approaching the detection limit of our velocity fields. A forward model with ~4 m of dike-like tensile opening predicts vertical velocities peaking at ~1 mm yr^{-1} within 10 km of the fault and decaying to ~0.5 mm yr^{-1} over 30 km. Given that the gulf is 20–24 km

wide, any uplift signal would be confined within the basins and largely undetectable onshore. Thus, independent evidence is needed to assess the long-term vertical strain.

However, campaign GNSS sites have vertical uncertainties of several millimeters per year, and continuous stations are too distant to measure local deformation. Geological and geomorphic indicators therefore provide essential complementary constraints. Both geodetic (Wdowinski et al., 2004; Reilinger et al., 2006; ArRajehi et al., 2010; Viltres et al., 2022) and structural studies (Ben-Avraham, 1985; Garfunkel & Ben-Avraham, 1996; Klinger et al., 1999; Ribot et al., 2021; Ribot et al., 2024) demonstrate that the gulf is an actively transtensional system where left-lateral shear is accompanied by crustal thinning and normal faulting.

The pronounced topographic relief between the 900–1800 m-deep bathymetric troughs of the Gulf of Aqaba and the flanking ~2000 m-high crystalline escarpments records the cumulative vertical offset from repeated oblique-normal faulting over multiple earthquake cycles (Ribot et al., 2021; Ribot, 2021). Both interseismic extension and coseismic slip contribute in the same vertical sense—subsiding the hanging wall and uplifting the footwall—leading to a progressive increase in basin depth and mountain relief. The InSAR-observed extension likely represents the elastic accumulation of extensional strain that is later released as permanent slip during major events such as the 1995 M_w 7.2 Nuweiba earthquake (Klinger et al., 1999; Vasyura-Bathke et al., 2024). Over repeated cycles, this behavior generates the observed crustal thinning and relief amplification characteristic of transtensional systems.

Overall, our results indicate that the southern Gulf of Aqaba behaves as a shallow transtensional domain, where left-lateral shear is partitioned with modest crustal extension within the upper lithosphere (< 40 km). The inferred tensile component from InSAR is consistent with mapped normal faults (Ribot et al., 2021) and focal mechanisms of recent seismicity, suggesting that oblique slip and localized opening are persistent features of this segment. Rather than reflecting an active throughgoing rift, the deformation represents intra-crustal strain accommodation within a strike-slip fault system that produces cumulative vertical and horizontal offsets over time. This framework links the short-term interseismic strain to long-term crustal modification, providing a view of how oblique shear and extension shape the evolving morphology of the southern Dead Sea Transform.

Residual velocity gradient and Sinai block motion

Beyond the near-fault deformation, our InSAR velocity fields reveal a coherent long-wavelength gradient, with a direction normal to the southern DST. From east side of the Gulf of Aqaba to the Sinai Peninsula, the ~1 mm yr^{-1}/100 km gradient is visible in both ascending and descending geometries. Campaign GNSS sites on the east side of gulf also generally show systematic residuals after that cannot be explained by the elastic locking of the DST (Castro-Perdomo et al., 2021).

Enhancing the tensile component in the elastic model does not reproduce the observed long-wavelength gradient. Although a dipping fault geometry potentially could, in principle, generate such asymmetry, the required magnitude and ~200 km spatial extent of the tilt would entail us extending the tensile crack from depths of ~25 km to more than 100 km—an unrealistic configuration for a local fault system. This suggests that the observed gradient reflects a broader, regional-scale effect rather than a localized structural feature.

One possibility is that the gradient arises from the rotation of the Sinai plate relative to Arabia. However, the predicted velocity gradient from this relative rotation is four to five times smaller than observed. This discrepancy implies either (1) the current Sinai–Arabia rotation underestimates motion in the southern peninsula, or (2) the residual deformation represents diffuse strain within the Sinai–Suez domain (Piersanti et al., 2001). In the first case, most GNSS stations constraining Sinai's angular velocity lie within 50 km of the Dead Sea and Jordan Valley, where near-fault strain obscures the block rotation constraint, leaving southern Sinai and the Suez–Aqaba junction largely unconstrained. In the second case, postseismic relaxation following the 1995 M_w 7.2 Nuweiba earthquake could explain the residual east–northeastward motion of < 1 mm yr^{-1} observed in GNSS data (Piersanti et al., 2001; Castro-Perdomo et al., 2021). A weak lower crust exhibiting ductile behavior on decadal timescales would allow such long-lived transients (Liu et al., 2021), which may be consistent with elevated regional heat flow near the nascent Red Sea rift.

Improved geodetic coverage across southern Sinai is therefore essential to distinguish between subtle microplate rotation and distributed postseismic or viscous deformation at the transition between the Dead Sea Transform and the Red Sea rift.

3.6 Conclusion

Our integrated InSAR–GNSS analysis reveals that interseismic deformation along the southern Dead Sea Transform departs from a simple strike-slip behavior. The

Table 3.1: Euler pole parameters for the Sinai plate in ITRF2014 from recent studies.

Study	**Latitude (°N)**	**Longitude (°E)**	**Angular rate (°/Myr)**
Castro-Perdomo et al. (2021)	54.7	347.8	0.42
Hamiel & Piatibratova (2019)	54.6	344.2	0.40
Viltres et al. (2022)	54.9	343.0	0.39

LOS velocity fields and forward elastic modeling require a finite tensile component of $\sim$ 3 mm yr^{-1} at seismogenic depths to reproduce the observed velocity gradient, implying that fault-normal extension contributes measurably to present-day strain. Locking depths vary systematically along strike, decreasing from ~10–15 km in the central DST to ~4 km beneath the southern Gulf of Aqaba. Vertical deformation associated with the extension is expected to be below 1 mm yr^{-1}, and is below the resolvability of the current InSAR technique.

These findings are consistent with structural and seismological evidence showing pervasive oblique-normal faulting and crustal thinning within the Gulf of Aqaba. The geodetically observed interseismic extension reflects elastic strain accumulation within a transtensional stress field, while the coseismic strike-slip and normal faulting during the 1995 M_w 7.2 Nuweiba earthquake record its episodic brittle release. Together, these observations indicate a coherent kinematic regime in which left-lateral shear is accompanied by fault-normal extension, shaping the long-term basin-mountain morphology of the central-southern DST through repeated earthquake cycles. This study provides complementary observational constraints from multi-geometry InSAR, highlighting how combined geodetic data can resolve the three-dimensional deformation of plate-boundary systems.

Chapter 4

INTERSEISMIC COUPLING ALONG THE ANDEAN MEGATHRUST FROM SENTINEL-1 INSAR AND GNSS OBSERVATIONS

ABSTRACT

We derive maps of interseismic deformation along the Peruvian–Chilean subduction margin using a decade of Sentinel-1 InSAR and GNSS observations (2014–2025). After atmospheric phase delay corrections and alignment to the South American plate defined in the ITRF2014 (International Terrestrial Reference Frame), the resulting long-wavelength velocity field spans ~2500 km of the Andean margin, capturing both coastal and forearc deformation. Coupling strengthens from 16°S southward to 17.8°S (offshore Arequipa) but decreases across the Arica Bend, where the subduction of the Iquique Ridge and Nazca Fracture Zone likely facilitates partial creep. A strongly coupled zone extends from 19.6°S (Pisagua) to 26°S (Chañaral), bounded by localized low-coupling patches south of the Mejillones Peninsula. Farther south, weak coupling near La Serena, Copiapó, and Taltal coincides with subducting bathymetric highs, suggesting that these ridges modulate frictional properties and promote persistent segmentation of the plate interface. Between Illapel and Santiago (32°–35°S), long-term postseismic relaxation following the 2010 M_w 8.8 Maule earthquake obscures the interseismic locking signals and thus our coupling estimates are likely biased. Overall, the joint InSAR–GNSS inversion delineates a first-order segmentation of the Andean megathrust governed by subducting morphological features. Additional analyses are needed to understand the residual long-wavelength deformation in the wider forearc region, and to evaluate hypotheses involving viscoelastic relaxation or microplate motion.

4.1 Introduction

The Peru-Chilean subduction zone, where the oceanic Nazca Plate converges beneath the South American Plate at a rate of ~67 mm yr^{-1} (Vigny et al., 2009; Argus et al., 2011), is among the most seismically active plate margins on Earth. The Peru to central Chilean megathrust has generated numerous great earthquakes in the instrumental era, including the 1995 M_w 8.0 Antofagasta, 2001 M_w 8.4 Arequipa, 2014 M_w 8.1 Iquique, and 2015 M_w 8.3 Illapel events. Farther north, near the Arica Bend, two great tsunamigenic earthquakes struck in 1868 and 1877 (M_w 8.9 and M_w 8.8, respectively; Figure 4.1; (Comte & Pardo, 1991; Lay & Nishenko, 2022)). Together, these earthquakes provide a remarkable record of recurrent megathrust failure along the Chile–Peru margin, illuminating both the destructive power and the apparent cyclic nature of subduction processes (Table 4.1). Decades of geological, geodetic, and seismological observations suggest that the Chilean megathrust may rupture as a series of quasi-independent segments. However, whether the regions between them act as partial or transient barriers to seismic slip remains uncertain. Thus, we need to to improve interseismic coupling models that can serve as quantitative maps to guide our understanding of how strain is stored and released along this complex subduction interface.

Understanding the extent to which interseismic locking varies along these segments, particularly in areas that last ruptured more than two centuries ago near the Arica Bend (Chlieh et al., 2011; Schurr et al., 2014) is essential for assessing present-day strain accumulation and seismic potential, as well as for testing hypotheses on conditioning stick-slip behaviors (e.g., Wang & Bilek, 2011; Noda & Lapusta, 2013). For example, along-strike differences in creeping behavior correlate with subducting bathymetric features—ridges like chains of oceanic ridges, seamount, and fracture zones (Klein et al., 2018b; Donoso et al., 2021; Münchmeyer et al., 2025). These seafloor morphologies are hypothesized to locally modify frictional, hydraulic, and thermal conditions along the megathrust interface, thereby promoting creeping (Fisher et al., 2003; Wang & Bilek, 2011; Socquet et al., 2024) and slow-slip behavior (Münchmeyer et al., 2025).

Between major earthquakes, the locked portions of the plate interface accumulate elastic strain that manifests as measurable interseismic deformation at the surface (**Chlieh.etal_2008_HeterogeneousCouplinga**; e.g., Savage, 1983; Moreno et al., 2011; Lin et al., 2015; Avouac, 2015; Jolivet et al., 2020). Previous coupling models, constrained primarily by data from Global Navigation Satellite System System

(GNSS) of the central Andean region, revealed first-order patterns of strain accumulation (e.g., Métois et al., 2012; Métois et al., 2016), but coverage near the trench sometimes remains effectively zero, and vertical constraints are also often lacking. Interferometric Synthetic Aperture Radar (InSAR) offers dense spatial sampling capable of resolving both short- to long-wavelength signals has been hampered by atmospheric and orbital artifacts—limitations that are recently addressed by improved tropospheric (Jolivet et al., 2014; Hersbach et al., 2020) and ionospheric corrections (Gomba et al., 2016; Fattahi et al., 2017b; Liang et al., 2019) and precise frame alignment (Peter, 2021; Peter, 2023). Consequently, we are now more able to recognize and reduce long-wavelength nuisance signals in InSAR time series, to the extent that constraining plate motions directly from InSAR has become feasible in regions with wide acquisition coverage and high temporal coherence (Stephenson et al., 2022; Liu et al., 2025).

Most previous inference on the interseismic coupling along the Peruvian-Chilean megathrust relied on deterministic inversions methods with ad hoc smoothing to tackle this ill-posed problem (e.g., Chlieh et al., 2004; Moreno et al., 2011; Lovery et al., 2024). Such regularization choices can be arbitrary and can strongly influence the amplitude and spatial pattern of inferred slip on the megathrust (Ozawa et al., 2011), while uncertainties are typically insufficiently accounted for (Ortega-Culaciati et al., 2021). Here, we adopt a Bayesian approach treats regularization as an explicit prior and yields posterior distributions that quantify uncertainty and trade-offs among parameters (Tarantola & Valette, 1982; Tarantola, 2005; Minson et al., 2013), allowing us to assess the ensemble of models that are consistent with the data.

Here, we present the first spatially continuous InSAR-derived interseismic velocity field spanning ~2500 km from southern Peru to central Chile, combining a decade of Sentinel-1 C-band data (2014–2025) together with spatially-sparse GNSS observations. Using a fully Bayesian framework, we infer interplate coupling and the associated uncertainties, providing a probabilistic view of how InSAR and GNSS jointly constrain the state of interseismic coupling along the Andean subduction zone. We compare with previous studies and against the locations of historical earthquake ruptures in the region, and discuss how residual long-wavelength signals may reflect ongoing postseismic relaxation or large-scale intraplate reference-frame motion. The resulting model reveals a first-order pattern in which zones of low coupling (creeping regions) correlate closely with the subduction of prominent

bathymetric features along the trench, consistent with the hypothesis that these morphological heterogeneities play a key role in modulating the frictional behavior of the megathrust (Fisher et al., 2003; Wang & Bilek, 2011; Socquet et al., 2024).

Table 4.1: Summary of large ($M_w \geq 7.7$) subduction earthquakes along the Chile–Peru margin whose coseismic slip contours are shown in this study. Pre-instrumental events are compiled from Lay & Nishenko (2022), Métois et al. (2013), and Comte & Pardo (1991), representing consensus rupture extents. For instrumentally recorded events, contours correspond to published models.

Year	Magnitude	Region	Contour (max slip)
1868	M8.5	Southern Peru	approx.
1877	M8.3	Northern Chile (Iquique)	approx.
1906	M8.4	Central Chile (Valparaíso)	approx.
1922	M8.4	Atacama	approx.
1985	M8.0	Central Chile (Valparaíso)	approx.
1995	M8.1	Antofagasta	2 m (Pritchard & Simons, 2006)
2001	M8.4	Arequipa, Peru	4 m (Pritchard et al., 2007)
2007	M7.7	Tocopilla, Chile	1 m (Béjar-Pizarro et al., 2013)
2007	M8.0	Pisco, Peru	2 m (Sladen et al., 2010)
2010	M8.8	Maule, Chile	2.5 m (Lin et al., 2013)
2014	M7.7	Iquique foreshock	1 m (Duputel et al., 2015)
2014	M8.1	Iquique mainshock	2 m (Duputel et al., 2015)
2015	M8.3	Illapel, Chile	2 m (Klein et al., 2017)

4.2 Method: Interferometric data preparation

Interferograms processing

The Atacama Desert of southern Peru and northern Chile is exceptionally well suited for radar interferometry due to its arid climate, minimal vegetation, and scarce cloud cover, all of which promote phase coherence between repeat SAR acquisitions (Pritchard & Simons, 2002; Pritchard, 2003). High coherence (values near 1) indicates that surface scattering properties remain stable between observations, whereas low coherence (near 0) reflects surface changes caused by rainfall, snow, vegetation growth, or anthropogenic disturbance.

Our processing workflow largely follows the approaches described in Chapter 2 and Chapter 3. Here, we use Sentinel-1 C-band SAR data to map interseismic deformation across the central Andes from October 2014 to July 2025. Both Sentinel-1A and Sentinel-1B platforms have provided dense and relatively even coverage in this region, and beginning in 2025, data from Sentinel-1C are also included (Figure 4.2).

We process multiple ascending and descending tracks of Sentinel-1 SLC images

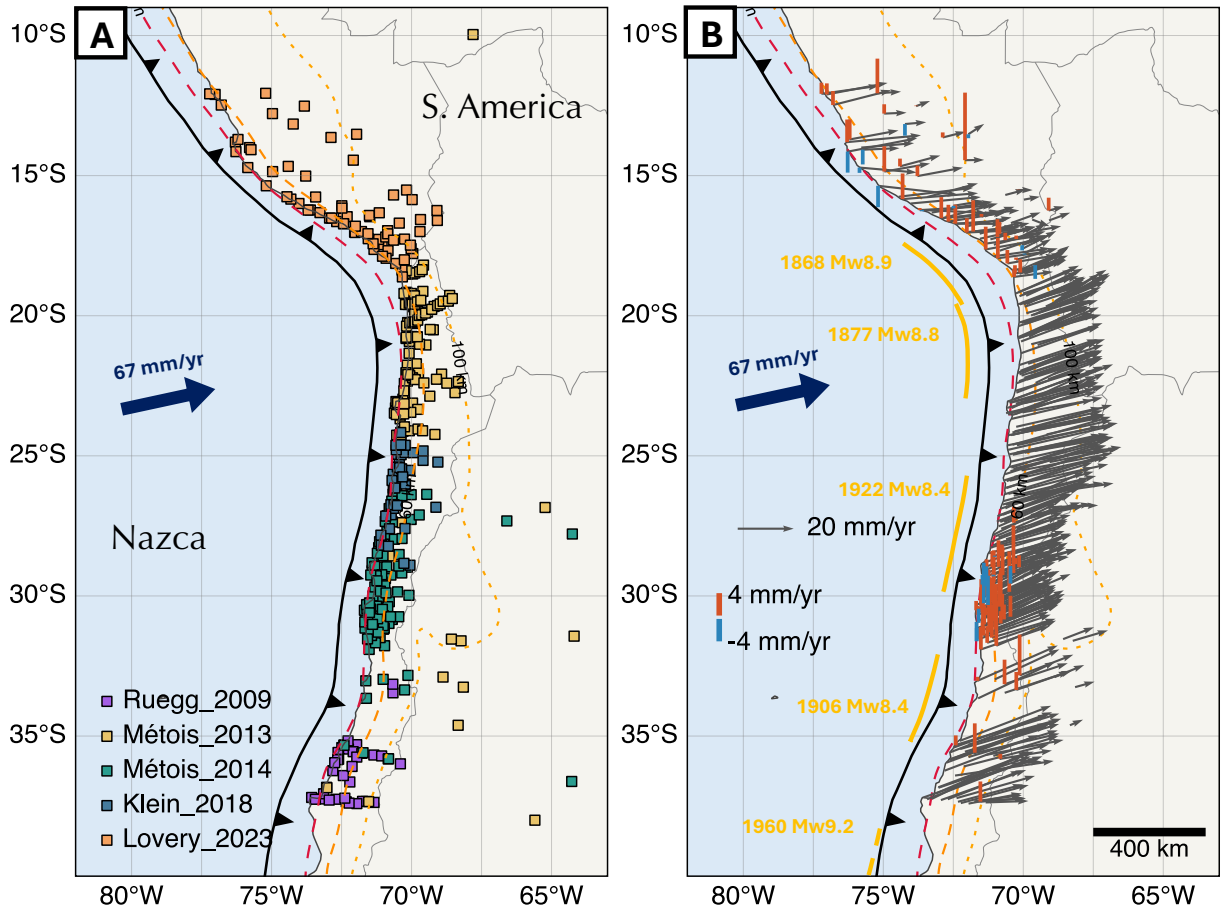

Figure 4.1: Chilean subduction margin and contemporary GNSS network. The Nazca Plate converges beneath the South American Plate at an average rate of ~67 mm yr^{-1} along the Chilean margin. **(A)** Map showing the distribution of published GNSS networks that provide late-interseismic deformation constraints (velocities not shown). Data are compiled from Ruegg et al. (2009), Métois et al. (2013), Métois et al. (2014), Klein et al. (2018a), and Lovery et al. (2024). The trench trace and slab-depth contours (30, 60, and 100 km) are derived from the Slab 2.0 model (Hayes et al., 2018). **(B)** Observed GNSS horizontal vectors and vertical velocity amplitude are shown relative to the stable South American reference frame. Rupture extent of major historical and pre-20th-century megathrust earthquakes are outlined in orange (Table 4.1).

using standard interferometric procedures: image co-registration, enhanced spectral diversity (ESD) refinement (Fattahi et al., 2017a), and formation of a dense interferometric network by pairing each acquisition with its five nearest neighbors (with a maximum temporal baseline of 60 days assuming a 12-day cadence). We also compute pairs that approximately bridge across four to six months to account for potential phase closure issues (Zheng et al., 2022). This configuration ensures

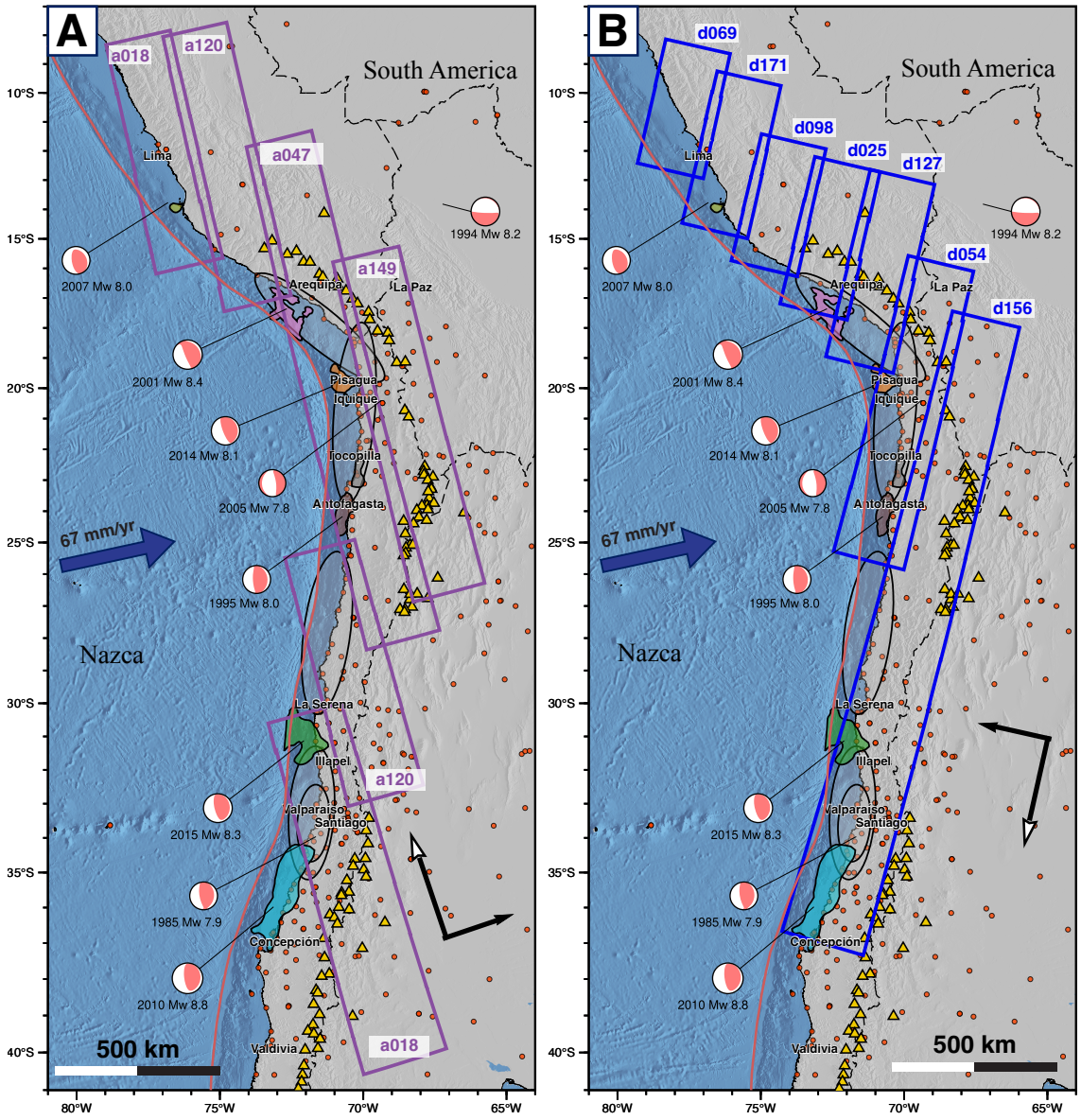

Figure 4.2: Satellite data used in this study, including Sentinel-1A, -1B, and -1C acquisitions from 2014 to 2025. **(A)** Ascending-track acquisition coverage. **(B)** Descending-track acquisition coverage. Major earthquakes during the past 30 years are outlined by their ~2 m coseismic slip contours, with GCMT focal mechanisms (Dziewonski et al., 1981; Ekström et al., 2012) shown at event centroids. Pre-instrumental and early historical ruptures (pre-20th century) are indicated as ellipses based on previously published sources. Red dots mark GNSS stations incorporated in this study, and yellow triangles denote Holocene volcanoes from the Global Volcanism Program database (Global Volcanism Program, 2025). The adopted coseismic slip contour for each earthquake is listed in Table 4.1.

a well-constrained temporal network for time-series inversion. Most of the Chilean and Peruvian forearc is well covered by the Sentinel-1 archive. However, regions around the Arica Bend and toward the transition into central Peru and central-south Chile (near Mendoza) frequently experience severe decorrelation and poor interferometric coherence. In these areas, acquisition modes were also inconsistent, and some frames are unavailable, preventing the formation of short-baseline interferometric pairs or the stitching of continuous scenes across long SAR swaths.

Despite these limitations, the section between ~16°S (Arequipa, southern Peru) and ~30°S (La Serena, northern Chile) provides an exceptional dataset. The Andean forearc in this region is largely arid, yielding high-coherence interferograms even at C-band wavelengths (e.g., Pritchard & Simons, 2002). This segment therefore allows robust estimation of long-wavelength ionospheric corrections and secular ground deformation.

In contrast, data quality deteriorates both north and south of this arid segment. North of Ica and Lima, the fold-and-thrust belt approaches the coastline, narrowing the low-relief forearc to only ~60–140 km before the terrain rises abruptly to altitudes exceeding 4 km. This steep relief induces wintertime decorrelation (due to snowfall) and strong tropospheric phase gradients. In coastal Peru, the persistent *Camanchaca* fog—a dense, saturated marine layer up to ~1 km thick—further contributes to short-wavelength tropospheric heterogeneity, which is not adequately captured by global weather reanalyses.

To mitigate such phase distortions, we first applied ERA5-derived tropospheric phase corrections directly to the wrapped interferograms, then performed phase unwrapping. This procedure effectively reduces phase gradients prior to unwrapping, stabilizing solutions across steep terrain (Cavalié et al., 2008). We subsequently reintroduced the modeled ERA5 phase to the unwrapped results, and finally correct them along with other correction terms in the time-series stage for a consistent workflow (Yunjun et al., 2019). Improvements were quantified by a reduction in cycle-misclosure statistics and by increased temporal coherence. We further refined unwrapping errors using both the bridging-phase and L1-norm closure correction methods, which adjust inconsistent interferometric loops between connected coherent regions (Yunjun et al., 2019). Although temporal coherence improved to values exceeding 0.8 in many cases, residual unwrapping artifacts persist in high-relief areas. Hence, manual inspection and selective removal of problematic interferograms remain necessary.

Since GNSS campaign stations often not provide with vertical components, InSAR provides key vertical sensitivity. A single LOS (line-of-sight) observation with incidence angle θ gives $\sigma_V \approx \sigma_{\mathrm{LOS}}/\cos\theta$, while an ascending–descending pair reduces this uncertainty by $\sqrt{2}$. For incidence angles of 29°–46°, vertical precision of 1–2 mm yr^{-1} can be achieved, and in coherent regions we obtain sub-millimeter annual uncertainty. Thus, InSAR complements GNSS by densely constraining vertical and long-wavelength deformation across the arc.

Ionospheric Correction

Despite the generally favorable conditions in central Chile, coherence can degrade in high-elevation areas where persistent snow and steep topography, especially around volcanic peaks exceeding 6000 m, disrupt phase stability.

Correcting for ionospheric phase delays is challenging in low-coherence regions such as vegetated valleys (outside the Atacama desert) and the high-altitude Andes. Coastal agricultural zones, such as those near Santiago, also exhibit strong temporal decorrelation, which degrades the applied split-spectrum ionospheric estimation. The default ISCE2 (Rosen et al., 2012) ionosphere correction algorithm applies an adaptive Gaussian filter to the short-wavelength ionospheric phase estimates, weighted by the local coherence raised to the 16th power. This scheme attempts to produce a smooth ionospheric interferogram while preserving local details, and the strong coherence weighting already penalizes low-quality pixels within the filter (Liang et al., 2019). However, problems remain when the interferogram contains several spatially isolated groups of coherent pixels (referred to as connected components). The interferometric phase between such components is likely discontinuous and prone to unwrapping errors; thus, filtering indiscriminately across their boundaries introduces artificial phase gradients throughout the interferogram.

To address the challenging regions where unwrapping errors prevail, we implemented an iterative masking approach based on updated connected components. The standard connected-component outputs from unwrapping algorithms such as SNAPHU or ICU often overestimate the true quality of unwrapping and may fail to capture subtle phase discontinuities (Oliver-Cabrera et al., 2022), particularly under strong multi-looking conditions. Our enhanced masking strategy incorporates several additional screening criteria: pixels with lower- or upper-band coherence below 0.7, elevations exceeding 4.5 km, or those corresponding to water bodies were masked out. The remaining pixels were segmented into isolated patches, we

then update the connected components from the unwrapping algorithm with our enhanced labeling. Only the largest coherent connected component was retained to constrain the ionospheric field.

We subsequently applied iterative gap filling and filtering following the method of Fattahi et al. (2017b). In each iteration, prior to adaptive Gaussian filtering, data gaps were filled using the nearest valid pixel. After filtering, the original values of valid pixels were restored, and only the invalid data were updated in subsequent iterations. Based on testing, two to three iterations are typically sufficient for convergence (Fattahi et al., 2017b). We performed five iterations to ensure stability. The resulting stack of spatially smoothed ionospheric interferograms was then manually inspected to identify and exclude anomalous pairs (see examples in (Liang et al., 2019)). The remaining interferograms were inverted using uniform weighting across all pairs to reconstruct the full time series, which was subsequently used to correct the corresponding displacement fields, following the same processing workflow described in Chapters 2 and 3.

4.3 Method: Static modeling of the finite fault

Slab geometry and the backslip model

We use the Slab 2.0 model (Hayes et al., 2018) together with a polygon outlining the subduction zone on the surface, extending from the trench to the back-arc region down to a maximum depth of 260 km (approximately corresponding to 65°W, which represents the western limit of our mesh). We construct a finite triangular mesh representing the subducting slab interface. The mesh resolution is tuned such that the shallowest patches have an area of $\sim 10^3$ km^2 (corresponding to an edge length of about 30 km), while the deepest patches have an area of $\sim 10^4$ km^2 (edge length of about 90 km).

Historically, the back-slip model (BSM) has provided a convenient framework for modeling subduction coupling (Savage, 1983). The BSM has been applied to many subduction and continental collision settings. However, the conventional BSM carries an important assumption: it neglects the finite thickness of the subducting plate and the flexural stress buildup within the slab (Kanda & Simons, 2010; Kanda & Simons, 2012). In the BSM formulation, the incoming plate is assumed not to subduct during the interseismic period. Instead, the locked portion of the plate interface is represented as a purely normal-faulting dislocation that simulates elastic strain accumulation of the fault locking, while the overriding plate is assumed to

remain unstrained (Savage, 1983).

Kanda & Simons (2010) and Kanda & Simons (2012)) provide a more reasonable kinematic model—the elastic subducting-plate model (ESPM), in which an elastic slab of finite thickness is explicitly considered. In the ESPM, both the lower interface of the slab and the down-dip extension of the upper interface continuously slip at the full plate-convergence rate, while the shallow locked portion does not slip during the interseismic period and only slips coseismically. This configuration better mimics the behavior of megathrusts. Elegantly, the BSM emerges as an end-member case of the ESPM when the plate thickness converges to zero, or equivalently when bending stresses within the subducting plate are fully relaxed either aseismically or episodically at depth. Under these limiting conditions, the ESPM reduces to the familiar representation of an infinitely thin dislocation embedded in an elastic half-space, reproducing the kinematic assumptions of the BSM.

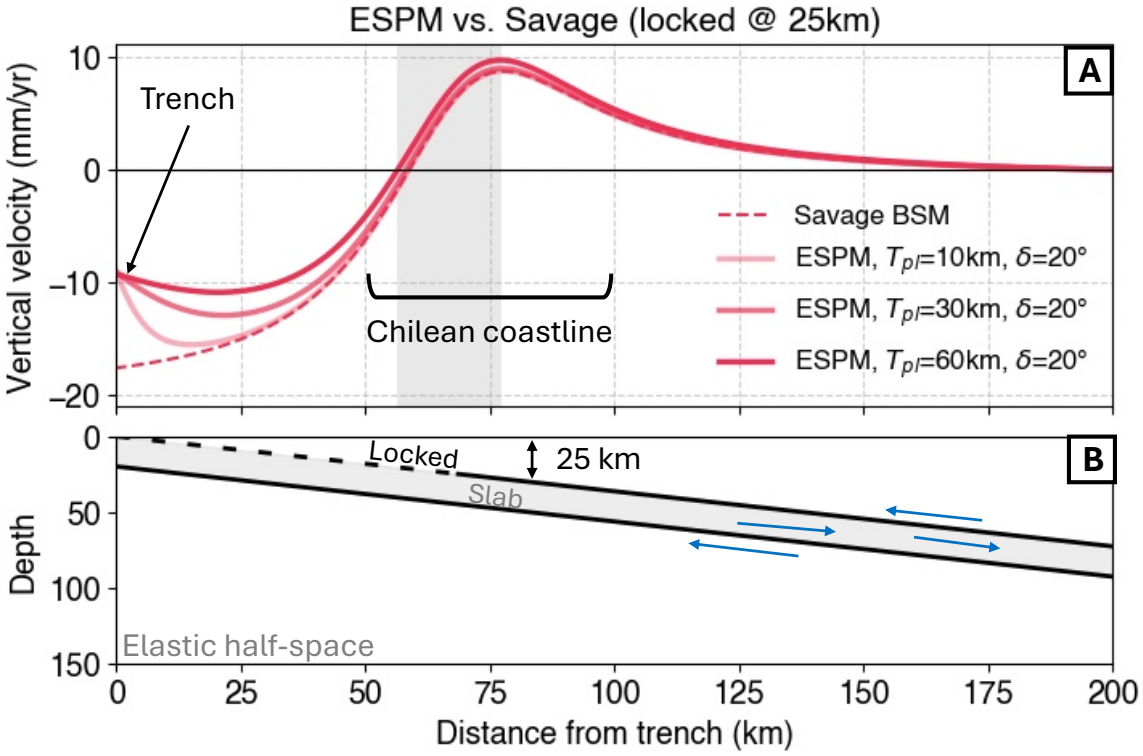

Figure 4.3: **(A)** Forward simulation of locking-induced deformation from a uniformly dipping slab using the Backslip Model (BSM) and the Elastic Subducting Plate Model (ESPM) with varying elastic thicknesses of the subducting plate. **(B)** The schematic picture from the depth. The vertical deformation component is modeled assuming a dip angle of 20° and a uniform locking depth of 25 km. Blue arrows denote the plate convergence direction at a rate of 67 mm yr^{-1}.

Using the BSM tends to produce larger vertical subsidence near the trench than models that account for plate thickness (Kanda & Simons, 2010; Kanda & Simons, 2012). However, detecting such differences requires geodetic receivers located very close to the trench (Figure 4.3), where we compare the BSM and ESPM for a constant-dip slab geometry. The same behavior applies to horizontal deformation components. Along most of the Chilean margin, the coastline lies approximately 70–100 km landward of the trench—too far for InSAR or GNSS observations to clearly discriminate between the BSM and ESPM with the assume elastic thickness of 30 km of the Nazca plate, except in a few locations such as the Mejillones Peninsula. Consequently, we adopt the BSM formulation in this chapter. A full ESPM implementation for the Chilean margin with a more realistic slab geometry can be considered.

Computation of Green's Functions for Static Elastic Deformation

Static Green's functions (GFs) provide the linear relationship between unit slip on fault patches and surface displacements at geodetic observation points. In the most general form, the forward problem is nonlinear, $\mathbf{d} = \mathcal{G}(\mathbf{m})$. However, applications in the static limit for interseismic and coseismic displacements, strain small in an elastic space allows the governing equations become linear with respect to slip. This linearization follows from the elastostatic equilibrium condition $\mu\nabla^2\mathbf{u} + (\lambda+\mu)\nabla(\nabla\cdot\mathbf{u}) = 0$, where λ and μ are the Lame parameters determined by seismic velocities (V_P, V_S) and density ρ through $\mu = \rho V_S^2$ and $\lambda = \rho V_P^2 - 2\mu$. Once the elastic structure is specified, the total displacement field can be represented as a linear superposition of responses to unit sources, $\mathbf{u}(\mathbf{x}) = G(\mathbf{x};\boldsymbol{\xi})\,\mathbf{m}$, where G is the Green's matrix and $\mathbf{m}$ the vector of fault slips. We calculate the Greens function following Zhu & Rivera (2002). The static elastic GFs are computed using the `fomosto` module of `pyrocko`, which interfaces with the `PSGRN/PSCMP` codes of Wang et al. (2003) and Wang et al. (2006). These programs implement the viscoelastic–gravitational dislocation theory of Wang (1999) and solve the elastostatic equations semi-analytically in the spectral domain for a horizontally layered, isotropic Earth. The background model is defined by layer thickness, V_P, V_S, ρ, which together determine the elastic parameters and density structure. For the Chilean margin, we adopt a model extending to 660 km depth, consistent with Duputel et al. (2015) and the local seismic profiles of Husen et al. (1999) (Figure 4.4). This layered model is treated as a purely elastic structure for the Green's function calculation, with no mantle attenuation constraints included.

Within `PSGRN/PSCMP`, the solution exploits cylindrical symmetry in a one-dimensional

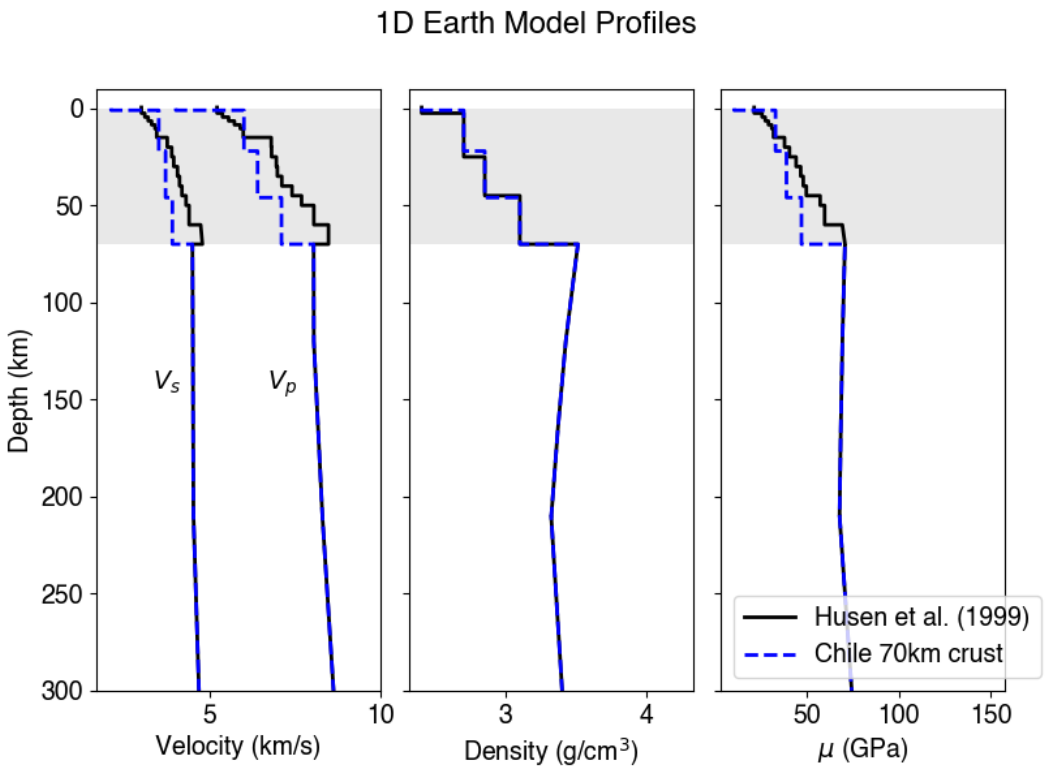

Figure 4.4: One-dimensional Earth model for the central Chile region. The blue dashed line shows the coarse model from Lüth & Wigger (2010), while the black line represents the model of Husen et al. (1999), which is adopted in this study. **Left:** Seismic velocity profile used to compute the Green's functions in a layered elastic half-space. **Middle:** Density structure of the elastic medium. **Right:** Shear modulus profile.

layered medium, so that the response depends only on the source depth z_s and horizontal epicentral distance r. We employ the *elastic10* configuration, which tabulates ten independent displacement–stress basis functions corresponding to the symmetry-reduced derivatives of the Green's tensor required for a complete moment-tensor source Wang et al. (2003) and Wang et al. (2006). We precompute a cylindrical Green's function database extending to 400 km depth (with 2 km vertical spacing) and a radial distance of 4000 km (with 2 km spacing). The GFs database provides displacement responses for strike-slip and dip-slip unit sources at arbitrary receiver depths, which can subsequently be queried for any source–receiver pair along the Chilean megathrust and linearly combined to represent any fault orientation or rake.

For each fault patch in our mesh, moment-tensor point sources are distributed at an approximately 32 km spacing. Depending on the size, each triangle patch are

subdivided by 4 to 64 smaller sub-triangles, each is approximated by a point source. The corresponding Green's functions are queried from the GFs database, rotated according to the local geometry (strike, dip, and rake from the Slab2.0 model (Hayes et al., 2018)), and summed over the patch area. Rather than using piece-wise constant slip for each triangular dislocation patch, we sum the point-source GFs according to the piece-wise linear tent function centered on each triangular node. The tent is a piece-wise linear basis centered on the node and interpolate the distributed point-source GFs from all neighboring triangles to produce a linear slip representation across the mesh. In total, 406 triangular patches form 688 tents (thus 688 nodes at the centers of each tent). The resulting system defines the Green's matrix G, which forms the forward operator in the inversion.

Bayesian Formulation of the Fault Coupling Inversion

We frame the finite-fault slip inversion problem in a Bayesian framework. Let $\mathbf{d}$ denote the observed geodetic data vector (GNSS three-component velocities and InSAR LOS velocity), and let $\mathbf{G}$ denote the Green's function (design) matrix mapping slip and nuisance parameters to predicted displacements at the surface. The unknown parameter vector is

$$\boldsymbol{\theta} = \begin{bmatrix} \mathbf{m}_{\text{slip}} \\ \mathbf{m}_{\text{ramp}} \end{bmatrix}, \tag{4.1}$$

where $\mathbf{m}_{\text{slip}} \in \mathbb{R}^{n_{\text{slip}}}$ are the slip parameters on triangular-tent basis functions, and $\mathbf{m}_{\text{ramp}} \in \mathbb{R}^{n_{\text{ramp}}}$ are the nuisance polynomial ramp parameters that absorb long-wavelength deformation fields.

The most general Bayesian posterior distribution is given by Bayes' theorem:

$$p(\boldsymbol{\theta} \mid \mathbf{d}) \propto p(\mathbf{d} \mid \boldsymbol{\theta})\, p(\boldsymbol{\theta}), \tag{4.2}$$

where $p(\mathbf{d} \mid \boldsymbol{\theta})$ is the likelihood of the observed data $\mathbf{d}$ given model parameters $\boldsymbol{\theta}$, and $p(\boldsymbol{\theta})$ represents prior knowledge or physical constraints.

Likelihood Formulation

Assuming Gaussian observational errors with covariance matrix $\mathbf{C}_d$, and model prediction

$$\boldsymbol{\mu} = \mathbf{G}\boldsymbol{\theta}, \tag{4.3}$$

the likelihood function can be expressed as

$$p(\mathbf{d} \mid \boldsymbol{\theta}) = \mathcal{L}(\boldsymbol{\theta}) \propto \exp\left[-\tfrac{1}{2}(\mathbf{d} - \mathbf{G}\boldsymbol{\theta})^T \mathbf{C}_d^{-1} (\mathbf{d} - \mathbf{G}\boldsymbol{\theta})\right]. \tag{4.4}$$

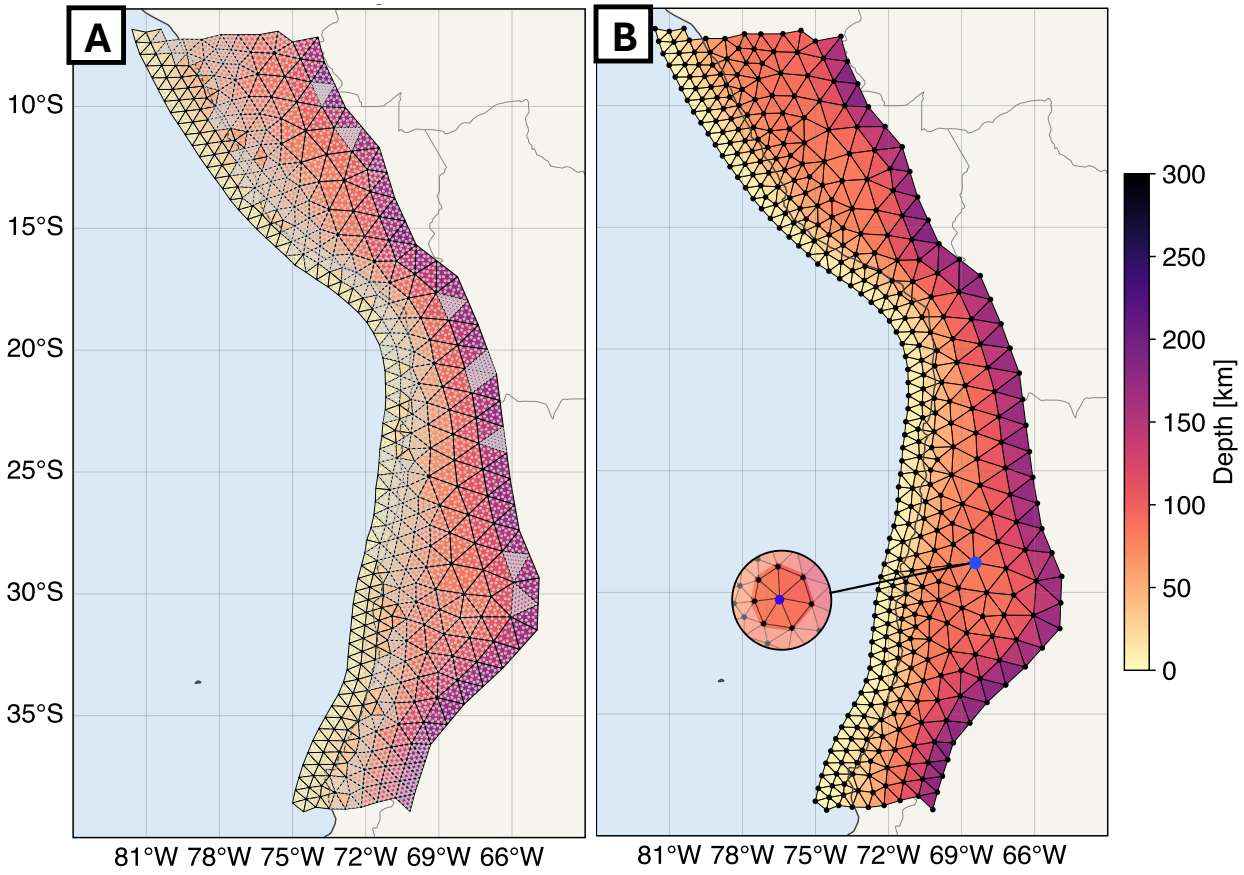

Figure 4.5: Fault geometry and triangular meshing. **(A)** Map view of the subducting slab mesh constructed using the geometry of the Slab 2.0 model, bounded by a customized contour line approximately following the 260 km iso-depth. The solid black lines delineate the triangular fault patches, and grey dots mark the randomly distributed point sources used to subdivide each large triangle into smaller subregions for computing GFs under the moment-tensor point-source approximation. **(B)** The same triangular mesh, highlighting the mesh vertices (nodes) and the piecewise-linear tent functions used to integrate GFs from neighboring triangles to each corresponding node, where the nodal GFs are evaluated for the inversion. The mesh consists of 688 triangular elements and 406 nodes. Hence, instead of 688 piecewise-constant GFs defined on each triangle, we obtain 406 piecewise-linear tent GFs centered at the nodes, based on a total of approximately 9,000 point sources.

Taking the logarithm gives the conventional quadratic misfit form, which we are interested in evaluating during the Bayesian sampling

$$\log \mathcal{L}(\boldsymbol{\theta}) \propto -\tfrac{1}{2}(\mathbf{d} - \mathbf{G}\boldsymbol{\theta})^T \mathbf{C}_d^{-1}(\mathbf{d} - \mathbf{G}\boldsymbol{\theta}), \tag{4.5}$$

assuming a full covariance matrix, $\mathbf{C}_d$, however we want to avoid storing the full covariance and doing the matrix multiplication in the Bayesian sampler since it is too expensive. To simplify this expression and improve numerical stability, we can diagonalize $\mathbf{C}_d$, which is by definition symmetric positive definite, using the Cholesky decomposition with the covariance matrix written as

$$\mathbf{C}_d = \mathbf{L}\mathbf{L}^T, \tag{4.6}$$

where $\mathbf{L}$ is a lower-triangular Cholesky factor (a square-root decomposition of $\mathbf{C}_d$). Multiplying the data equation by $\mathbf{L}^{-T}$ yields the "decorrelated and normalized" data array and Green's function,

$$\tilde{\mathbf{d}} = \mathbf{L}^{-T}\mathbf{d}, \qquad \tilde{\mathbf{G}} = \mathbf{L}^{-T}\mathbf{G}, \tag{4.7}$$

such that the transformed errors have unit variance and are uncorrelated. This operation of decorrelating the correlations in the error by diagonalizing the covariance matrix is sometimes called a whitening transformation, because the error structure becomes independent (white) noise. In this whitened space, the log-likelihood becomes

$$\log \mathcal{L}(\boldsymbol{\theta}) \propto -\tfrac{1}{2}\|\tilde{\mathbf{d}} - \tilde{\mathbf{G}}\boldsymbol{\theta}\|^2, \tag{4.8}$$

which is algebraically equivalent to minimizing the weighted least-squares objective $(\mathbf{d}-\mathbf{G}\boldsymbol{\theta})^T\mathbf{C}_d^{-1}(\mathbf{d}-\mathbf{G}\boldsymbol{\theta})$. The Cholesky decomposition used here is computationally efficient and guarantees positive-definiteness. The Cholesky factor acts as a lower-triangular scaling in the original basis, while the eigen-decomposition performs an equivalent orthogonal rotation and normalization. The likelihood is evaluated in a decorrelated and normalized data space, ensuring that residuals are properly weighted by the observational covariance.

Model priors

We do not invert directly for the coupling coefficient (a scalar between 0 and 1). Instead, we sample the actual slip rate over a broader range from zero to the 120% of the assumed plate rate. Because convergence along the subduction interface is often oblique, it is more natural to resolve the slip into components oriented approximately along the expected rake direction. To conveniently impose positivity on the oblique slip vectors on the megathrust, we rotate the conventional strike–dip basis into an oblique basis defined by rake +45° and rake −45° directions. This parameterization

improves the conditioning of the inverse problem by enforcing positivity in each component while allowing the slip to have a flexible angle around the prescribed convergence direction. Such a formulation is particularly advantageous in regions of oblique convergence, such as Sumatra-Andaman and Chilean megathrusts. Since the Euler pole of the Nazca–South America system provides a well-defined expected rake direction (N78°E), we use this azimuth to rotate GFs between the local strike–dip system and the rake ±45° basis for each patch.

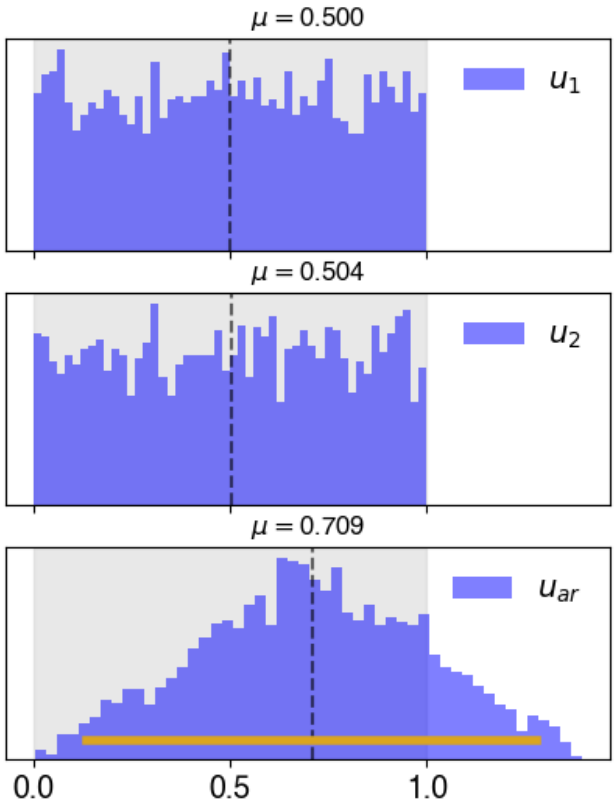

Figure 4.6: **Top** Uniform prior distribution from 0 to 1 for rake +45° direction. **Middle** Uniform prior distribution from 0 to 1 for rake −45° direction. **Bottom** Projected and re-combined along-rake distribution from rake +45° and rake −45° components. The yellow bar indicate the 2-sigma of the combined distribution, centered at the mean, which is approximately 0.71, higher than the mean of the prior in individual component.

Using the rake ±45° formulation, however, introduces a small statistical bias for poorly resolved patches. Geometrically, the sum of two independent uniform priors at ±45° produces an approximately Gaussian-like resultant slip distribution centered at a normalized magnitude of about 0.7 (Figure 4.6). This bias toward higher slip rates arises purely from the choice of parameterization. In contrast, if we had

retained a direct prior on coupling, the unconstrained patches would have a uniform prior centered at a normalized slip of 0.5, corresponding to half coupling relative to the full plate convergence rate.

Slip is defined here as the coupled fraction of the plate convergence, scaled by the convergence rate u_b. For each model patch m_i, we assign a uniform prior:

$$m_i \sim [0, u_b], \qquad \text{for } i \in \mathcal{I}_{\text{interior}}, \tag{4.9}$$

where $\mathcal{I}_{\text{interior}}$ denotes the interior set of nodes that participate in the inversion that are not the boundary nodes. This prior enforces positivity (no backslip opposite to plate motion) and caps the maximum slip rate roughly at the plate convergence rate. To allow the trench to have flexible slip values, the trench nodes also have $[0, u_b]$ prior.

For patches at the boundary of the fault mesh (both lateral and down-dip at 260 km depth), the tent basis functions are "one-sided" and prone to spurious slip due to lack of balancing support across the mesh boundary. To suppress artifacts at these locations, we impose an additional Gaussian penalty centered at zero with a very small variance:

$$m_j \sim \mathcal{N}(0, \sigma^2), \qquad \sigma = 10^{-6}\,\text{m/yr}, \qquad j \in \mathcal{I}_{\text{boundary}}. \tag{4.10}$$

Because the original uniform prior still applies ($m_j \geq 0$), the effective prior distribution is

$$p(m_j) \propto \exp\left[-\tfrac{1}{2}\left(\frac{m_j}{\sigma}\right)^2\right], \quad 0 \leq m_j \leq u_b, \tag{4.11}$$

which is equivalent to a truncated Gaussian prior, extremely narrow around zero, effectively regularizing the boundary nodes to negligible slip while still allowing infinitesimal fluctuations for numerical stability. In other words, the assumption is that deep slip (or slip at the general boundaries, except the trench) is not resolvable and we let it taper to zero to avoid contaminating the inversion in the mesh interior.

To absorb long-wavelength errors in InSAR and GNSS data (e.g., orbital ramps, network translations and rotations), we introduce polynomial ramp parameters. Each ramp coefficient r_k is assigned a weak uniform prior:

$$r_k \sim \text{Uniform}(-1, 1)\,\text{m/yr}, \qquad k = 1, \ldots, n_{\text{ramp}}. \tag{4.12}$$

These nuisance parameters ensure that the inversion does not map long-wavelength trends directly into fault slip.

Posterior and Monte Carlo Sampling

Following the general form of Bayes' theorem in Equation 4.2, the likelihood and prior terms can be expressed in matrix form as

$$L(\mathbf{m}) \propto \exp\left[-\tfrac{1}{2}(\mathbf{d}-\mathbf{G}\mathbf{m})^{\top}\mathbf{C}_d^{-1}(\mathbf{d}-\mathbf{G}\mathbf{m})\right], \tag{4.13}$$

where $\mathbf{m} = [\mathbf{m}_{\text{slip}}^{\top}, \mathbf{m}_{\text{ramp}}^{\top}]^{\top}$. $\mathbf{C}_d$ denotes the data covariance matrix, typically assumed diagonal if observational errors are uncorrelated.

The prior model constraint is written in a consistent quadratic form as

$$P(\mathbf{m}) \propto \exp\left[-\tfrac{1}{2}(\mathbf{m}-\mathbf{m}_0)^{\top}\mathbf{C}_m^{-1}(\mathbf{m}-\mathbf{m}_0)\right], \tag{4.14}$$

where $\mathbf{m}_0$ represents the reference or nominal model within the prescribed physical bounds (e.g., uniform between 0 and u_b), and $\mathbf{C}_m$ is the prior covariance or regularization matrix. In a fully Bayesian treatment where no explicit regularization is applied, $\mathbf{C}_m$ reduces to the identity matrix $\mathbf{I}$.

The Bayesian formulation above can be approached in several ways. A deterministic or frequentists' inversion would seek the model that maximizes the posterior (or equivalently, minimizes the negative log-posterior), leading to an optimization form expressed as a regularized least-squares problem, where the prior information enters as a penalty term (e.g., Tarantola, 2005; Ortega-Culaciati et al., 2021).

The model that maximizes the posterior probability density is equivalently the one that minimizes the cost function

$$\min_{\mathbf{m}} \left[(\mathbf{G}\mathbf{m}-\mathbf{d}^{\text{obs}})^{\text{T}}\mathbf{C}_{\chi}^{-1}(\mathbf{G}\mathbf{m}-\mathbf{d}^{\text{obs}}) + (\mathbf{H}\mathbf{m}-\mathbf{h}^{0})^{\text{T}}\mathbf{C}_h^{-1}(\mathbf{H}\mathbf{m}-\mathbf{h}^{0})\right], \tag{4.15}$$

where $\mathbf{C}_{\chi}$ and $\mathbf{C}_h$ are the covariance matrices of the data and the prior, respectively, and $\mathbf{H}$ is a regularization operator (e.g., the identity, gradient, or Laplacian). Equation (4.15) can be equivalently written in (described in e.g., Ortega-Culaciati et al., 2021) the conventional weighted least-squares form,

$$\min_{\mathbf{m}} \left\|\mathbf{W}_{\chi}(\mathbf{G}\mathbf{m}-\mathbf{d}^{\text{obs}})\right\|_2^2 + \left\|\mathbf{W}_h(\mathbf{H}\mathbf{m}-\mathbf{h}^{0})\right\|_2^2, \tag{4.16}$$

where $\mathbf{W}_{\chi} = \mathbf{C}_{\chi}^{-1/2}$ and $\mathbf{W}_h = \mathbf{C}_h^{-1/2}$ are the data and prior weighting matrices, respectively. This formulation is statistically consistent with the Bayesian framework, where $\mathbf{C}_{\chi}$ and $\mathbf{C}_h$ represent the data and prior covariances. No arbitrary damping parameter is introduced; the trade-off between data misfit and model smoothness is governed entirely by the relative magnitudes of these covariance matrices. Different

choices of the regularization operator **H** correspond to zeroth-, first-, or second-order smoothing, favoring small slip amplitudes, smooth gradients, or smooth curvature in the model.

Such bounded linear least-squares can be solved using standard algorithms implemented in optimization libraries or quadratic programming packages such as `SciPy` or `CVXOPT` (Virtanen et al., 2020; Dahl & Vandenberghe, 2006). These methods provide a single best-fit (maximum-a-posteriori) solution with propagated model errors.

Here, we instead employ a fully Bayesian sampling approach and explore the posterior distribution directly using Markov Chain Monte Carlo (MCMC) techniques (Hastings, 1970). Modern gradient-based samplers such as the Hamiltonian Monte Carlo (HMC) and No-U-Turn Sampler (NUTS) (Neal, 2011; Hoffman & Gelman, 2011) efficiently handle the high-dimensional, correlated parameter spaces typical of geodetic inverse problems. We thus implemented our probabilistic inference using the `PyMC` software (Abril-Pla et al., 2023), which performs adaptive step-size control and automatic differentiation of the log-posterior.

We conducted several sets of MCMC forward samplings of the model parameters (hereafter simply referred to as our inversions) described above. The resulting posterior distributions provide probabilistic estimates of fault slip at each model node. For each fault patch, we represent the slip value by the median of its posterior distribution. The model consists of 406 triangular tent nodes across the entire mesh, and for each node we invert for two components: the rake+45° and rake−45° directions, yielding a total of 812 slip parameters. In addition to the slip parameters, we also have 64 nuisance transformation parameters (InSAR bilinear ramps and GNSS 2D translation plus rotation) to account for reference frame in geodetic datasets.

For each node, the two orthogonal slip components are projected and combined along the nominal rake direction (N78°W of Nazca-South America motion) to obtain the along-rake backslip magnitude. Normalizing the backslip values by the plate convergence rate yields the interplate coupling coefficient of the megathrust. The assumed plate convergence rate is 58 mm yr^{-1}, derived from the 67 mm yr^{-1} Nazca–South America relative motion minus the 9 mm yr^{-1} motion accommodated by the previously proposed Andean Sliver rotation.

Information gain, statistical distance, and divergence

Historically, the concept of model resolution has been used to assess the resolvability of model parameters. In linear inverse theory, the model resolution matrix $\mathbf{R}$ quantifies how well the estimated model $\hat{\mathbf{m}}$ reproduces the true model $\mathbf{m}^{\text{true}}$ under a given regularization scheme (Backus & Gilbert, 1968; Tarantola & Valette, 1982). For a regularized least-squares estimator

$$\hat{\mathbf{m}} = (\mathbf{G}^T\mathbf{C}_d^{-1}\mathbf{G} + \mathbf{C}_m^{-1})^{-1}\mathbf{G}^T\mathbf{C}_d^{-1}\mathbf{d},$$

the corresponding model resolution matrix is

$$\mathbf{R} = (\mathbf{G}^T\mathbf{C}_d^{-1}\mathbf{G} + \mathbf{C}_m^{-1})^{-1}\mathbf{G}^T\mathbf{C}_d^{-1}\mathbf{G}.$$

If $\mathbf{R} = \mathbf{I}$ (where $\mathbf{I}$ is identity matrix), each parameter is perfectly recovered, while off-diagonal elements reflect spatial leakage or trade-offs between neighboring patches. However, $\mathbf{R}$ intrinsically assumes that the observations can be linearly related to a "true" model through $\mathbf{d}^{\text{obs}} = \mathbf{G}\mathbf{m}^{\text{true}}$, neglecting uncertainties in both the data and the forward model (Backus & Gilbert, 1968; Tarantola & Valette, 1982; Ortega-Culaciati et al., 2021).

In practice, $\mathbf{R}$ contains assumptions of our data coverage, geometry, Earth's structure, parameterization of the fault, and parameters smoothing, but it does not provide any measure of uncertainty regarding these assumptions. Thus, while useful for simple linear problems, $\mathbf{R}$ provides maybe only a simplified heuristic view of model resolution (e.g., Ortega-Culaciati et al., 2021, and references therein).

A fully Bayesian framework, on the other hand, yields the complete posterior probability density function $p(\mathbf{m} \mid \mathbf{d})$, which allows one to assess parameter resolvability directly through the information gain between the prior and posterior distributions. Information gain quantifies how much the posterior distribution differs from the prior. In other words, the information gain shows how much the data reduce uncertainty by narrowing the range of plausible model parameters, different from the given prior.

This difference can be measured using statistical divergence metrics such as the Kullback–Leibler divergence (Kullback & Leibler, 1951; Gelman et al., 1995; Sanz-Alonso et al., 2023) or its symmetric variant, the Jensen–Shannon divergence (D_{JS}; Sanz-Alonso et al., 2023).

In information theory, the Shannon entropy of a probability distribution $P(x)$ measures the expected uncertainty (in bits; Shannon, 1948):

$$H(P) = -\sum_x P(x)\ \log_2 P(x).$$

For a fair binary event, $P = (0.5, 0.5)$, the entropy is $H = 1$ bit, representing the maximal uncertainty between two equally likely outcomes. If one outcome becomes more probable, for instance $P = (0.9, 0.1)$, the entropy drops to $H \simeq 0.47$ bits, meaning the uncertainty has been reduced by roughly half. To compare two distributions $P(x)$ and $Q(x)$, the Jensen–Shannon divergence measures their mean information difference:

$$\mathrm{D_{JS}}(P\|Q) = \tfrac{1}{2} D_{\mathrm{KL}}(P\|M) + \tfrac{1}{2} D_{\mathrm{KL}}(Q\|M), \qquad M = \tfrac{1}{2}(P+Q),$$

where D_{KL} is the Kullback–Leibler divergence (Kullback & Leibler, 1951; Gray, 2013). If logarithms are base 2, the D_{JS} is measured in bits and satisfies $0 \leq \mathrm{D_{JS}} \leq 1$. The square root, $d_{\mathrm{JS}} = \sqrt{\mathrm{D_{JS}}}$, defines a true metric distance in probability space. When $\mathrm{D_{JS}} = 0$, the two distributions are identical (no information gain), whereas $\mathrm{D_{JS}} = 1$ corresponds to completely disjoint distributions—the observer gains one full bit of information (complete certainty about which model is correct). Intermediate values quantify partial constraint; for example, $\mathrm{D_{JS}} = 0.1$ (or $d_{\mathrm{JS}} \approx 0.32$) corresponds to roughly 0.1 bit of information gain, meaning the posterior uncertainty has been reduced by about 10%.

A useful approximation relates the D_{JS} to the Hellinger affinity $A = \int \sqrt{P(x)\,Q(x)}\,dx$ (Le Cam, 1986):

$$A \approx 1 - \tfrac{1}{2}\,\mathrm{D_{JS}}(P, Q),$$

so that larger D_{JS} implies smaller overlap between the two distributions. For example, $\mathrm{D_{JS}} = 0.13$ implies $A \approx 0.90$, i.e. the prior and posterior still share about 90% of their probability mass (Figure 4.7).

In our Bayesian megathrust coupling inversion, we apply the Jensen-Shannon divergence (D_{JS}) to quantify where the data meaningfully constrain the slip distribution (Rousset et al., 2016). Empirically, we mask regions where $d_{\mathrm{JS}} < 0.3$, corresponding to a $\mathrm{D_{JS}} = 0.1$. This threshold effectively removes areas too far from the geodetic coverage—such as near the trench and at the northern and southern margins of the Chilean segment—while retaining regions with relatively higher information gain. This approach provides a probabilistically consistent analogue to the traditional resolution matrix, but directly gauged from the posterior distribution.

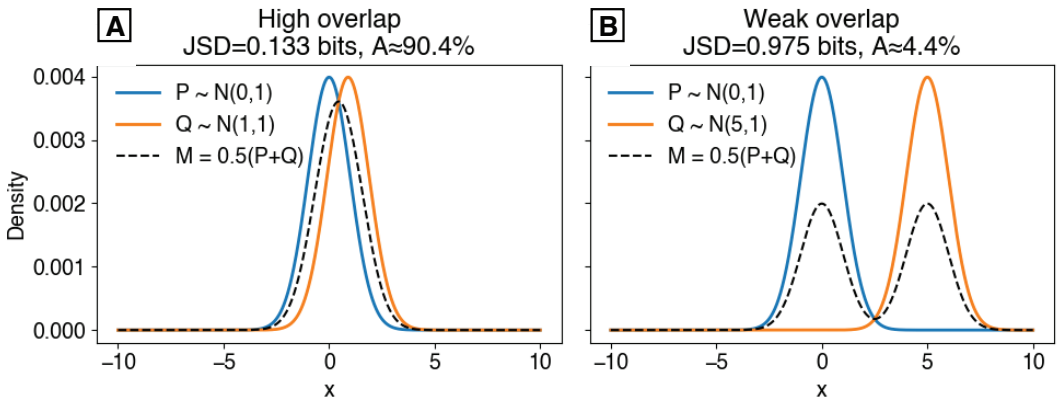

Figure 4.7: The statistical distance between two normal distributions, P and Q, and their mean distribution (dashed line) used in the computation of the Jensen–Shannon divergence (D_{JS}). **Left:** $P \sim \mathcal{N}(0,1)$ and $Q \sim \mathcal{N}(2,1)$. The computed D_{JS} is 0.133 bits, equivalent to a Hellinger affinity of 0.904. The two distributions show substantial overlap and are therefore quite similar. **Right:** $P \sim \mathcal{N}(0,1)$ and $Q \sim \mathcal{N}(5,1)$. The computed D_{JS} is 0.975 bits, equivalent to a Hellinger affinity of 0.0404. The two distributions overlap minimally and are thus highly distinct.

Epistemic Model Error from Fault Dip and Elastic Structure

In addition to observational noise, we aim in future work to quantify epistemic model error arising from uncertainty in the Earth's elastic structure and fault geometry.

Physically, dip errors tend to shift the centroid of deformation and bias the apparent location of interplate locking, whereas uncertainties in the elastic structure primarily scale the predicted deformation field through variations in the shear modulus μ and Poisson's ratio ν. In an isotropic elastic half-space, the displacement scales approximately as $\mathbf{u}(\mathbf{x}) \propto \mu^{-1}\mathcal{F}(\nu, \text{geometry})$, so an underestimation of μ amplifies the displacement field, while changes in ν modify the horizontal–vertical partitioning. This study adopts a fixed reference structure of the Earth and fault geometry (Husen et al., 1999; Hayes et al., 2018). Future implementations could incorporate the above formalism to propagate structural and geometric uncertainties into the full posterior covariance (Duputel et al., 2014; Ragon et al., 2018; Ragon et al., 2019).

4.4 Results: Secular deformation due to the locking of the megathrust interface

This section describes the secular deformation derived from InSAR data averaged over the period 2014–2025. We fit a linear trend to each pixel's time series, combined with annual and semi-annual sinusoidal terms to account for seasonal oscillations

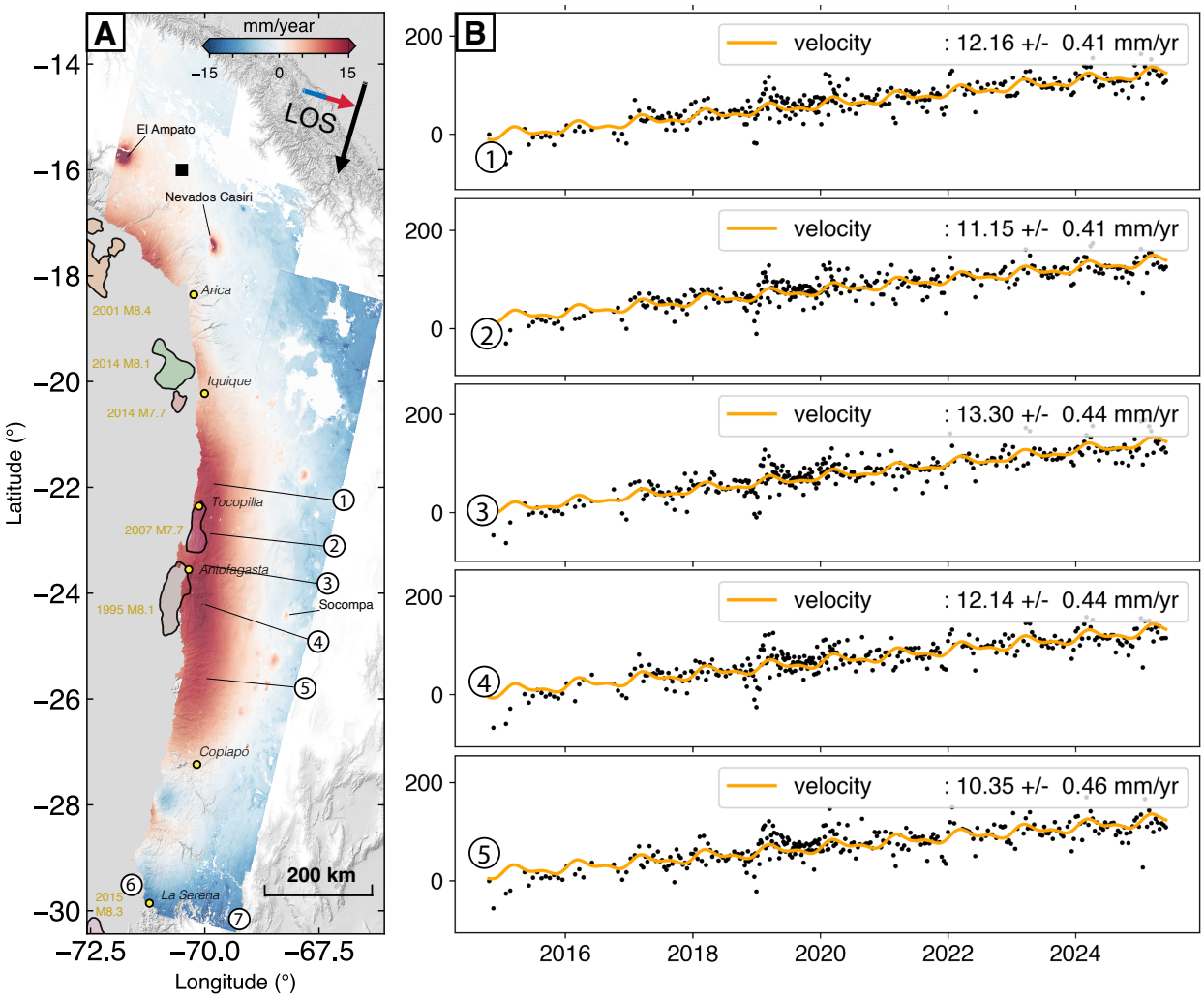

Figure 4.8: InSAR line-of-sight (LOS) deformation in Central Chile from the Arica bend in the north to La Serena in the south. Velocity relative to the square box, in the souther Peru near the foothill of the frontal arc. **(A)** Secular LOS velocity estimated from descending track 127, 54, 156 from west to east. LOS displacements are defined as positive if motion is toward the satellite (see satellite LOS symbol in panel (A)). Megathrust earthquakes happened in the last three decades are marked. Recent volcanic unrest including Socompa (Chile-Argentina border), Nevados Casiri (Peru-Chile border), and El Ampato (southern Peru). **(B)** LOS displacement time series and corresponding linear velocity fits at locations along the coastal plain.

in the InSAR phase time series. The formulation of the temporal functions follows the approach described in Chapter 2 and Chapter 3 (Hetland et al., 2012; Minchew et al., 2017; Zhong et al., 2023). However, the present analysis focuses solely on the secular velocity field; the analysis and physical interpretation of the seasonal components is beyond the scope of this chapter.

Several segments of the Chilean megathrust have experienced large earthquakes in recent decades, and consequently, estimates of the interseismic trend are significantly affected by the residual coseismic and postseismic deformation associated with these events. We initially attempted to account for early-cycle deformation within each InSAR velocity track by fitting temporal functions that include both step and logarithmic terms in regions affected by major megathrust events (2014 Mw 8.1 Iquique and 2015 Mw 8.4 Illapel). However, this procedure is limited, particularly in modeling the long-lived postseismic signals. Introducing additional transient parameters globally across all pixels leads to severe trade-offs with the secular rate estimates, especially in inland areas where transient deformation is negligible. We acknowledge that more sophisticated, scale-aware approaches could be employed to model these signals, for example, fitting the time-series with different sets of basis function that varies in radius from the earthquake epicenter or explicitly model the rheological relaxation in the mantle. These are beyond the scope of this chapter.

To mitigate the contamination from such transients, we instead visually inspected the InSAR time series and excluded intervals dominated by the rupture and subsequent relaxation of the major earthquakes. Specifically, we removed the early-stage deformation associated with the 2015 Mw 8.4 Illapel (e.g., Klein et al., 2017) and 2014 Mw 8.3 Iquique (e.g., Duputel et al., 2015) earthquakes. After truncating approximately three years of postseismic deformation following each event (after which the deformation time series manifests as a linear trend), the remaining signals are assumed to represent the quasi-steady interseismic behavior during the later stage of the earthquake cycle. Under this assumption, fitting a linear secular trend provides a first-order approximation. We note, however, that for a characteristic mantle wedge viscosity at the order of 10^{17} – 10^{18} Pa s under a single Maxwell relaxation model and for large coseismic slip amplitudes, postseismic relaxation can persist for decades with an almost monotonic, near-linear temporal evolution that is difficult to distinguish from steady interseismic locking (Trubienko et al., 2013; Guo et al., 2019; Luo et al., 2025). Hence, our approach should be regarded as a pragmatic simplification rather than an exhaustive correction for all viscoelastic or afterslip transients.

InSAR velocity fields

In this section, I present the results of the secular velocity field along the entire Andean megathrust margin. Between the Arica Bend (~ 16°S) and Copiapó (~ 28°S) in central Chile, this ~1000 km-long segment has not experienced any great

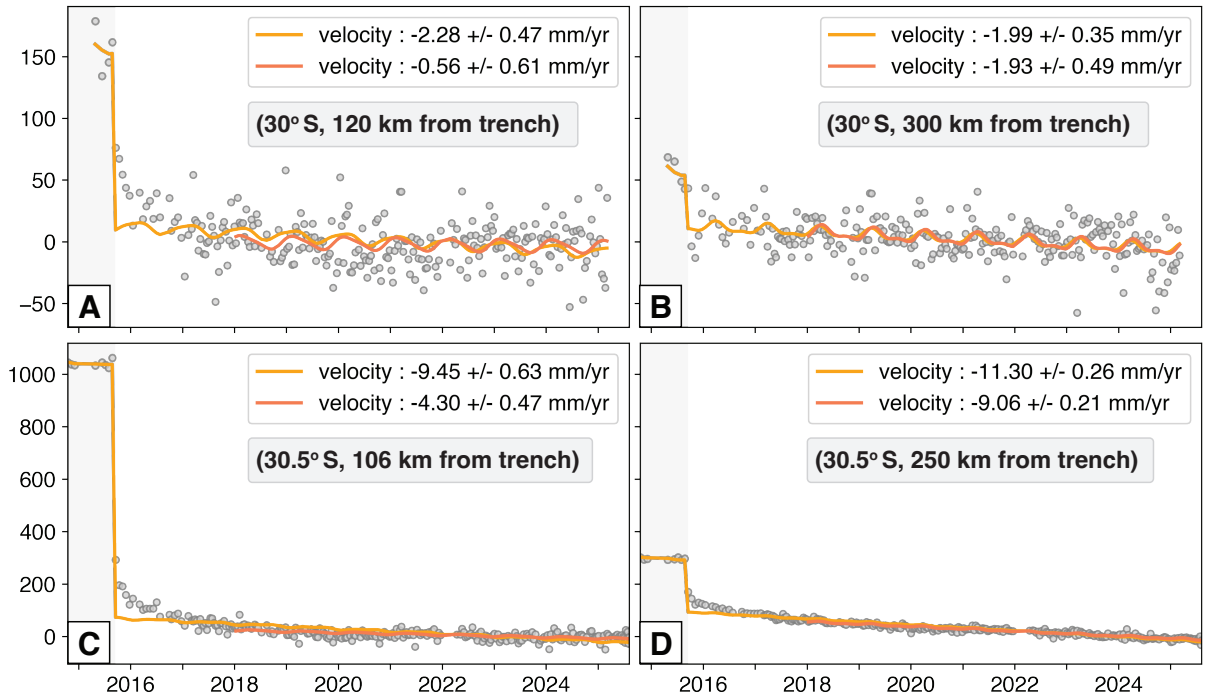

Figure 4.9: Descending track displacement time series in proximity to the 2015 Mw 8.4 Illapel earthquake (number 6 and 7 in Figure 4.8). The orange line shows the temporal function fit to the data, consisted of secular velocity, annual and semi-annual periodics, a step function at the time of the coseismic event, and a logarithmic relaxation term to capture postseismic deformation immediately following the earthquake. The dark orange line is the model fit to the data since January 2018. **(A)** Time series at 30°S, 120 km landward from trench. **(B)** Time series at 30°S, 300 km landward from trench. **(C)** Time series at 30.5°S, 106 km landward from trench. **(D)** Time series at 30.5°S, 250 km landward from trench.

($M_w > 8$) earthquakes in the past three decades. Therefore, the observed geodetic deformation provides a reasonable approximation of the interseismic, quasi-steady-state deformation (Figure 4.8). The deformation is characterized primarily by uplift and shortening of the coastal plain relative to stable South America. This interseismic signal, resulting from locking along the subduction interface, extends up to ~200 km inland from the coast toward the volcanic arc, expressed as positive LOS velocity (ground motion toward the satellite), particularly evident in descending-track observations. Relative to the foothills of the frontal arc, the LOS velocity reaches its maximum near the Tocopilla and Antofagasta region, with values up to ~14 mm yr^{-1}. By combining ascending and descending track observations, the estimated quasi-vertical uplift in this zone is approximately 12 mm yr^{-1}.

Near Tocopilla and Antofagasta (around 23°S), where strong interseismic strain is evident from plate locking, the coastal plain exhibits pronounced positive LOS motion in the InSAR data, exceeding 12 mm yr^{-1} relative to the foothills to the east (Figure 4.8). In contrast, regions influenced by significant co- and postseismic transients, such as those associated with the 2015 M_w 8.4 Illapel earthquake (30–31°S), display more complex temporal behavior (Figure 4.9). We do not currently quantify how much of the long-lasting postseismic signal from the Illapel earthquake contributes to the apparent plate-locking component.

In addition to the megathrust deformation, multiple volcanic and non-tectonic processes contribute to localized vertical ground motion across the Andes (Figure 4.8A), including inflation at El Ampato, Socompa Liu et al., 2023 since 2023 and the Nevados Casiri since 2013 (Popescu et al., 2024; Popescu et al., 2025), as well as deformation associated with the Salar de Uyuni, Salar de Atacama and so on (Pritchard, 2003; Ruch & Walter, 2010; Ruch et al., 2012). Broader geodetic surveys in the volcanic arc regions provide regional context for these observations (Pritchard & Simons, 2002; Pritchard & Simons, 2004; Biggs et al., 2014; Biggs et al., 2022). The perturbations from volcanic inflation, salt-flat uplift and subsidence, deep intraslab earthquakes, and moderate crustal events—are left uncorrected. Their spatially confined nature and limited long-wavelength bias are expected to have minimal impact on the overall secular velocity field and on the near-trench megathrust coupling models derived from it.

In general, the descending-track velocities follow the expected pattern associated with shallow megathrust locking, with the largest interseismic strain concentrated between the Arica Bend and La Serena, where the coastline is oriented roughly perpendicular to the plate-convergence direction (Figure 4.10). Exceptions occur in a few regions, most notably near Illapel (south of 29°S) and Copiapó, where persistent slow-slip activity has been identified (Klein et al., 2018b; Donoso et al., 2021; Socquet et al., 2024; Münchmeyer et al., 2025).

Because of the opposing sensitivities of the LOS to horizontal and vertical components of deformation, the ascending-track velocities generally show weaker signals. In regions west of the hinge line—closer to the trench—subsidence and landward motion combine constructively, producing negative LOS displacements (e.g., near Mejillones at 24°S, Chañaral at 26.2°S, and Sarco at 29°S). Farther inland, east of the hinge line, uplift and landward motion partially cancel, reducing the LOS velocity amplitude. Regions around La Serena and Illapel, the velocity estimates

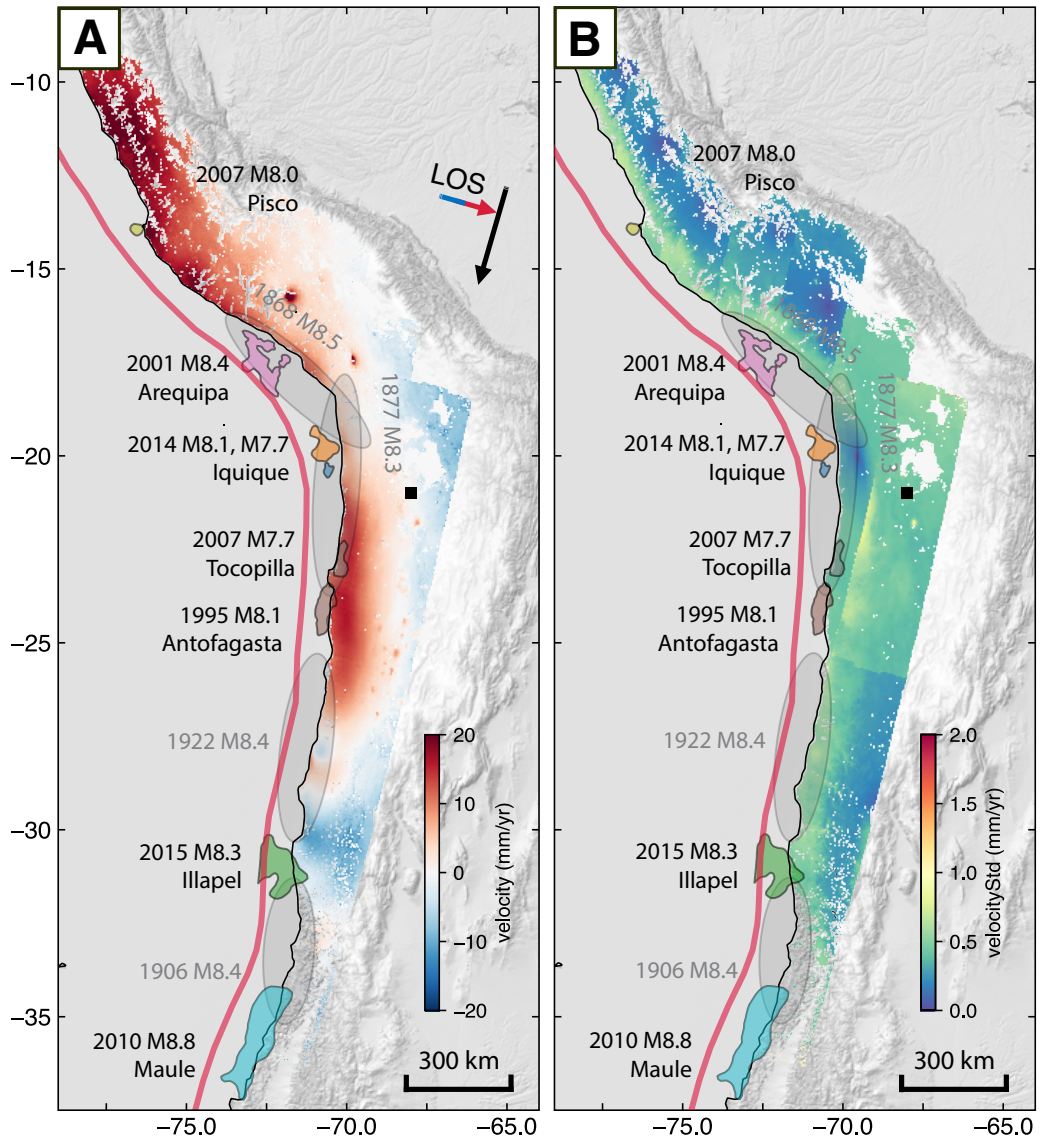

Figure 4.10: Satellite line-of-sight (LOS) velocity for all descending tracks, mosaicked together after correcting for constant offsets between neighboring tracks. **(A)** LOS velocity fields for all descending tracks from Peru to south-central Chile. **(B)** Uncertainty (1σ) of the LOS velocity estimates. The polygons marks the recent coseismic rupture controus and the extent of pre-instrumented earthuqakes described in Table 4.1.

may still be influenced by large-scale ongoing postseismic response in the mantle, and thus are less representative of steady interseismic locking. In these regions, the uplift signal weakens and many areas instead exhibit negative LOS displacements (Figure 4.11A).

Not all parts of the Chilean and Peruvian margins are characterized by arid, decorrelation-free conditions. Ascending track 18, covering northern Peru and the southern Illapel region, suffers from substantial gaps in the interferometric network (1.5–2 years) and strong decorrelation caused by vegetation near Santiago and by steep topography and moisture variability along the Peruvian coast. Consequently, the uncertainty of the velocity estimates in these areas is considerably higher than in other datasets (Figure 4.11B), and conservative quality masking was applied prior to inversion.

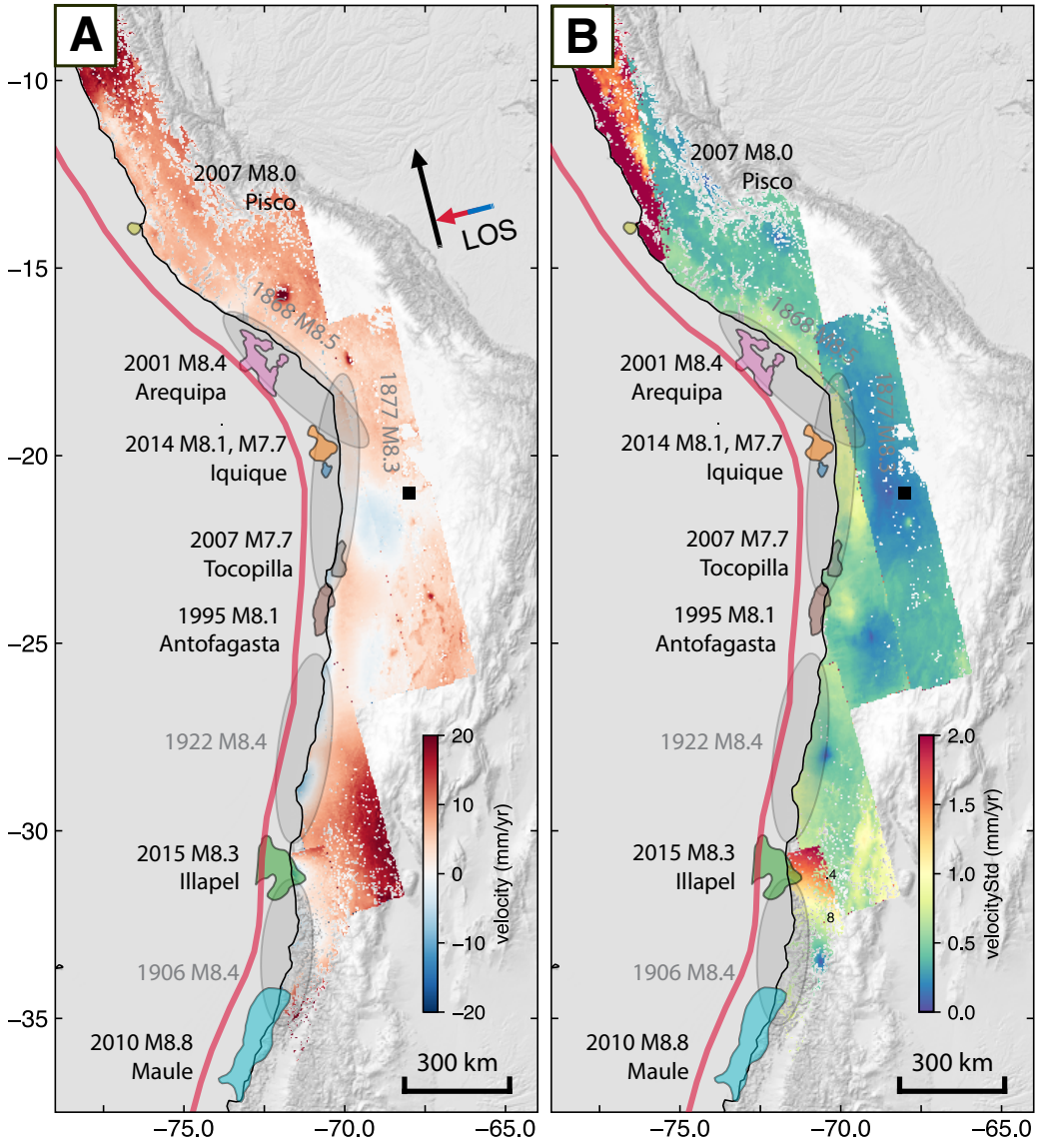

Figure 4.11: Satellite LOS velocity for all ascending tracks, shown in the same format as Figure 4.10.

4.5 Results: Geodetic Coupling Distribution

We perform Bayesian inversions of interseismic deformation along the Chilean margin, testing a suite of model configurations. These include: (1) models with shallow (250 km) versus deep (600 km) down-dip extents; (2) models with and without a tapering constraint that forces slip to zero at the down-dip edge; and (3) inversions using separate GNSS-only, InSAR-only, and joint GNSS–InSAR datasets. Results for all configurations are shown in Figures 4.12–4.14. Each inversion provides estimates of the interplate coupling coefficient, which is expressed as the normalized backslip in the plate-convergence direction along the entire slab interface. Coupling values near one represent fully locked patches; values near zero indicate creeping regions. We also compute the statistical divergence between the prior and posterior distributions to quantify the information gain in each model, allowing us to assess the contribution and complementarity of the different datasets.

Our GNSS- (Figure 4.13A, B), InSAR- (Figure 4.14E, F), and joint-inversion (Figure 4.13C, D) models reveal broadly consistent first-order patterns of interplate coupling along the Chilean megathrust. The posterior distributions of coupling from all model configurations indicate shallow coupling (hereafter defined as < 60 km) on the plate interface. Despite their overall agreement at the macroscale, the models constrained primarily by GNSS data exhibit sharper, more localized variations in coupling, whereas those derived solely from InSAR data display smoother and more laterally continuous patterns. This contrast stems from the intrinsic observational characteristics of the two techniques. The lower uncertainties of continuous GNSS time series yields a more heterogeneous posterior model that fits the observations tightly—reflected in generally higher Jensen–Shannon divergence values for the GNSS-only inversion. Conversely, the spatially correlated and larger-magnitude noise inherent to InSAR, dominated by tropospheric and orbital residuals (Sudhaus & Jónsson, 2009; Lohman & Simons, 2005), acts as an implicit regularization through the data covariance matrix C_d, steering the posterior toward smoother fields closer to the prior mean. Nevertheless, the dense spatial sampling of InSAR provides superior coverage, effectively capturing along-strike continuity where GNSS stations are sparse. The resulting information gain surface from InSAR exhibits more gradual spatial variation (Figure 4.14F), with fewer abrupt transitions between well- and poorly-constrained regions compared to the GNSS-only solution (Figure 4.13B).

The shallow, highly coupled zone (above ~60 km depth) is pervasive along most

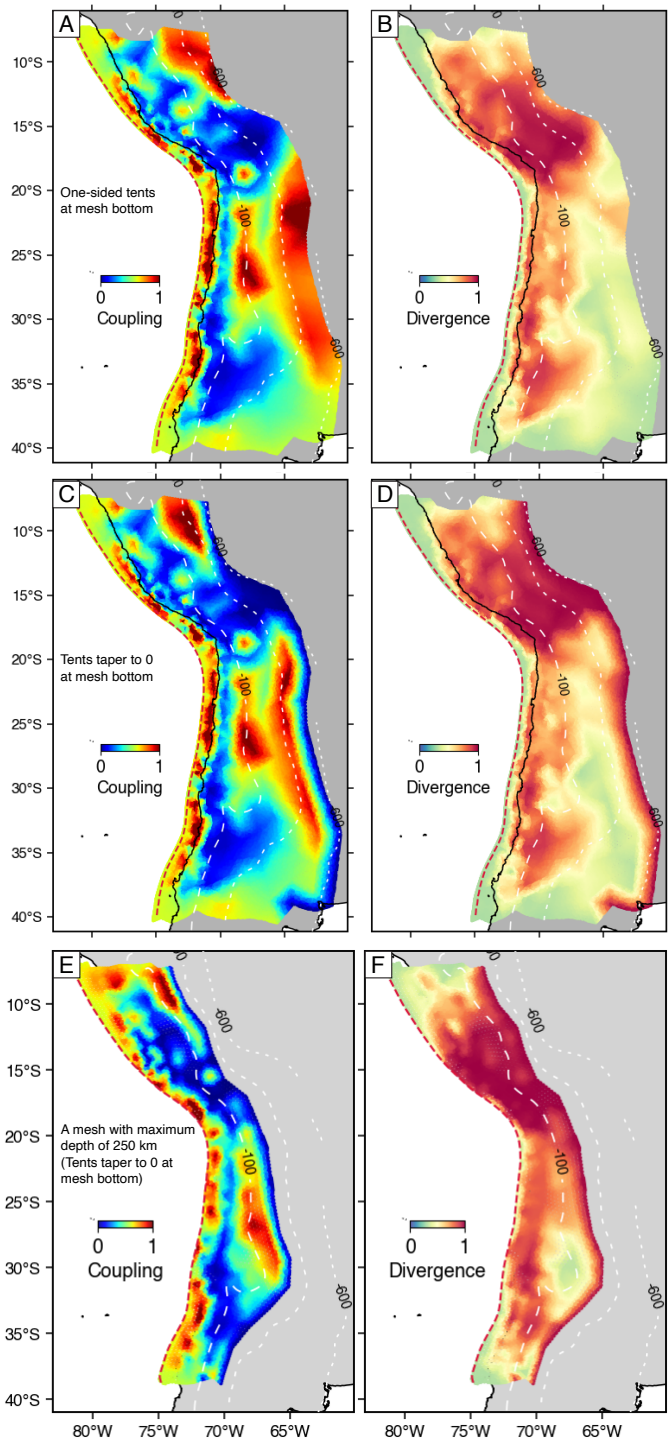

Figure 4.12: Posterior coupling coefficient from joint GNSS and InSAR inversion. Depth contours show the trench axis (0 km, red dashed), 100 km, 300 km, and 600 km depths (white dashed) based on Slab 2.0 model (Hayes et al., 2018). **(A,C,E)** Coupling coefficient. **(B,D,F)** Jensen–Shannon divergence (D_{JS}) between prior and posterior probability density functions, showing Bayesian information gain. **(A,B)** Inversion with tent function allowing slip at the bottom edge of the slab mesh. **(C,D)** Inversion with tent function tapered to zero at the bottom edge of the slab mesh. **(E,F)** Inversion with tent function tapered to zero at the bottom edge, where the mesh bottom is at 250 km depth.

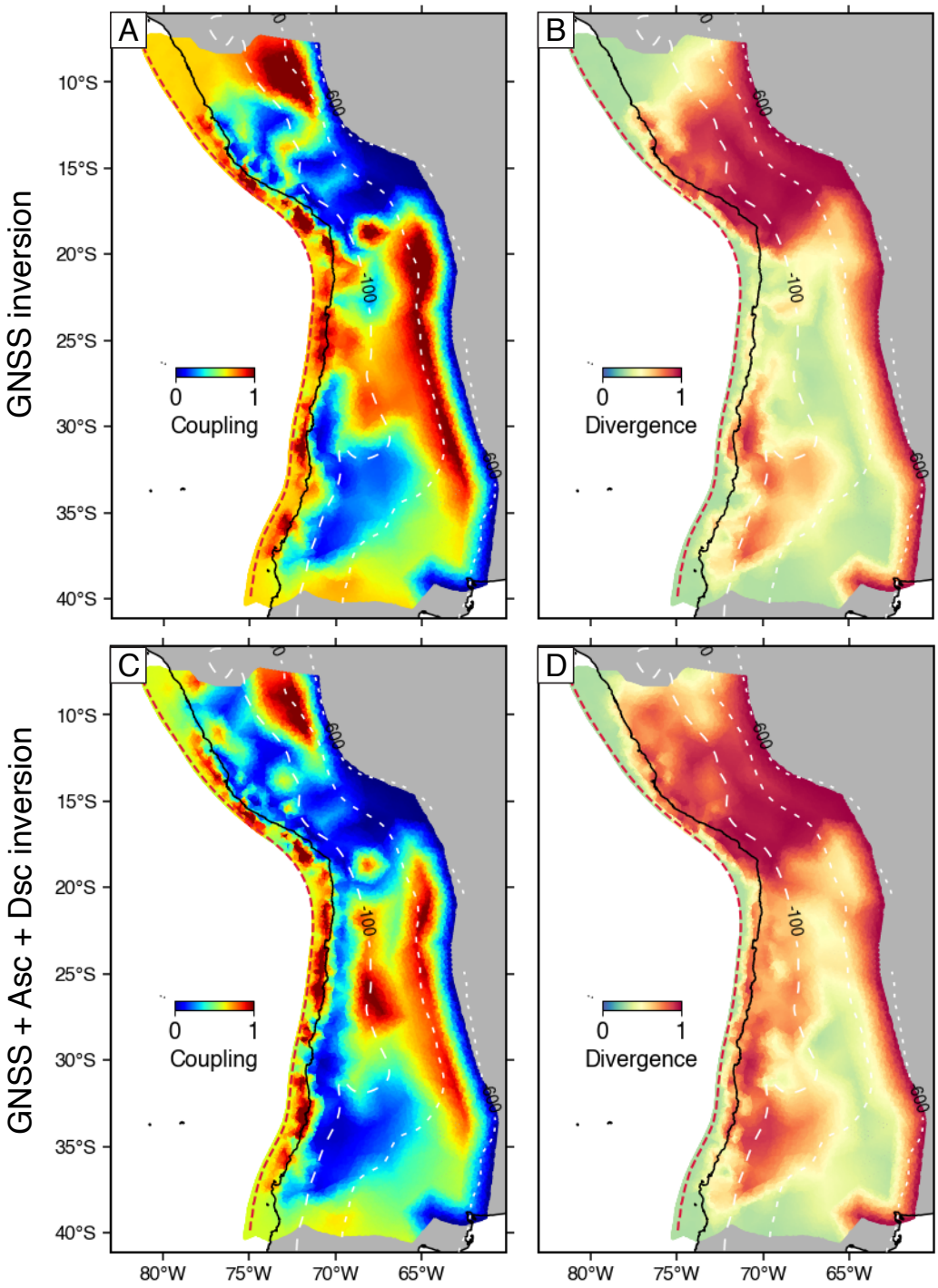

Figure 4.13: Same as Figure 4.12. **(A,B)** GNSS-only inversion results. **(C,D)** Joint GNSS and InSAR inversion (ascending and descending tracks).

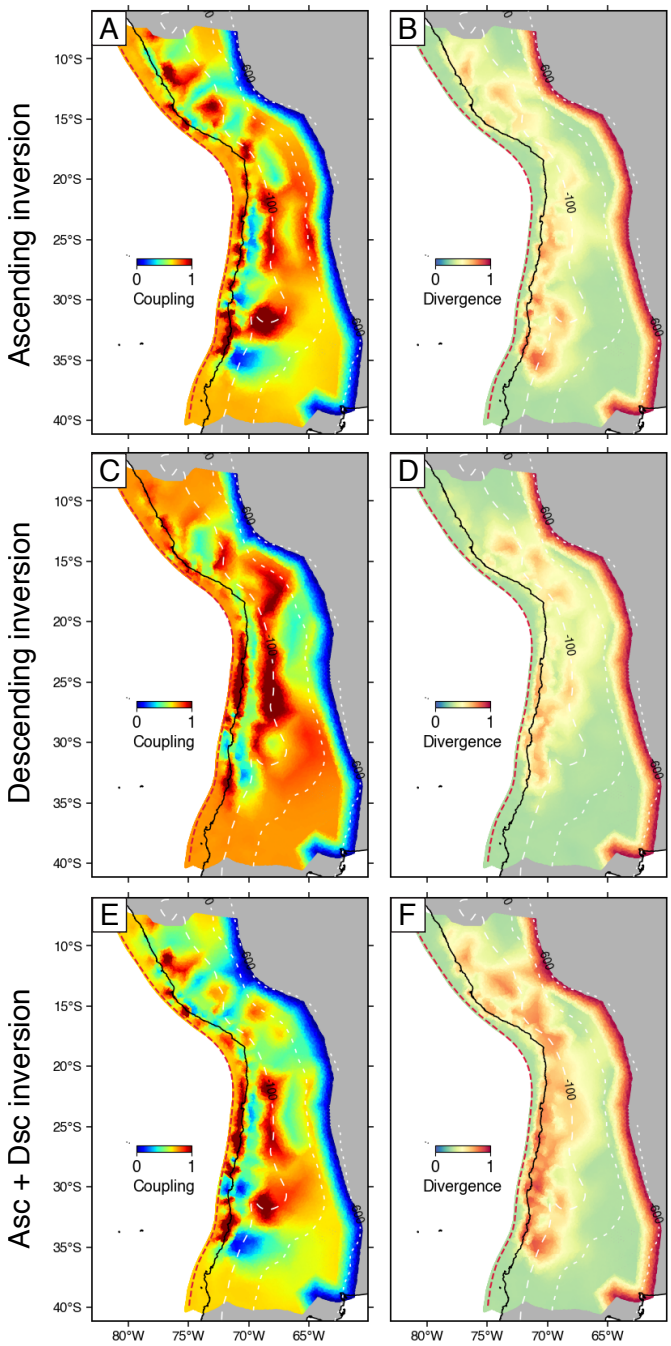

Figure 4.14: Same as Figure 4.12. **(A,B)** Ascending InSAR data only. **(C,D)** Descending InSAR data only. **(E,F)** Combined ascending and descending data.

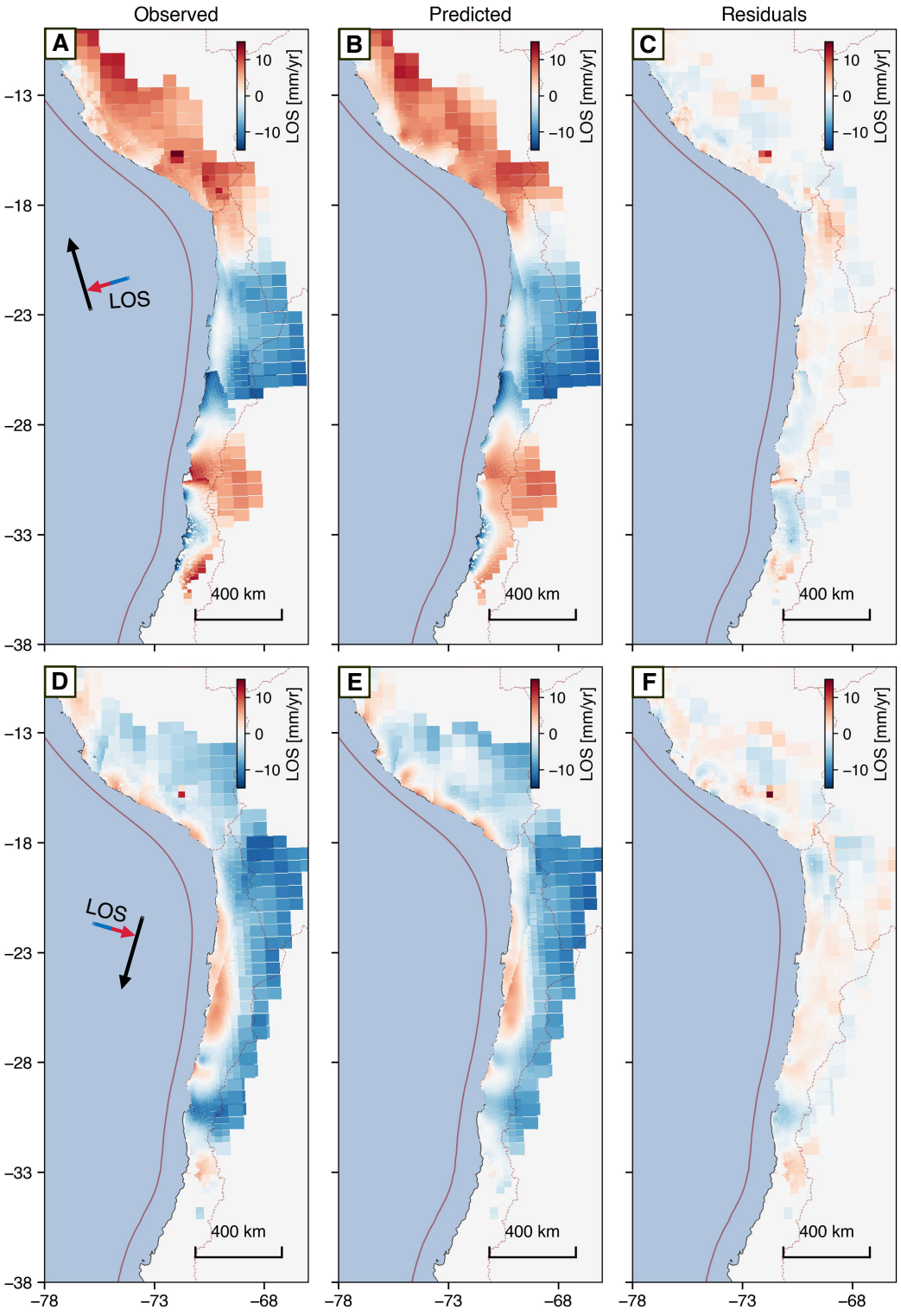

Figure 4.15: InSAR LOS velocity, model fit, and residuals for ascending (A, B, C) and descending (D, E, F) tracks. LOS vectors for ascending and descending tracks are shown as arrows in panels A and D, respectively. The BSM coupling model includes backslip over the entire mesh. Estimated bilinear empirical polynomials and arbitrary constant offsets have been removed from each track. For visualization purposes, median values have been subtracted from both observed and model-predicted fields.

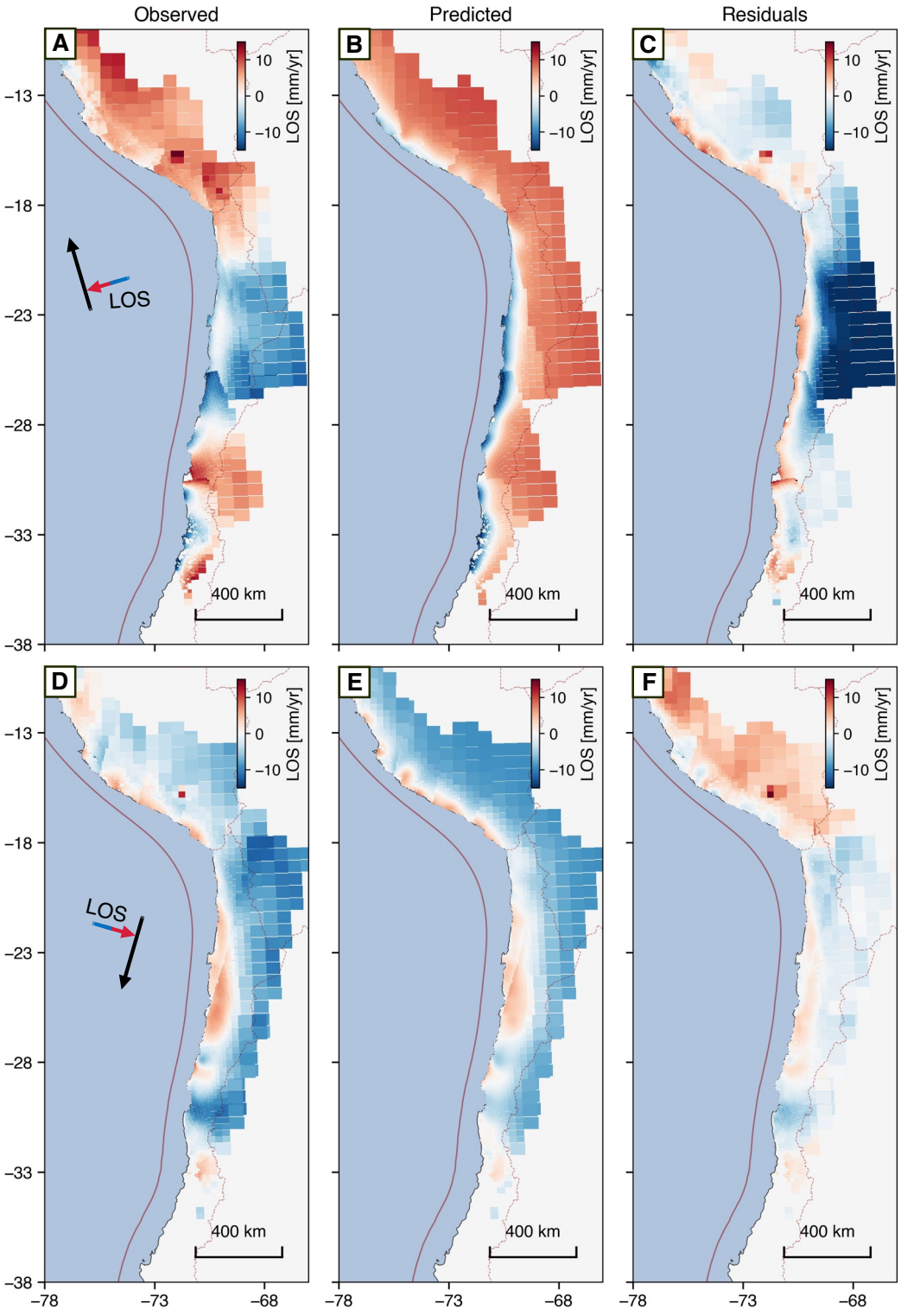

Figure 4.16: Same as Figure 4.15, except that the BSM coupling model prediction includes only shallow backslip (depths < 60 km). The largest residuals occur in the ascending tracks to the east, near the backarc Subandes (between 20°–28° S and east of 72.5° W).

of the megathrust between 14°S and 36°S, with localized sections exhibiting intermediate to low coupling coefficients. Inversions of GNSS, ascending InSAR, and descending InSAR datasets yield similar results, revealing consistent along-strike variations in shallow coupling (Figure 4.13–4.14). Although the very shallowest part of the interface off-shore appears less coupled, we later show that resolution is limited in the immediate near-trench region (top ~20 km of the slab, corresponding to within ~60–70 km of the trench). A particularly consistent and important observation is that the down-dip termination of the shallow coupled zone aligns closely with the coastline, which overlies the slab interface at a depth of approximately 30–50 km.

At depths greater than 60 km, high coupling appears in two distinct zones: one near ~100 km and another below 300 km, extending to the base of the model mesh (Figure 4.12A,B). Both ascending and descending InSAR data require a high-coupling zone spatially confined around 100 km depth between 20°S and 30°S, while GNSS data support strong coupling from ~300 km down to 600 km between 18°S and 36°S. Since the deeper coupling zone coincides with the bottom edge of the slab mesh, it could be contaminated by edge effects where the Green's functions are truncated. To minimize this, we apply a slip-tapering constraint through a strong Bayesian prior that regularizes slip toward zero at the bottom boundary nodes, allowing the tent basis functions to taper slips linearly to zero. This constraint shifts the bottom high-coupling zone upward from the mesh boundary, concentrating it near ~300 km depth (Figure 4.12C,D). In contrast, when the slab mesh extends only to 250 km depth, edge effects and the two coupling zones merge into a single band at 100–150 km depth, making it difficult to distinguish from different origins (Figure 4.12E,F). Thus, although a 600 km mesh extends beyond depths at which the slab behaves elastically, the larger model domain provides the necessary degrees of freedom to separate interfering deformation signals at long wavelengths. These intermediate and deep coupling bands have minimal impact on near-trench deformation but accommodate long-wavelength velocity gradients hundreds of kilometers inland, primarily near and behind the Andean arc, as we will discussed in the Discussion section.

Our backslip model extending down to 600 km depth provides an adequate fit to the geodetic data. For visualize the observations, model fits, and residuals, we removed a bilinear ramp and constant offset for each individual InSAR dataset, and subtracted the mean value from the ascending and descending mosaics separately (Figure 4.15).

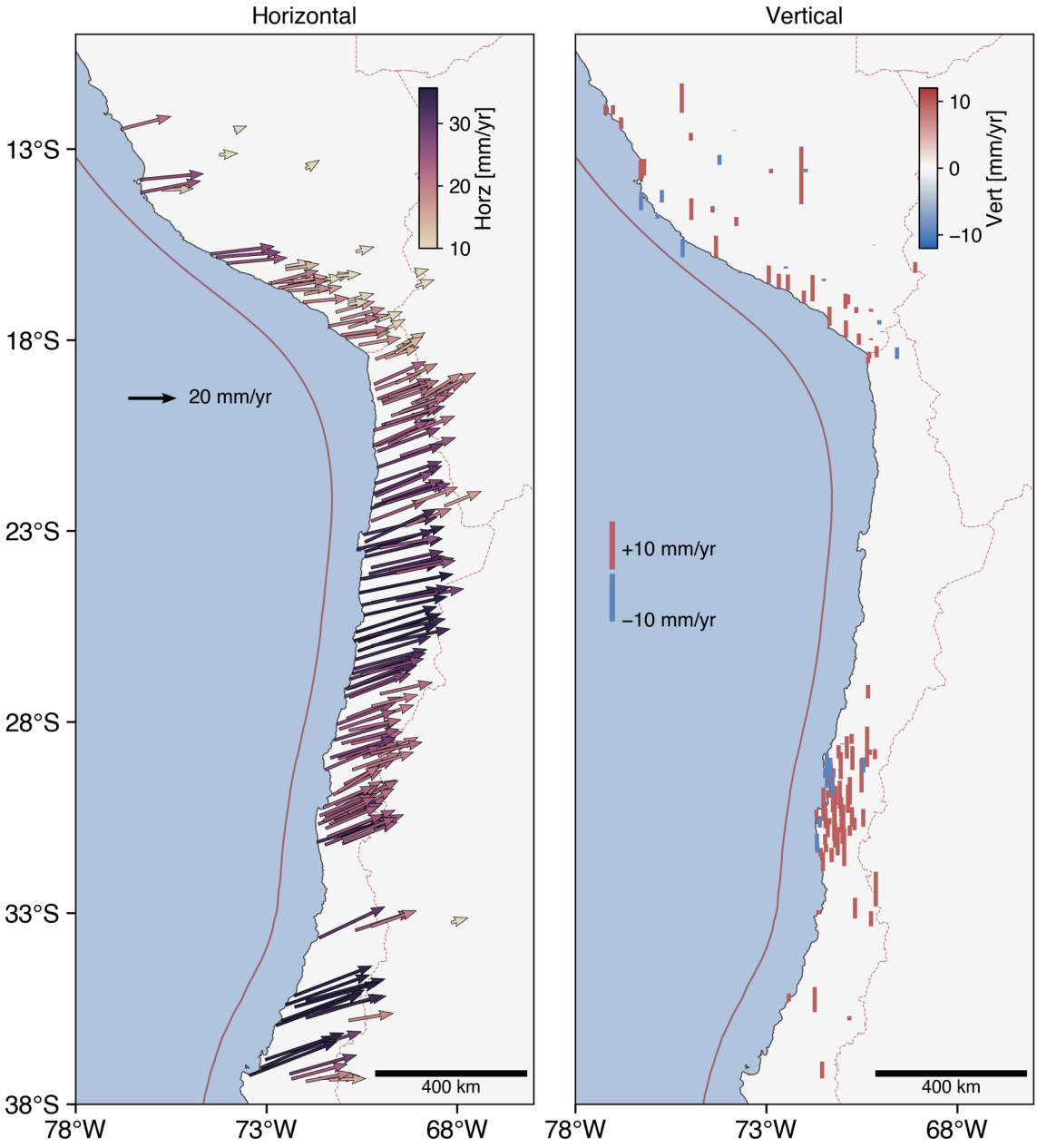

Figure 4.17: Observed GNSS horizontal (left) and vertical (right) velocities across the Chile subduction zone. For clarity, only every other horizontal station is plotted to reduce vector overlap, while all available vertical measurements are shown. Note that vertical velocity estimates are unavailable at many stations.

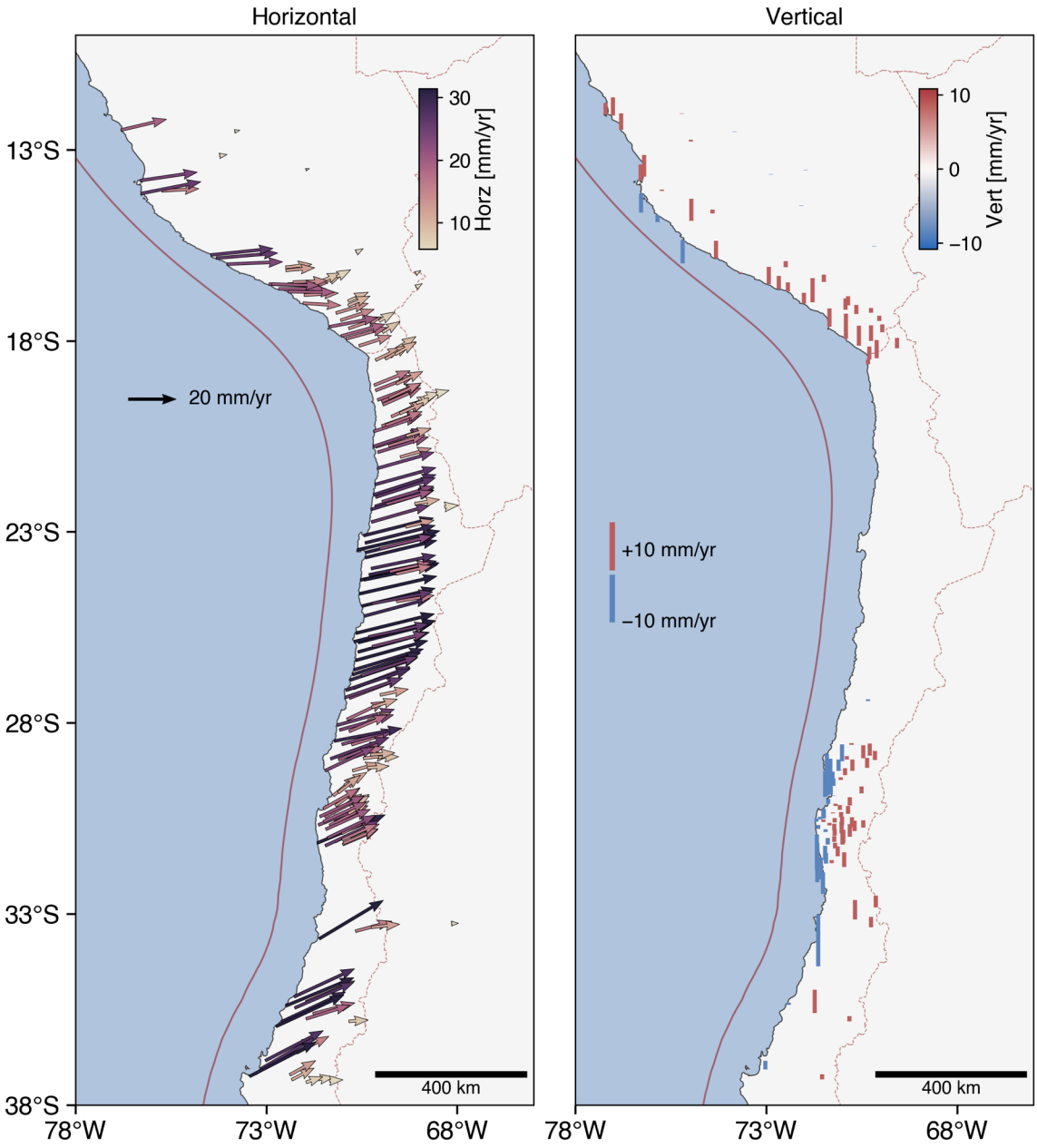

Figure 4.18: Predicted GNSS horizontal (left) and vertical (right) velocities from the shallow interseismic locking model, computed using the back-slip model (BSM) with slip constrained to depths shallower than 60 km. Predictions are evaluated at all GNSS station locations.

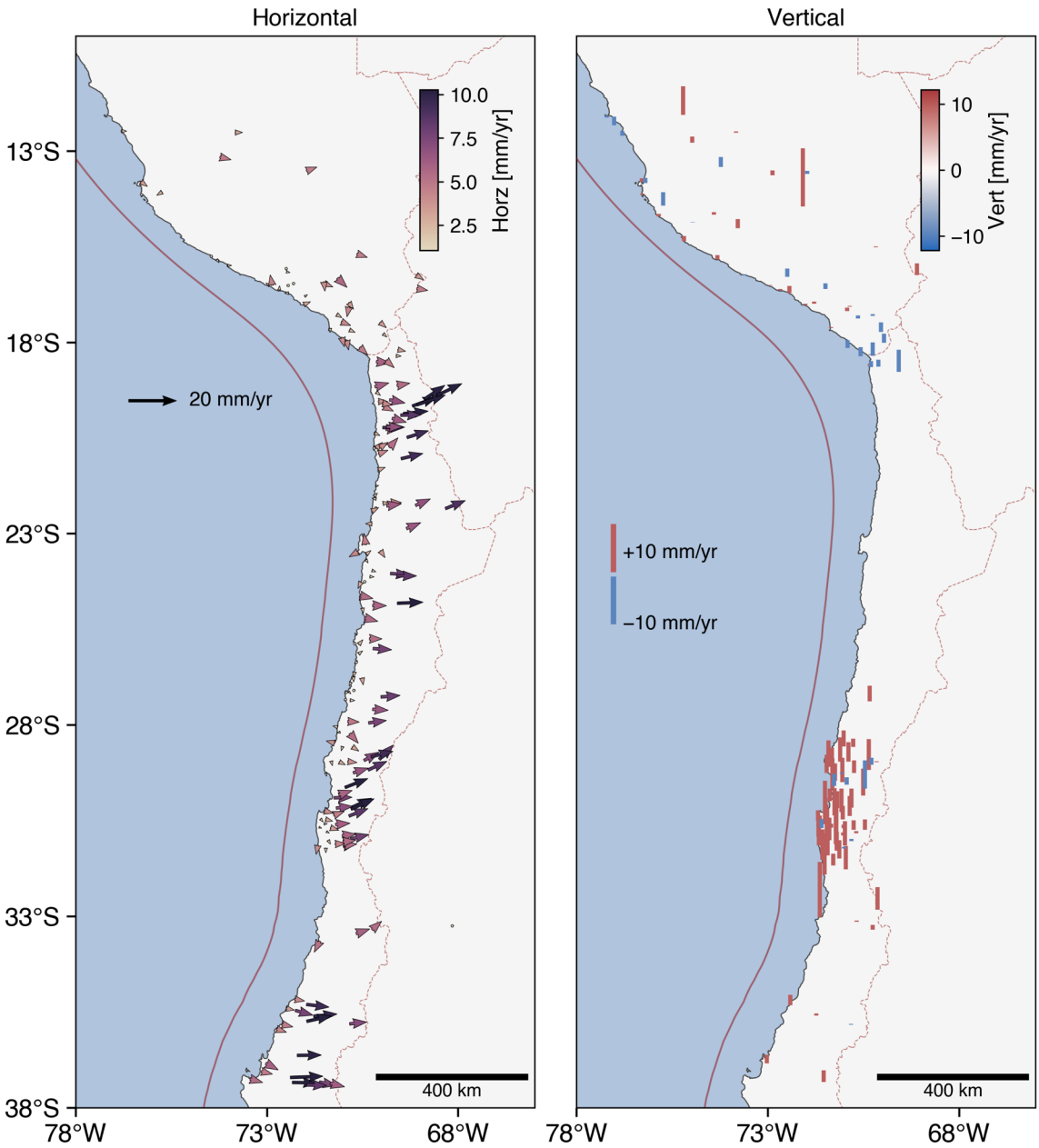

Figure 4.19: GNSS velocity residuals after removing the contribution from shallow (<60 km) megathrust locking. The residual field highlights long-wavelength deformation components not captured by the shallow coupling model.

Aside from localized uplift at El Ampato, no major systematic residuals remain.

To isolate lithospheric megathrust deformation from longer-wavelength signals originating in the backarc or at greater depths, we directly compare predictions from the full slab model with those produced by shallow backslip alone (i.e., setting all deeper backslip values to zero). We define the shallow zone as the upper 60 km, approximating the average lithosphere–asthenosphere boundary in the upper plate (e.g., Yuan et al., 2000; Gilbert et al., 2006). This comparison helps to separate the interseismic slip-deficit field from broader, non-megathrust contributions to surface deformation.

The predicted LOS velocities from shallow coupling consist of two main deformation components: (1) horizontal eastward shortening of the upper plate that decays inland (Armijo et al., 2010; Métois et al., 2016; Jolivet et al., 2020), and (2) vertical motion that transitions from trench-proximal subsidence to inland uplift (e.g., Kanda & Simons, 2010; Béjar-Pizarro et al., 2013). These components project with opposite signs onto the ascending and descending LOS geometries (positive is motion toward the satellite): eastward motion is negative in the ascending track and positive in the descending track, while subsidence is negative in both. Their superposition generates the characteristic LOS patterns. In the ascending track, coastal subsidence and landward motion reinforce, producing a dynamic range from −16 to 10 mm/yr (Figure 4.16B). Farther inland, uplift opposes the horizontal motion, diminishing the LOS signal. In the descending track, the landward component initially cancels subsidence and later aligns with uplift, yielding a smoother transition from 5 to −8 mm/yr (Figure 4.16E).

Significant residuals remain when only shallow slip is considered. For the descending InSAR data, a broad misfit is evident in the backarc, with $\sim 4mm/year$ positive residuals in southern Peru and negative $\sim 2-3mm/year$ residuals in northern-central Chile (Figure 4.16F). The ascending data show positive $\sim 4mm/year$ residuals along most of the coast and a significant negative residual (up to 1 cm/year) in the backarc of northern Chile (20°S–28°S).

The GNSS velocities show a consistent landward motion exceeding 20 mm/year across the Peru-Chile coast (Figure 4.17). The shallow coupling model reproduces this pattern but systematically underestimates its magnitude by several mm/year (Figure 4.18). Sites near the Coastal Cordillera show landward residuals of nearly 8 mm/year. A residual rotation pattern is observed around the Arica bend, with counter-clockwise rotation in southern Peru and clockwise rotation in northern Chile

(Figure 4.19). Near the Illapel region, the residual horizontal velocities are complex, showing seaward motion immediately at the coast rotating to northeastward motion inland (up to 4–5 mm/year), accompanied by widespread uplift. This complex pattern is likely influenced by postseismic deformation following the 2015 Illapel earthquake Klein et al. (2018a) and Luo & Wang (2021).

The final joint InSAR–GNSS coupling model is shown with information-based masking. We apply three Jensen–Shannon divergence thresholds ($D_{JS} > 0.2$, 0.3, and 0.5) to the median posterior coupling (Figure 4.20), with higher thresholds imposing stricter masks. Even under the most conservative criterion ($D_{JS} > 0.5$), much of the offshore region out to 50–60 km remains constrained, except near $\sim 20°$S, just south of the Arica Bend, where the coastline lies farther from the trench and GNSS coverage is lacking. For subsequent analyses we adopt $D_{JS} > 0.33$ unless noted otherwise. A robust feature across all thresholds is that the down-dip limit of locking aligns with the coastline, or at $50 - 60$ km depth. High coupling also coincides with major historical ruptures—including the 2001 M_w 8.4 Arequipa, 2014 M_w 8.1 Iquique/Pisagua, 1995 M_w 8.0 Antofagasta, 2015 M_w 8.3 Illapel, and 2010 M_w 8.8 Maule earthquakes, whereas reduced coupling appears near the Arica Bend and the Illapel segment. The along-strike profile of mean coupling between 10–60 km depth (using $D_{JS} > 0.33$; Figure 4.21) agrees well with the model of Métois et al. (2016).

4.6 Discussion

Coupling distribution, seafloor morphology, and historic earthquakes

The spatial distribution of interplate coupling along the Chilean subduction zone inferred from our joint inversion (Figure 4.20) broadly agrees with previous kinematic models based on GNSS observations (Métois et al., 2012; Métois et al., 2013; Métois et al., 2014; Métois et al., 2016; Klein et al., 2018a; Lovery et al., 2024). Several robust coupling features emerge consistently between these models and ours (Figure 4.21). Reduced coupling near La Serena (~30°S), between 24°S and 26°S near Taltal, Baranquilla (~27.5°S), and immediately south of the Mejillones Peninsula. In contrast, a strongly coupled domain is evident between the Paranal and Chañaral segments (24°–26°S), suggesting an asperity capable of accumulating substantial elastic strain. This particular segment has historically had limited GNSS coverage (Métois et al., 2013; Métois et al., 2014). By merging campaign GNSS with dense InSAR constraints, our inversion improves spatial coverage and coherently resolves this heterogeneous coupling pattern.

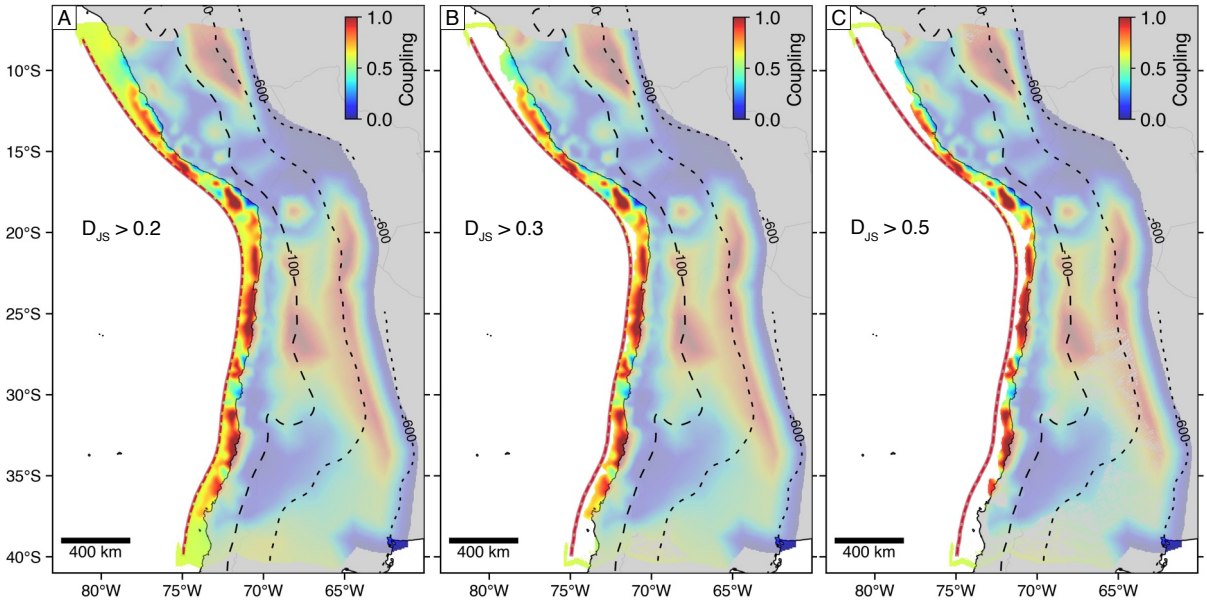

Figure 4.20: The final joint inversion model for interseismic coupling (derived from combined GNSS and InSAR datasets spanning the period 2010–2015). Spatial distribution of the coupling on the subducting slab along Peru-Chile margin, ranging from 0 (fully creeping) to 1 (fully locked). Three coupling maps are the same joint-inversion results, but with different D_{JS} divergence masking. From **(A)** to **(C)**: $D_{JS} > 0.33$, $D_{JS} > 0.5$, and $D_{JS} > 0.75$, respectively. The on-shore coupling model fades beneath the land for visualization purpose. The inset curves show along-strike mean coupling as a function of latitude, computed for the depth range 20–40 km. Red is from our model with 2σ range of coupling values within along-strike latitude bins. The mean coupling model from Métois et al. (2016) is plotted as the blue curve.

From Lima to Pisco (north of 15°S), the trench lies far offshore, and the sparse distribution of coastal GNSS stations, combined with low InSAR coherence along the humid Peruvian margin, limits our ability to constrain interseismic coupling. Southward from Marcona to Arequipa (16°–17°S), coupling strengthens markedly. Although the rupture zone of the 2001 M_w 8.4 Arequipa earthquake exhibits locally reduced coupling, this likely reflects persistent postseismic relaxation and incomplete relocking. Farther south, across the Arica Bend (~19°S), where two major 19th-century tsunamigenic ruptures overlapped, coupling decreases again, indicating a partially creeping interface. This creeping behavior may be structurally controlled by subducting bathymetric anomalies: the Nazca Ridge underthrusts the Arequipa region, whereas the Arica Bend receives the subduction of the Iquique Ridge and the Nazca Fracture Zone.

The 2014 M_w 8.1 Iquique mainshock area near Pisagua remains highly coupled. From Pisagua (19°S) to Chañaral (26.5°S), the megathrust forms a major coupled segment, with coupling ratios commonly exceeding 0.7. Within this zone, modest local minima occur near the 2014 M_w 7.7 Iquique aftershock area and the Mejillones Peninsula. This region, lying between the 1995 Antofagasta and 2007 Tocopilla ruptures, coincides with an intersegment boundary that experienced significant aseismic afterslip following the 1995 M_w 8.1 Antofagasta earthquake (Pritchard & Simons, 2006), consistent with velocity-strengthening behavior and incomplete interseismic relocking. South of Antofagasta, into the Taltal segment, the coupling decreases again (Figure 4.21).

In central Chile, the most prominent low-coupling patch lies near La Serena (30°S). This latitude region has been noted as the Pampean flat slab where the Nazca plate subducts sub-horizontally at ~100 km depth (Jordan et al., 1983; Jordan & Allmendinger, 1986) (Figure 4.22), a geometry that has the potential to cease arc magmatism (Kay et al., 1991) and redistribute seismogenic coupling between near-trench shallow interface and the slab far inland due to buoyancy (Gutscher, 2002; Gans et al., 2011). A more direct spatial correlation for this localized low-coupling anomaly may come from its agreement with the subduction of the Challenger Fracture Zone (CFZ), a major oceanic structural feature that could alter the frictional properties of the plate interface independently of or in conjunction with the flat slab's dynamic effects (Yáñez et al., 2002; Contreras-Reyes & Carrizo, 2011; Gans et al., 2011). CFZ has long been recognized as a structural barrier that likely governs the southern termination of the 2015 M_w 8.4 Illapel earthquake. Similar correlations between seafloor bathymetric highs and weakly coupled regions are evident near Baranquilla and Taltal, where the subducted Copiapó Ridge and Sala y Gómez Ridge (or Taltal Ridge) enter the trench. The consistent alignment of low-coupling zones with subducting ridges and fracture zones suggests that topographic irregularities on the downgoing plate modulate the mechanical and maybe hydrological behavior of the shallowest portion of the megathrust interface (Fisher et al., 2003; Wang & Bilek, 2011).

The Copiapó segment, in particular, exemplifies this interplay between structure, fluids, and transient deformation. Recent geodetic and seismic observations reveal a depth-partitioned slow slip regime: long-term, deep transient slips in the transition zone (~40–60 km; e.g., 2014–2016, 2020) and short-term, shallow events within the seismogenic zone (~10–25 km; in 2023). Both are interpreted as fluid-assisted

aseismic slip episodes modulated by subducted ridge topography, with shallow events often closely associated with seismic swarms (Klein et al., 2018b; Socquet et al., 2024; Münchmeyer et al., 2025). These transients indicate a mechanically and hydraulically segmented interface, where migrating fluids and local rheological contrasts modulate the transition between locked, creeping, and episodically slipping domains. The recurrence of such slow-slip phenomena along subducting topographic highs underscores their dual role as both structural asperities and fluid conduits that influence the depth extent, segmentation, and temporal evolution of interseismic strain accumulation and release along the Chilean megathrust (Figure 4.21).

Between Illapel and Santiago (32°–35°S), where our model overlaps with the northern limit of the 2010 M_w 8.8 Maule rupture, we infer high coupling values of 0.8–0.9—significantly higher than the ~0.5 reported in previous studies. This discrepancy likely reflects the long-lived postseismic relaxation of the Maule earthquake being partially mapped into our elastic dislocation model. Southward toward Concepción, which coincides with the main coseismic slip zone of the Maule event, coupling decreases to roughly half-locked levels, consistent with earlier results (Métois et al., 2016).

Across the margin, one persistent feature is that the down-dip limit of locking follows the coastline, coinciding with the 30–60 km depth range of the plate interface. This relationship, often recognized in earlier studies, reflects the structural geometry of the wedge and may record long-term inelastic uplift of the overriding plate (Béjar-Pizarro et al., 2013; Jolivet et al., 2020). Moreover, recent and historical great earthquakes lie within or partially overlap with high-coupling areas, including the 2001 M_w 8.4 Arequipa, 2014 M_w 8.1 Iquique/Pisagua, 1995 M_w 8.0 Antofagasta, 2015 M_w 8.3 Illapel, and 2010 M_w 8.8 Maule events. Their correspondence with the strongly locked segments is consistent with the notion that the coupling distribution inferred here delineates the principal seismogenic zones capable of hosting future megathrust ruptures (e.g., Moreno et al., 2010; Chlieh et al., 2011; Avouac, 2015; Métois et al., 2016).

Locking signals masked by large postseismic relaxation

As emphasized by previous studies (Métois et al., 2012; Métois et al., 2014; Métois et al., 2016; Klein et al., 2021), deriving a consistent interseismic velocity field along the Chilean margin remains challenging because each segment is at a different

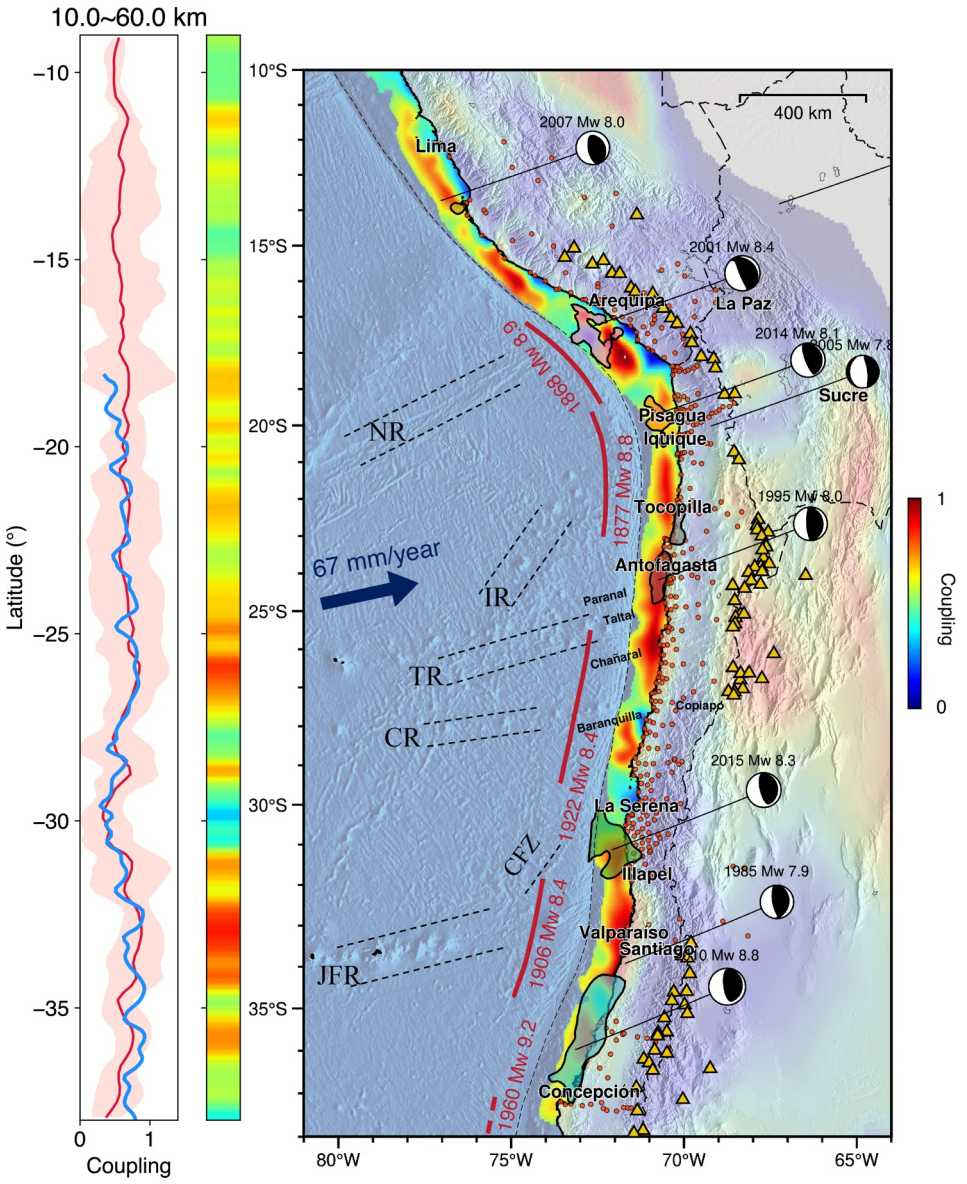

Figure 4.21: Final coupling model across the Chilean subduction zone. The red profile shows the along-strike mean coupling as a function of latitude, computed for a depth range of 10 to 60 km. The shading denotes the $1-\sigma$ scatter within the latitude bins. Blue profile is the mean coupling derived from Métois et al. (2016). The colorbar to the side of the profile shows our same mean coupling displayed in gradient color. The map on the right is thecoupling model. Historic earthquake rupture areas from early and pre-20th-century events are outlined, and recent $M_w > 8$ earthquakes within the last 30 years are shown with their GCMT focal mechanisms (Dziewonski et al., 1981; Ekström et al., 2012). Major bathymetric and structural features are annotated: NR– Nazca Ridge, IR–Iquique Ridge, TR–Taltal Ridge (or Sala y Gómez Ridge), CR–Copiapó Ridge, CFZ–Challenger Fracture Zone, and JFR–Juan Fernández Ridge. Red dots indicate GNSS sites used in this study, and yellow triangles mark Holocene volcanoes from the Global Volcanism Program database.

stage of the seismic cycle. Although the InSAR record begins in 2014–2015, much of the region continues to be affected by long-lived postseismic relaxation following the 2010 Maule and 2015 Illapel earthquakes, whose effects extend north to La Serena (29.5°S). Between 32.5°S and 29°S, deformation associated with the Illapel event persists well beyond 2018, indicating that the crust has not yet returned to a steady interseismic state. To achieve a clean interseismic signal; future work must explicitly model and correct for postseismic relaxation or rely on pre-event GNSS data for this region.

In contrast, postseismic contamination in the northernmost part of the study area, from Lima to Arequipa, is likely minor, except locally around the 2001 Mw 8.4 Arequipa rupture. There, the secular velocity field should represent a reliable approximation of quasi-steady interseismic deformation. Similarly, between the Arica Bend to Antofagasta, the postseismic transients from the 2014 Iquique and 1995 Antofagasta earthquakes were shorter-lived and of smaller amplitude. South of that toward the Atacama Desert (19°–28°S), the margin has remained comparatively quiescent, allowing for better the late-seismic cycle deformation to be captured with greater fidelity.

Reference-frame motion and long-wavelength consistency

At long wavelengths, both GNSS and InSAR observations are sensitive to the reference-frame motion relative to stable plate interiors (Kreemer et al., 2014; Stephenson et al., 2022; Liu et al., 2025). After correcting for ionospheric (Gomba et al., 2017; Chen & Zebker, 2012; Liang et al., 2019) and tropospheric delays (Jolivet et al., 2014; Cao et al., 2021) and adopting the ITRF2014 South American plate motion (Stephenson et al., 2022; Liu et al., 2025), the residual InSAR velocities align well with GNSS observations within the forearc. In this chapter, we are focused on relative deformation associated with shallow megathrust loading; thus, residual long-wavelength trends are treated as nuisance parameters: a bilinear ramp per InSAR track and a planar translation–rotation field for the GNSS network (Fattahi & Amelung, 2014; Peng et al., 2017). Future work could replace these empirical corrections with physically motivated Euler rotations or strain tensors to jointly estimate reference motion and coupling (Bletery et al., 2020) instead of arbitrarily flattening InSAR to the GNSS network.

Assuming quasi-steady conditions late in the interseismic cycle, one interpretation of remaining residual motion involves the proposed Andean sliver or microplate

model: in northern Chile (18°–24°S), ~10–12 mm yr^{-1} of the Nazca–South America convergence may be accommodated by clockwise rotation of a forearc block (Métois et al., 2013). However, recent models increasingly attribute this motion to distributed crustal strain rather than rigid block rotation (Yáñez-Cuadra et al., 2022). Testing this hypothesis requires detailed comparison of GNSS horizontal velocities and InSAR-derived deformation in a common reference frame.

Residual long-wavelength deformation beyond shallow megathrust coupling

Residual velocities after removing predicted shallow megathrust backslip (< 60 km) reveal a coherent, long-wavelength signal unexplained by our elastic coupling model. This broad, inland-distributed gradient appears in both GNSS and InSAR datasets, indicating an epistemic limitation of the model. Our purely elastic dislocation representation is only valid for near-field (near-trench) deformation and cannot capture longer-wavelength processes occurring in the far-field (backarc). Consequently, the inversion either leaves these signals as residuals or erroneously maps them into spurious zones of high apparent coupling at depth. Consequently, the elongated zones of high coupling at ~100 km depth (20°S–28°S) and below 300 km depth are not physical slip deficits, but mathematical artifacts of the elastic model attempting to absorb deformation from unmodeled processes.

The central Andean Plateau translates eastward at ~ 10 mm/yr relative to stable South America. Most of this shortening localizes between 65°W and 63°W, near the Bolivia–Argentina border, within the Subandean backarc orogenic wedge (Brooks et al., 2011; Weiss et al., 2015). Deformation there is generally attributed to a system of west-dipping thrust faults rooted in a low-angle décollement that slips continuously at depth but remains locked in its upper ~ 20 km (Brooks et al., 2011; Weiss et al., 2015). This fold-and-thrust system drives both vertical uplift and horizontal contraction of the eastern Altiplano, similar to active orogenic wedges such as Taiwan (Simoes et al., 2007; Hsu et al., 2009). Potentially, the upper-plate deformation spanning a ~ 200-km swath produced by this backarc wedge may be misinterpreted as deep megathrust backslip (>~ 300 km depth) in a purely elastic subduction-interface model (Figure 4.22).

Second, intra-slab seismicity at intermediate depths (60–100 km) reflects the tensile stress regime generated by slab pull mechanism (Fujita & Kanamori, 1981; Ide & Takeo, 1996). A prominent example beneath northern Chile is the 2005 M_w 7.7 Tarapacá earthquake, which ruptured a sub-horizontal fault at ~ 98 km depth (Peyrat

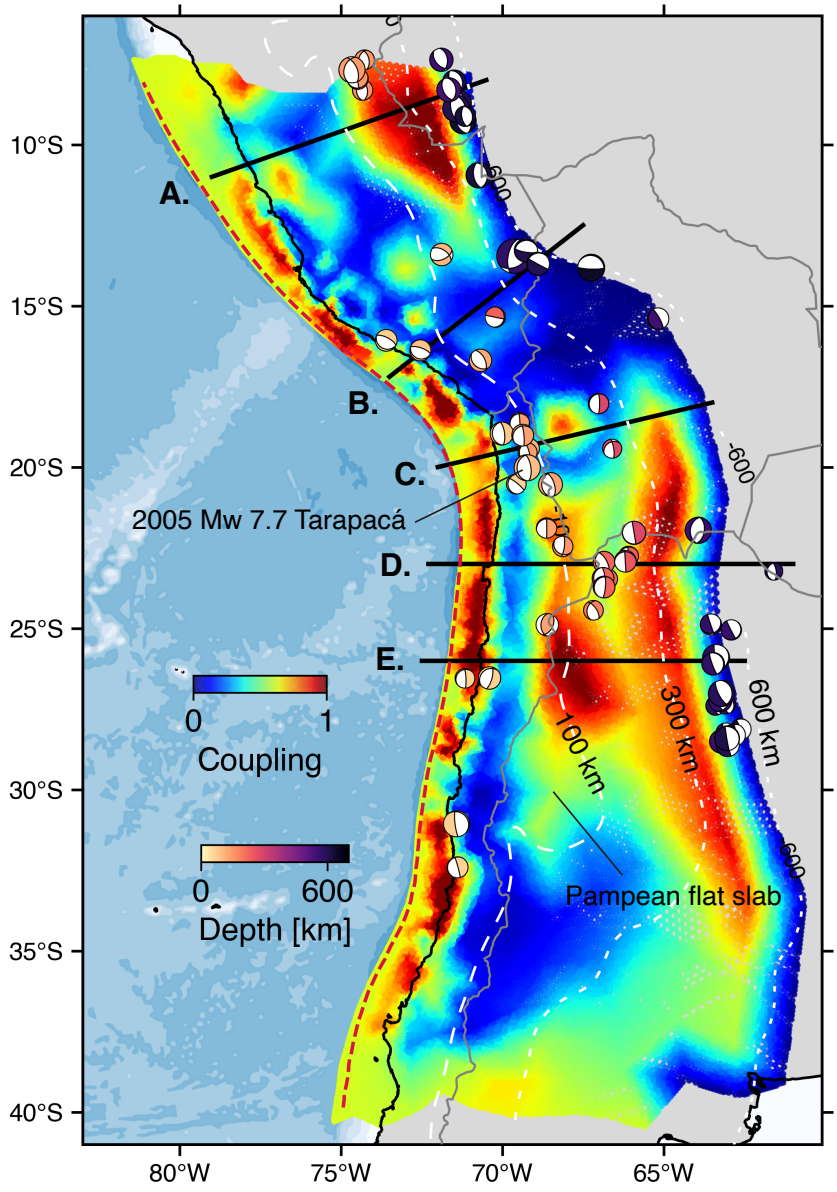

Figure 4.22: Jointly inverted interseismic coupling, overlaid with focal mechanisms for earthquakes deeper than 60 km and with magnitudes larger than Mw 6.5 from the Global Centroid Moment Tensor catalog (Dziewonski et al., 1981; Ekström et al., 2012).

et al., 2006; Sippl et al., 2022). Numerous similar events occur within the downgoing slab and coincide spatially with zones of apparently high coupling near ~ 100 and ~ 300 km depth in our model (Figure 4.22). The extent to which intermediate-depth slab seismicity produces any measurable long-wavelength deformation at the surface and contribute to the intermediate and deep coupling estimates in our model remains unexplored.

Other contributing factors likely include the hypothesis of an Andean microplate or rigid forearc sliver (Brooks et al., 2003; Allmendinger et al., 2007; Wang et al., 2007; Chlieh et al., 2011; Métois et al., 2013), long-wavelength viscoelastic relaxation in the upper plate from past great earthquakes (Luo & Wang, 2021; Luo et al., 2025), distributed crustal strain within the overriding plate (Yáñez-Cuadra et al., 2022), and the distinct mechanical behavior of the Pampean flat slab further south (Jordan et al., 1983; Gutscher, 2002; Gans et al., 2011), which coincides with the termination of the high-coupling anomaly near 29°S at ~100 km depth. Taken together, these high apparent coupling zones in our simple model are likely an elastic projection originating from a compound of processes unrelated to megathrust locking. Reducing epistemic errors in megathrust coupling estimates will require future inversions to explicitly incorporate these broader, non-megathrust components of the surface deformation field.

4.7 Conclusion

This study provides the first continuous interseismic deformation field across the Peruvian–Chilean subduction margin, derived from Sentinel-1 InSAR (2014–2025) combined with GNSS observations. After correcting for ionospheric and tropospheric delays and aligning the data to ITRF2014, we recover stable long-wavelength velocity fields spanning ~2500 km from Lima to Concepción. We truncate three years of early postseismic following the Illapel Earthquake to isolate the quasi-steady late-interseismic signal.

A first-order observation is that most segments of the megathrust are locked at shallow depths (< 60 km), consistent with previous studies (Chlieh et al., 2011; Métois et al., 2016; Klein et al., 2018a). The down-dip limit of this shallow interplate coupling zone aligns closely with the coastline, generally supporting the idea that the width of the seismogenic zone has a major relationship with long-term coastal morphology (Béjar-Pizarro et al., 2013; Jolivet et al., 2020). Recent and historical great earthquakes fall largely within, or partially overlap, these coupled regions—

including the 2001 M_w 8.4 Arequipa, 2014 M_w 8.1 Iquique/Pisagua, 1995 M_w 8.0 Antofagasta, 2015 M_w 8.3 Illapel, and 2010 M_w 8.8 Maule events—highlighting that these segments indeed host major ruptures (e.g., Moreno et al., 2010; Chlieh et al., 2011; Avouac, 2015; Métois et al., 2016; Lovery et al., 2024). Along-strike variations in decoupled patches potentially correlate with changes in the geometry and roughness of the subducting Nazca Plate. Coupling intensifies from Marcona to Arequipa but weakens sharply across the Arica Bend, where the Nazca, Iquique, and Nazca Fracture-Zone ridges enter the trench, producing a creeping segment. South of Pisagua, between 19°S and 26°S, the megathrust is strongly coupled ($\chi > 0.7$) except for minor low-coupling patches near Mejillones and Taltal. In central Chile, weak coupling near La Serena, Copiapó, and Taltal coincides with the Challenger Fracture Zone, Copiapó Ridge, and Tatal Ridge (or Sala y Gómez Ridge), respectively, confirming the dominant role of subducting topography in defining mechanical segmentation and potentially hosting slow-slip transients (Wang & Bilek, 2011; Klein et al., 2018b; Münchmeyer et al., 2025).

Between Illapel and Santiago (32°–35°S), coupling remains anomalously high (0.8–0.9), likely reflecting long-lived postseismic relaxation from the 2010 M_w 8.8 Maule earthquake that is largely mapped into our elastic coupling model. Southward toward Concepción, coupling decreases to half-coupled levels, which may mark the southern limit of this postseismic stress-shadow effect and a transition to regions where deformation is again dominated by shallow megathrust locking (Klein et al., 2017; Klein et al., 2018a).

Apparent deep backslip around 100 km and below 300 km depth is unphysical and is likely compensating for unmodeled long-wavelength deformation, where the origins are unclear. Possible explanations include the eastward motion of Andean orogenic wedge and surface deformation associated with intra-slab events at intermediate depths. Other contributions may arise from a crustal forearc sliver or a distinct microplate (e.g., Brooks et al., 2003; Allmendinger & González, 2010; Métois et al., 2013), upper-plate inelastic flow following past large earthquakes (e.g., Wang et al., 2012; Luo & Wang, 2021), distributed crustal strain (Yáñez-Cuadra et al., 2022), etc. Clarifying the specific cause of these long-wavelength deformation near and in the backarc remains beyond the scope of this study. Overall, the close agreement between GNSS and InSAR residuals indicates that the joint dataset captures both near-trench and broad-scale crustal deformation. Future work should incorporate postseismic relaxation and more realistic elastic dislocation models that account

for slab thickness, flexure bending, and mechanical layering to better represent the stress evolution and coupling dynamics of the Andean megathrust.

BIBLIOGRAPHY

Abril-Pla, O., V. Andreani, C. Carroll, L. Dong, C. J. Fonnesbeck, M. Kochurov, R. Kumar, J. Lao, C. C. Luhmann, O. A. Martin, M. Osthege, R. Vieira, T. Wiecki & R. Zinkov (2023). "PyMC: A Modern, and Comprehensive Probabilistic Programming Framework in Python". In: *PeerJ Comput. Sci.*, 9. DOI: 10.7717/peerj-cs.1516.

Agram, P. S. & M. Simons (2015). "A Noise Model for InSAR Time Series". In: *JGR Solid Earth*, 120. DOI: 10.1002/2014JB011271.

Aki, K. (1965). "Maximum Likelihood Estimate of b in the Formula Log N= A-bM and Its Confidence Limits". In: *Bull, Earthq, Res, Inst, Tokyo Univ,* 43.

Allmendinger, R. W. & G. González (2010). "Invited Review Paper: Neogene to Quaternary Tectonics of the Coastal Cordillera, Northern Chile". In: *Tectonophysics*, 495(1). DOI: 10.1016/j.tecto.2009.04.019.

Allmendinger, R. W., R. Reilinger & J. Loveless (2007). "Strain and Rotation Rate from GPS in Tibet, Anatolia, and the Altiplano". In: *Tectonics*, 26(3). DOI: 10.1029/2006TC002030.

Altamimi, Z., L. Métivier & X. Collilieux (2012). "ITRF2008 Plate Motion Model". In: *J. Geophys. Res.: Solid Earth*, 117(B7). DOI: 10.1029/2011JB008930.

Altamimi, Z., L. Métivier, P. Rebischung, H. Rouby & X. Collilieux (2017). "ITRF2014 Plate Motion Model". In: *Geophys. J. Int.*, 209. DOI: 10.1093/gji/ggx136.

Anderson, K. R., I. A. Johanson, M. R. Patrick, M. Gu, P. Segall, M. P. Poland, E. K. Montgomery-Brown & A. Miklius (2019). "Magma Reservoir Failure and the Onset of Caldera Collapse at Kīlauea Volcano in 2018". In: *Science*, 366(6470). DOI: 10.1126/science.aaz1822.

Argus, D. F. & R. G. Gordon (1996). "Tests of the Rigid-Plate Hypothesis and Bounds on Intraplate Deformation Using Geodetic Data from Very Long Baseline Interferometry". In: *J. Geophys. Res.: Solid Earth*, 101. DOI: 10.1029/95JB03775.

Argus, D. F., R. G. Gordon & C. DeMets (2011). "Geologically Current Motion of 56 Plates Relative to the No-Net-Rotation Reference Frame". In: *Geochem. Geophys. Geosystems*, 12. DOI: 10.1029/2011GC003751.

Armijo, R., R. Rauld, R. Thiele, G. Vargas, J. Campos, R. Lacassin & E. Kausel (2010). "The West Andean Thrust, the San Ramón Fault, and the Seismic Hazard for Santiago, Chile". In: *Tectonics*, 29(2). DOI: 10.1029/2008TC002427.

ArRajehi, A., S. McClusky, R. Reilinger, M. Daoud, A. Alchalbi, S. Ergintav, F. Gomez, J. Sholan, F. Bou-Rabee, G. Ogubazghi, B. Haileab, S. Fisseha, L. Asfaw, S. Mahmoud, A. Rayan, R. Bendik & L. Kogan (2010). "Geodetic Constraints on Present-Day Motion of the Arabian Plate: Implications for Red Sea and Gulf of Aden Rifting". In: *Tectonics*, 29. DOI: 10.1029/2009TC002482.

Avouac, J.-P. (2015). "From Geodetic Imaging of Seismic and Aseismic Fault Slip to Dynamic Modeling of the Seismic Cycle". In: *Annu. Rev. Earth Planet. Sci.*, 43(1). DOI: 10.1146/annurev-earth-060614-105302.

Backus, G. & F. Gilbert (1968). "The Resolving Power of Gross Earth Data". In: *Geophys. J. R. Astron. Soc.*, 16(2). DOI: 10.1111/j.1365-246X.1968.tb00216.x.

Baer, G., D. Sandwell, S. Williams, Y. Bock & G. Shamir (1999). "Coseismic Deformation Associated with the November 1995, $M_W = 7.1$ Nuweiba Earthquake, Gulf of Elat (Aqaba), Detected by Synthetic Aperture Radar Interferometry". In: *J. Geophys. Res.: Solid Earth*, 104(B11). DOI: 10.1029/1999jb900216.

Bähr, H. (2013). "Orbital Effects in Spaceborne Synthetic Aperture Radar Interferometry". Dissertation (External).

Bähr, H., S. Samiei-Esfahany & R. F. Hanssen (2012). "On the Effect of Reference Frame Motion on InSAR Deformation Estimates". In: *Fringe 2011*. Vol. 697. Proc. Fringe 2011.

Bakun, W., B. Aagaard, B. Dost, W. Ellsworth, J. Hardebeck, R. Harris, C. Ji, M. Johnston, J. Langbein, J. Lienkaemper, et al. (2005). "Implications for Prediction and Hazard Assessment from the 2004 Parkfield Earthquake". In: *Nature*, 437(7061). DOI: 10.1038/nature04067.

Barbot, S., N. Lapusta & J.-P. Avouac (2012). "Under the Hood of the Earthquake Machine: Toward Predictive Modeling of the Seismic Cycle". In: *Science*, 336(6082). DOI: 10.1126/science.1218796.

Barjous, M. & S. Mikbel (1990). "Tectonic Evolution of the Gulf of Aqaba-Dead Sea Transform Fault System". In: *Tectonophysics*, 180(1). DOI: 10.1016/0040-1951(90)90371-E.

Béjar-Pizarro, M., A. Socquet, R. Armijo, D. Carrizo, J. Genrich & M. Simons (2013). "Andean Structural Control on Interseismic Coupling in the North Chile Subduction Zone". In: *Nat. Geosci.*, 6(6). DOI: 10.1038/ngeo1802.

Bektaş, Z., U. Avşar, M. Ribot, Y. Klinger & S. Jónsson (2024). "Seismo-Turbidites Reveal Locations of Major Earthquakes during the Past Millennium in the Gulf of Aqaba, Southern Dead Sea Fault". In: *Earth Planet. Sci. Lett.*, 629. DOI: 10.1016/j.epsl.2024.118595.

Ben-Avraham, Z. (1985). "Structural Framework of the Gulf of Elat (AQABA), Northern Red Sea". In: *J. Geophys. Res.: Solid Earth*, 90(B1). DOI: 10.1029/jb090ib01p00703.

Ben-Avraham, Z. & G. Tibor (1993). “The Northern Edge of the Gulf of Elat”. In: *Tectonophysics*, 226(1). DOI: 10.1016/0040-1951(93)90125-4.

Ben-Zion, Y. & V. Lyakhovsky (2006). “Analysis of Aftershocks in a Lithospheric Model with Seismogenic Zone Governed by Damage Rheology”. In: *Geophys. J. Int.*, 165(1). DOI: 10.1111/j.1365-246X.2006.02878.x.

Ben-Zion, Y., J. R. Rice & R. Dmowska (1993). “Interaction of the San Andreas Fault Creeping Segment with Adjacent Great Rupture Zones and Earthquake Recurrence at Parkfield”. In: *J. Geophys. Res.: Solid Earth*, 98(B2). DOI: 10.1029/92JB02154.

Ben-Zion, Y. & C. G. Sammis (2003). “Characterization of Fault Zones”. In: *Pure Appl. Geophys.*, 160(3). DOI: 10.1007/PL00012554.

Berardino, P., G. Fornaro, R. Lanari & E. Sansosti (2002). “A New Algorithm for Surface Deformation Monitoring Based on Small Baseline Differential SAR Interferograms”. In: *IEEE Trans. Geosci. Remote Sens.*, 40. DOI: 10.1109/TGRS.2002.803792.

Biggs, J., S. K. Ebmeier, W. P. Aspinall, Z. Lu, M. E. Pritchard, R. S. J. Sparks & T. A. Mather (2014). “Global Link between Deformation and Volcanic Eruption Quantified by Satellite Imagery”. In: *Nat. Commun.*, 5(1). DOI: 10.1038/ncomms4471.

Biggs, J., N. Anantrasirichai, F. Albino, M. Lazecky & Y. Maghsoudi (2022). “Large-Scale Demonstration of Machine Learning for the Detection of Volcanic Deformation in Sentinel-1 Satellite Imagery”. In: *Bull. Volcanol.*, 84(12). DOI: 10.1007/s00445-022-01608-x.

Biggs, J., T. Wright, Z. Lu & B. Parsons (2007). “Multi-Interferogram Method for Measuring Interseismic Deformation: Denali Fault, Alaska”. In: *Geophys. J. Int.*, 170. DOI: 10.1111/j.1365-246X.2007.03415.x.

Bird, P., Y. Y. Kagan, D. D. Jackson, F. P. Schoenberg & M. J. Werner (2009). “Linear and Nonlinear Relations between Relative Plate Velocity and Seismicity”. In: *Bull. Seismol. Soc. Am.*, 99(6). DOI: 10.1785/0120090082.

Bird, P. (2003). “An Updated Digital Model of Plate Boundaries”. In: *Geochem. Geophys. Geosystems*, 4. DOI: 10.1029/2001GC000252.

Bletery, Q., O. Cavalié, J.-M. Nocquet & T. Ragon (2020). “Distribution of Interseismic Coupling along the North and East Anatolian Faults Inferred from InSAR and GPS Data”. In: *Geophys. Res. Lett.*, 47. DOI: 10.1029/2020GL087775.

Blewitt, G., W. Hammond & C. Kreemer (2018). “Harnessing the GPS Data Explosion for Interdisciplinary Science”. In: *Eos.*, 99(2).

Bowring, B. R. (1976). “Transformation from Spatial to Geographical Coordinates”. In: *Surv. Rev.*, 23. DOI: 10.1179/sre.1976.23.181.323.

Brace, W. F. & J. D. Byerlee (1966). “Stick-Slip as a Mechanism for Earthquakes”. In: *Science*, 153(3739). DOI: 10.1126/science.153.3739.990.

Brooks, B. A., M. Bevis, R. Smalley Jr., E. Kendrick, R. Manceda, E. Lauría, R. Maturana & M. Araujo (2003). "Crustal Motion in the Southern Andes (26°–36°S): Do the Andes Behave like a Microplate?" In: *Geochem. Geophys. Geosyst.*, 4(10). DOI: 10.1029/2003GC000505.

Brooks, B. A., M. Bevis, K. Whipple, J. Ramon Arrowsmith, J. Foster, T. Zapata, E. Kendrick, E. Minaya, A. Echalar, M. Blanco, P. Euillades, M. Sandoval & R. J. Smalley (2011). "Orogenic-Wedge Deformation and Potential for Great Earthquakes in the Central Andean Backarc". In: *Nat. Geosci.*, 4(6). DOI: 10.1038/ngeo1143.

Brouwer, W. S. & R. F. Hanssen (2023). "A Treatise on InSAR Geometry and 3-D Displacement Estimation". In: *IEEE Trans. Geosci. Remote Sens.*, 61. DOI: 10.1109/TGRS.2023.3322595.

Bürgmann, R. (2018). "The Geophysics, Geology and Mechanics of Slow Fault Slip". In: *Earth Planet. Sci. Lett.*, 495. DOI: 10.1016/j.epsl.2018.04.062.

Bürgmann, R., P. A. Rosen & E. J. Fielding (2000). "Synthetic Aperture Radar Interferometry to Measure Earth's Surface Topography and Its Deformation". In: *Annu. Rev. Earth Planet. Sci.*, 28. DOI: 10.1146/annurev.earth.28.1.169.

Cao, Y., S. Jónsson & Z. Li (2021). "Advanced InSAR Tropospheric Corrections from Global Atmospheric Models That Incorporate Spatial Stochastic Properties of the Troposphere". In: *J. Geophys. Res.: Solid Earth*, 126. DOI: 10.1029/2020JB020952.

Castro-Perdomo, N., R. Viltres, F. Masson, Y. Klinger, S. Liu, M. Dhahry, P. Ulrich, J.-D. Bernard, R. Matrau, A. Alothman, H. Zahran, R. Reilinger, P. M. Mai & S. Jónsson (2021). "Interseismic Deformation in the Gulf of Aqaba from GPS Measurements". In: *Geophys. J. Int.*, 228. DOI: 10.1093/gji/ggab353.

Cavalié, O., C. Lasserre, M. .-. Doin, G. Peltzer, J. Sun, X. Xu & Z. .-. Shen (2008). "Measurement of Interseismic Strain across the Haiyuan Fault (Gansu, China), by InSAR". In: *Earth Planet. Sci. Lett.*, 275. DOI: 10.1016/j.epsl.2008.07.057.

Chaussard, E., R. Bürgmann, H. Fattahi, C. W. Johnson, R. Nadeau, T. Taira & I. Johanson (2015a). "Interseismic Coupling and Refined Earthquake Potential on the Hayward-Calaveras Fault Zone". In: *J. Geophys. Res.: Solid Earth*, 120. DOI: 10.1002/2015JB012230.

Chaussard, E., R. Bürgmann, H. Fattahi, R. M. Nadeau, T. Taira, C. W. Johnson & I. Johanson (2015b). "Potential for Larger Earthquakes in the East San Francisco Bay Area Due to the Direct Connection between the Hayward and Calaveras Faults". In: *Geophys. Res. Lett.*, 42. DOI: 10.1002/2015GL063575.

Chaussard, E., C. W. Johnson, H. Fattahi & R. Bürgmann (2016). "Potential and Limits of InSAR to Characterize Interseismic Deformation Independently of GPS Data: Application to the Southern San Andreas Fault System". In: *Geochem. Geophys. Geosystems*, 17. DOI: 10.1002/2015GC006246.

Chen, C. & H. Zebker (2002). “Phase Unwrapping for Large SAR Interferograms: Statistical Segmentation and Generalized Network Models”. In: *IEEE Trans. Geosci. Remote Sens.*, 40. DOI: 10.1109/TGRS.2002.802453.

Chen, J. & H. A. Zebker (2012). “Ionospheric Artifacts in Simultaneous L-Band InSAR and GPS Observations”. In: *IEEE Trans. Geosci. Remote Sens.*, 50(4). DOI: 10.1109/TGRS.2011.2164805.

Chinnery, M. A. & J. A. Petrak (1968). “The Dislocation Fault Model with a Variable Discontinuity”. In: *Tectonophysics*, 5(6). DOI: 10.1016/0040-1951(68)90008-5.

Chlieh, M., J. B. De Chabalier, J. C. Ruegg, R. Armijo, R. Dmowska, J. Campos & K. L. Feigl (2004). “Crustal Deformation and Fault Slip during the Seismic Cycle in the North Chile Subduction Zone, from GPS and InSAR Observations”. In: *Geophys. J. Int.*, 158(2). DOI: 10.1111/j.1365-246x.2004.02326.x.

Chlieh, M., H. Perfettini, H. Tavera, J.-P. Avouac, D. Remy, J.-M. Nocquet, F. Rolandone, F. Bondoux, G. Gabalda & S. Bonvalot (2011). “Interseismic Coupling and Seismic Potential along the Central Andes Subduction Zone”. In: *J. Geophys. Res.*, 116(B12). DOI: 10.1029/2010jb008166.

Comte, D. & M. Pardo (1991). “Reappraisal of Great Historical Earthquakes in the Northern Chile and Southern Peru Seismic Gaps”. In: *Nat. Hazard.*, 4(1). DOI: 10.1007/BF00126557.

Contreras-Reyes, E. & D. Carrizo (2011). “Control of High Oceanic Features and Subduction Channel on Earthquake Ruptures along the Chile–Peru Subduction Zone”. In: *Phys. Earth Planet. Inter.*, 186(1). DOI: 10.1016/j.pepi.2011.03.002.

Corral, Á. (2004). “Universal Local versus Unified Global Scaling Laws in the Statistics of Seismicity”. In: *Physica A*, 340(4). DOI: 10.1016/j.physa.2004.05.010.

Cox, A. & R. B. Hart (1986). *Plate Tectonics: How It Works*. John Wiley & Sons.

d’Alessio, M. A., I. A. Johanson, R. Bürgmann, D. A. Schmidt & M. H. Murray (2005). “Slicing up the San Francisco Bay Area: Block Kinematics and Fault Slip Rates from GPS-derived Surface Velocities”. In: *J. Geophys. Res.: Solid Earth*, 110. DOI: 10.1029/2004JB003496.

Dahl, J. & L. Vandenberghe (2006). “Cvxopt: A python package for convex optimization”. In: *Proc. eur. conf. op. res*. Vol. 2, p. 3.

De Zan, F., A. Parizzi, P. Prats-Iraola & P. López-Dekker (2014). “A SAR Interferometric Model for Soil Moisture”. In: *IEEE Trans. Geosci. Remote Sens.*, 52. DOI: 10.1109/TGRS.2013.2241069.

DeMets, C., R. G. Gordon & D. F. Argus (2010). “Geologically Current Plate Motions”. In: *Geophys. J. Int.*, 181. DOI: 10.1111/j.1365-246X.2009.04491.x.

DiCaprio, C. J. & M. Simons (2008). “Importance of Ocean Tidal Load Corrections for Differential InSAR”. In: *Geophys. Res. Lett.*, 35. DOI: 10.1029/2008GL035806.

Dieterich, J. (1994). “A Constitutive Law for Rate of Earthquake Production and Its Application to Earthquake Clustering”. In: *J. Geophys. Res.: Solid Earth*, 99(B2). DOI: 10.1029/93JB02581.

Donoso, F., M. Moreno, F. Ortega-Culaciati, J. R. Bedford & R. Benavente (2021). “Automatic Detection of Slow Slip Events Using the PICCA: Application to Chilean GNSS Data”. In: *Front. Earth Sci.*, 9. DOI: 10.3389/feart.2021.788054.

Duputel, Z., J. Jiang, R. Jolivet, M. Simons, L. Rivera, J.-P. Ampuero, B. Riel, S. E. Owen, A. W. Moore, S. V. Samsonov, F. Ortega Culaciati & S. E. Minson (2015). “The Iquique Earthquake Sequence of April 2014: Bayesian Modeling Accounting for Prediction Uncertainty”. In: *Geophys. Res. Lett.*, 42(19). DOI: 10.1002/2015GL065402.

Duputel, Z., P. S. Agram, M. Simons, S. E. Minson & J. L. Beck (2014). “Accounting for Prediction Uncertainty When Inferring Subsurface Fault Slip”. In: *Geophys. J. Int.*, 197(1). DOI: 10.1093/gji/ggt517.

Duputel, Z., L. Rivera, Y. Fukahata & H. Kanamori (2012). “Uncertainty Estimations for Seismic Source Inversions”. In: *Geophys. J. Int.*, 190. DOI: 10.1111/j.1365-246X.2012.05554.x.

Dziewonski, A. M., T.-A. Chou & J. H. Woodhouse (1981). “Determination of Earthquake Source Parameters from Waveform Data for Studies of Global and Regional Seismicity”. In: *J. Geophys. Res.: Solid Earth*, 86(B4). DOI: 10.1029/JB086iB04p02825.

Ekström, G., M. Nettles & A. M. Dziewoński (2012). “The Global CMT Project 2004–2010: Centroid-moment Tensors for 13,017 Earthquakes”. In: *Phys. Earth Planet. Inter.*, 200–201. DOI: 10.1016/j.pepi.2012.04.002.

Elliott, J. L., C. F. Larsen, J. T. Freymueller & R. J. Motyka (2010). “Tectonic Block Motion and Glacial Isostatic Adjustment in Southeast Alaska and Adjacent Canada Constrained by GPS Measurements”. In: *J. Geophys. Res.: Solid Earth*, 115. DOI: 10.1029/2009JB007139.

Emardson, T. R., M. Simons & F. H. Webb (2003). “Neutral Atmospheric Delay in Interferometric Synthetic Aperture Radar Applications: Statistical Description and Mitigation”. In: *J. Geophys. Res.: Space Phys.*, 108. DOI: 10.1029/2002JB001781.

Farr, T. G., P. A. Rosen, E. Caro, R. Crippen, R. Duren, S. Hensley, M. Kobrick, M. Paller, E. Rodriguez, L. Roth, D. Seal, S. Shaffer, J. Shimada, J. Umland, M. Werner, M. Oskin, D. Burbank & D. Alsdorf (2007). “The Shuttle Radar Topography Mission”. In: *Rev. Geophys.*, 45. DOI: 10.1029/2005RG000183.

Fattahi, H., P. Agram & M. Simons (2017a). “A Network-Based Enhanced Spectral Diversity Approach for TOPS Time-Series Analysis”. In: *IEEE Trans. Geosci. Remote Sens.*, 55. DOI: 10.1109/TGRS.2016.2614925.

Fattahi, H. & F. Amelung (2013). “DEM Error Correction in InSAR Time Series”. In: *IEEE Trans. Geosci. Remote Sens.*, 51. DOI: 10.1109/TGRS.2012.2227761.

Fattahi, H. & F. Amelung (2014). “InSAR Uncertainty Due to Orbital Errors”. In: *Geophys. J. Int.*, 199. DOI: 10.1093/gji/ggu276.

Fattahi, H. & F. Amelung (2015). “InSAR Bias and Uncertainty Due to the Systematic and Stochastic Tropospheric Delay”. In: *J. Geophys. Res.: Solid Earth*, 120. DOI: 10.1002/2015JB012419.

Fattahi, H., M. Simons & P. Agram (2017b). “InSAR Time-Series Estimation of the Ionospheric Phase Delay: An Extension of the Split Range-Spectrum Technique”. In: *IEEE Trans. Geosci. Remote Sens.*, 55(10). DOI: 10.1109/TGRS.2017.2718566.

Feinstein, S., M. Eyal, B. P. Kohn, M. S. Steckler, K. M. Ibrahim, B. K. Moh’d & Y. Tian (2013). “Uplift and Denudation History of the Eastern Dead Sea Rift Flank, SW Jordan: Evidence from Apatite Fission Track Thermochronometry”. In: *Tectonics*, 32(5). DOI: 10.1002/tect.20082.

Fialko, Y. (2006). “Interseismic Strain Accumulation and the Earthquake Potential on the Southern San Andreas Fault System”. In: *Nature*, 441. DOI: 10.1038/nature04797.

Fialko, Y., M. Simons & D. Agnew (2001). “The Complete (3-D) Surface Displacement Field in the Epicentral Area of the 1999 M7.1 Hector Mine Earthquake, California, from Space Geodetic Observations”. In: *Geophys. Res. Lett.*, 28. DOI: 10.1029/2001GL013174.

Field, E. H., R. J. Arrowsmith, G. P. Biasi, P. Bird, T. E. Dawson, K. R. Felzer, D. D. Jackson, K. M. Johnson, T. H. Jordan, C. Madden, et al. (2014). “Uniform California Earthquake Rupture Forecast, Version 3 (UCERF3)—the Time-Independent Model”. In: *Bull. Seismol. Soc. Am.*, 104(3). DOI: 10.1785/0120130164.

Fisher, A. T., C. A. Stein, R. N. Harris, K. Wang, E. A. Silver, M. Pfender, M. Hutnak, A. Cherkaoui, R. Bodzin & H. Villinger (2003). “Abrupt Thermal Transition Reveals Hydrothermal Boundary and Role of Seamounts within the Cocos Plate”. In: *Geophys. Res. Lett.*, 30(11). DOI: 10.1029/2002GL016766.

Fournier, T., M. E. Pritchard & N. Finnegan (2011). “Accounting for Atmospheric Delays in InSAR Data in a Search for Long-Wavelength Deformation in South America”. In: *IEEE Trans. Geosci. Remote Sens.*, 49(10). DOI: 10.1109/TGRS.2011.2139217.

Fujita, K. & H. Kanamori (1981). “Double Seismic Zones and Stresses of Intermediate Depth Earthquakes”. In: *Geophys. J. Int.*, 66(1). DOI: 10.1111/j.1365-246X.1981.tb05950.x.

Gans, C. R., S. L. Beck, G. Zandt, H. Gilbert, P. Alvarado, M. Anderson & L. Linkimer (2011). "Continental and Oceanic Crustal Structure of the Pampean Flat Slab Region, Western Argentina, Using Receiver Function Analysis: New High-Resolution Results". In: *Geophys. J. Int.*, 186(1). DOI: 10.1111/j.1365-246X.2011.05023.x.

Garfunkel, Z. & Z. Ben-Avraham (1996). "The Structure of the Dead Sea Basin". In: *Tectonophysics*, 266(1-4). DOI: 10.1016/s0040-1951(96)00188-6.

Gelman, A., J. B. Carlin, H. S. Stern & D. B. Rubin (1995). *Bayesian Data Analysis*. Chapman and Hall/CRC.

Geudtner, D., R. Torres, P. Snoeij, M. Davidson & B. Rommen (2014). "Sentinel-1 System Capabilities and Applications". In: *2014 IEEE Geosci. Remote Sens. Symp.* IEEE. DOI: 10.1109/IGARSS.2014.6946711.

Gilbert, H., S. Beck & G. Zandt (2006). "Lithospheric and Upper Mantle Structure of Central Chile and Argentina". In: *Geophys. J. Int.*, 165(1). DOI: 10.1111/j.1365-246X.2006.02867.x.

Global Volcanism Program (2025). *Volcanoes of the World (v. 5.3.2; 30 Sep 2025)*. DOI: 10.5479/si.GVP.VOTW5-2025.5.3.

Goldstein, R. M. & C. L. Werner (1998). "Radar Interferogram Filtering for Geophysical Applications". In: *Geophys. Res. Lett.*, 25. DOI: 10.1029/1998GL900033.

Gomba, G., A. Parizzi, F. De Zan, M. Eineder & R. Bamler (2016). "Toward Operational Compensation of Ionospheric Effects in SAR Interferograms: The Split-Spectrum Method". In: *IEEE Trans. Geosci. Remote Sens.*, 54. DOI: 10.1109/TGRS.2015.2481079.

Gomba, G., F. Rodríguez González & F. De Zan (2017). "Ionospheric Phase Screen Compensation for the Sentinel-1 TOPS and ALOS-2 ScanSAR Modes". In: *IEEE Trans. Geosci. Remote Sens.*, 55. DOI: 10.1109/TGRS.2016.2604461.

Goudarzi, M. A., M. Cocard & R. Santerre (2014). "EPC: Matlab Software to Estimate Euler Pole Parameters". In: *GPS Solutions*, 18. DOI: 10.1007/s10291-013-0354-4.

Grandin, R., E. Klein, M. Métois & C. Vigny (2016). "Three-Dimensional Displacement Field of the 2015 Mw8.3 Illapel Earthquake (Chile) from across- and along-Track Sentinel-1 TOPS Interferometry". In: *Geophys. Res. Lett.*, 43. DOI: 10.1002/2016GL067954.

Gray, A. L., K. E. Mattar & G. Sofko (2000). "Influence of Ionospheric Electron Density Fluctuations on Satellite Radar Interferometry". In: *Geophys. Res. Lett.*, 27. DOI: 10.1029/2000GL000016.

Gray, R. M. (2013). *Entropy and Information Theory First Edition, Corrected*.

Guarnieri, A. M. & S. Tebaldini (2008). “On the Exploitation of Target Statistics for SAR Interferometry Applications”. In: *IEEE Trans. Geosci. Remote Sens.*, 46. DOI: 10.1109/TGRS.2008.2001756.

Guo, R., Y. Zheng, J. Xu & M. S. Riaz (2019). “Transient Viscosity and Afterslip of the 2015 Mw 8.3 Illapel, Chile, Earthquake”. In: *Bull. Seismol. Soc. Am.*, 109(6). DOI: 10.1785/0120190114.

Gutscher, M.-A. (2002). “Andean Subduction Styles and Their Effect on Thermal Structure and Interplate Coupling”. In: *J. South Am. Earth Sci.*, 15(1). DOI: 10.1016/S0895-9811(02)00002-0.

Hainzl, S., C. Sippl & B. Schurr (2019). “Linear Relationship between Aftershock Productivity and Seismic Coupling in the Northern Chile Subduction Zone”. In: *J. Geophys. Res.: Solid Earth*, 124(8). DOI: 10.1029/2019JB017764.

Hainzl, S., F. Scherbaum & C. Beauval (2006). “Estimating Background Activity Based on Interevent-Time Distribution”. In: *Bull. Seismol. Soc. Am.*, 96(1). DOI: 10.1785/0120050053.

Hamiel, Y. & O. Piatibratova (2019). “Style and Distribution of Slip at the Margin of a Pull-Apart Structure: Geodetic Investigation of the Southern Dead Sea Basin”. In: *J. Geophys. Res.: Solid Earth*, 124(11). DOI: 10.1029/2019JB018456.

Hanssen, R. F. (2001). *Radar Interferometry: Data Interpretation and Error Analysis*. Springer Science & Business Media.

Harris, R. A. (2017). “Large Earthquakes and Creeping Faults”. In: *Rev. Geophys.*, 55(1). DOI: 10.1002/2016RG000539.

Hartman, G., T. M. Niemi, G. Tibor, Z. Ben-Avraham, A. Al-Zoubi, Y. Makovsky, E. Akawwi, A.-R. Abueladas & R. Al-Ruzouq (2014). “Quaternary Tectonic Evolution of the Northern Gulf of Elat/Aqaba along the Dead Sea Transform”. In: *J. Geophys. Res.: Solid Earth*, 119(12). DOI: 10.1002/2013JB010879.

Hastings, W. K. (1970). “Monte Carlo Sampling Methods Using Markov Chains and Their Applications”. In: *Biometrika*, 57(1). DOI: 10.1093/biomet/57.1.97.

Hayes, G. P., G. L. Moore, D. E. Portner, M. Hearne, H. Flamme, M. Furtney & G. M. Smoczyk (2018). “Slab2, a Comprehensive Subduction Zone Geometry Model”. In: *Science*, 362(6410). DOI: 10.1126/science.aat4723.

Heki, K., G. R. Foulger, B. R. Julian & C.-H. Jahn (1993). “Plate Dynamics near Divergent Boundaries: Geophysical Implications of Postrifting Crustal Deformation in NE Iceland”. In: *J. Geophys. Res.: Solid Earth*, 98(B8). DOI: 10.1029/93JB00781.

Hersbach, H., B. Bell, P. Berrisford, S. Hirahara, A. Horányi, J. Muñoz-Sabater, J. Nicolas, C. Peubey, R. Radu, D. Schepers, A. Simmons, C. Soci, S. Abdalla, X. Abellan, G. Balsamo, P. Bechtold, G. Biavati, J. Bidlot, M. Bonavita, G. De Chiara, P. Dahlgren, D. Dee, M. Diamantakis, R. Dragani, J. Flemming, R.

Forbes, M. Fuentes, A. Geer, L. Haimberger, S. Healy, R. J. Hogan, E. Hólm, M. Janisková, S. Keeley, P. Laloyaux, P. Lopez, C. Lupu, G. Radnoti, P. de Rosnay, I. Rozum, F. Vamborg, S. Villaume & J.-N. Thépaut (2020). "The ERA5 Global Reanalysis". In: *Q. J. R. Meteorol. Soc.*, 146. DOI: 10.1002/qj.3803.

Hetland, E. A., P. Musé, M. Simons, Y. N. Lin, P. S. Agram & C. J. DiCaprio (2012). "Multiscale InSAR Time Series (MInTS) Analysis of Surface Deformation". In: *J. Geophys. Res.: Space Phys.*, 117. DOI: 10.1029/2011JB008731.

Hoffman, M. D. & A. Gelman (2011). *The No-U-Turn Sampler: Adaptively Setting Path Lengths in Hamiltonian Monte Carlo*. DOI: 10.48550/arXiv.1111.4246. arXiv: 1111.4246 [stat].

Hooper, A. (2008). "A Multi-Temporal InSAR Method Incorporating Both Persistent Scatterer and Small Baseline Approaches". In: *Geophys. Res. Lett.*, 35(16). DOI: 10.1029/2008GL034654.

Hsu, Y.-J., J.-P. Avouac, S.-B. Yu, C.-H. Chang, Y.-M. Wu & J. Woessner (2009). "Spatio-Temporal Slip, and Stress Level on the Faults within the Western Foothills of Taiwan: Implications for Fault Frictional Properties". In: *Pure Appl. Geophys.*, 166(10). DOI: 10.1007/s00024-009-0510-5.

Husen, S., E. Kissling, E. Flueh & G. Asch (1999). "Accurate Hypocentre Determination in the Seismogenic Zone of the Subducting Nazca Plate in Northern Chile Using a Combined On-/Offshore Network". In: *Geophys. J. Int.*, 138(3). DOI: 10.1046/j.1365-246x.1999.00893.x.

Ide, S. (2013). "The Proportionality between Relative Plate Velocity and Seismicity in Subduction Zones". In: *Nat. Geosci.*, 6(9). DOI: 10.1038/ngeo1901.

Ide, S. & M. Takeo (1996). "The Dynamic Rupture Process of the 1993 Kushiro-Oki Earthquake". In: *J. Geophys. Res.: Solid Earth*, 101(B3). DOI: 10.1029/95JB00959.

International Seismological Centre (2025). *ISC-GEM Earthquake Catalogue*. DOI: 10.31905/d808b825.

Jarrin, P., J.-M. Nocquet, F. Rolandone, H. Mora-Páez, P. Mothes & D. Cisneros (2023). "Current Motion and Deformation of the Nazca Plate: New Constraints from GPS Measurements". In: *Geophys. J. Int.*, 232(2). DOI: 10.1093/gji/ggac353.

Jiang, J. & N. Lapusta (2016). "Deeper Penetration of Large Earthquakes on Seismically Quiescent Faults". In: *Science*, 352(6291). DOI: 10.1126/science.aaf1496.

Jolivet, R., R. Grandin, C. Lasserre, M.-P. Doin & G. Peltzer (2011). "Systematic InSAR Tropospheric Phase Delay Corrections from Global Meteorological Reanalysis Data". In: *Geophys. Res. Lett.*, 38. DOI: 10.1029/2011GL048757.

Jolivet, R., M. Simons, P. S. Agram, Z. Duputel & Z.-K. Shen (2015). "Aseismic Slip and Seismogenic Coupling along the Central San Andreas Fault". In: *Geophys. Res. Lett.*, 42. DOI: 10.1002/2014GL062222.

Jolivet, R., M. Simons, Z. Duputel, J.-A. Olive, H. S. Bhat & Q. Bletery (2020). "Interseismic Loading of Subduction Megathrust Drives Long-Term Uplift in Northern Chile". In: *Geophys. Res. Lett.*, 47(8). DOI: 10.1029/2019gl085377.

Jolivet, R., P. S. Agram, N. Y. Lin, M. Simons, M.-P. Doin, G. Peltzer & Z. Li (2014). "Improving InSAR Geodesy Using Global Atmospheric Models". In: *J. Geophys. Res.: Solid Earth*, 119. DOI: 10.1002/2013JB010588.

Jónsson, S., H. Zebker, P. Segall & F. Amelung (2002). "Fault Slip Distribution of the 1999 Mw 7.1 Hector Mine, California, Earthquake, Estimated from Satellite Radar and GPS Measurements". In: *Bull. Seismol. Soc. Am.*, 92. DOI: 10.1785/0120000922.

Jordan, T. E. & R. W. Allmendinger (1986). "The Sierras Pampeanas of Argentina; a Modern Analogue of Rocky Mountain Foreland Deformation". In: *Am. J. Sci.*, 286(10). DOI: 10.2475/ajs.286.10.737.

Jordan, T. E., B. L. Isacks, R. W. Allmendinger, J. A. Brewer, V. A. Ramos & C. J. Ando (1983). "Andean Tectonics Related to Geometry of Subducted Nazca Plate". In: *GSA Bull.*, 94(3). DOI: 10.1130/0016-7606(1983)94<341:ATRTGO>2.0.CO;2.

Kagan, Y. Y. & L. Knopoff (1981). "Stochastic Synthesis of Earthquake Catalogs". In: *J. Geophys. Res.: Solid Earth*, 86(B4). DOI: 10.1029/JB086iB04p02853.

Kanamori, H. & E. E. Brodsky (2004). "The Physics of Earthquakes". In: *Rep. Prog. Phys.*, 67(8). DOI: 10.1088/0034-4885/67/8/R03.

Kanda, R. V. S. & M. Simons (2010). "An Elastic Plate Model for Interseismic Deformation in Subduction Zones". In: *J. Geophys. Res.: Solid Earth*, 115(B3). DOI: 10.1029/2009JB006611.

Kanda, R. V. S. & M. Simons (2012). "Practical Implications of the Geometrical Sensitivity of Elastic Dislocation Models for Field Geologic Surveys". In: *Tectonophysics*, 560–561. DOI: 10.1016/j.tecto.2012.06.040.

Kaneko, Y., J. P. Avouac & N. Lapusta (2010). "Towards Inferring Earthquake Patterns from Geodetic Observations of Interseismic Coupling". In: *Nat. Geosci.*, 3(5). DOI: 10.1038/ngeo843.

Kay, S. M., C. Mpodozis, V. A. Ramos & F. Munizaga (1991). "Magma Source Variations for Mid–Late Tertiary Magmatic Rocks Associated with a Shallowing Subduction Zone and a Thickening Crust in the Central Andes (28 to 33°S)". In: *Andean Magmatism and Its Tectonic Setting*. Ed. by R. S. Harmon & C. W. Rapela. Geological Society of America. DOI: 10.1130/SPE265-p113.

Khoshmanesh, M. & M. Shirzaei (2018). “Episodic Creep Events on the San Andreas Fault Caused by Pore Pressure Variations”. In: *Nat. Geosci.*, 11(8). DOI: 10.1038/s41561-018-0160-2.

Klein, E., M. Métois, G. Meneses, C. Vigny & A. Delorme (2018a). “Bridging the Gap between North and Central Chile: Insight from New GPS Data on Coupling Complexities and the Andean Sliver Motion”. In: *Geophys. J. Int.*, 213(3). DOI: 10.1093/gji/ggy094.

Klein, E., Z. Duputel, D. Zigone, C. Vigny, J.-P. Boy, C. Doubre & G. Meneses (2018b). “Deep Transient Slow Slip Detected by Survey GPS in the Region of Atacama, Chile”. In: *Geophys. Res. Lett.*, 45(22). DOI: 10.1029/2018GL080613.

Klein, E., B. Potin, F. Pasten-Araya, R. Tissandier, K. Azua, Z. Duputel, C. Herrera, L. Rivera, J. M. Nocquet, J. C. Baez, D. Zigone, R. Madariaga, J. P. Ampuero, S. Ruiz & C. Vigny (2021). “Interplay of Seismic and A-Seismic Deformation during the 2020 Sequence of Atacama, Chile”. In: *Earth Planet. Sci. Lett.*, 570. DOI: 10.1016/j.epsl.2021.117081.

Klein, E., C. Vigny, L. Fleitout, R. Grandin, R. Jolivet, E. Rivera & M. Métois (2017). “A Comprehensive Analysis of the Illapel 2015 Mw8.3 Earthquake from GPS and InSAR Data”. In: *Earth Planet. Sci. Lett.*, 469. DOI: 10.1016/j.epsl.2017.04.010.

Klinger, Y., J. P. Avouac, N. Abou Karaki, L. Dorbath, D. Bourles & J. L. Reyss (2000). “Slip Rate on the Dead Sea Transform Fault in Northern Araba Valley (Jordan)”. In: *Geophys. J. Int.*, 142(3). DOI: 10.1046/j.1365-246x.2000.00165.x.

Klinger, Y., L. Rivera, H. Haessler & J.-C. Maurin (1999). “Active Faulting in the Gulf of Aqaba: New Knowledge from the MW 7.3 Earthquake of 22 November 1995”. In: *Bull. Seismol. Soc. Am.*, 89. DOI: 10.1785/BSSA0890041025.

Konca, A. O., J. P. Avouac, A. Sladen, A. J. Meltzner, K. Sieh, P. Fang, Z. Li, J. Galetzka, J. Genrich, M. Chlieh, D. H. Natawidjaja, Y. Bock, E. J. Fielding, C. Ji & D. V. Helmberger (2008). “Partial Rupture of a Locked Patch of the Sumatra Megathrust during the 2007 Earthquake Sequence”. In: *Nature*, 456(7222). DOI: 10.1038/nature07572.

Kreemer, C., G. Blewitt & E. C. Klein (2014). “A Geodetic Plate Motion and Global Strain Rate Model”. In: *Geochem. Geophys. Geosystems*, 15. DOI: 10.1002/2014GC005407.

Kullback, S. & R. A. Leibler (1951). “On Information and Sufficiency”. In: *Ann. Math. Stat.*, 22(1). DOI: 10.1214/aoms/1177729694.

Lay, T. & S. P. Nishenko (2022). “Updated Concepts of Seismic Gaps and Asperities to Assess Great Earthquake Hazard along South America”. In: *Proc. Natl. Acad. Sci.*, 119(51). DOI: 10.1073/pnas.2216843119.

Lazecký, M., A. J. Hooper & P. Piromthong (2023). "InSAR-Derived Horizontal Velocities in a Global Reference Frame". In: *Geophys. Res. Lett.*, 50(10). DOI: 10.1029/2022GL101173.

Lazecký, M., K. Spaans, P. J. González, Y. Maghsoudi, Y. Morishita, F. Albino, J. Elliott, N. Greenall, E. Hatton, A. Hooper, D. Juncu, A. McDougall, R. J. Walters, C. S. Watson, J. R. Weiss & T. J. Wright (2020). "LiCSAR: An Automatic InSAR Tool for Measuring and Monitoring Tectonic and Volcanic Activity". In: *Remote Sens,* 12. DOI: 10.3390/rs12152430.

Le Beon, M., Y. Klinger, A. Q. Amrat, A. Agnon, L. Dorbath, G. Baer, J.-C. Ruegg, O. Charade & O. Mayyas (2008). "Slip Rate and Locking Depth from GPS Profiles across the Southern Dead Sea Transform". In: *J. Geophys. Res.: Solid Earth*, 113(B11). DOI: 10.1029/2007jb005280.

Le Cam, L. (1986). *Asymptotic Methods in Statistical Decision Theory*. New York: Springer. DOI: 10.1007/978-1-4612-4946-7.

Le Pichon, X. & C. Kreemer (2010). "The Miocene-to-Present Kinematic Evolution of the Eastern Mediterranean and Middle East and Its Implications for Dynamics". In: *Annu. Rev. Earth Planet. Sci.*, 38. DOI: 10.1146/annurev-earth-040809-152419.

Lefevre, M., Y. Klinger, M. Al-Qaryouti, M. Le Béon & K. Moumani (2018). "Slip Deficit and Temporal Clustering along the Dead Sea Fault from Paleoseismological Investigations". In: *Sci. Rep.*, 8(1). DOI: 10.1038/s41598-018-22627-9.

Lemrabet, L., M.-P. Doin, C. Lasserre & P. Durand (2023). "Referencing of Continental-Scale InSAR-derived Velocity Fields: Case Study of the Eastern Tibetan Plateau". In: *J. Geophys. Res.: Solid Earth*, 128. DOI: 10.1029/2022JB026251.

Li, X. (2023). "Present-Day Deformation of the Dead Sea Fault Using InSAR Analysis". PhD thesis. King Abdullah University of Science and Technology.

Li, X., S. Jónsson & Y. Cao (2021). "Interseismic Deformation from Sentinel-1 Burst-Overlap Interferometry: Application to the Southern Dead Sea Fault". In: *Geophys. Res. Lett.*, 48. DOI: 10.1029/2021GL093481.

Li, X., S. Jónsson, S. Liu, Z. Ma, N. Castro-Perdomo, S. Cesca, F. Masson & Y. Klinger (2024). "Resolving the Slip-Rate Inconsistency of the Northern Dead Sea Fault". In: *Sci. Adv.*, 10. DOI: 10.1126/sciadv.adj8408.

Liang, C., P. Agram, M. Simons & E. J. Fielding (2019). "Ionospheric Correction of InSAR Time Series Analysis of C-band Sentinel-1 TOPS Data". In: *IEEE Trans. Geosci. Remote Sens.*, 57. DOI: 10.1109/TGRS.2019.2908494.

Lin, Y. N., R. Jolivet, M. Simons, P. S. Agram, H. R. Martens, Z. Li & S. H. Lodi (2015). "High Interseismic Coupling in the Eastern Makran (Pakistan) Subduction Zone". In: *Earth Planet. Sci. Lett.*, 420. DOI: 10.1016/j.epsl.2015.03.037.

Lin, Y. N., A. Sladen, F. Ortega-Culaciati, M. Simons, J.-P. Avouac, E. J. Fielding, B. A. Brooks, M. Bevis, J. Genrich, A. Rietbrock, C. Vigny, R. Smalley & A. Socquet (2013). "Coseismic and Postseismic Slip Associated with the 2010 Maule Earthquake, Chile: Characterizing the Arauco Peninsula Barrier Effect". In: *J. Geophys. Res.: Solid Earth*, 118(6). DOI: 10.1002/jgrb.50207.

Liu, F., J. R. Elliott, S. K. Ebmeier, T. J. Craig, A. Hooper, C. Novoa Lizama & F. Delgado (2023). "First Onset of Unrest Captured at Socompa: A Recent Geodetic Survey at Central Andean Volcanoes in Northern Chile". In: *Geophys. Res. Lett.*, 50(10). DOI: 10.1029/2022GL102480.

Liu, S., Z.-K. Shen, R. Bürgmann & S. Jónsson (2021). "Thin Crème Brûlée Rheological Structure for the Eastern California Shear Zone". In: *Geology*, 49(2). DOI: 10.1130/G47729.1.

Liu, Y.-K., Z. E. Ross, E. S. Cochran & N. Lapusta (2022). "A Unified Perspective of Seismicity and Fault Coupling along the San Andreas Fault". In: *Sci. Adv.*, 8(8). DOI: 10.1126/sciadv.abk1167.

Liu, Y.-K., Z. Yunjun & M. Simons (2025). "Inferring Tectonic Plate Rotations From InSAR Time Series". In: *Geophys. Res. Lett.*, 52(12). DOI: 10.1029/2025GL115137.

Lohman, R. B. & M. Simons (2005). "Some Thoughts on the Use of InSAR Data to Constrain Models of Surface Deformation: Noise Structure and Data Downsampling". In: *Geochem. Geophys. Geosyst.*, 6. DOI: 10.1029/2004GC000841.

Loveless, J. P. & B. J. Meade (2010). "Geodetic Imaging of Plate Motions, Slip Rates, and Partitioning of Deformation in Japan". In: *J. Geophys. Res.: Solid Earth*, 115. DOI: 10.1029/2008JB006248.

Lovery, B., M. Chlieh, E. Norabuena, J. C. Villegas-Lanza, M. Radiguet, N. Cotte, A. Tsapong-Tsague, W. Quiroz, C. Sierra Farfán, M. Simons, J. M. Nocquet, H. Tavera & A. Socquet (2024). "Heterogeneous Locking and Earthquake Potential on the South Peru Megathrust From Dense GNSS Network". In: *J. Geophys. Res.: Solid Earth*, 129(2). DOI: 10.1029/2023jb027114.

Luo, H. & K. Wang (2021). "Postseismic Geodetic Signature of Cold Forearc Mantle in Subduction Zones". In: *Nat. Geosci.*, 14(2). DOI: 10.1038/s41561-020-00679-9.

Luo, H., K. Wang, L. Feng & E. M. Hill (2025). "Interseismic Secondary Zone of Subsidence during Earthquake Cycles in Subduction Zones". In: *Nat. Geosci.* DOI: 10.1038/s41561-025-01778-1.

Lüth, S. & P. Wigger (2010). "A Crustal Model along 39°S from a Seismic Refraction Profile- ISSA 2000". In: *Andean Geol.*, 30(1).

Mahmoud, S., R. Reilinger, S. McClusky, P. Vernant & A. Tealeb (2005). “GPS Evidence for Northward Motion of the Sinai Block: Implications for E. Mediterranean Tectonics”. In: *Earth Planet. Sci. Lett.*, 238. DOI: 10.1016/j.epsl.2005.06.063.

Marsan, D., M. Bouchon, B. Gardonio, H. Perfettini, A. Socquet & B. Enescu (2017). “Change in Seismicity along the Japan Trench, 1990–2011, and Its Relationship with Seismic Coupling”. In: *J. Geophys. Res.: Solid Earth*, 122(6). DOI: 10.1002/2016JB013715.

Marsan, D., E. Prono & A. Helmstetter (2013). “Monitoring Aseismic Forcing in Fault Zones Using Earthquake Time Series”. In: *Bull. Seismol. Soc. Am.*, 103(1). DOI: 10.1785/0120110304.

Martens, H. R., L. Rivera & M. Simons (2019). “LoadDef: A Python-Based Toolkit to Model Elastic Deformation Caused by Surface Mass Loading on Spherically Symmetric Bodies”. In: *Earth Space Sci.*, 6(2). DOI: 10.1029/2018EA000462.

Massonnet, D. & K. L. Feigl (1998). “Radar Interferometry and Its Application to Changes in the Earth’s Surface”. In: *Rev. Geophys.*, 36. DOI: 10.1029/97RG03139.

Massonnet, D., M. Rossi, C. Carmona, F. Adragna, G. Peltzer, K. Feigl & T. Rabaute (1993). “The Displacement Field of the Landers Earthquake Mapped by Radar Interferometry”. In: *Nature*, 364. DOI: 10.1038/364138a0.

Maurer, J. & K. Johnson (2014). “Fault Coupling and Potential for Earthquakes on the Creeping Section of the Central San Andreas Fault”. In: *J. Geophys. Res.: Solid Earth*, 119(5). DOI: 10.1002/2013JB010741.

McCaffrey, R. (2005). “Block Kinematics of the Pacific–North America Plate Boundary in the Southwestern United States from Inversion of GPS, Seismological, and Geologic Data”. In: *J. Geophys. Res.: Solid Earth*, 110. DOI: 10.1029/2004JB003307.

McKenzie, D. P. & R. L. Parker (1967). “The North Pacific: An Example of Tectonics on a Sphere”. In: *Nature*, 216. DOI: 10.1038/2161276a0.

McLaskey, G. C. & S. D. Glaser (2011). “Micromechanics of Asperity Rupture during Laboratory Stick Slip Experiments”. In: *Geophys. Res. Lett.*, 38(12). DOI: 10.1029/2011GL047507.

Meade, B. J. & J. P. Loveless (2009). “Block Modeling with Connected Fault-Network Geometries and a Linear Elastic Coupling Estimator in Spherical Coordinates”. In: *Bull. Seismol. Soc. Am.*, 99. DOI: 10.1785/0120090088.

Métois, M., A. Socquet & C. Vigny (2012). “Interseismic Coupling, Segmentation and Mechanical Behavior of the Central Chile Subduction Zone”. In: *J. Geophys. Res.: Solid Earth*, 117(B3). DOI: 10.1029/2011JB008736.

Métois, M., A. Socquet, C. Vigny, D. Carrizo, S. Peyrat, A. Delorme, E. Maureira, M.-C. Valderas-Bermejo & I. Ortega (2013). "Revisiting the North Chile Seismic Gap Segmentation Using GPS-derived Interseismic Coupling". In: *Geophys. J. Int.*, 194(3). DOI: 10.1093/gji/ggt183.

Métois, M., C. Vigny & A. Socquet (2016). "Interseismic Coupling, Megathrust Earthquakes and Seismic Swarms Along the Chilean Subduction Zone (38°–18°S)". In: *Pure Appl. Geophys.*, 173(5). DOI: 10.1007/s00024-016-1280-5.

Métois, M., C. Vigny, A. Socquet, A. Delorme, S. Morvan, I. Ortega & C.-M. Valderas-Bermejo (2014). "GPS-derived Interseismic Coupling on the Subduction and Seismic Hazards in the Atacama Region, Chile". In: *Geophys. J. Int.*, 196(2). DOI: 10.1093/gji/ggt418.

Meyer, F. (2010). "A Review of Ionospheric Effects in Low-Frequency SAR — Signals, Correction Methods, and Performance Requirements". In: *2010 IEEE Int. Geosci. Remote Sens. Symp.* DOI: 10.1109/IGARSS.2010.5654258.

Milbert, D. (2018). *Solid Earth Tide*.

Minchew, B. M., M. Simons, B. Riel & P. Milillo (2017). "Tidally Induced Variations in Vertical and Horizontal Motion on Rutford Ice Stream, West Antarctica, Inferred from Remotely Sensed Observations". In: *J. Geophys. Res.: Earth Surf.*, 122(1). DOI: 10.1002/2016JF003971.

Minson, S. E., M. Simons & J. L. Beck (2013). "Bayesian Inversion for Finite Fault Earthquake Source Models I—Theory and Algorithm". In: *Geophys. J. Int.*, 194(3). DOI: 10.1093/gji/ggt180.

Molchan, G. (2005). "Interevent Time Distribution in Seismicity: A Theoretical Approach". In: *Pure Appl. Geophys.*, 162(6-7). DOI: 10.1007/s00024-004-2664-5.

Moore, D. E. & M. J. Rymer (2007). "Talc-Bearing Serpentinite and the Creeping Section of the San Andreas Fault". In: *Nature*, 448(7155). DOI: 10.1038/nature06064.

Moreno, M., D. Melnick, M. Rosenau, J. Bolte, J. Klotz, H. Echtler, J. Baez, K. Bataille, J. Chen, M. Bevis, H. Hase & O. Oncken (2011). "Heterogeneous Plate Locking in the South–Central Chile Subduction Zone: Building up the next Great Earthquake". In: *Earth Planet. Sci. Lett.*, 305(3). DOI: 10.1016/j.epsl.2011.03.025.

Moreno, M., M. Rosenau & O. Oncken (2010). "2010 Maule Earthquake Slip Correlates with Pre-Seismic Locking of Andean Subduction Zone". In: *Nature*, 467(7312). DOI: 10.1038/nature09349.

Morgan, W. J. (1968). "Rises, Trenches, Great Faults, and Crustal Blocks". In: *J. Geophys. Res.-space Phys. 1896-1977*, 73. DOI: 10.1029/JB073i006p01959.

Münchmeyer, J., D. Molina-Ormazabal, M. Radiguet, D. Marsan, J.-C. Baez, F. Ortega-Culaciati, A. Tassara, M. Moreno & A. Socquet (2025). "Seismic Swarms Unveil the Mechanisms Driving Shallow Slow Slip Dynamics in the Copiapó Ridge, Northern Chile". In: *Geophys. Res. Lett.*, 52(8). DOI: 10.1029/2024GL113953.

Muto, K. (1932). "A Study of Displacements of Triangulation Points". In: *Bull, Earthq, Res, Inst, Univ, Tokyo*, 10.

Nadeau, R. M. & T. V. McEvilly (2004). "Periodic Pulsing of Characteristic Microearthquakes on the San Andreas Fault". In: *Science*, 303(5655). DOI: 10.1126/science.1090353.

Neal, R. M. (2011). "MCMC Using Hamiltonian Dynamics". In: *Handbook of Markov Chain Monte Carlo*. Chapman and Hall/CRC.

Neely, W. R., A. A. Borsa & F. Silverii (2020). "GInSAR: A cGPS Correction for Enhanced InSAR Time Series". In: *IEEE Trans. Geosci. Remote Sens.*, 58. DOI: 10.1109/TGRS.2019.2934118.

Noda, H. & N. Lapusta (2013). "Stable Creeping Fault Segments Can Become Destructive as a Result of Dynamic Weakening". In: *Nature*, 493(7433). DOI: 10.1038/nature11703.

Nof, R. N., A. Ziv, M.-P. Doin, G. Baer, Y. Fialko, S. Wdowinski, Y. Eyal & Y. Bock (2012). "Rising of the Lowest Place on Earth Due to Dead Sea Water-Level Drop: Evidence from SAR Interferometry and GPS". In: *J. Geophys. Res.: Solid Earth*, 117. DOI: 10.1029/2011JB008961.

Noll, C. E. (2010). "The Crustal Dynamics Data Information System: A Resource to Support Scientific Analysis Using Space Geodesy". In: *Adv. Space Res.*, 45. DOI: 10.1016/j.asr.2010.01.018.

Ogata, Y. (1988). "Statistical Models for Earthquake Occurrences and Residual Analysis for Point Processes". In: *J. Am. Stat. Assoc.*, 83(401). DOI: 10.1080/01621459.1988.10478560.

Ogata, Y. (1999). "Seismicity Analysis through Point-Process Modeling: A Review". In: *Seism. patterns their stat. significance phys. mean.* DOI: 10.1007/978-3-0348-8677-2_14.

Oliver-Cabrera, T., C. E. Jones, Z. Yunjun & M. Simard (2022). "InSAR Phase Unwrapping Error Correction for Rapid Repeat Measurements of Water Level Change in Wetlands". In: *IEEE Trans, Geosci, Remote Sens.*, 60. DOI: 10.1109/TGRS.2021.3108751.

Onn, F. & H. A. Zebker (2006). "Correction for Interferometric Synthetic Aperture Radar Atmospheric Phase Artifacts Using Time Series of Zenith Wet Delay Observations from a GPS Network". In: *J. Geophys. Res.: Solid Earth*, 111. DOI: 10.1029/2005JB004012.

Ortega-Culaciati, F., M. Simons, J. Ruiz, L. Rivera & N. Díaz-Salazar (2021). "An EPIC Tikhonov Regularization: Application to Quasi-Static Fault Slip Inversion". In: *J. Geophys. Res.: Solid Earth*, 126(7). DOI: 10.1029/2020JB021141.

Ou, Q., S. Daout, J. R. Weiss, L. Shen, M. Lazecký, T. J. Wright & B. E. Parsons (2022). "Large-Scale Interseismic Strain Mapping of the NE Tibetan Plateau From Sentinel-1 Interferometry". In: *J. Geophys. Res.: Solid Earth*, 127(6). DOI: 10.1029/2022JB024176.

Ozawa, S., T. Nishimura, H. Suito, T. Kobayashi, M. Tobita & T. Imakiire (2011). "Coseismic and Postseismic Slip of the 2011 Magnitude-9 Tohoku-Oki Earthquake". In: *Nature*, 475(7356). DOI: 10.1038/nature10227.

Pacheco, J. F., L. R. Sykes & C. H. Scholz (1993). "Nature of Seismic Coupling along Simple Plate Boundaries of the Subduction Type". In: *J. Geophys. Res.: Solid Earth*, 98(B8). DOI: 10.1029/93JB00349.

Parizzi, A., R. Brcic & F. De Zan (2021). "InSAR Performance for Large-Scale Deformation Measurement". In: *IEEE Trans. Geosci. Remote Sens.*, 59. DOI: 10.1109/TGRS.2020.3039006.

Peng, W., Q. Wang & Y. Cao (2017). "Analysis of Ocean Tide Loading in Differential InSAR Measurements". In: *Remote Sens.*, 9(2). DOI: 10.3390/rs9020101.

Peter, H. (2021). *Copernicus Sentinel-1, -2 and -3 Precise Orbit Determination Service (CPOD)*. Handbook. European Space Agency (ESA).

Peter, H. (2023). *3rd Generation of the Copernicus Precise Orbit Determination Service (CPOD3)*. Handbook. European Space Agency (ESA).

Peter, H., J. Fernández & P. Féménias (2020). "Copernicus Sentinel-1 Satellites: Sensitivity of Antenna Offset Estimation to Orbit and Observation Modelling". In: *Adv. Geosci.*, 50. DOI: 10.5194/adgeo-50-87-2020.

Peter, H., M. Fernández, D. Arnold, B. Duan, W. Simons, F. Gini, M. Wermuth, S. Hackel, J. Fernández, A. Jäggi, U. Hugentobler, P. Visser, R. Zandbergen & P. Féménias (2021). *Copernicus POD Service - Orbit Reprocessing for Copernicus Sentinel-1 Satellites*. DOI: 10.5194/egusphere-egu21-5296.

Peyrat, S., J. Campos, J. B. de Chabalier, A. Perez, S. Bonvalot, M.-P. Bouin, D. Legrand, A. Nercessian, O. Charade, G. Patau, E. Clévédé, E. Kausel, P. Bernard & J.-P. Vilotte (2006). "Tarapacá Intermediate-Depth Earthquake (Mw 7.7, 2005, Northern Chile): A Slab-Pull Event with Horizontal Fault Plane Constrained from Seismologic and Geodetic Observations". In: *Geophys. Res. Lett.*, 33(22). DOI: 10.1029/2006GL027710.

Piersanti, A., C. Nostro & F. Riguzzi (2001). "Active Displacement Field in the Suez–Sinai Area: The Role of Postseismic Deformation". In: *Earth Planet. Sci. Lett.*, 193(1-2). DOI: 10.1016/S0012-821X(01)00485-X.

Pietrantonio, G., R. Devoti, S. Mahmoud & F. Riguzzi (2016). “Kinematics of the Suez-Sinai Area from Combined GPS Velocity Field”. In: *J. Geodyn.*, 102. DOI: 10.1016/j.jog.2016.10.003.

Popescu, R., N. Anantrasirichai & J. Biggs (2025). “Unsupervised Anomaly Detection for Volcanic Deformation in InSAR Imagery”. In: *Earth Space Sci.*, 12(6). DOI: 10.1029/2024EA003892.

Popescu, R. G., N. Anantrasirichai & J. Biggs (2024). “Anomaly Detection for the Identification of Volcanic Unrest in Satellite Imagery: 31st IEEE International Conference on Image Processing, ICIP 2024”. In: *2024 IEEE Int. Conf. Image Process. ICIP 2024 - Proc.* DOI: 10.1109/ICIP51287.2024.10647957.

Pritchard, M. E., E. O. Norabuena, C. Ji, R. Boroschek, D. Comte, M. Simons, T. H. Dixon & P. A. Rosen (2007). “Geodetic, Teleseismic, and Strong Motion Constraints on Slip from Recent Southern Peru Subduction Zone Earthquakes”. In: *J. Geophys. Res.: Solid Earth*, 112(B3). DOI: 10.1029/2006JB004294.

Pritchard, M. E. & M. Simons (2004). “An InSAR-based Survey of Volcanic Deformation in the Southern Andes”. In: *Geophys. Res. Lett.*, 31(15). DOI: 10.1029/2004GL020545.

Pritchard, M. E. & M. Simons (2006). “An Aseismic Slip Pulse in Northern Chile and Along-Strike Variations in Seismogenic Behavior”. In: *J. Geophys. Res.: Solid Earth*, 111. DOI: 10.1029/2006JB004258.

Pritchard, M. E. & M. Simons (2002). “A Satellite Geodetic Survey of Large-Scale Deformation of Volcanic Centres in the Central Andes”. In: *Nature*, 418(6894). DOI: 10.1038/nature00872.

Pritchard, M. E. (2003). “Recent Crustal Deformation in West-Central South America”. PhD thesis. United States – California: California Institute of Technology.

Ragon, T., A. Sladen & M. Simons (2018). “Accounting for Uncertain Fault Geometry in Earthquake Source Inversions – I: Theory and Simplified Application”. In: *Geophys. J. Int.*, 214. DOI: 10.1093/gji/ggy187.

Ragon, T., A. Sladen & M. Simons (2019). “Accounting for Uncertain Fault Geometry in Earthquake Source Inversions – II: Application to the Mw 6.2 Amatrice Earthquake, Central Italy”. In: *Geophys. J. Int.*, 218. DOI: 10.1093/gji/ggz180.

Reid, H. F. (1910). “The California Earthquake of April 18, 1906”. In: *Report of the State Earthquake Investigation Commission*, 2.

Reilinger, R., S. McClusky, P. Vernant, S. Lawrence, S. Ergintav, R. Cakmak, H. Ozener, F. Kadirov, I. Guliev, R. Stepanyan, M. Nadariya, G. Hahubia, S. Mahmoud, K. Sakr, A. ArRajehi, D. Paradissis, A. Al-Aydrus, M. Prilepin, T. Guseva, E. Evren, A. Dmitrotsa, S. V. Filikov, F. Gomez, R. Al-Ghazzi & G. Karam (2006). “GPS Constraints on Continental Deformation in the Africa-arabia-eurasia Continental Collision Zone and Implications for the Dynamics

of Plate Interactions". In: *J. Geophys. Res.: Space Phys.*, 111. DOI: 10.1029/2005JB004051.

Ribot, M. (2021). "Quantification of the tectonic uplift in the Gulf of Aqaba, Levant fault". PhD thesis. Université Paris Cité.

Ribot, M., Y. Klinger, S. Jónsson, U. Avsar, E. Pons-Branchu, R. Matrau & F. L. Mallon (2021). "Active Faults' Geometry in the Gulf of Aqaba, Southern Dead Sea Fault, Illuminated by Multibeam Bathymetric Data". In: *Tectonics*, 40(4). DOI: 10.1029/2020tc006443.

Ribot, M., M. Lefèvre, Y. Klinger, E. Pons-Branchu, A. Dapoigny & S. Jónsson (2024). "Vertical Deformation Along a Strike-Slip Plate Boundary: The Uplifted Marine Terraces of the Gulf of Aqaba and Tiran Island, at the Southern End of the Dead Sea Fault". In: *Tectonics*, 43(9). DOI: 10.1029/2023TC007977.

Riel, B., P. Milillo, M. Simons, P. Lundgren, H. Kanamori & S. Samsonov (2015). "The Collapse of Bárðarbunga Caldera, Iceland". In: *Geophys. J. Int.*, 202(1). DOI: 10.1093/gji/ggv157.

Rikuti, S. (1930). "Re-Survey of the Kwanto District after the Great Earthquake of 1923". In: *Bull. Imp. Earthq. Investig. Comm.*, 11.

Rosen, P. A., G. W. Bawden, P. Barela, B. Chapman, H. Fattahi, C. E. Jones, I. R. Joughin, M. Lavalle, R. B. Lohman, M. Simons, et al. (2025). "The NASA-ISRO SAR Mission: A Summary". In: *IEEE Geosci. Remote Sens. Mag.* DOI: 10.1109/MGRS.2025.3578258.

Rosen, P. A., E. Gurrola, G. F. Sacco & H. Zebker (2012). "The InSAR Scientific Computing Environment". In: *EUSAR 2012 9th Eur. Conf. Synth. Aperture Radar*.

Rosen, P. A. & R. Kumar (2021). "NASA-ISRO SAR (NISAR) Mission Status". In: *2021 IEEE Radar Conf. RadarConf21*. DOI: 10.1109/RadarConf2147009.2021.9455211.

Ross, Z. E., E. Hauksson & Y. Ben-Zion (2017). "Abundant Off-Fault Seismicity and Orthogonal Structures in the San Jacinto Fault Zone". In: *Sci. Adv.*, 3(3). DOI: 10.1126/sciadv.1601946.

Rousset, B., R. Jolivet, M. Simons, C. Lasserre, B. Riel, P. Milillo, Z. Çakir & F. Renard (2016). "An Aseismic Slip Transient on the North Anatolian Fault". In: *Geophys. Res. Lett.*, 43(7). DOI: 10.1002/2016GL068250.

Rubin, A. M., D. Gillard & J. L. Got (1999). "Streaks of Microearthquakes along Creeping Faults". In: *Nature*, 400(6745). DOI: 10.1038/23196.

Ruch, J. & T. R. Walter (2010). "Relationship between the InSAR-measured Uplift, the Structural Framework, and the Present-Day Stress Field at Lazufre Volcanic Area, Central Andes". In: *Tectonophysics*, 492(1). DOI: 10.1016/j.tecto.2010.06.003.

Ruch, J., J. Warren, F. Risacher, T. Walter & R. Lanari (2012). “Salt Lake Deformation Detected from Space”. In: *Earth Planet. Sci. Lett.*, 331–332. DOI: 10.1016/j.epsl.2012.03.009.

Ruegg, J. C., A. Rudloff, C. Vigny, R. Madariaga, J. B. de Chabalier, J. Campos, E. Kausel, S. Barrientos & D. Dimitrov (2009). “Interseismic Strain Accumulation Measured by GPS in the Seismic Gap between Constitución and Concepción in Chile”. In: *Phys. Earth Planet. Inter.*, 175(1). DOI: 10.1016/j.pepi.2008.02.015.

Ruiz, J. A., G. P. Hayes, D. Carrizo, H. Kanamori, A. Socquet & D. Comte (2014). “Seismological Analyses of the 2010 March 11, Pichilemu, Chile Mw 7.0 and Mw 6.9 Coastal Intraplate Earthquakes”. In: *Geophys. J. Int.*, 197(1). DOI: 10.1093/gji/ggt513.

Ryder, I. & R. Bürgmann (2008). “Spatial Variations in Slip Deficit on the Central San Andreas Fault from InSAR”. In: *Geophys. J. Int.*, 175(3). DOI: 10.1111/j.1365-246X.2008.03938.x.

Ryder, I., B. Parsons, T. J. Wright & G. J. Funning (2007). “Post-Seismic Motion Following the 1997 Manyi (Tibet) Earthquake: InSAR Observations and Modelling”. In: *Geophys. J. Int.*, 169. DOI: 10.1111/j.1365-246X.2006.03312.x.

Saffer, D. M. & L. M. Wallace (2015). “The Frictional, Hydrologic, Metamorphic and Thermal Habitat of Shallow Slow Earthquakes”. In: *Nat. Geosci.*, 8(8). DOI: 10.1038/ngeo2490.

Sanders, C. O. & H. Kanamori (1984). “A Seismotectonic Analysis of the Anza Seismic Gap, San Jacinto Fault Zone, Southern California”. In: *J. Geophys. Res.: Solid Earth*, 89(B7). DOI: 10.1029/JB089iB07p05873.

Sandwell, D., R. Mellors, X. Tong, M. Wei & P. Wessel (2011). “Open Radar Interferometry Software for Mapping Surface Deformation”. In: *EOS Trans. Trans. Am. Geophys. Union*, 92(28). DOI: 10.1029/2011EO280002.

Sanz Subirana, J., J. Juan Zornoza & M. Hernández-Pajares (2011a). *Ellipsoidal and Cartesian Coordinates Conversion - Navipedia*.

Sanz Subirana, J., J. Juan Zornoza & M. Hernández-Pajares (2011b). *Transformations between ECEF and ENU Coordinates - Navipedia*.

Sanz-Alonso, D., A. M. Stuart & A. Taeb (2023). *Inverse Problems and Data Assimilation*. DOI: 10.48550/arXiv.1810.06191. arXiv: 1810.06191 [stat].

Savage, J. C. (1983). “A Dislocation Model of Strain Accumulation and Release at a Subduction Zone”. In: *J. Geophys. Res.: Solid Earth*, 88(B6). DOI: 10.1029/jb088ib06p04984.

Savage, J. C. & R. O. Burford (1973). “Geodetic Determination of Relative Plate Motion in Central California”. In: *J. Geophys. Res.*, 78(5). DOI: 10.1029/JB078i005p00832.

Schaff, D. P. & F. Waldhauser (2005). “Waveform Cross-Correlation-Based Differential Travel-Time Measurements at the Northern California Seismic Network”. In: *Bull. Seismol. Soc. Am.*, 95(6). DOI: 10.1785/0120040221.

Scholz, C. H. (1998). “Earthquakes and Friction Laws”. In: *Nature*, 391(6662). DOI: 10.1038/34097.

Schurr, B., G. Asch, S. Hainzl, J. Bedford, A. Hoechner, M. Palo, R. Wang, M. Moreno, M. Bartsch, Y. Zhang, O. Oncken, F. Tilmann, T. Dahm, P. Victor, S. Barrientos & J.-P. Vilotte (2014). “Gradual Unlocking of Plate Boundary Controlled Initiation of the 2014 Iquique Earthquake”. In: *Nature*, 512(7514). DOI: 10.1038/nature13681.

Schwartz, D. P. (2018). “Past and Future Fault Rupture Lengths in Seismic Source Characterization—the Long and Short of It”. In: *Bull. Seismol. Soc. Am.*, 108(5A). DOI: 10.1785/0120160110.

Segall, P. (2010). *Earthquake and Volcano Deformation*. Princeton University Press. DOI: 10.1515/9781400833856.

Shannon, C. E. (1948). “A Mathematical Theory of Communication”. In: *Bell Syst. Tech. J.*, 27. DOI: 10.1002/j.1538-7305.1948.tb01338.x.

Shearer, P. M. (2002). “Parallel Fault Strands at 9-Km Depth Resolved on the Imperial Fault, Southern California”. In: *Geophys. Res. Lett.*, 29(14). DOI: 10.1029/2002GL015302.

Shelly, D. R. (2010). “Migrating Tremors Illuminate Complex Deformation beneath the Seismogenic San Andreas Fault”. In: *Nature*, 463(7281). DOI: 10.1038/nature08755.

Sieh, K. E. (1978). “Slip along the San Andreas Fault Associated with the Great 1857 Earthquake”. In: *Bull. Seismol. Soc. Am.*, 68(5).

Sieh, K. E. & R. H. Jahns (1984). “Holocene Activity of the San Andreas Fault at Wallace Creek, California”. In: *Geol. Soc. Am. Bull.*, 95(8). DOI: 10.1130/0016-7606(1984)95<883:HAOTSA>2.0.CO;2.

Simoes, M., J. P. Avouac & Y.-G. Chen (2007). “Slip Rates on the Chelungpu and Chushiang Thrust Faults Inferred from a Deformed Strath Terrace along the Dungpuna River, West Central Taiwan”. In: *J. Geophys. Res.: Solid Earth*, 112(B3). DOI: 10.1029/2005JB004200.

Simons, M. (2002). “Coseismic Deformation from the 1999 Mw 7.1 Hector Mine, California, Earthquake as Inferred from InSAR and GPS Observations”. In: *Bull. Seismol. Soc. Am.*, 92(4). DOI: 10.1785/0120000933.

Simons, M., Y. Fialko & L. Rivera (2002). “Coseismic Deformation from the 1999 Mw 7.1 Hector Mine, California, Earthquake as Inferred from InSAR and GPS Observations”. In: *Bull. Seismol. Soc. Am.*, 92. DOI: 10.1785/0120000933.

Simons, M. & P. Rosen (2015). "Interferometric Synthetic Aperture Radar Geodesy". In: *Treatise on Geophysics*. Elsevier. DOI: 10.1016/B978-0-444-53802-4.00061-0.

Sippl, C., A. Dielforder, T. John & S. M. Schmalholz (2022). "Global Constraints on Intermediate-Depth Intraslab Stresses from Slab Geometries and Mechanisms of Double Seismic Zone Earthquakes". In: *Geochem. Geophys. Geosyst.*, 23(9). DOI: 10.1029/2022GC010498.

Sladen, A., H. Tavera, M. Simons, J. P. Avouac, A. O. Konca, H. Perfettini, L. Audin, E. J. Fielding, F. Ortega & R. Cavagnoud (2010). "Source Model of the 2007 Mw 8.0 Pisco, Peru Earthquake: Implications for Seismogenic Behavior of Subduction Megathrusts". In: *J. Geophys. Res.: Solid Earth*, 115(B2). DOI: 10.1029/2009JB006429.

Socquet, A., D. Molina, J. Münchmeyer, M. Radiguet, M.-P. Doin, D. Marsan, A. Vezinet, M. Moreno, J. C. C. Baez, F. Ortega, A. Tassara & N. Hernandez Soto (2024). "Deep and Shallow Slow Slip Events Imaged by GNSS and Seismicity in Copiapo Ridge, Chile : Kinematics and Segmentation Driven by Interactions between Fluids and Subducted Seamounts". In: *AGU Fall Meeting Abstracts*. Vol. 2024.

Stephenson, O. L., Y.-K. Liu, Z. Yunjun, M. Simons, P. Rosen & X. Xu (2022). "The Impact of Plate Motions on Long-Wavelength InSAR-derived Velocity Fields". In: *Geophys. Res. Lett.*, 49. DOI: 10.1029/2022GL099835.

Sudhaus, H. & S. Jónsson (2009). "Improved Source Modelling through Combined Use of InSAR and GPS under Consideration of Correlated Data Errors: Application to the June 2000 Kleifarvatn Earthquake, Iceland". In: *Geophys. J. Int.*, 176(2). DOI: 10.1111/j.1365-246X.2008.03989.x.

Sun, T., D. Saffer & S. Ellis (2020). "Mechanical and Hydrological Effects of Seamount Subduction on Megathrust Stress and Slip". In: *Nat. Geosci.*, 13(3). DOI: 10.1038/s41561-020-0542-0.

Tarantola, A. (2005). *Inverse Problem Theory and Methods for Model Parameter Estimation*. SIAM.

Tarantola, A. & B. Valette (1982). "Generalized Nonlinear Inverse Problems Solved Using the Least Squares Criterion". In: *Rev. Geophys.*, 20(2). DOI: 10.1029/RG020i002p00219.

Tarayre, H. & D. Massonnet (1996). "Atmospheric Propagation Heterogeneities Revealed by ERS-1 Interferometry". In: *Geophys. Res. Lett.*, 23. DOI: 10.1029/96GL00622.

Thomas, A. M., R. M. Nadeau & R. Bürgmann (2009). "Tremor-Tide Correlations and near-Lithostatic Pore Pressure on the Deep San Andreas Fault". In: *Nature*, 462(7276). DOI: 10.1038/nature08654.

Titus, S. J., C. DeMets & B. Tikoff (2006). "Thirty-Five-Year Creep Rates for the Creeping Segment of the San Andreas Fault and the Effects of the 2004 Parkfield Earthquake: Constraints from Alignment Arrays, Continuous Global Positioning System, and Creepmeters". In: *Bull. Seismol. Soc. Am.*, 96(4B). DOI: 10.1785/0120050811.

Titus, S. J., M. Dyson, C. DeMets, B. Tikoff, F. Rolandone & R. Bürgmann (2011). "Geologic versus Geodetic Deformation Adjacent to the San Andreas Fault, Central California". In: *Bull. Cl. Sci. Math. Nat. Sci. Math.*, 123(5-6).

Toké, N. A. & J. R. Arrowsmith (2013). *Paleoseismic Investigation along the Inferred Northernmost Extent of the 1857 Rupture: Do Large Southern San Andreas Fault (SAF) Ruptures Extend into the Creeping Section?* Tech. rep. SCEC Annual Report #12050.

Tong, X., D. T. Sandwell & B. Smith-Konter (2013a). "High-Resolution Interseismic Velocity Data along the San Andreas Fault from GPS and InSAR". In: *J. Geophys. Res.: Solid Earth*, 118(1). DOI: 10.1029/2012JB009442.

Tong, X., D. T. Sandwell & B. Smith-Konter (2013b). "High-Resolution Interseismic Velocity Data along the San Andreas Fault from GPS and InSAR". In: *J. Geophys. Res.: Solid Earth*, 118. DOI: 10.1029/2012JB009442.

Tong, X., B. Smith-Konter & D. T. Sandwell (2014). "Is There a Discrepancy between Geological and Geodetic Slip Rates along the San Andreas Fault System?" In: *J. Geophys. Res.: Solid Earth*, 119. DOI: 10.1002/2013JB010765.

Tough, J. A., D. Blacknell & S. Quegan (1995). "A Statistical Description of Polarimetric and Interferometric Synthetic Aperture Radar Data". In: *Proc. R. Soc. Lond. A*, 449. DOI: 10.1098/rspa.1995.0059.

Trubienko, O., L. Fleitout, J.-D. Garaud & C. Vigny (2013). "Interpretation of Interseismic Deformations and the Seismic Cycle Associated with Large Subduction Earthquakes". In: *Tectonophysics*, 589. DOI: 10.1016/j.tecto.2012.12.027.

Tsuboi, C. (1932). "Investigation on the Deformation of the Earth's Crust Found by Precise Geodetic Means". In: *Jpn. J. Astron. Geophys. Vol, 10 p, 93*, 10.

Tymofyeyeva, E. & Y. Fialko (2015). "Mitigation of Atmospheric Phase Delays in InSAR Data, with Application to the Eastern California Shear Zone". In: *J. Geophys. Res.: Solid Earth*, 120(8). DOI: 10.1002/2015JB011886.

U.S. Geological Survey and California Geological Survey (2006). "Quaternary Fault and Fold Database for the United States". In: *Quat. fault fold database U. S.*

Uchida, N. & R. Bürgmann (2019). "Repeating Earthquakes". In: *Annu. Rev. Earth Planet. Sci.*, 47(1). DOI: 10.1146/annurev-earth-053018-060119.

Uchida, N. & T. Matsuzawa (2013). "Pre- and Postseismic Slow Slip Surrounding the 2011 Tohoku-Oki Earthquake Rupture". In: *Earth Planet. Sci. Lett.*, 374. DOI: 10.1016/j.epsl.2013.05.021.

Utsu, T. & Y. Ogata (1995). "The Centenary of the Omori Formula for a Decay Law of Aftershock Activity". In: *J. Phys. Earth*, 43(1). DOI: 10.4294/jpe1952.43.1.

Vasyura-Bathke, H., J. Dettmer, R. Dutta, P. M. Mai & S. Jónsson (2021). "Accounting for Theory Errors with Empirical Bayesian Noise Models in Nonlinear Centroid Moment Tensor Estimation". In: *Geophys. J. Int.*, 225. DOI: 10.1093/gji/ggab034.

Vasyura-Bathke, H., A. Steinberg, F. Krüger, G. Feng, P. M. Mai & S. Jónsson (2024). "Discontinuous Transtensional Rupture during the Mw 7.2 1995 Gulf of Aqaba Earthquake". In: *Seismica*, 3. DOI: 10.26443/seismica.v3i1.1135.

Vigny, C., P. Huchon, J.-C. Ruegg, K. Khanbari & L. M. Asfaw (2006). "Confirmation of Arabia Plate Slow Motion by New GPS Data in Yemen". In: *J. Geophys. Res.: Solid Earth*, 111. DOI: 10.1029/2004JB003229.

Vigny, C., A. Rudloff, J.-C. Ruegg, R. Madariaga, J. Campos & M. Alvarez (2009). "Upper Plate Deformation Measured by GPS in the Coquimbo Gap, Chile". In: *Phys. Earth Planet. Inter.*, 175(1). DOI: 10.1016/j.pepi.2008.02.013.

Viltres, R., S. Jónsson, A. Alothman, S. Liu, S. Leroy, F. Masson, C. Doubre & R. Reilinger (2022). "Present-Day Motion of the Arabian Plate". In: *Tectonics*, 41. DOI: 10.1029/2021TC007013.

Virtanen, P., R. Gommers, T. E. Oliphant, M. Haberland, T. Reddy, D. Cournapeau, E. Burovski, P. Peterson, W. Weckesser, J. Bright, S. J. van der Walt, M. Brett, J. Wilson, K. J. Millman, N. Mayorov, A. R. J. Nelson, E. Jones, R. Kern, E. Larson, C. J. Carey, İ. Polat, Y. Feng, E. W. Moore, J. VanderPlas, D. Laxalde, J. Perktold, R. Cimrman, I. Henriksen, E. A. Quintero, C. R. Harris, A. M. Archibald, A. H. Ribeiro, F. Pedregosa, P. van Mulbregt & SciPy 1.0 Contributors (2020). "SciPy 1.0: Fundamental Algorithms for Scientific Computing in Python". In: *Nat. Methods*, 17. DOI: 10.1038/s41592-019-0686-2.

Wald, D. J., H. Kanamori, D. V. Helmberger & T. H. Heaton (1993). "Source Study of the 1906 San Francisco Earthquake". In: *Bull. Seismol. Soc. Am.*, 83(4). DOI: 10.1785/BSSA0830040981.

Waldhauser, F. (2009). "Near-Real-Time Double-Difference Event Location Using Long-Term Seismic Archives, with Application to Northern California". In: *Bull. Seismol. Soc. Am.*, 99(5). DOI: 10.1785/0120080294.

Waldhauser, F. & D. P. Schaff (2008). "Large-scale Relocation of Two Decades of Northern California Seismicity Using Cross-correlation and Double-difference Methods". In: *J. Geophys. Res.: Solid Earth*, 113(B8). DOI: 10.1029/2007JB005479.

Wang, K. & S. L. Bilek (2011). "Do Subducting Seamounts Generate or Stop Large Earthquakes?" In: *Geology*, 39(9). DOI: 10.1130/G31856.1.

Wang, K. & T. Dixon (2004a). ""Coupling" Semantics and Science in Earthquake Research". In: *EOS Trans. Trans. Am. Geophys. Union*, 85(18). DOI: 10.1029/2004EO180005.

Wang, K. & T. Dixon (2004b). ""Coupling" Semantics and Science in Earthquake Research". In: *EOS Trans. Trans. Am. Geophys. Union*, 85(18). DOI: 10.1029/2004EO180005.

Wang, K., Y. Hu, M. Bevis, E. Kendrick, R. Smalley Jr., R. B. Vargas & E. Lauría (2007). "Crustal Motion in the Zone of the 1960 Chile Earthquake: Detangling Earthquake-Cycle Deformation and Forearc-Sliver Translation". In: *Geochem. Geophys. Geosyst.*, 8(10). DOI: 10.1029/2007GC001721.

Wang, K., Y. Hu & J. He (2012). "Deformation Cycles of Subduction Earthquakes in a Viscoelastic Earth". In: *Nature*, 484(7394). DOI: 10.1038/nature11032.

Wang, R. (1999). "A Simple Orthonormalization Method for Stable and Efficient Computation of Green's Functions". In: *Bull. Seismol. Soc. Am.*, 89. DOI: 10.1785/BSSA0890030733.

Wang, R., F. Lorenzo-Martín & F. Roth (2003). "Computation of Deformation Induced by Earthquakes in a Multi-Layered Elastic Crust". In: *Comput. Geosci.*, 29. DOI: 10.1016/S0098-3004(02)00111-5.

Wang, R., F. Lorenzo-Martín & F. Roth (2006). "PSGRN/PSCMP—a New Code for Calculating Co- and Post-Seismic Deformation, Geoid and Gravity Changes Based on the Viscoelastic-Gravitational Dislocation Theory". In: *Comput. Geosci.*, 32. DOI: 10.1016/j.cageo.2005.08.006.

Watson, A. R., J. R. Elliott, M. Lazecký, Y. Maghsoudi, J. D. McGrath & R. J. Walters (2024). "An InSAR-GNSS Velocity Field for Iran". In: *Geophys. Res. Lett.*, 51(10). DOI: 10.1029/2024GL108440.

Wdowinski, S., Y. Bock, G. Baer, L. Prawirodirdjo, N. Bechor, S. Naaman, R. Knafo, Y. Forrai & Y. Melzer (2004). "GPS Measurements of Current Crustal Movements along the Dead Sea Fault". In: *J. Geophys. Res.: Solid Earth*, 109(B5). DOI: 10.1029/2003jb002640.

Weiss, J. R., B. A. Brooks, J. R. Arrowsmith & G. Vergani (2015). "Spatial and Temporal Distribution of Deformation at the Front of the Andean Orogenic Wedge in Southern Bolivia". In: *J. Geophys. Res.: Solid Earth*, 120(3). DOI: 10.1002/2014JB011763.

Weiss, J. R., R. J. Walters, Y. Morishita, T. J. Wright, M. Lazecky, H. Wang, E. Hussain, A. J. Hooper, J. R. Elliott, C. Rollins, C. Yu, P. J. González, K. Spaans, Z. Li & B. Parsons (2020). "High-Resolution Surface Velocities and Strain for Anatolia from Sentinel-1 InSAR and GNSS Data". In: *Geophys. Res. Lett.*, 47. DOI: 10.1029/2020GL087376.

Wiemer, S. & M. Wyss (2000). "Minimum Magnitude of Completeness in Earthquake Catalogs: Examples from Alaska, the Western United States, and Japan". In: *Bull. Seismol. Soc. Am.*, 90(4). DOI: 10.1785/0119990114.

Woessner, J. & S. Wiemer (2005). “Assessing the Quality of Earthquake Catalogues: Estimating the Magnitude of Completeness and Its Uncertainty”. In: *Bull. Seismol. Soc. Am.*, 95(2). DOI: 10.1785/0120040007.

Wright, T. J., B. E. Parsons & Z. Lu (2004). “Toward Mapping Surface Deformation in Three Dimensions Using InSAR”. In: *Geophys. Res. Lett.*, 31. DOI: 10.1029/2003GL018827.

Xu, X. & D. T. Sandwell (2020). “Toward Absolute Phase Change Recovery with InSAR: Correcting for Earth Tides and Phase Unwrapping Ambiguities”. In: *IEEE Trans. Geosci. Remote Sens.*, 58. DOI: 10.1109/TGRS.2019.2940207.

Xu, X., D. T. Sandwell, E. Klein & Y. Bock (2021). “Integrated Sentinel-1 InSAR and GNSS Time-Series along the San Andreas Fault System”. In: *J. Geophys. Res.: Solid Earth*, 126. DOI: 10.1029/2021JB022579.

Yáñez, G., J. Cembrano, M. Pardo, C. Ranero & D. Selles (2002). “The Challenger–Juan Fernández–Maipo Major Tectonic Transition of the Nazca–Andean Subduction System at 33–34°S: Geodynamic Evidence and Implications”. In: *J. South Am. Earth Sci.*, 15(1). DOI: 10.1016/S0895-9811(02)00004-4.

Yáñez-Cuadra, V., F. Ortega-Culaciati, M. Moreno, A. Tassara, N. Krumm-Nualart, J. Ruiz, A. Maksymowicz, M. Manea, V. C. Manea, J. Geng & R. Benavente (2022). “Interplate Coupling and Seismic Potential in the Atacama Seismic Gap (Chile): Dismissing a Rigid Andean Sliver”. In: *Geophys. Res. Lett.*, 49(11). DOI: 10.1029/2022GL098257.

Yang, W. & Y. Ben-Zion (2009). “Observational Analysis of Correlations between Aftershock Productivities and Regional Conditions in the Context of a Damage Rheology Model”. In: *Geophys. J. Int.*, 177(2). DOI: 10.1111/j.1365-246X.2009.04145.x.

Yu, C., N. T. Penna & Z. Li (2017). “Generation of Real-Time Mode High-Resolution Water Vapor Fields from GPS Observations”. In: *J. Geophys. Res. Atmospheres*, 122. DOI: 10.1002/2016JD025753.

Yu, C., N. T. Penna & Z. Li (2020). “Ocean Tide Loading Effects on InSAR Observations Over Wide Regions”. In: *Geophys. Res. Lett.*, 47(15). DOI: 10.1029/2020GL088184.

Yuan, X., S. V. Sobolev, R. Kind, O. Oncken, G. Bock, G. Asch, B. Schurr, F. Graeber, A. Rudloff, W. Hanka, K. Wylegalla, R. Tibi, C. Haberland, A. Rietbrock, P. Giese, P. Wigger, P. Röwer, G. Zandt, S. Beck, T. Wallace, M. Pardo & D. Comte (2000). “Subduction and Collision Processes in the Central Andes Constrained by Converted Seismic Phases”. In: *Nature*, 408(6815). DOI: 10.1038/35050073.

Yunjun, Z., H. Fattahi & F. Amelung (2019). “Small Baseline InSAR Time Series Analysis: Unwrapping Error Correction and Noise Reduction”. In: *Comput. Geosci.*, 133. DOI: 10.1016/j.cageo.2019.104331.

Yunjun, Z., H. Fattahi, X. Pi, P. Rosen, M. Simons, P. Agram & Y. Aoki (2022). "Range Geolocation Accuracy of C-/L-band SAR and Its Implications for Operational Stack Coregistration". In: *IEEE Trans. Geosci. Remote Sens.*, 60. DOI: 10.1109/TGRS.2022.3168509.

Zakharova, O., S. Hainzl, D. Lange & B. Enescu (2017). "Spatial Variations of Aftershock Parameters and Their Relation to Geodetic Slip Models for the 2010 Mw8.8 Maule and the 2011 Mw9.0 Tohoku-Oki Earthquakes". In: *Pure Appl. Geophys.*, 174(1). DOI: 10.1007/s00024-016-1408-7.

Zaliapin, I. & Y. Ben-Zion (2013). "Earthquake Clusters in Southern California I: Identification and Stability". In: *J. Geophys. Res.: Solid Earth*, 118(6). DOI: 10.1002/jgrb.50179.

Zebker, M. S., J. Chen & M. A. Hesse (2023). "Robust Surface Deformation and Tropospheric Noise Characterization From Common-Reference Interferogram Subsets". In: *IEEE Trans. Geosci. Remote Sens.*, 61. DOI: 10.1109/TGRS.2023.3288019.

Zhang, B., E. Hestir, Z. Yunjun, M. E. Reiter, J. H. Viers, D. Schaffer-Smith, K. Sesser & T. Oliver-Cabrera (2024). "Automated Reference Points Selection for InSAR Time Series Analysis on Segmented Wetlands". In: *IEEE Geosci. Remote Sens. Lett.*, 21. DOI: 10.1109/LGRS.2024.3390568.

Zheng, Y., H. Fattahi, P. Agram, M. Simons & P. Rosen (2022). "On Closure Phase and Systematic Bias in Multilooked SAR Interferometry". In: *IEEE Trans. Geosci. Remote Sens.*, 60. DOI: 10.1109/TGRS.2022.3167648.

Zhong, M., M. Simons, B. Minchew & L. Zhu (2023). "Inferring Tide-Induced Ephemeral Grounding in an Ice-Shelf-Stream System: Rutford Ice Stream, West Antarctica". In: *J. Geophys. Res.: Earth Surf.*, 128(2). DOI: 10.1029/2022JF006789.

Zhu, L. & L. A. Rivera (2002). "A Note on the Dynamic and Static Displacements from a Point Source in Multilayered Media: A Note on the Dynamic and Static Displacements from a Point Source". In: *Geophys. J. Int.*, 148(3). DOI: 10.1046/j.1365-246X.2002.01610.x.